UNIVERSITÀ
DEGLI STUDI
DI PADOVA

SEDE AMMINISTRATIVA: UNIVERSITÀ DEGLI STUDI DI PADOVA

DIPARTIMENTO DI SCIENZE CHIMICHE

CORSO DI DOTTORATO DI RICERCA IN SCIENZA ED INGEGNERIA DEI MATERIALI

CICLO XXIX

NITROGEN, SULPHUR AND PLATINUM FUNCTIONAL MESOPOROUS CARBONS: SYNTHESIS, CHARACTERIZATION AND PERFORMANCE TOWARD OXYGEN REDUCTION REACTION

COORDINATORE: Ch.mo Prof. Gaetano Granozzi

SUPERVISORE: Ch.mo Prof. Armando Gennaro

DOTTORANDA: Valentina Perazzolo

Index

Acronyms

AFC	Alkaline Fuel Cell
BE	Binding Energy
BET	Brunauer Emmett Teller
CA	Chrono Amperometry
CB	Carbon Black
CNT	Carbon Nanotube
CV	Cyclic Voltammetry
DFT	Density Functional Theory
DMFC	Direct Methanol Fuel Cell
DOMC	Disordered Mesoporous Carbon
ECSA	Electrochemical Surface Area
EW	Equivalent Weight
FC	Fuel Cell
FWHM	Full Wight Half Maximum
GC	Glassy Carbon
GDL	Gas Diffusion Layer
ICP	Inductively Coupled Plasma
IEC	Ion Exchange Capability
I/C	Ionomer/Carbon ratio
LSV	Linear Sweep Voltammetry
MA	Mass Activity
MEA	Membrane Electrode Assembly
MC	Mesoporous Carbon
MCFC	Molten Carbonate Fuel Cell
N-MC	Nitrogen doped Mesoporous Carbon
N,S-MC	Nitrogen and Sulfur doped Mesoporous Carbon
NP	Nanoparticle
NPG	Non Platinum Group
OMC	Ordered Mesoporous Carbon
ORR	Oxygen Reduction Reaction
PAFC	Phosphoric Acid Fuel Cell
PEM	Proton Exchange Membrane
PEMFC	Proton Exchange Membrane Fuel Cell
PFSA	Perfluorosulphonic Acid
PTFE	Polytetrafluoroethylene
RDE	Rotating Disk Electroe
RH	Relative Humidity
RHE	Reversible Hydrogen Electrode

RPM	Rotations Per Minute
RRDE	Rotating Ring Disk Electrode
S-MC	Sulfur doped Mesoporous Carbon
SA	Specific Activity
SCCM	Standard Cubic Centimeters per Minute
SCE	Saturated Calomel Electrode
SEM	Scanning Electron Microscopy
SOFC	Solid Oxide Fuel Cell
TEM	Trasmission Electron Microscopy
TGA	Thermogravimetric analysis
TKK	Tanaka, Pt on high surface area carbon, 46%$_w$
XPS	X-rays Photoelectron Spectroscopy

Abstract

Proton Exchange Membrane (PEM) Fuel Cells are a promising technology for the clean energy production, especially in the automotive field. Actually, the main commercial catalysts employed in this system are based on Pt Nanoparticles supported on high surface area Carbon. The main issues associated to PEM Fuel Cells deal with the sluggish kinetic of oxygen reduction (ORR) at Platinum based electrode, with the low stability of both the carbon support and the metal phase, that tend respectively to oxidize and dissolve or diffuse and with the high cost due to rare and expensive Pt. In fact, nowadays high costs and low durability are the two factors that make PEM fuel cells still not competitive with internal combustion engine. For these reasons, research now focuses on obtaining more stable material with higher performances toward ORR. Two strategies are possible to improve catalyst for oxygen reduction. The first one deals with the enhancing of Pt activity modifying its electronic properties by alloying Pt with other transition metal (ligand effect) or by reducing the Pt-Pt distance (geometric effect). In both cases a Pt d-band shift occurs, which is responsible for the modification of adsorption and desorption energies of all species involved in ORR, and has as a direct consequence a modulation in the electrochemical activity. The second strategy deals with with the utilization of supports more stable respect to corrosion, like graphene, carbon nanotubes or mesoporous carbons. Furthermore, doping of carbon support with heteroatoms like N or S, can help to stabilize the metallic nanoparticles. In fact, doping creates homogeneous and narrow dispersion of small metallic nanoparticles, strongly bound to the surface of carbon support and with a higher resistance to agglomeration. Furthermore, doping has as well an influence on the electronic structure of the Pt catalyst, resulting in a modulation of its electrochemical activity. Doping is not beneficial only in noble-metal catalyst, but may also modify properties of the carbon support in which heteroatoms are present. Wettability, electrical conductivity and electrochemical activity are generally boosted when heteroatoms are inserted in carbonaceous substrates such as carbon blacks (CBs).

The goal of this Ph.D. project consists in synthesizing nitrogen and sulphur doped and co-doped Mesoporous Carbons. MCs are highly porous materials, which offer high surface area (>1000 m^2/g), pore diameter in the range between 2 and 50 nm, controlled pore structure, good mechanical and thermal stability and good mass transport. The syntheses of differently doped MCs is conducted via hard template, a technique which allow to obtain materials with a well-

defined structure, originating directly from the used template. The effect of template, pyrolysis temperature and carbon precursor on the final properties of synthesized MCs is evaluated. SEM, TEM, elemental analysis, XPS, BET and TGA are employed to characterize morphology, chemical composition and functional groups, surface are, pore dimension and thermal stability of MCs, respectively. Electrochemical performance toward oxygen reduction are evaluated via cyclic voltammetry in steady state conditions, with rotating disk electrode and with rotating ring disk electrode. Electrochemical stability tests are conducted to highlight stability of differently doped MCs and the modification occurring to functional groups.

The synthesized MCs are modified with Pt nanoparticles. An exhaustive deposition investigation is conducted via both chemical reduction and solid state reduction of several Pt salts, in order to find the conditions which allow to have the best Pt distribution on the whole surface of the carbon support. The catalysts made of Pt NPs on doped MCs are characterized by TEM, ICP and TGA techniques. Cyclic Voltammetry in steady conditions and with Rotating Disk Electrode are employed for the determination of electrochemical surface area (ECSA) and catalytic activity toward ORR, respectively, and compared to a commercial Pt/C catalyst. Electrochemical stability tests are conducted in order to assess both Pt degradation and C corrosion. In particular, the comparison of ECSA evolution between doped and reference catalyst determines if there is an enhancement of bounding which can mitigate Ostwald ripening. Finally, Pt on nitrogen and sulphur doped MC are incorporated in a membrane electrode assembly, in order to evaluate their performance and stability during operation as cathode material in a PEM Fuel Cell. Beyond catalytic properties, oxygen transport resistance was evaluated, knowing that all these properties are strongly influenced by the more severe condition of PEMFC environment.

Chapter 1

PEM Fuel Cells

1.1 Fuel Cells: brief history, environmental and healthy relevance

Fuel Cells are electrochemical devices which convert chemical energy of fuels in electricity. Their invention is dated back to middle of 19th century by Sir William Groove and by Christian Friedrich Schönbein, who discovered the theoretical principles. Fuel cells are considered to be one of the oldest electrical energy conversion devices known to mankind. Anyway, the development of fuel cells was hindered for at least one century after their invention because of high costs, materials issues, certain inadequacies in the operation of electrochemical devices together with abundance and low costs of primary energy sources such as coal and oil [1][2]. The most important results during 20th century were achieved by Francis Bacon, who developed the first fuel cell operating with hydrogen and oxygen with practical application. During World War II Bacon developed fuel cells to be employed in Royal Navy submarines, and in 1958 he produced an alkaline fuel cell representing the prototype of the systems employed in Apollo spacecraft [3]. Since 1960 huge improvements in fuel cell systems have been performed, leading to the discovery of new materials and technologies. For example, the synthesis of polytetrafluoroethylene, called Teflon, helped the development of the actual aqueous electrolyte fuel cells. Phosphoric acid, molten carbonate and conducting ceramic oxide fuel cells were realized by several groups. Attempts to decrease diffusion limitation issues, high costs and to improve performance and lifetime have been carried out since 1970. Petroleum fuels were used as well, and a fuel-reforming unit was required. During 1990, the first methanol fuel cell was developed by NASA laboratory [3]. In Figure 1.1 all the milestones in fuel cells technology development, described by J. Andújar et al. in ref. [3] are reported.

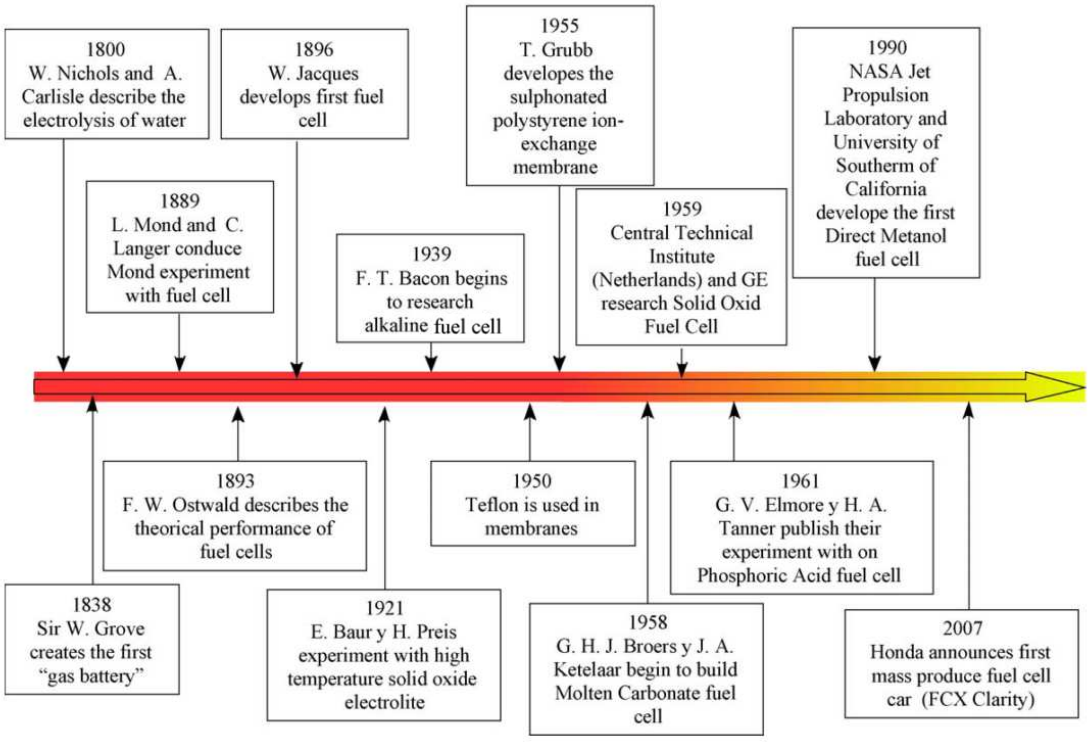

Figure 1.1 Historical review of fuel cells, described in ref. [3]. Reprinted from Renewable Sustainable Energy Reviews, 13, J.M. Andújar and F. Segura, Fuel cells: History and updating. A walk along two centuries, 2309–2322, Copyright 2013, with permission from Elsevier.

Nowadays many sectors use fuel cells as energy source, the most important being the automotive one [4]. Most vehicle manufacturers are currently developing fuel cell cars for research or testing, and Toyota is one of the first company that commercialized a fuel cell car in 2015. Fuel cells are employed as stationary electricity generators [4], portable devices and micro devices. Stationary applications are present in domestic built environment such as hospitals, shelters, hotels, offices and schools [5], and they might be connected to the grid to provide additional power to the plant, or used as independent systems for electricity generation in isolated areas. Micro devices are useful in the field of telecommunications, since they can be employed as electricity source in mobiles and laptops with a longer battery life than traditional batteries [6].

The importance of fuel cell technology lies in reducing the noxious and toxic emissions generated from fossil fuels combustion, produced by combustion in vehicle engines, power plants and industrial processes. This is the main source of outdoor air pollution, followed by industrial processes, waste incineration, agricultural and natural processes. Pollutants consist mainly in nitrogen and sulphur oxides with different oxidation states (labelled NO_x and SO_x respectively), CO, CO_2 and particulate matter [2]. In recent years air pollution is proved to be

responsible for several health and environmental damages. The International Agency for Research on Cancer (IARC) classified outdoor air pollution and particulate matter from outdoor air pollution as carcinogenic to humans (IARC Group 1) [7]. Air pollution triggers other lung issues than cancer, such as asthma and chronic obstructive pulmonary diseases in both acute and long term exposure. In a study carried out in ten European cities, 14% of all the cases of childhood incident asthma is triggered by air pollution, and the same factor is responsible for the 15% of exacerbations of asthma in children [8]. Lastly, fine particulate matter air pollution is responsible for cardiovascular diseases and acute cardiac events such as myocardial infarction [9].

The second factor which makes fuel cells, and in general all renewable energy, so important is linked to the limited availability of fossil fuel resources. In fact, the actual consumption rate may assure known and economically exploitable fuel supply for only around 50 years. For this reason it is fundamental to develop new renewable energy based technologies that can be substitute to the common fossil fuel based system for energy production [10].

1.2 Fuel Cells: operation and classification

The overall process occurring at a fuel cell, and in general at every electrochemical cell, is described by equation 1.1, where 1 and 2 represent the species fed to the anode and at the cathode which undergo redox reactions, and the stoichiometric coefficients are represented by the letters a, b, c and d.

$$\mathrm{a}_{\mathrm{ox}_1} + \mathrm{b}_{\mathrm{red}_2} \rightarrow \mathrm{c}_{\mathrm{red}_1} + \mathrm{d}_{\mathrm{ox}_2} \qquad \text{Eq. 1.1}$$

The equilibrium potential for each half cell process is described by Nernst equation (Eq. 1.2) where E_o is the equilibrium electrode potential at a selected temperature, $E^{\ominus}$ is the standard electrode potential, R is the gas constant, T is the temperature, n is the number of electrons involved in the redox process and F is the Faraday constant. The voltage of the cell ΔE is given by equation 1.3, and is represented by the difference in the equilibrium potentials obtained in Eq. 1.2.

$$E_0 = E^{\ominus} + \frac{RT}{\mathrm{n}F}\frac{[\mathrm{ox}]}{[\mathrm{red}]} \qquad \text{Eq. 1.2}$$

$$\Delta E = E_{0,1} - E_{0,2} = E_1^{\ominus} - E_2^{\ominus} + \frac{RT}{nF} ln \frac{[ox_1]^a[red_2]^b}{[ox_2]^d[red_1]^c} \quad \text{Eq. 1.3}$$

$$\Delta G = -nF\Delta E = \Delta G^{\ominus} + RT\, ln \frac{[ox_2]^a[red_1]^b}{[ox_1]^d[red_2]^c} \quad \text{Eq. 1.4}$$

The reactions involved in a fuel cell are hydrogen or methanol oxidation at the anode, and oxygen reduction at the cathode. Pure oxygen or synthetic air can be fed to the cathode. Oxygen reduction is the most problematic reaction, given that it occurs with high overpotential even on Pt, the metal that nowadays best catalyses this process. Oxygen reduction may follow two different pathways in both alkaline and acid environment: the first one is a four-electron reduction which led directly to the formation of water, the second one is a double bi-electronic step with intermediate formation of hydrogen peroxide. The double bi-electronic pathway is to be avoided, because it has the lowest efficiency and oxidant species such as hydrogen peroxide may damage the fuel cell system. In any case, both mechanisms consist of several steps in which O_2 is adsorbed, dissociated, reduced and recombined with hydrogen ions to give H_2O_2 and, eventually, H_2O. The detailed mechanism will be described in Chapter 2. Hydrogen oxidation, on the contrary, has a fast kinetic and it occurs quite easily on Pt based electrodes and in fuel cells at higher current there is a mass transport limitation. The mechanism involves the adsorption of $H_{2\,(gas)}$ on the Pt surface, by dissociation of the molecule and electrochemical oxidation to H^+, according to equations 1.5 and 1.6. The overall process is represented in equation 1.7 and has a standard potential of 0.0 V.

$$2Pt_{(s)} + H_2 \rightarrow Pt - H_{ads.} + Pt - H_{ads.} \quad \text{Eq. 1.5}$$

$$Pt - H_{ads.} \rightarrow H^+ + e^- + Pt_{(s)} \quad \text{Eq. 1.6}$$

$$H_2 \rightarrow 2H^+ + 2e^- \quad \text{Eq.1.7}$$

The methanol oxidation is catalysed by Pt-based materials, because they can adsorb the reagent and well catalyse the process. The overall reaction involves several deprotonation steps, which lead to the formation of CO. Carbon monoxide may block the active site of the catalyst, so usually a second metal is added to Pt to help the CO oxidation to CO_2. The typical reaction pathway is reported in Figure 1.2 [1][11]. The scheme reported in Figure 1.2 is only a possible pathway for methanol oxidation, and generally other products are generated from oxidation of

intermediates, such as CH_2O, HCOOH and $HCOOCH_3$. The reaction pathway is strongly influenced by methanol concentration, temperature, electrode roughness and electrolysis time [11].

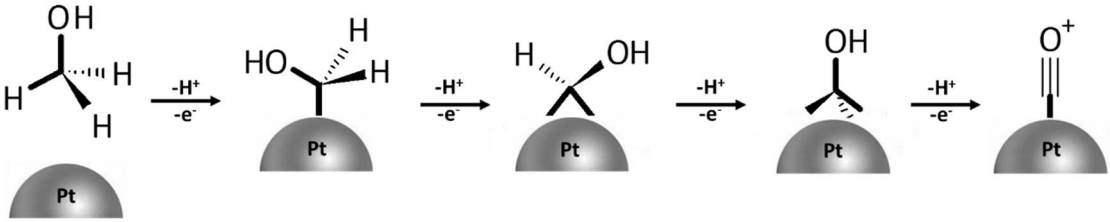

Figure 1.2 Scheme of methanol oxidation on Pt showing the consecutive stripping of hydrogen atoms**.**

There are several types of fuel cells, which can be divided according to the electrolyte employed in the cell or according to the operating temperature, which can be low (around 100 °C) or high (included between 500 and 1000 °C). Alkaline fuel cell (AFC), Proton Exchange Membrane fuel cell (PEMFC, also known as Polymer Electrolyte fuel cell, PEFC, or Solid Polymer Electrolyte fuel cell, SPEFC), Direct Methanol fuel cell (DMFC) and Phosphoric Acid Fuel Cell (PAFC) are operating at low temperature. Molten Carbonate Fuel Cell (MCFC) and Solid Oxide Fuel Cell (SOFC), on the contrary, operate at high temperature. These systems are described in the following sections.

1.2.1 Proton Exchange Membrane Fuel Cells

PEMFCs are employed typically for both transportation and stationary applications. They operate at low temperature, around 80 °C, allowing a quick start-up time, and possess a favourable power-to-weight ratio. The core of this system is the Membrane Electrode Assembly (MEA), made up of a solid proton-conductive polymeric electrolyte that has on both sides catalysts for anodic and cathodic compartments. The polymeric membrane assure electrical insulations, so the conductive catalyst of anode and cathode are not in touch, but at the same time allow migration of protons [12]. The catalysts are based on Pt nanoparticles (NPs) on high surface area carbon. Pt nowadays is the metal that best catalyses oxygen reduction in acidic environment. Catalytic properties are improved alloying Pt with other metals, or using high graphitic supports [13][14]. On the contrary, non Pt catalysts are still not competitive in term of catalytic activity for oxygen reduction. In Figure 1.3 a scheme of a proton exchange membrane fuel cell is reported. H_2 is fed to the cathode and oxidized to H^+, O_2 is fed at the cathode and is

reduced to O^{2-}. H^+ migrates through the proton exchange membrane and combine with O^{2-} at the cathode to give H_2O as product.

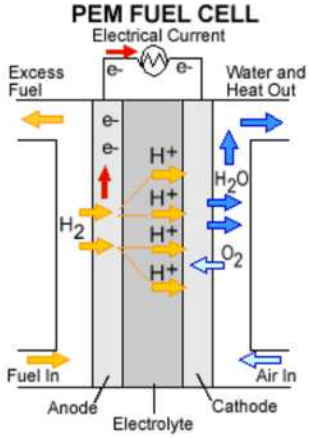

Figure 1.3 Scheme of a proton exchange membrane fuel cell. H_2 is fed to the anode and oxidized to H^+, O_2 is fed at the cathode and is reduced to O^{2-}. H^+ migrates through the proton exchange membrane and combine with O^{2-} at the cathode to give H_2O as product [12].

1.2.2 Direct methanol fuel cells

DMFC is a technology similar to PEMFC, where methanol is employed instead of H_2 at the anode. Methanol has some advantages over hydrogen: there are no storage problems and it's easier to transport [12]. Catalysts for methanol oxidation are made of Pt with other co-metals such as Re, Ru, Os, Rh, Mo, Pb, Bi and Sn [1]. The main issue associated to DMFC is methanol crossover from anodic to cathodic site. Analogous system is represented by direct ethanol fuel cell (DEFC), in which ethanol is fed to the anode instead of methanol. Advantages are represented by the lower toxicity and the ease to supply than methanol [3].

1.2.3 Alkaline Fuel Cells

AFCs represent one of the first kind of fuel cells technologies developed, used in space programs for electricity and water production. The electrolyte is made up of a solution of KOH, and latest systems possess anionic polymer membrane, which make the fuel cell analogous to the PEMFCs [15]. The catalyst employed in AFCs consist in non-precious metals on high surface area support, which in alkaline environment possess comparable catalytic activity to Pt [16][12][17]. The main issue associated to AFCs is the CO_2 induced poisoning which damages the system due to carbonate formation. This problem might be solved if a recirculating operation mode that allows

electrolyte regeneration is implemented. However, this is not the best solution, given that liquid electrolyte promotes shunt current and wettability, corrosion and differential pressure issues are indeed present. Alkaline membranes improve partially the issues encountered with liquid electrolytes, but CO_2 poisoning remains a challenge [12]. In Figure 1.4 a scheme of an alkaline fuel cell is reported: O_2 is fed to the cathode and reduced, OH^- ions migrate through the anionic membrane and combine with H^+ at the anode to give H_2O as product.

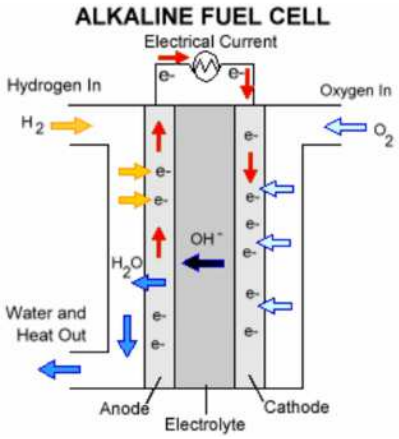

Figure 1.4 Scheme of an alkaline fuel cell. O_2 is fed to the cathode and reduced, OH^- ions migrate through the anionic membrane and combine with H^+ at the anode to give H_2O as product [12].

1.2.4 Phosphoric Acid Fuel Cells

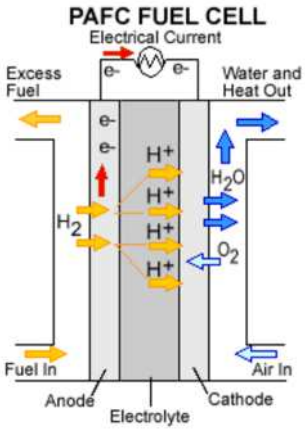

Figure 1.5 Scheme of a Phosphoric Acid Fuel Cell. H_2 is fed to the anode and oxidized to H^+, O_2 is fed at the cathode and is reduced to O^{2-}. H^+ migrate through the phosphoric acid electrolyte and combine with O^{2-} at the cathode to give H_2O as product [12].

PAFCs use liquid H_3PO_4 contained in a teflon-bonded silicon carbide matrix and Pt based electrode supported on porous carbon. This kind of cell was used first in commercial applications, especially in stationary applications because it's heavy. The construction is easy and it has a good thermal, chemical and electrochemical stability [2]. In Figure 1.5 the scheme of such technology is represented. The operation is the same as the PEMFC, and usually air instead of pure oxygen is fed to the cathode because their higher tolerance towards CO_2 (up to 30%) [12][3].

1.2.5 Molten Carbonate Fuel Cell

MCFCs are systems operating at high temperature, around 650 °C. MCFCs are made of molten carbonate salt suspended in porous, chemically inert ceramic lithium aluminium oxide matrix. Non noble and cheap metal can be used in both anode and cathode because of the high operating temperature. The reagents consist in O_2 and H_2 and the operations is the same as in a PEMFC. H_2 may be produced directly at the cathode, via internal reforming: the high temperature realises the conversion of fuels such as methane and other light hydrocarbons to hydrogen [12]. The efficiency of a MCFC might reach 65%. In Figure 1.6 a MCFC is depicted.

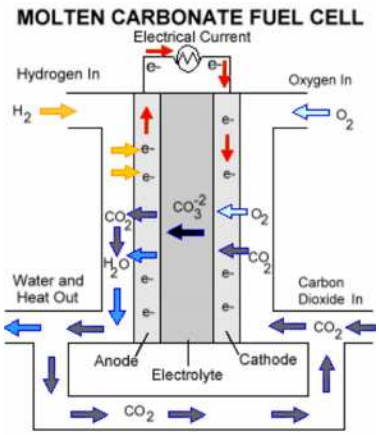

Figure 1.6 Scheme of a Molten Carbonate Fuel Cell. H_2 is formed at the anode via internal reforming and oxidized to H^+, O_2 is fed to the cathode together CO_2, and is reduced to CO_3^{2-}. CO_3^{2-} migrates through the molten carbonate electrolyte and combine with H^+ at the anode to give H_2O and CO_2as products [12].

1.2.6 Solid Oxide Fuel Cell

SOFCs use a hard, non-porous ceramic compound as the electrolyte which conducts O^{2-} from the cathode to the anode. The operating temperature is around 1000 °C, so non noble metals

well catalyse the electrochemical reactions and internal reforming may occur as in the case of MCFCs. SOFCs are very resistant toward S and CO poisoning. For these reasons, natural gas, biogas and gas made from coal can be used as fuel. The high temperature is responsible for long start-up time, and a proper shielding is necessary.

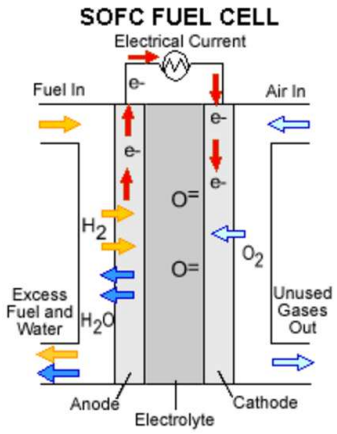

Figure 1.7 Scheme of a Solid Oxide Fuel Cell. H_2 is formed at the anode via internal reforming and oxidized to H^+, O_2 is fed to the cathode and is reduced to O^{2-}. O^{2-} migrates through the solid electrolyte and combine with H^+ at the anode to give H_2O as product [12].

1.2.7 Summary: types of Fuel Cells

In Table 1.1 the operating conditions, the electrochemical reactions and the generated power for all the fuel cell technology described in the previous part of this section are reported.

Table 1.1 Summary of operation conditions for the fuel cells described in the section.

	Operating *T (°C)*	***Anode reaction***	***Cathode reaction***	***Power*** (kW)	***Charge carrier***
PEMFC	60-120	$H_2 \rightarrow 2H^+ + 2e^-$	$½O_2 + 2H^+ + 2e^- \rightarrow H_2O$	5-250	H^+
AFC	<100	$H_2 + 2OH^- \rightarrow 2H_2O + 2e^-$	$½O_2 + H_2O + 2e^- \rightarrow 2OH^-$	5-150	OH^-
DMFC	60-120	$CH_3OH + H_2O \rightarrow CO_2 + 6H^+ + 6e^-$	$^3/_2O_2 + 6H^+ + 6e^- \rightarrow 3H_2O$	5	H^+
PAFC	160-220	$H_2 \rightarrow 2H^+ + 2e^-$	$½O_2 + 2H^+ + 2e^- \rightarrow H_2O$	50-11000	H^+
MCFC	600-800	$H_2 + CO_3^{2-} \rightarrow H_2O + CO_2 + 2e^-$	$½O_2 + CO_2 + 2e^- \rightarrow CO_3^{2-}$	100-2000	CO_3^{2-}
SOFC	800-1000	$H_2 + O^{2-} \rightarrow H_2O + 2e^-$	$½O_2 + 2e^- \rightarrow O^{2-}$	100-250	O^{2-}

1.3 PEM Fuel Cells

In the previous section the operations at a PEM fuel cell, such as half-cell reactions and operating temperature, were briefly described. Here the main components of a PEM fuel cell are described in detail, in particular the core of this system consisting of the Membrane Electrode Assembly (MEA). In Figure 1.8 a single PEM fuel cell and all the necessary components for the operation are represented. The system has a symmetrical shape, with the MEA occupying the central position, surrounded on both sides by gas diffusion layers (GDLs), gas directing plates, current collectors and end plates. The end plates are non-conductive part of the cell, and realize the connection with flow channels/paths and cooling system. In a stack of cells the unit represented in Figure 1.8 is repeated several times in order to assure the required power.

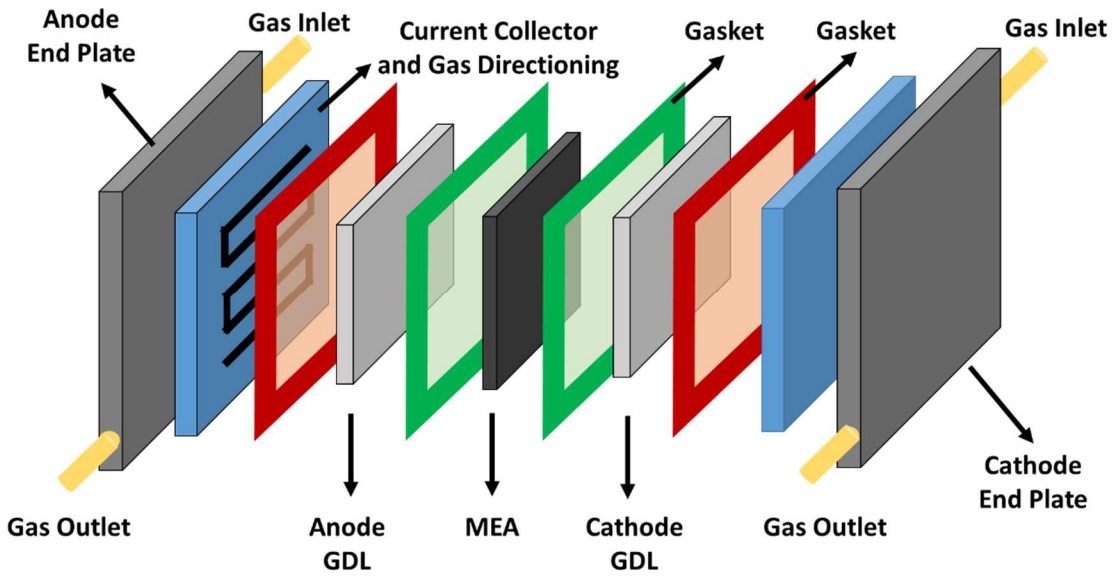

Figure 1.8 Single PEM fuel cell. It is possible to appreciate all the components in the following order: end plate, current collector, plate for gas directing, gas diffusion layer, gasket and MEA.

Complex processes occurring in a MEA involve heat transfer, reactants and charge transfer, multi-phase gas flows and electrochemical reactions. Operation includes pumping of hydrogen and air in order to flow in the gas channels and GDLs to reach the porous layer of anode and cathode, respectively. The term porous layer indicates the totality of gas diffusion layer and catalyst layer. H_2 and Air flow initially through the gas diffusion layers of anode and cathode respectively, and then diffuse to the respective catalyst layers through the polymer. H_2 is oxidized at the anode, O_2 is reduced at the cathode. H^+ ions migrate through the proton conductive membrane to the cathodic side. Electrons migrate through the gas diffusion layer till

the current collector plate of anode and reach the cathode through the external circuit. Water produced at the cathode is removed via the gas diffusion layer. Heat is generated mainly in the cathode catalyst layer due to the sluggish oxygen reduction reaction (ORR), and is conducted out of the cell via carbon support and bipolar plate [18]. These processes are represented in Figure 1.9, taken from reference [18].

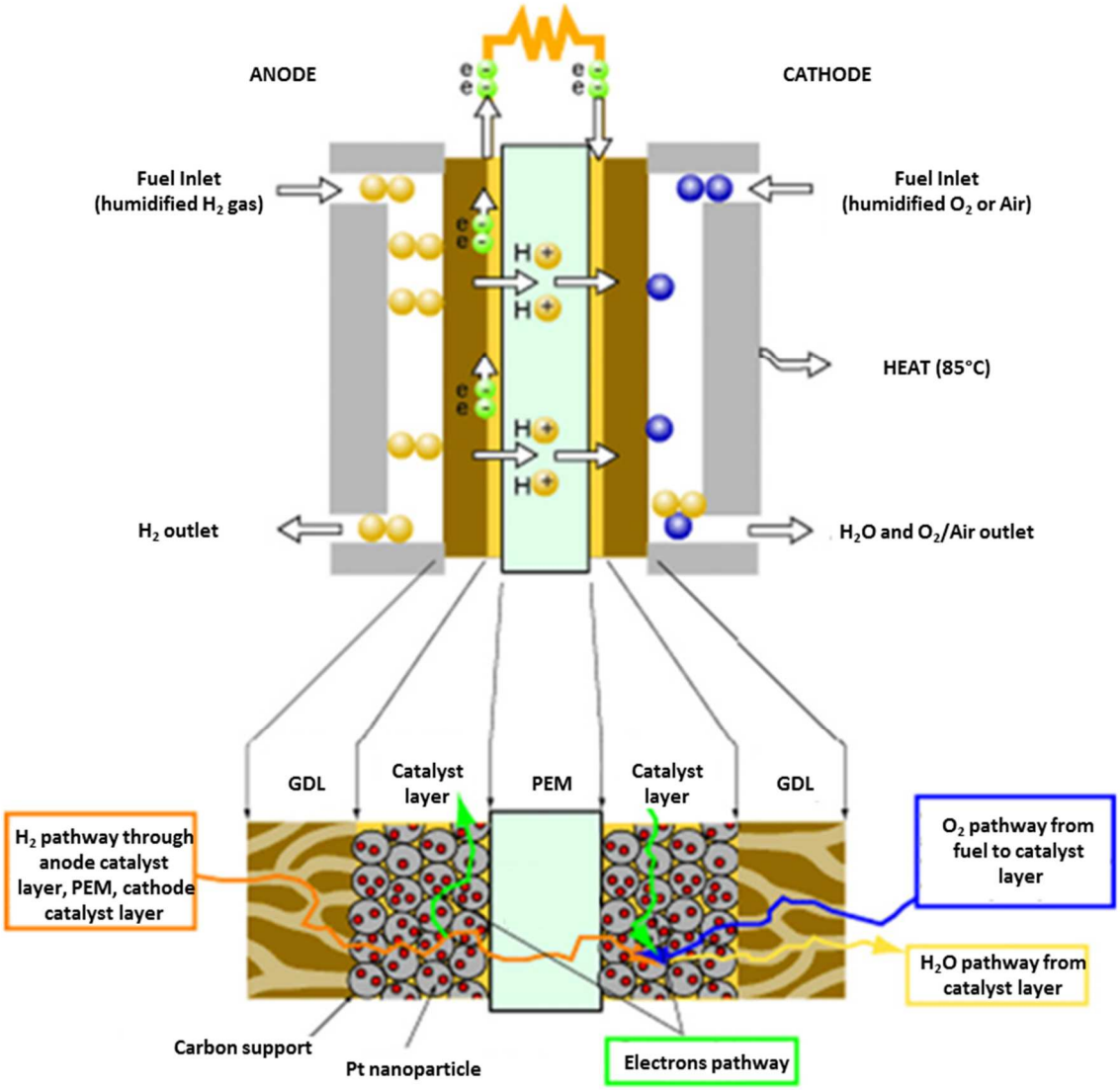

Figure 1.9 Image describing all the phenomena occurring in a PEM fuel cell [18].

1.3.1 Membrane Electrode Assembly

The MEA is the core of the fuel cells, and is made up of a polymeric proton conductive membrane (PEM) supporting on its both sides the catalyst layers (CLs) for anodic (H_2 oxidation) and cathodic

(O_2 reduction) compartments (Figure 1.9, below). The employed commercial catalyst is made of Pt NPs supported on high surface area graphitic carbon for both cathodic and anodic reactions, but the Pt loading at the cathode is higher than that at the anode, because of the high overvoltage needed for the reaction to occur. The ideal electrode structure maximizes the active Pt surface per unit mass of Pt and per unit of electrode area, minimizes transport and resistance issues and gives stable performance with time and it's mechanically, thermally and chemically stable [19]. An example of cathodic catalyst layers is reported in Figure 1.10: ORR is clearly pictured and the PEM is responsible for proton conduction from anode to cathode.

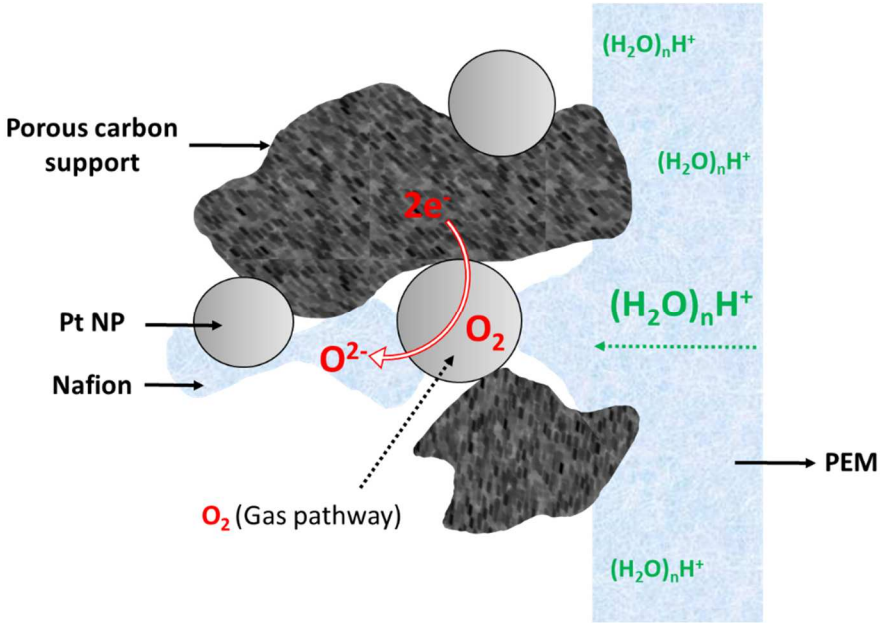

Figure 1.10 Cathodic catalyst layer in a PEM fuel cell, in which the three-phase boundary is clearly pictured. On the right side the proton exchange membrane is represented in blue, and hydrogen ions are migrating through it to reach the cathode.

Catalyst layers consist in a mixture of catalyst and proton conductive membrane, such as Nafion. It's fundamental the realization of a three-phase boundary, in which the Pt catalyst is in contact with the carbon conductor for electrons supply/removal and with the ionic conductor (Nafion) that allow the diffusion of O_2 and H_2 to the Pt, and removal of hydrated H^+. The ionic conductor is also responsible for in situ generated H_2O removal, and for this reason sometimes it's mixed with small amount of polytetrafluoroethylene (PTFE), an hydrophobic polymer that help avoiding flooding issues (i.e. H_2O obstructing the pores that hinders gas flow and diffusion toward catalyst). The ionic membrane bound to the catalyst is then in contact with the proton conductive membrane which separates anode and cathode [1].

The proton exchange membrane (PEM) that divide cathode and anode is a thin layer of electrolyte, which dimensions are included between 10 and 100 µm. The function of the PEM include: proton conduction from anode to cathode, high ionic conductivity, avoiding electronic conductivity, avoiding cross-over phenomena (O_2 transport to anodic site and H_2 transport to cathodic side). Furthermore, the PEM should be insoluble in H_2O, but should solubilise H_2O in a reversible way and should have high chemical, thermal and electrochemical stability [19]. Most of membranes are made of perfluorosulphonic acid (PFSA) and Nafion is the most characterized material. PFSA membranes possess a hydrophobic fluorocarbon backbone [21] with hydrophilic sulphonic acid side chains. In Figure 1.11 Nafion, Aquivion and 3M PFSA membranes are reported, each of them characterized by different chain length of both the fluorocarbon backbone and the sulphonic side chains. Different PFSA membranes have an influence over their properties during operation [19].

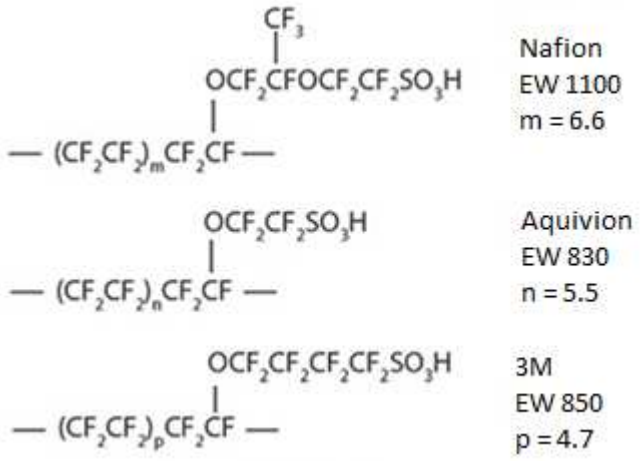

Figure 1.11 Examples of three perfluorosulphonic acid ionomer with different properties produced by different companies**.**

The high proton conductivity and mechanical strength are obtained thanks to the hydrophilic sulphonic groups and the hydrophobic fluorocarbon backbone, respectively. The sulphonic groups provide charge sites for proton transport. These two components determine phase separation between the hydrophobic and hydrophilic parts of the polymer, that originates a random nanostructured network [21][22]. A membrane for PEM fuel cell is evaluated according specific conductivity, density, H_2 and O_2 permeability, ion exchange capability, tensile strength, percent elongation at break, creep, cycling between freeze and operating temperature consequences on mechanical properties, thickness change, linear expansion, water uptake, hydrodynamic water permeability and electro-osmotic permeability. Thicker membranes

generally show lower permeability to gases and reactant crossover, determining higher cell performance at low current densities and higher durability compared to a thinner membrane. The Nafion membrane conductivity strongly depends on the water content and varies from 1 mS/cm at 20% relative humidity (RH) to 100 mS/cm at 100% RH. Ion exchange capability, casting procedure and pre-treatment temperature influence as well the conductivity of a membrane. In particular, the higher the heat treatment, the lower the conductivity, because of the decrease of water uptake. Three form may be found: expanded (E) form without heat treatment, normal (N) form treated at 80 °C and shrunken (S) form, treated at 105 °C. The effect of hydration was explained by Kreuer in reference [22]. The proton transport features depends on the H_2O confinement in the hydrophilic domains and on the interaction of H_2O molecules themselves with acidic sulphonic groups. In fact, if each hydrophilic domain contains low amount of H_2O, hydrogen bonds are tightened, leading to a decrease in dielectric constant and in particular to a reduced rate of bond breaking and forming. The latter property is considered to be the fundamental step for proton conductivity, and it's clear that PFSA membranes show better performance when operating at high RH. The proton conduction might be described with two different mechanism: the 'proton hopping' or 'Grotthus' mechanism and the 'diffusion' mechanism. In the 'proton hopping' process, each H^+ jump from a hydrolysed ionic site (SO_3^- H_3O^+) to another through the membrane. This process can be seen as a diffusion of proton excess (or defect) along the membrane. The 'diffusion mechanism', also known as vehicular mechanism, involves the diffusion of hydrated protons through the aqueous medium as a consequence of electrochemical potential difference. In detail, it is possible to consider the species $H^+(H_2O)_x$ (water connected protons) that carry themselves together with one or more H_2O molecules through the membrane thanks to electro-osmosis [23].

Nowadays research focuses on characterizing new membranes for automotive applications which can operate at low water content, so no humidifiers are needed to maintain high proton conductivity. This is very important for PEM fuel cells operating at a temperature slightly higher than 100 °C, which can improve ORR kinetics [24]. Membranes with low equivalent weight (EW) and high ion exchange capacity (IEC) are currently being developed, but low EW still show lower mechanical stability than Nafion membranes. An example of improved membrane developed by 3M contains super-acid imide groups. Imide groups lead to a lower equivalent weight of the membrane, but at the same time avoid loss in crystallinity of the backbone structure during hydration. These groups are stronger acid than the sulphonic ones, allowing higher proton conductivity in drier conditions [24][25]. Another type of membranes consists in the hydrocarbon-based membranes. Advantages includes low costs and better

resistance to O_2 and H_2 crossover and better mechanical properties than PFSA materials. An example consists in bulky side groups modified poly(phenylene disulfonic acid): the rigid structure generates nano-sized channels lined with sulphonic groups. This structure contains H_2O molecules and provides preferential pathways for proton conduction, which approach 100 mS/cm even at 15% RH [24].

The preparation of a MEA generally involves the synthesis of a catalyst ink that is applied on the PEM or on the GDL. The structure in which catalyst layer is applied to GDL is called catalyst coated substrate (CCS), while the one obtained by applying anodic and cathodic catalyst layers to the PEM is called catalyst coated membrane (CCM). Then, for the fabrication of the MEA, two CCSs are applied on a PEM, or two GDLs are applied to the CCM, obtaining a five-layers membrane [19]. The preparation of MEAs by CCM consists in spreading the Nafion containing catalyst ink onto a Teflon support which is then transferred to the PEM by hot pressing. The Teflon support is then removed by peeling, and the catalyst coated membrane is put between two gas diffusion layers. On the contrary, the preparation of MEAs by CCS consists on spreading catalyst containing ink on the GDLs, followed by hot pressing of the two CCS layers on the membrane. It is known from literature that the CCM method allows to reach better performance than CCS, Pt and C loading and Ionomer/Carbon ratio (I/C) being equal [26][27]. All the steps for MEA preparation are fundamental to obtain good performance, from the ink preparation, to the CCM or CCS synthesis, till the hot pressing of all the components. The ink is prepared simply by mixing the catalyst on proper solvent and Ionomer, in order to obtain a homogeneous ink. The catalyst should be perfectly suspended to maximise Pt utilization. Nafion has a glass transition temperature equal to 150 °C, so if a press temperature much lower than 150 °C is applied avoid the Nafion to flow, and bad ionomer-catalyst contacts are formed resulting in incomplete utilisation of the Pt. On the contrary, if a too high press temperature is applied the MEA may be damaged, because Nafion might partially loose its ability to retain water, the ionomer might be damaged by acid sites and the catalyst might be removed [19]. For these reasons the hot pressing in generally conducted at 120-160 °C at 5000-15000 kPa. In Figure 1.12a the section of the internal part of a MEA is represented: GDLs, Catalyst Layers and PEM. In Figure 1.12b and c the morphology of a membrane obtained via CCM and CCS techniques, respectively, is depiced, which clearly shows the better ionomer-catalyst contact in the case of materials prepared by CCM.

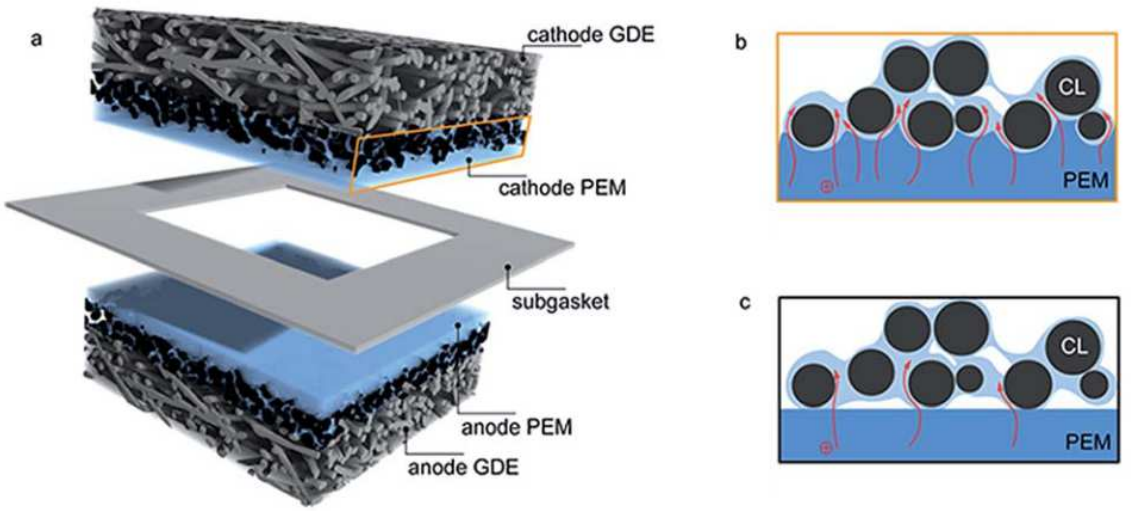

Figure 1.12 Image of MEA preparation. a) Representation in section of the internal part of a MEA: GDLs, CLs and PEM. b) Morphology of a membrane obtained via CCM technique and c) image of a membrane obtained via CCS technique [28]. M. Klingele, M. Breitwieser, R. Zengerle, S. Thiele, Direct deposition of proton exchange membranes enabling high performance hydrogen fuel cells, J. Mater. Chem. A, 3 (2015) 11239-11245, published by The Royal Society of Chemistry.

1.3.2 Gas Diffusion Layers

GDL is a carbon fiber paper or clothes which is responsible for gas distribution on the MEA, water management from humidified gases and from cathode side of the fuel cell and current collection. Furthermore the GDLs should support mechanically the MEA and transport heat. GDLs have specific hydrophobic/hydrophilic balance depending on each fuel cell operation, in order to manage water properly, avoiding flooding phenomena. Carbon fibers may be partially covered with PTFE, and this material also help in keeping the pores opened. Sometimes the inner surface of the GDL is covered with high surface area carbon mixed with PTFE. This part is called microporous layer and the purpose is to balance the water retention and the water release property, to keep the best combination of membrane conductivity and opened pores for H_2 and O_2 flows [29][30][19].

1.4 Catalyst for PEM fuel Cells

Actually, main commercial catalysts employed for PEM fuel cells are based on Pt NPs on high surface area carbon materials, such as carbon blacks. Platinum is the metal that best catalyses

the oxygen reduction, and it is deposited on carbon based materials with high surface area. This catalyst structure is to be preferred to the bulk metal in order to realize a much higher electrochemical active surface area, but at the same time to keep the total precious metal loading on the carbon support low enough to reduce cost. In the last years a huge work in order to obtain better catalyst for oxygen reduction was carried out. The main issues associated to this kind of catalyst deals with their low stability in PEM fuel cells conditions and slow ORR kinetic. Pt may encounter dissolution or Ostwald ripening processes, while C is oxidised. Furthermore, Pt is a rare and expensive metal. The Pt degradation phenomena, represented in Figure 1.13, lead to a lowering in performance toward ORR because of loss in Pt active area as a consequence of particles agglomeration, and to a lowering in Pt loading due to Pt dissolution [31]. As depicted by the Deparment of Energy (DOE) in 2013 (Figure 1.14), high cost and low durability are the two main factors that still make PEM fuel cells not competitive with internal combustion engine [32].

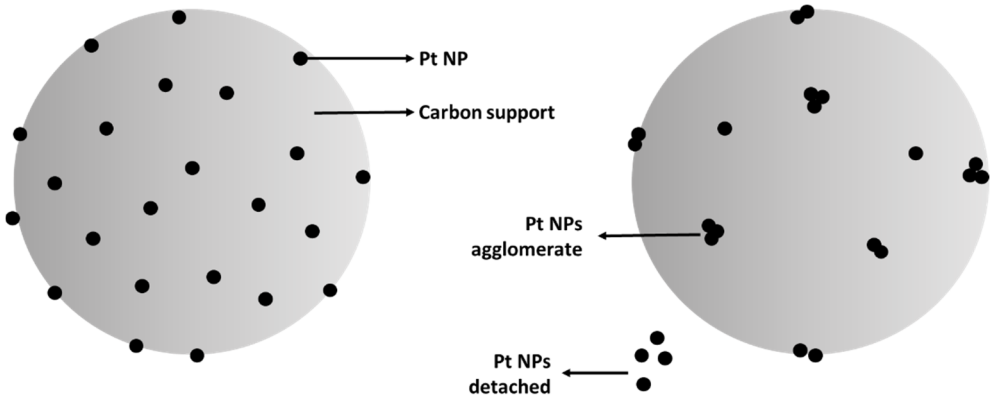

Figure 1.13 Schematic representation of Pt agglomeration via Ostwald ripening and of Pt dissolution.

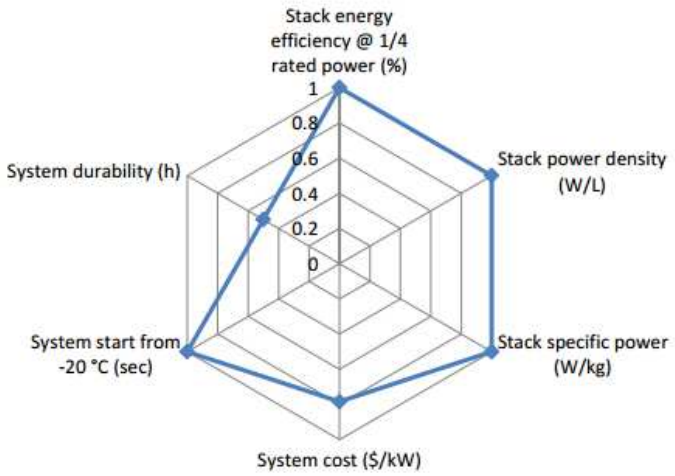

Figure 1.14 Fuel Cell targets (grey) and actual status (blue) indicated as a fraction of the targets [32].

Several strategies are employed nowadays to improve catalysts for PEM fuel cells, and they are described in the following section.

1.4.1 Improving catalyst for ORR: crystallographic control

Different crystallographic orientations of Pt single crystal possess different activities toward oxygen reduction. For example, a non-adsorbing electrolyte, such as $HClO_4$, determines the following order of electrocatalytic activity of low index single-crystal Pt(110) > Pt (111) > Pt(100) [33]. This behaviour is in agreement with the strength of interaction between O_2 and the Pt surface. If a different electrolyte is employed, for example H_2SO_4, Pt(111) becomes the less active surface among the three described [34]. Again, if an alkaline electrolyte, such as KOH, is employed, the order is still different, and Pt(111) turns out to be the most active surface [35]. So, a first strategy to obtain better catalyst could deal with the proper index surface, but probably is difficult to implement this catalyst on an industrial scale.

1.4.2 Improving catalyst for ORR: ligand and geometric effects

A second way to improve catalyst for PEM fuel cells deals with the modification of electronic structure and/or geometry of Pt metal. Two effect, named ligand and geometric effect, are responsible for these modifications, and both of them involve the enhancing of Pt activity due to a second chemical elements. In all cases a Pt d-band shift occurs, which is responsible for the modification of adsorption and desorption energies of all species involved in ORR, and has, as a direct consequence, a modulation in the electrochemical activity. The ligand effect is generated when Pt is close to transition metals with different electronegativity and an interaction between them takes place and is active, typically, over one to three monolayers. The geometric effect is realized as the Pt-Pt distance is modified, thanks to another chemical element, which is not alloyed with the Pt and generally is removed from the catalyst before operations [14].

An example of modified ORR activity is reported in a paper by V. Stamenkovic et al. [36], in which three different Pt skin surfaces are alloyed with Ni and tested toward ORR in 0.1 M $HClO_4$. In Figure 1.15 the obtained results are reported. First of all the same activity trend of Pt(111), Pt(100) and Pt(110) highlighted by N.M. Markovic et al. [33] is confirmed. Secondly, when these three crystallographic surfaces are bonded with a transition metal, i.e. Ni, a further increase in catalytic activity (defined as Specific Activity, SA, given by the ratio of limiting current

over electrochemical active area) is present. Also in this case, different activities arise because of the different adsorption energies of OH species, which is competitive with O_2 adsorption. Anyway, under very same experimental conditions (same surface atomic density, topmost layer and surface composition) but different electronic structure, Pt(111) skin shows a ten times fold increase in activity toward ORR than Pt(111). This performance is related to the d-band center, that is 0.34 eV more negative for Pt(111) skin than Pt(111).

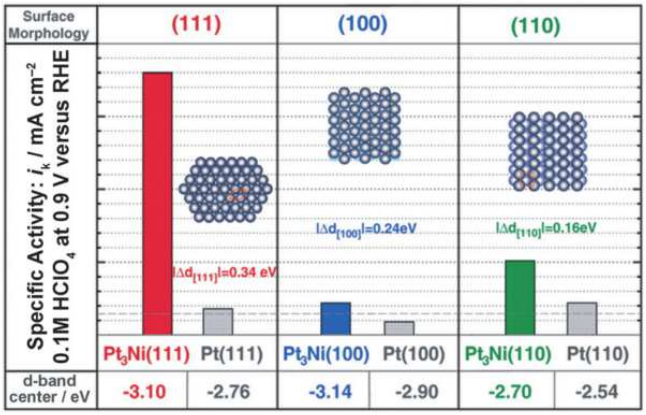

Figure 1.15 RRDE measurements for ORR in 0.1 M $HClO_4$ at 333 K at 1600 rpm on Pt_3Ni(hkl) surfaces as compared to the corresponding Pt(hkl) surfaces. The dashed horizontal grey line corresponds to the Pt activity. Values of d-band center position are listed for each surface m Pt_3Ni(hkl) and Pt(hkl) surfaces [36]. From V. Stamenkovic, B. Fowler, B.S. Mun, G. Wang, P.N. Ross, C.A. Lucas, N.M. Markovic, Improved Oxygen Reduction Activity on Pt3Ni(111) via Increased Surface Site Availability, Science 315 (2007) 493-497. Reprinted with permission from AAAS.

The catalytic activity of several Pt bimetallic alloys is represented in the so called 'Volcano plot' [37]. This graph shows the performance towards ORR as a function of oxygen adsorption energy, a good descriptor for catalytic activity of different Pt-based catalysts. The oxygen adsorption energy and the limiting current densities are all relative to bulk Pt. This volcano plot is obtained according to the methodology explained by V. Stamenkovich et al. in reference [37]. First of all, free energies of all the intermediates of the oxygen reduction are obtained as a function of applied potential with density functional theory (DFT) calculations. Then a kinetic model is developed which gives the ORR rate at a certain potential as a function of the oxygen chemisorption energy (ΔEO). The results of this analysis lead to the graph reported in Figure 1.16, where it is clear the volcano-shaped dependence of ORR activity as a function of ΔEO (both values are relative to Pt bulk). The first group of catalyst highlighted in this graph includes the materials on left side of the volcano plot, which possess an oxygen chemisorption energy higher than bulk Pt, and show a decrease in performance toward ORR as their ΔE_O increases. These materials bind oxygen too strongly, and ORR kinetics is slow because of hindered removal of adsorbed O and OH species. The second group of catalysts includes the

materials on the right side of the volcano plot, which possess a lower oxygen chemisorption energy than bulk Pt. In this case O is bound too weakly to the catalyst, and the ORR rate is limited by electrons and protons transfer to adsorbed O_2. Volcano plot confirms also that Pt binds O_2 a little too strongly, and that the ideal catalyst have a surface which binds O_2 around 0.2 eV more weakly [37].

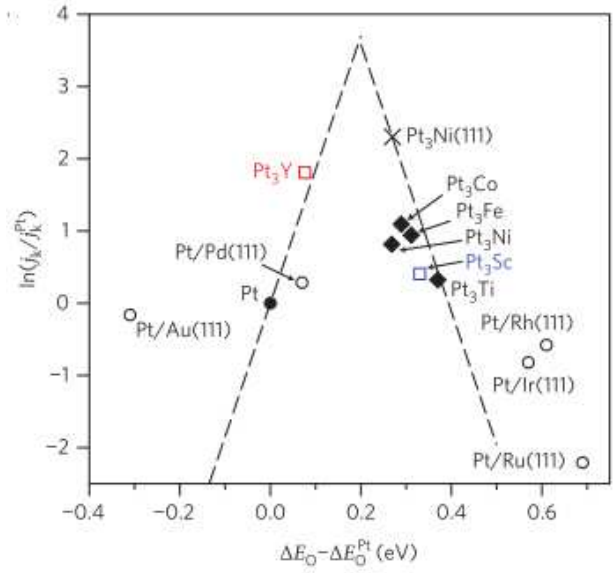

Figure 1.16 Kinetic current density for a series of alloy electrocatalysts with Pt 'skins', plotted as a function of the calculated oxygen adsorption energy, ΔE_O. All data are shown relative to Pt [37]. V. Stamenkovic, B.S. Mun, K.J.J. Mayrhofer, P.N. Ross, N.M. Markovic, J. Rossmeisl, J. Greeley, J.K. Nørskov, Changing the activity of electrocatalysts for oxygen reduction by tuning the surface electronic structure, Angew. Chemie - Int. Ed. 45 (2006) 2897–2901.

1.4.3 Improving catalyst for ORR: innovative supports

A third important strategy to improve catalysts for oxygen reduction deals with the enhancing of the support, in particular it's fundamental to improve the resistance to oxidation and to create strong metal-support interaction that can stabilize the metal phase. The choice of the catalyst support is strongly influenced by properties like electrical conductivity, surface area, hydrophobicity, morphology, porosity and corrosion resistance.

Carbon blacks (CBs) are carbon materials widely employed as catalyst support in low-temperature PEM fuel cells [38]. CBs consist in spherical graphitic particles with mean diameter around 50 nm. The most common procedure to synthesize them deals with the pyrolysis of hydrocarbons such as natural gas or oil fraction from petroleum processing. CBs generally need to be activated before their employment as catalyst support. Both chemical and thermal

treatments are applied in order to improve properties of CBs. Chemical treatment consists in acid, alkaline or oxidative treatments with HNO_3, KOH, H_2O_2, O_2 or O_3. The result of each of this treatment is an improvement of oxide surface groups, which increase their wettability as well. Many papers report a positive effect on the deposition of Pt nanoparticles and on the electrochemical activity of Pt on chemically modified CBs [39][40][41][42][43], but generally oxygen groups are deleterious for stability of carbon materials. Thermal treatment of CBs is performed as well in both inert atmosphere at 800-1100 °C and air/steam at 400-500 °C [44]. The aim is to eliminate surface impurities, to increase capacitive current, graphitization degree and electrochemical active area of the metal phase deposited on it [45]. Despite activation, CBs still show some drawbacks, associated to the presence of micropores and to the oxidation in PEM fuel cell conditions. The micropores prevent nafion particles entering them, so Pt NPs located in smaller pores are not in touch with the ionomer and then they do not participate to the electrochemical process [44].

High graphitized carbon materials, such as carbon nanotubes (CNTs), graphene, and mesoporous carbons, represent innovative metal support in fuel cells environment. First of all, high graphitization degree is responsible for an increased electrical conductivity of the carbon support. Secondly, a strong interaction between Pt NPs and graphitic domain of carbon support is found [46][47][48], and it's considered to play a fundamental role in increasing Pt stability. Furthermore high graphitization is responsible also for a higher resistance toward oxidation, important in the strong oxidant conditions realized during operation in fuel cells [13]. CNTs consist in cylindrical graphite layers closed at both ends [49]. They possess high surface area, good electrical conductivity and stability, higher corrosion resistance respect to CBs and they can be used as support for metal catalyst in PEM fuel cell. The deposition of the metal phase may occur after proper modification of CNTs, because of their chemical inertness. Two kind of modifications can be applied: covalent and non-covalent. In the first situation a chemical modification (i.e. oxidative treatment) is applied, in the second one a doping element is introduced [38]. Carbon nanofibers (CNFs) are similar to CNTs, except for the absence of cavities in their structure, and generally are wider and longer than CNTs. CNFs are made of a stack of graphene sheets, such as stacked platelets, herringbone and ribbons shapes. They have good thermal and electrical conductivities, and higher resistance to oxidation than CBs as well [38]. Graphene is one of the most important allotropes of carbon, consists in a two-dimensional one atom thick sheet with a honeycomb-like structure. The graphene sheet is 0.34 nm thick and represents the building block for fullerene, CNTs and graphite; it is a high conductive material with the highest electron transfer capability [38]. Graphene and its oxygen doped form are

employed in fuel cells not only as a catalyst support, but also as bipolar plate and membrane [50]. Graphene is doped as well in order to provide anchoring sites for metallic nanoparticles for the improvement of its properties as fuel cells catalyst support.

1.5 Mesoporous Carbons

Mesoporous Carbons (MCs) are innovative materials with peculiar properties, such as high surface area, controlled porous structure, good thermal and chemical stability, good thermal conductivity and low density. These properties make MCs suitable for applications not only as carbon support in PEM fuel cells, but also as supercapacitors and hydrogen storage material [38]. Pores are classified according their diameter in micropores (less than 2 nm), mesopores (included between 2 and 50 nm) and macropores (bigger than 50 nm). Mesoporous range is suitable for application as carbon support in PEM fuel cells, because it allows both Pt NPs and Ionomer unit to enter the pores.

A key parameter for application of MCs as catalyst support is the electrical conductivity: generally, in high surface area materials this property is lower than other support such as CNTs or graphene. Several strategies to improve electrical conductivity in MCs and make it comparable to other carbon materials are possible. First of all suitable carbon precursor should be used: aromatic and polyaromatic compounds give graphitic carbon structures by pyrolysis at 900 °C, while non aromatic molecules could originate graphitic domains if treated at higher temperatures (i.e. at least 1500 °C) [51]. Anyway, the best procedure to obtain a high graphitization degree consists in applying a heat treatment at 2500 °C under inert atmosphere. The con of this treatment is the lowering of surface area due to a shrinkage of the carbon structure, which determines loss in micropososity [51]. Transition from amorphous to graphitized carbon starts at around 2000 °C, and is associated to a densification of the carbon structure. Then the graphitization determines also a restructuring of the carbon material, responsible for the formation of fractures in the walls [51]. A last strategy to improve the electrical conductivity is the catalytic graphitization, in which the pyrolysis of carbon precursor occurs in the presence of metal nanoparticles like cobalt, nickel or iron. In this case however, a catalyst removal treatment is required, and it might modify the pore structure [51][52]. Low electrical conductivity arises also as carbon particles are not well connected, for example if they're too big and big voids are present among them. A possible strategy to overcome this

problem might be consistent with the bridging of ordered mesoporous carbons (OMCs) particles with CNTs [53]. Both this latter strategy and the catalytic graphitization can generate an up to two order increase in electrical conductivity [54].

MCs might be classified according their pore structure in ordered mesoporous carbons (OMCs) and disordered mesoporous carbons (DOMCs). OMCs are generally obtained via nanocasting of ordered silica templates and possess better properties than DOMCs, such as narrower pore distribution and better pores interconnection, resulting in better conductivity, mass transport and surface area. A broad pore distribution in DOMCs is not deleterious, unless an important fraction of pores is smaller than 4 nm, situation in which Pt NPs don't participate to the reaction [55]. The mesopores are supposed to be responsible for a better mass transport than CNTs, in particular the gas flow is favoured in mesopores in a higher degree than the inner cavities of a CNT [56]. In a study conducted by S. Song et al., described in reference [57], two mesoporous carbon are employed as Pt support in the cathodic site of a PEM fuel cell. They consist in an OMC CMK-3 type and a DOMC with a wormhole structure with similar pore volume, BET surface area and mesopores size but different pore structure. Pt NPs are deposited on both supports with the same loading and particle size. Cyclic voltammetries recorded in 0.5 M H_2SO_4 on Pt/CMK-3 and Pt/WMC show higher capacitive current for the sample that possess ordered pore structure with interconnected pores. Determination of Pt electrochemical surface area shows a one fold increase for Pt/CMK-3 with respect to Pt/WMC, indicating a higher number of exposed active site. Rotating disk electrode analysis proves the higher electrocatalytic activity toward ORR of Pt/CMK-3 material. So, the effect of pore morphology on electrochemical activity is found to be fundamental for the electrochemical properties of the catalyst: in particular, ordered and interconnected pores allow a better mass transport and accessibility to Pt sites. On the contrary, bad pores connection hinder reactants transportation, especially to the active sites located far from the pore entrance. A second study done by L. Zhang et al. [58] takes into account ordered mesoporous carbon spheres with different pore size of 22, 35 and 50 nm, modified with iron catalyst for oxygen reduction. In this case better performance in terms of current density at 0.55 V/RHE are obtained when the catalyst with biggest pore size is employed. This indicates as well a strong influence of the pore dimension over the reaction, i.e. a better mass transport to and from the active sites.

1.5.1 Synthesis of mesoporous carbons: hard template

The first and easy way to synthesize MCs is hard template. This technique involves the employment of two main reactants: an inorganic template, whose porous structure is transferred to the synthesizing material, and a carbon source, molecules which may pyrolyse to give carbon structures. A general procedure to synthesize MCs via hard template consists in the wetting of an inorganic template with a solution of a proper carbon precursor. Two heating treatment are then applied: the first one at low temperature (<300 °C) to start an early reticulation of the carbon precursor molecules and remove solvent residual; the second one at high temperature (>900 °C) under inert atmosphere to perform the pyrolysis and to obtain a graphitic carbon material. Lastly, the inorganic template should be separated from the carbon material with a chemical treatment that breaks its structure down without damaging the carbon material [59][60]. In Figure 1.17 the three fundamental steps of hard template process for porous carbon synthesis are reported: impregnation of template with the carbon precursor, pyrolysis and template selective removal. The obtained carbon structure is the negative replica of the template: the pores of the silica are filled with the carbon precursor, which becomes the continuous carbon framework, while the silica becomes the pores of the carbon structure after chemical etching [59].

Figure 1.17 Hard template process for mesoporous carbon synthesis: mixing of inorganic template and carbon precursor, followed by pyrolysis and chemical etching of the template.

The template and the carbon precursor have a strong influence over the properties of the final porous carbon. Typical carbon precursors that can be pyrolysed consist in aromatic compound such as divinylbenzene, pyrrole, petroleum pitch and mesophase pitch, but non aromatic compounds might be used as well [51]. Generally, a high number of heteroatoms in the carbon precursor is responsible for failure in the pyrolysis, because many volatile compounds instead of a carbon framework may be formed. The pore size of an OMC obtained via hard template depends on the pore wall thickness of the starting silica, which in turn is

determined by its synthesis parameters. Shrinkage of carbon structure generally occurs during pyrolysis, leading to smaller structures and slightly bigger pore size than what expected from the cell parameter of the template. The shrinkage is higher if non aromatic compounds are employed, leading to smaller pore size, lower surface area and pore volume, but higher mechanical resistance [59]. An important parameter consists in interconnected pore structure in silica template. This is consistent with micropores interconnected with the main mesoporous systems, which are filled with carbon precursor and give to the porous material high mechanical resistance, preventing the structure from collapsing. An example of carbon structure in which the main framework is mechanically supported by a microsized secondary scaffold is represented in Figure 1.18. In Figure 1.19 a and b a comparison between a DOMC and an OMC is reported: the properties of the starting silica template determine the carbon structure. DOMC is obtained in case a, where a silica with bad pore connection is employed; the structure of the silica template that generates them is basically the same, exception for the micropores connecting the main porous system in sample b, absent in sample a. DOMC is generated from silica a, while OMC from silica b.

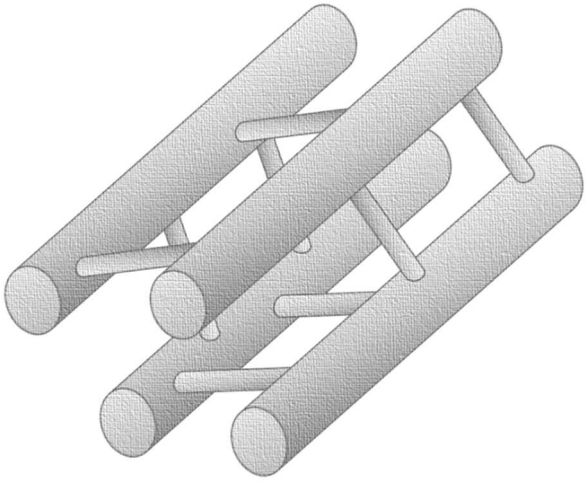

Figure 1.18 Carbon structure obtained from a template with an interconnected pore structure, fundamental for the mechanical resistance of the material.

In reference [61] the synthesis of an OMC from sucrose and silica SBA-15 as template is described. SBA-15 consists of a hexagonal arrangement of cylindrical tubes with 9 nm diameter, with random micrometric sized interconnection among the tubes. This structure is also similar to the honeycomb structure of silica MCM-41, except for the absence of interconnections in this last sample. The carbon obtained from SBA-15 is labelled CMK-3 and it is the exact replica of the silica. It's made of carbon nanorods with 7 nm diameter, the center of adjacent rods is 10 nm

apart and the surface of each rod is 3 nm far from the others. Pore size of mesoporous carbon is equal to the wall thickness of the silica template. Furthermore nanorods are interconnected by spacers. XRD confirms for CMK-3 the same fully-ordered structure as SBA-15. On the contrary, XRD analysis shown no hexagonal structural order if MCM-41 is used as template, because of the absence of interconnection, as pictured in Figure 1.19**.** If another precursor, such as furfuryl alcohol pyrolised under vacuum is employed, carbon nanotubes or nanopipes are obtained. Tube-type carbon possesses, in fact, two different porosities: one originating from the silica walls, the same present also in rod-type carbon, and a second one originating from silica pores.

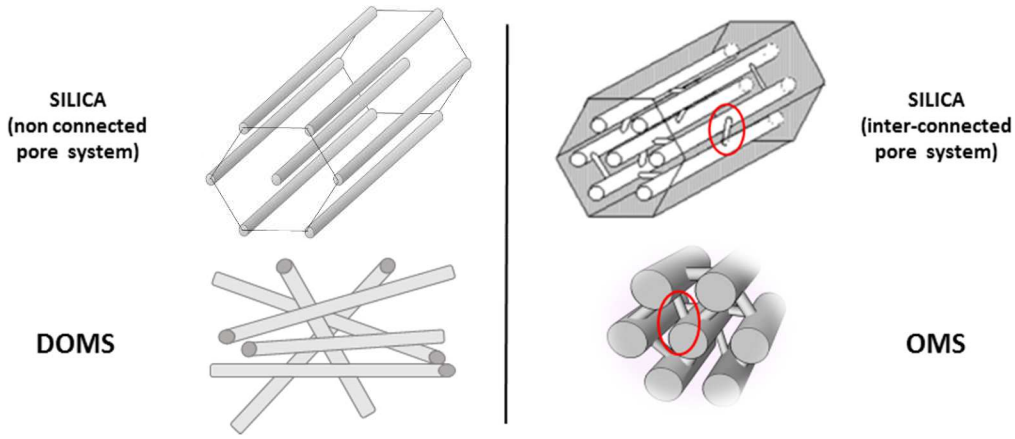

Figure 1.19 On the left: structure of silica template without interconnection among pores and the resulting disordered mesoporous carbon. On the right: structure of silica template with interconnection among pores and the resulting ordered mesoporous carbon**.**

1.5.2 Synthesis of mesoporous carbon: soft template

Soft template is the synthesis of porous materials starting from amphiphilic molecules such as surfactants and copolymers, and offers an alternative route to the traditional and well characterized hard template. Four requirement have to be strictly respected to succeed in synthesizing carbon materials via soft template:

i. Ability of precursors materials to self-assembly into nanostructures
ii. Presence of at least one pore-forming and one carbon-yielding component
iii. Stability of pore-forming component during high temperature pyrolysis for the curing of carbon-yielding component, but at the same time easily decomposition
iv. Ability of carbon-yielding component to form a highly cross-linked polymeric material that has to maintain its structure during pore-forming removal

An example of porous nanocarbon obtained via soft template is reported by Matyjaszewski in reference [62]. A block copolymer made of polyacrylonitrile (PAN) and poly(n-butyl acrylate) (PBA) is prepared via atom transfer radical polymerization (ATRP). PAN is a nitrogen containing polymer, so N functionalities will be found in the carbon as well. A former stabilization of PAN is done at 280 °C under air to promote cyclization and cross-linking, necessary for the stabilization of the material during the pyrolysis step under inert atmosphere. The polymer was dropcasted on a Si substrate, in order to obtain a thin film which can undergo AFM image as well. Four different carbon materials are obtained from different ratios of PAN and PBA in the starting copolymer and different degree of polymerization. These parameter influence the geometry (filaments, cylinders, branch). Bulk copolymer are more desirable in practical application, but the same synthesis lead to different pore size and surface area, bigger and smaller than thin film, respectively. Surface areas of carbon materials obtained via soft template are generally around 400-500 m^2/g, much smaller than the values obtained with hard template process.

1.5.3 Doping of mesoporous carbons

Doping consists in the chemical modification of carbon materials via heteroatom insertion in their structure. It consists in an important strategy to modify or improve properties of materials. The most common structure modification consists in the insertion of N heteroatoms, but also S, P, B are employed to tailor carbon properties [63]. N functional groups depend strongly on the applied temperature. Generally, at low temperature N groups are not included in aromatic ring and they possess a localized charge. On the contrary, at high temperature aromatic ring incorporated N groups are formed, and their charge is delocalized on the structure. N heteroatoms play an important role in catalysis, as reported in reference [64]. First of all, N creates charge separation, i.e. polarity, which modifies the interaction between the carbon material and other species. In particular, all interactions with polar species turn out to be favoured in an N-modified carbon material. As a consequence, a better interaction with H_2O molecules (or any other polar solvent) is determined, corresponding to an improved wettability of the carbon. This is fundamental in MEA production, when an excellent catalyst dispersion is required for production of good catalyst layers. N atoms modifies also the conductivity of carbon materials, which can be improved compared to the analogous non-doped material. In a paper by Z. Ismagilov et al. [64], the effect of nitrogen functionality in carbon fibers on electrical conductivity is evaluated: three different amount of N included between 1.7 and 8.3%$_w$ are

evaluated and compared with a non-doped carbon fiber material. N-doped materials show a non-linear dependence of electrical conductivity on N content, which reaches a maximum at 3.1 $\%_w$ of N, and decreases for lower and higher values. This loading corresponds to an improved electrical conductivity than non-doped carbon fibers [65]. Furthermore, doping alone can modify the reactivity towards ORR, in particular N doping is responsible for an increase of electrochemical activity toward the process, and this is important in the so called 'metal-free catalyst' [66][67][68][69][70][71][72].

Nowadays the most important reason for doping carbon support employed in fuel cells is linked to the modification of the interaction between carbon support and metal nanoparticles. In particular N doping appears to be responsible for the creation of strong and favourable interaction which may enhance the catalytic properties of catalyst, and at the same time may reduce the Pt loading. According to reference [73], the effect of nitrogen doping on the activity of Pt based catalyst is responsible for the following effects:

I. Alteration of catalyst nucleation and growth behaviour.
   Smaller Pt NPs and narrower size distribution are obtained on N-doped carbon materials, also in the case when high Pt loading is realized. This indicates a fundamental role in support chemistry in the determination of dimension and distribution of Pt NPs. Generally, high rate of nucleation are realized when the surface is defective and surface energy in high.
II. Alteration of support/catalyst binding.
   Nitrogen functionalities are supposed to act as tethers, i.e. chemical binding sites. This allows better dispersion and improves the stability of Pt NPs with respect to agglomeration and coarsening.
III. Alteration of catalyst electronic structure.

These reasons show that N doped carbons are promising materials to be used as catalyst supports in PEM fuel cells. Analogous findings are reported also in reference [74] for sulphur doped graphene employed as support for Pt NPs. In this case, X-rays photoelectron spectroscopy (XPS) highlights an enhanced interaction between the metal and the support, corresponding to a charge transfer from Pt to carbon, which results in a better electrocatalytic property towards ORR.

N functionalities may be inserted in the structure of a carbon material during the pyrolysis step under inert atmosphere, starting from N-containing precursors such as

phenanthroline or melamine [66][70][75], or with nitrogen-containing reagents such as NH_3 or HNO_3 [76][77]. The advantage of this route is the single step necessary to obtain the doped carbon: during the pyrolysis heat treatment in fact both the carbon framework and the functionalities are generated. A second route consists in the post-functionalization, i.e. a nitrogenation in gas or liquid phase, after the pyrolysis step. Suitable compounds to be used in this process consist in NH_3-air mixture, HNO_3, HCN, urea, N,N-dymethylformamide, aniline or melamine. According to the physical state of each chemical, this treatment may be conducted in both liquid and gas phase.

Bibliography

[1] L. Carrette, K. Friedrich, U. Stimming, Fuel Cells - Fundamentals and Applications, Fuel Cells. 1 (2001) 5–39. doi:10.1002/1615-6854(200105)1:1<5::AID-FUCE5>3.0.CO;2-G.

[2] L. Carrette, K. a Friedrich, U. Stimming, Fuel cells: principles, types, fuels, and applications., Chemphyschem. 1 (2000) 162–93. doi:10.1002/1439-7641(20001215)1:4<162::AID-CPHC162>3.0.CO;2-Z.

[3] J.M. Andújar, F. Segura, Fuel cells: History and updating. A walk along two centuries, Renew. Sustain. Energy Rev. 13 (2009) 2309–2322. doi:10.1016/j.rser.2009.03.015.

[4] S.P.S. Badwal, S. Giddey, A. Kulkarni, J. Goel, S. Basu, Direct ethanol fuel cells for transport and stationary applications - A comprehensive review, Appl. Energy. 145 (2015) 80–103. doi:10.1016/j.apenergy.2015.02.002.

[5] T. Elmer, M. Worall, S. Wu, S.B. Riffat, Fuel cell technology for domestic built environment applications: State of-the-art review, Renew. Sustain. Energy Rev. 42 (2015) 913–931. doi:10.1016/j.rser.2014.10.080.

[6] M.O. Abdullah, Y.K. Gan, Feasibility study of a mini fuel cell to detect interference from a cellular phone, J. Power Sources. 155 (2006) 311–318. doi:10.1016/j.jpowsour.2005.05.013.

[7] D. Loomis, Y. Grosse, atrice Lauby-Secretan, F. El Ghissassi, ronique Bouvard, L. Benbrahim-Tallaa, N. Guha, R. Baan, H. Mattock, K. Straif, on behalf of the International Agency for Research on Cancer Monograph Working Group IARC, The carcinogenicity of outdoor air pollution, Lancet Oncol. 14 (2013) 1262–1263. doi:10.1016/S1470-2045(13)70487-X.

[8] M. Guarnieri, J.R. Balmes, Outdoor air pollution and asthma, Lancet. 383 (2014) 1581–1592. doi:10.1016/S0140-6736(14)60617-6.

[9] B.A. Franklin, R. Brook, C.A. Pope III, Air Pollution and Cardiovascular Disease, Curr. Probl. Cardiol. 40 (2015) 207–238. doi:10.1016/j.cpcardiol.2015.01.003.

[10] ORGANISATION FOR ECONOMIC CO-OPERATION AND DEVELOPMENT, Energy: the next fifty years., (n.d.). doi:10.1016/0040-1625(80)90092-X.

[11] T. Iwasita, Electrocatalysis of methanol oxidation, Electrochim. Acta. 47 (2002) 3663–3674. doi:10.1016/S0013-4686(02)00336-5.

[12] Department of Energy, Types of Fuel Cells, (n.d.). http://energy.gov/eere/fuelcells/types-fuel-cells.

[13] Y. Luo, N. Alonso-Vante, The Effect of Support on Advanced Pt-based Cathodes towards the Oxygen Reduction Reaction. State of the Art, Electrochim. Acta. 179 (2015) 108–118. doi:10.1016/j.electacta.2015.04.098.

[14] L. Su, W. Jia, C.-M. Li, Y. Lei, Mechanisms for enhanced performance of platinum-based electrocatalysts in proton exchange membrane fuel cells., ChemSusChem. 7 (2014) 361–78. doi:10.1002/cssc.201300823.

[15] G. Merle, M. Wessling, K. Nijmeijer, Anion exchange membranes for alkaline fuel cells: A review, J. Memb. Sci. 377 (2011) 1–35. doi:10.1016/j.memsci.2011.04.043.

[16] I. Kruusenberg, L. Matisen, Q. Shah, A.M. Kannan, K. Tammeveski, Non-platinum cathode catalysts for alkaline membrane fuel cells, Int. J. Hydrogen Energy. 37 (2012) 4406–4412. doi:10.1016/j.ijhydene.2011.11.143.

[17] M. Piana, M. Boccia, A. Filpi, E. Flammia, H.A. Miller, M. Orsini, F. Salusti, S. Santiccioli, F. Ciardelli, A. Pucci, H 2 /air alkaline membrane fuel cell performance and durability, using novel ionomer and non-platinum group metal cathode catalyst, J. Power Sources. 195 (2010) 5875–5881. doi:10.1016/j.jpowsour.2009.12.085.

[18] http://www.physics.nist.gov/MajResFac/NIF/pemFuelCells.html. Consulted on October 1, 2016.

[19] S.S. Kocha, Principles of MEA preparation, in: Handb. Fuel Cells, John Wiley & Sons, Ltd, Chichester, UK, 2010. doi:10.1002/9780470974001.f303047.

[20] Y. Xiao, M. Dou, J. Yuan, M. Hou, W. Song, B. Sundén, Fabrication Process Simulation of a PEM Fuel Cell Catalyst Layer and Its Microscopic Structure Characteristics, J. Electrochem. Soc. 159 (2012) 308–314. doi:10.1149/2.064203jes.

[21] N.J. Economou, J.R. O'Dea, T.B. McConnaughy, S.K. Buratto, Morphological differences in short side chain and long side chain perfluorosulfonic acid proton exchange membranes at low and high water contents, RSC Adv. 3 (2013) 19525. doi:10.1039/c3ra41976b.

[22] K. Kreuer, On the complexity of proton conduction phenomena, Solid State Ionics. 136–137 (2000) 149–160. doi:10.1016/S0167-2738(00)00301-5.

[23] S.J. Peighambardoust, S. Rowshanzamir, M. Amjadi, Review of the proton exchange membranes for fuel cell applications, Elsevier Ltd, 2010. doi:10.1016/j.ijhydene.2010.05.017.

[24] J.S. Spendelow, D.C. Papageorgopoulos, Progress in PEMFC MEA component R&D at the DOE fuel cell technologies program, Fuel Cells. 11 (2011) 775–786. doi:10.1002/fuce.201000189.

[25] Q. Li, J.O. Jensen, R.F. Savinell, N.J. Bjerrum, High temperature proton exchange membranes based on polybenzimidazoles for fuel cells, Prog. Polym. Sci. 34 (2009) 449–477. doi:10.1016/j.progpolymsci.2008.12.003.

[26] H. Tang, S. Wang, S.P. Jiang, M. Pan, A comparative study of CCM and hot-pressed MEAs for PEM fuel cells, J. Power Sources. 170 (2007) 140–144. doi:10.1016/j.jpowsour.2007.03.062.

[27] V. Mehta, J.S. Cooper, Review and analysis of PEM fuel cell design and manufacturing, J. Power Sources. 114 (2003) 32–53. doi:10.1016/S0378-7753(02)00542-6.

[28] M. Klingele, M. Breitwieser, R. Zengerle, S. Thiele, Direct deposition of proton exchange membranes enabling high performance hydrogen fuel cells, J. Mater. Chem. A 3 (2015) 11239-11245. doi:10.1039/c5ta01341k.

[29] Parts of a Fuel Cell | Department of Energy, http://energy.gov/eere/fuelcells/parts-fuel-cell#gdl.

[30] A. Arvay, E. Yli-Rantala, C.-H. Liu, X.-H. Peng, P. Koski, L. Cindrella, P. Kauranen, P.M. Wilde, A.M. Kannan, Characterization techniques for gas diffusion layers for proton

exchange membrane fuel cells – A review, J. Power Sources. 213 (2012) 317–337. doi:10.1016/j.jpowsour.2012.04.026.

[31] X. Yu, S. Ye, Recent advances in activity and durability enhancement of Pt/C catalytic cathode in PEMFC Part II: Degradation mechanism and durability enhancement of carbon supported platinum catalyst, J. Power Sources. 172 (2007) 145–154. doi:10.1016/j.jpowsour.2007.07.048.

[32] Fuel Cell Technical Team Roadmap, http://energy.gov/sites/prod/files/2014/02/f8/fctt_roadmap_june2013.pdf.

[33] N.M. Marković, R.R. Adžić, B.D. Cahan, E.B. Yeager, Structural effects in electrocatalysis: oxygen reduction on platinum low index single-crystal surfaces in perchloric acid solutions, J. Electroanal. Chem. 377 (1994) 249–259. doi:10.1016/0022-0728(94)03467-2.

[34] N. M. Markovic, H. a. Gasteiger, P.N. Ross, Oxygen Reduction on Platinum Low-Index Single-Crystal Surfaces in Sulfuric Acid Solution: Rotating Ring-Pt(hkZ) Disk Studies, J. Phys. Chem. 99 (1995) 3411. doi:10.1021/j100011a001.

[35] H. Gasteiger, P.N. Ross, Oxygen Reduction on Platinum Low-Index Single-Crystal Surfaces in Alkaline Solution: Rotating Ring DiskPt(hkl) Studies, J. Phys. Chem. 100 (1996) 6715–6721. doi:10.1021/jp9533382.

[36] V. Stamenkovic, B. Fowler, B.S. Mun, G. Wang, P.N. Ross, C.A. Lucas, N.M. Markovic, Improved Oxygen Reduction Activity on $Pt_3Ni(111)$ via Increased Surface Site Availability, Science 315 (2007) 493-497. OK

[37] V. Stamenkovic, B.S. Mun, K.J.J. Mayrhofer, P.N. Ross, N.M. Markovic, J. Rossmeisl, J. Greeley, J.K. Nørskov, Changing the activity of electrocatalysts for oxygen reduction by tuning the surface electronic structure, Angew. Chemie - Int. Ed. 45 (2006) 2897–2901. doi:10.1002/anie.200504386.

[38] S. Shahgaldi, J. Hamelin, Improved carbon nanostructures as a novel catalyst support in the cathode side of PEMFC: A critical review, Carbon N. Y. 94 (2015) 705–728. doi:10.1016/j.carbon.2015.07.055.

[39] G. Torres, E. Jablonski, G. Baronetti, A. Castro, S. de Miguel, O. Scelza, M. Pefia Jim, J. Fierro, Effect of the carbon pre-treatment on the properties and performance for nitrobenzene hydrogenation of Pt/C catalysts, Appl. Catal. A Gen. 161 (1997) 213–226. doi:10.1016/S0926-860X(97)00071-9.

[40] C. Prado-Burguete, A. Linares-Solano, F. Rodríguez-Reinoso, C.S.M. de Lecea, The effect of oxygen surface groups of the support on platinum dispersion in Pt/carbon catalysts, J. Catal. 115 (1989) 98–106. doi:10.1016/0021-9517(89)90010-9.

[41] Dong Jin Suh, P. Tae-Jin, I. Son-Ki, Effect of surface oxygen groups of carbon supports on the characteristics of Pd/C catalysts, Carbon N. Y. 31 (1993) 427–435. doi:10.1016/0008-6223(93)90130-3.

[42] S.. de Miguel, O.. Scelza, M.. Román-Martínez, C. Salinas-Martínez de Lecea, D. Cazorla-Amorós, A. Linares-Solano, States of Pt in Pt/C catalyst precursors after impregnation, drying and reduction steps, Appl. Catal. A Gen. 170 (1998) 93–103. doi:10.1016/S0926-860X(98)00029-5.

[43] M.J. Lázaro, L. Calvillo, E.G. Bordejé, R. Moliner, R. Juan, C.R. Ruiz, Functionalization of ordered mesoporous carbons synthesized with SBA-15 silica as template, Microporous Mesoporous Mater. 103 (2007) 158–165. doi:10.1016/j.micromeso.2007.01.047.

[44] E. Antolini, Carbon supports for low-temperature fuel cell catalysts, Appl. Catal. B Environ. 88 (2009) 1–24. doi:10.1016/j.apcatb.2008.09.030.

[45] A.L.N. Pinheiro, A. Oliveira Neto, E.C. de Souza, J. Perez, V.A. Paganin, E.A. Ticianelli, E.R. Gonzalez, Electrocatalysis on Noble Metal Alloys dispersed on high surface area carbon, J. New Mater. Electrochem. Syst. 6 (2003) 1–8.

[46] J. Ma, a. Habrioux, N. Guignard, N. Alonso-Vante, Functionalizing effect of increasingly graphitic carbon supports on carbon-supported and TiO \n 2-carbon composite-supported Pt nanoparticles, J. Phys. Chem. C. 116 (2012) 21788–21794. doi:10.1021/jp304947y.

[47] Y. Shao, S. Zhang, C. Wang, Z. Nie, J. Liu, Y. Wang, Y. Lin, Highly durable graphene nanoplatelets supported Pt nanocatalysts for oxygen reduction, J. Power Sources. 195 (2010) 4600–4605. doi:10.1016/j.jpowsour.2010.02.044.

[48] J. Ma, A. Habrioux, C. Morais, A. Lewera, W. Vogel, Y. Verde-Gómez, G. Ramos-Sanchez, P.B. Balbuena, N. Alonso-Vante, Spectroelectrochemical probing of the strong interaction between platinum nanoparticles and graphitic domains of carbon, ACS Catal. 3 (2013) 1940–1950. doi:10.1021/cs4003222.

[49] P. Trogadas, T.F. Fuller, P. Strasser, Carbon as catalyst and support for electrochemical energy conversion, Carbon N. Y. 75 (2014) 5–42. doi:10.1016/j.carbon.2014.04.005.

[50] S. Sharma, B.G. Pollet, Support materials for PEMFC and DMFC electrocatalysts - A review, J. Power Sources. 208 (2012) 96–119. doi:10.1016/j.jpowsour.2012.02.011.

[51] K.P. Gierszal, M. Jaroniec, T.-W. Kim, J. Kim, R. Ryoo, High temperature treatment of ordered mesoporous carbons prepared by using various carbon precursors and ordered mesoporous silica templates, New J. Chem. 32 (2008) 981. doi:10.1039/b716735k.

[52] W. Niu, L. Li, J. Liu, N. Wang, W. Li, Z. Tang, W. Zhou, S. Chen, Graphene-Supported Mesoporous Carbons Prepared with Thermally Removable Templates as Efficient Catalysts for Oxygen Electroreduction, Small. (2016) 1900–1908. doi:10.1002/smll.201503542.

[53] F. Su, X.S. Zhao, Y. Wang, J.Y. Lee, Bridging mesoporous carbon particles with carbon nanotubes, Microporous Mesoporous Mater. 98 (2007) 323–329. doi:10.1016/j.micromeso.2006.09.030.

[54] M. Sevilla, A.B. Fuertes, Catalytic graphitization of templated mesoporous carbons, Carbon N. Y. 44 (2006) 468–474. doi:10.1016/j.carbon.2005.08.019.

[55] Y. Shao, J. Liu, Y. Wang, Y. Lin, Novel catalyst support materials for PEM fuel cells: current status and future prospects, J. Mater. Chem. 19 (2009) 46–59. doi:10.1039/b808370c.

[56] K.-Y. Chan, J. Ding, J. Ren, S. Cheng, K.Y. Tsang, Supported mixed metal nanoparticles as electrocatalysts in low temperature fuel cells, J. Mater. Chem. 14 (2004) 505. doi:10.1039/b314224h.

[57] S. Song, Y. Liang, Z. Li, Y. Wang, R. Fu, D. Wu, P. Tsiakaras, Effect of pore morphology of

mesoporous carbons on the electrocatalytic activity of Pt nanoparticles for fuel cell reactions, "Applied Catal. B, Environ. 98 (2010) 132–137. doi:10.1016/j.apcatb.2010.05.021.

[58] L. Zhang, J. Kim, E. Dy, S. Ban, K. Tsay, H. Kawai, Z. Shi, J. Zhang, Effect of template size on the synthesis of mesoporous carbon spheres and their supported Fe-based ORR electrocatalysts, Electrochim. Acta. 108 (2013) 814–819. doi:10.1016/j.electacta.2013.07.037.

[59] C. Liang, Z. Li, S. Dai, Mesoporous carbon materials: Synthesis and modification, Angew. Chemie - Int. Ed. 47 (2008) 3696–3717. doi:10.1002/anie.200702046.

[60] T.-Y. Ma, L. Liu, Z.-Y. Yuan, Direct synthesis of ordered mesoporous carbons., Chem. Soc. Rev. 42 (2013) 3977–4003. doi:10.1039/c2cs35301f.

[61] S. Jun, S.H. Joo, R. Ryoo, M. Kruk, Synthesis of New , Nanoporous Carbon with Hexagonally Ordered Mesostructure, (2000) 10712–10713. doi:10.1021/JA002261E.

[62] M. Zhong, C. Tang, E.K. Kim, M. Kruk, E.B. Celer, M. Jaroniec, K. Matyjaszewski, T. Kowalewski, Preparation of porous nanocarbons with tunable morphology and pore size from copolymer templated precursors, (n.d.). doi:10.1039/c3mh00084b.

[63] J.P. Paraknowitsch, A. Thomas, Doping carbons beyond nitrogen: an overview of advanced heteroatom doped carbons with boron, sulphur and phosphorus for energy applications, Energy Environ. Sci. 6 (2013) 2839. doi:10.1039/c3ee41444b.

[64] M. Seredych, D. Hulicova-Jurcakova, G.Q. Lu, T.J. Bandosz, Surface functional groups of carbons and the effects of their chemical character, density and accessibility to ions on electrochemical performance, Carbon N. Y. 46 (2008) 1475–1488. doi:10.1016/j.carbon.2008.06.027.

[65] Z.R. Ismagilov, A.E. Shalagina, O.Y. Podyacheva, A. V. Ischenko, L.S. Kibis, A.I. Boronin, Y.A. Chesalov, D.I. Kochubey, A.I. Romanenko, O.B. Anikeeva, T.I. Buryakov, E.N. Tkachev, Structure and electrical conductivity of nitrogen-doped carbon nanofibers, Carbon N. Y. 47 (2009) 1922–1929. doi:10.1016/j.carbon.2009.02.034.

[66] V. Perazzolo, C. Durante, R. Pilot, A. Paduano, J. Zheng, G.A. Rizzi, A. Martucci, G. Granozzi, A. Gennaro, Nitrogen and sulfur doped mesoporous carbon as metal-free electrocatalysts for the in situ production of hydrogen peroxide, Carbon N. Y. 95 (2015) 949–963. doi:10.1016/j.carbon.2015.09.002.

[67] T.-P. Fellinger, F. Hasché, P. Strasser, M. Antonietti, Mesoporous nitrogen-doped carbon for the electrocatalytic synthesis of hydrogen peroxide., J. Am. Chem. Soc. 134 (2012) 4072–5. doi:10.1021/ja300038p.

[68] X. Liu, H. Zhu, X. Yang, One-step synthesis of dopamine-derived micro/mesoporous nitrogen-doped carbon materials for highly efficient oxygen-reduction catalysts, J. Power Sources. 262 (2014) 414–420. doi:10.1016/j.jpowsour.2014.04.023.

[69] R. Silva, D. Voiry, M. Chhowalla, T. Asefa, E ffi cient Metal-Free Electrocatalysts for Oxygen Reduction: Polyaniline-Derived N- and O - Doped Mesoporous Carbons, J. Am. Chem. Soc. 135 (2013) 7823–7826. doi:dx.doi.org/10.1021/ja402450a.

[70] R. Wang, T. Zhou, H. Li, H. Wang, H. Feng, J. Goh, S. Ji, Nitrogen-rich mesoporous carbon derived from melamine with high electrocatalytic performance for oxygen reduction

reaction, J. Power Sources. 261 (2014) 238–244. doi:10.1016/j.jpowsour.2014.03.057.

[71] W. Wei, H. Liang, K. Parvez, X. Zhuang, X. Feng, K. Müllen, Nitrogen-doped carbon nanosheets with size-defined mesopores as highly efficient metal-free catalyst for the oxygen reduction reaction, Angew. Chemie - Int. Ed. 53 (2014) 1570–1574. doi:10.1002/anie.201307319.

[72] W.Y. Wong, W.R.W. Daud, a. B. Mohamad, a. a. H. Kadhum, K.S. Loh, E.H. Majlan, Recent progress in nitrogen-doped carbon and its composites as electrocatalysts for fuel cell applications, Int. J. Hydrogen Energy. 38 (2013) 9370–9386. doi:10.1016/j.ijhydene.2012.12.095.

[73] Y. Zhou, K. Neyerlin, T.S. Olson, S. Pylypenko, J. Bult, H.N. Dinh, T. Gennett, Z. Shao, R. O'Hayre, Enhancement of Pt and Pt-alloy fuel cell catalyst activity and durability via nitrogen-modified carbon supports, Energy Environ. Sci. 3 (2010) 1437. doi:10.1039/c003710a.

[74] D. Higgins, M.A. Hoque, M.H. Seo, R. Wang, F. Hassan, J.-Y. Choi, M. Pritzker, A. Yu, J. Zhang, Z. Chen, Development and Simulation of Sulfur-doped Graphene Supported Platinum with Exemplary Stability and Activity Towards Oxygen Reduction, Adv. Funct. Mater. 24 (2014) 4325–4336. doi:10.1002/adfm.201400161.

[75] Y. Shin, G.E. Fryxell, M.H. Engelhard, G.J. Exarhos, Functional mesoporous carbon built from the 1,10-phenanthroline building block: A new class of catalyst support, Inorg. Chem. Commun. 10 (2007) 1541–1544. doi:10.1016/j.inoche.2007.09.021.

[76] W. Shen, W. Fan, Nitrogen-containing porous carbons: synthesis and application, J. Mater. Chem. A. 1 (2013) 999–1013. doi:10.1039/C2TA00028H.

[77] L. Perini, C. Durante, M. Favaro, V. Perazzolo, S. Agnoli, O. Schneider, G. Granozzi, A. Gennaro, Metal–Support Interaction in Platinum and Palladium Nanoparticles Loaded on Nitrogen-Doped Mesoporous Carbon for Oxygen Reduction Reaction, ACS Appl. Mater. Interfaces. 7 (2015) 1170–1179. doi:10.1021/am506916y.

Chapter 2

Oxygen Reduction Reaction

In this chapter the mechanism for oxygen reduction reaction (ORR) on different surfaces such as Pt, bare carbon and N-modified carbon is described. ORR may follow two different pathways: the first one is a direct four-electrons reaction which lead directly to H_2O, the second one is a double bi-electronic step in which H_2O_2 is formed as intermediate and then is further reduced to H_2O. In the equations below the ORR reduction pathways in acid (Eq. 2.1 – 2.3) and alkaline (Eq. 2.4 -2.6) media, with the standard potentials at 25 °C and 1 atm are reported:

$$O_2 + 4H^+ + 4e^- \leftrightarrow 2H_2O \qquad E^{\ominus} = 1.229 \qquad \text{(Eq. 2.1)}$$

$$O_2 + 2H^+ + 2e^- \leftrightarrow H_2O_2 \qquad E^{\ominus} = 0.700 \qquad \text{(Eq. 2.2)}$$

$$H_2O_2 + 2H^+ + 2e^- \leftrightarrow 2H_2O \qquad E^{\ominus} = 1.760 \qquad \text{(Eq. 2.3)}$$

$$O_2 + H_2O + 4e^- \leftrightarrow 4OH^- \qquad E^{\ominus} = 0.401 \qquad \text{(Eq. 2.4)}$$

$$O_2 + H_2O + 2e^- \leftrightarrow HO_2^- + OH^- \qquad E^{\ominus} = -0.065 \qquad \text{(Eq. 2.5)}$$

$$HO_2^- + H_2O + 2e^- \leftrightarrow 3OH^- \qquad E^{\ominus} = 0.867 \qquad \text{(Eq. 2.6)}$$

These reduction reactions consist in the half-cell process occurring in an electrochemical systems such as fuel cells, the second half-cell reaction consists in the hydrogen oxidation, with standard potential equal to 0.0 V in standard conditions. All the mechanisms for ORR reported in this chapter are taken from reference [1]. The reduction pathway is influenced by the adsorption geometry of molecular oxygen on the catalytic surface. When O_2 is adsorbed on a single active site, the direct four-electron pathway is favoured (case of Pauling and Griffith models, Figure 2.1 b and c, respectively), while, when a bridge adsorption on two active sites is realized, H2O2 formation is promoted (Yeager model, Figure 2.1a) [2].

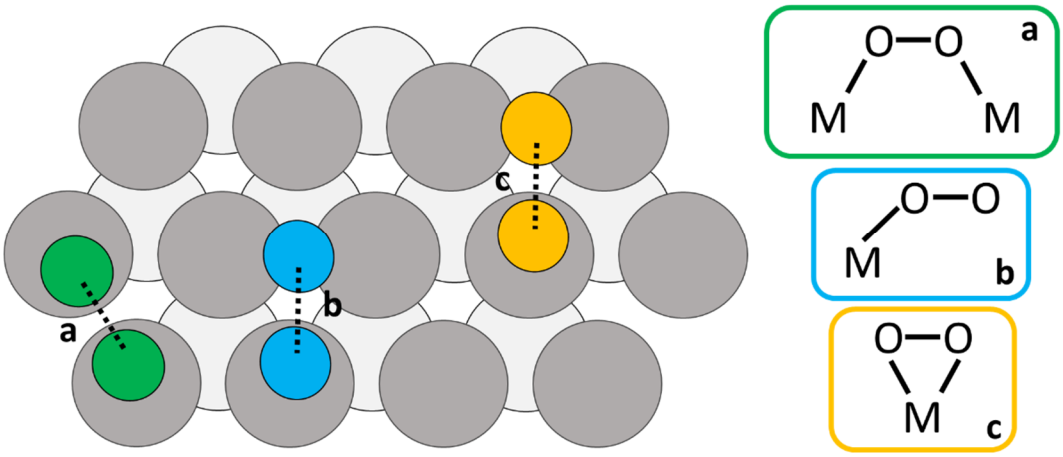

Figure 2.1 Molecular oxygen adsorption on a (111) surface with fcc structure. a) Yeager model, b) Pauling model and c) Griffith model.

2.1 ORR on Pt

The oxygen reduction mechanism on Pt generally follows the direct four-electron pathway described in Eq. 2.1 and 2.4 for acid and alkaline media, respectively. However, the reaction mechanism is complex and it involves several elementary steps, as shown in the equations 2.7 – 2.12 for the acid environment [1].

$$Pt + O_2 \rightleftarrows Pt - O_{2\,(ads)} \quad \text{(Eq. 2.7)}$$

$$Pt - O_{2\,(ads)} + H^+ + e^- \rightarrow Pt - O_2\,H_{(ads)} \quad \text{(Eq. 2.8)}$$

$$x(Pt - O_2\,H_{(ads)} + H^+ + e^- \rightarrow Pt - O_2\,H_{2\,(ads)}) \quad \text{(Eq. 2.9)}$$

$$x(Pt - O_2\,H_{2\,(ads)} \rightarrow Pt + H_2\,O_2) \quad \text{(Eq. 2.10)}$$

$$(1-x)(Pt + Pt - O_2\,H_{(ads)} + H^+ + e^- \rightarrow 2Pt - OH_{(ads)}) \quad \text{(Eq. 2.11)}$$

$$2(1-x)(Pt - OH_{(ads)} + H^+ + e^- \rightarrow Pt + H_2O) \quad \text{(Eq. 2.12)}$$

The mechanism starts with the adsorption of molecular oxygen on an active site (Eq. 2.7), a reversible reaction considered to be at equilibrium. The rate determining step (RDS) is the first single-electron reduction, in Eq. 2.8. A fraction x of $Pt - O_2\,H_{(ads)}$ formed in step 2.8 is reduced to H_2O_2 through reactions 2.9 and 2.10, while a fraction (1-x) is reduced to H_2O through reactions 2.11 and 2.12. Normally, ORR follows a mixed two- and four- electron pathway, so the term x represent the molecules which undergo the two electron reduction and (1-x) is the fraction of molecules undergoing the four-electron pathway. If x is equal to 1, the mechanism proceeds totally via H_2O_2 formation, if x is equal to 0 the mechanism is a direct four electron

reduction to H_2O. In the case of Pt catalyst x is much smaller than 1, resulting in a dominant four-electron pathway reduction.

In the case of Pt-skin and Pt-skeleton structure the same reduction mechanism as Pt bulk is confirmed. Nonetheless, a higher activity might be found for these structure because of the higher availability of active sites for adsorption of O_2 with respect to bulk Pt. In fact, the difference in O_2 binding energy and the reaction intermediates are very small [1].

2.2 ORR on Carbon Materials

The oxygen reduction mechanism on metal free carbon materials follows a two electron reduction pathway, leading to the formation of hydrogen peroxide as the main product. The reduction pathway is described by equations 2.13-2.16.

$$O_2 \rightleftarrows O_{2\,(ads)} \quad \text{(Eq. 2.13)}$$

$$O_{2\,(ads)} + e^- \rightarrow O^{\bullet -}_{2(ads)} \quad \text{(Eq. 2.14)}$$

$$O^{\bullet -}_{2(ads)} + H_2O \rightarrow HO^{\bullet}_{2(ads)} + OH^- \quad \text{(Eq. 2.15)}$$

$$HO^{\bullet}_{2(ads)} + e^- \rightarrow HO^-_{2(aq)} \quad \text{(Eq. 2.16)}$$

The mechanism proceeds via the formation of the superoxide anion $O^{\bullet -}_{2(ads)}$, followed by a protonation step, which leads to hydroperoxide radical and the consecutive reduction to form hydroperoxide. Depending on pH the RDS may vary: at pH > 10 the adsorption on active site is considered to be the RDS, while at pH < 10 it's represented by equation 2.14 [3].

2.3 ORR on N-modified carbon

The oxygen reduction mechanism on N-modified carbon materials depends on charge profile induced in the carbon backbone due to the more electronegative N atoms. In fact, the partial charge separation induced by N atom favours the interaction of molecular O_2 with C atoms located near N heteroatoms [4][5]. The exact mechanism for oxygen reduction on carbon

material is still not fully determined, in particular it is still not clear the adsorption configuration [4]. In literature different results are obtained: it is reported, for example, that N-doped graphene or nanotubes promote the direct four-electron reduction of O_2 to H_2O [6][7], but the H_2O_2 pathway was highlighted on N-doped mesoporous carbon [8]. The mechanism for oxygen reduction might be described as the one for Pt (Eq. 2.7 – 2.12). A paper from T. Sharifi et al. highlights N functionalities with different activity toward ORR. In detail: pyridinic and edge plane N functionalities are responsible for direct four-electron reduction, while bulk quaternary N promote H_2O_2 formation [9]. In Figure 2.2, taken from reference [4], are highlighted several O_2 reduction pathways.

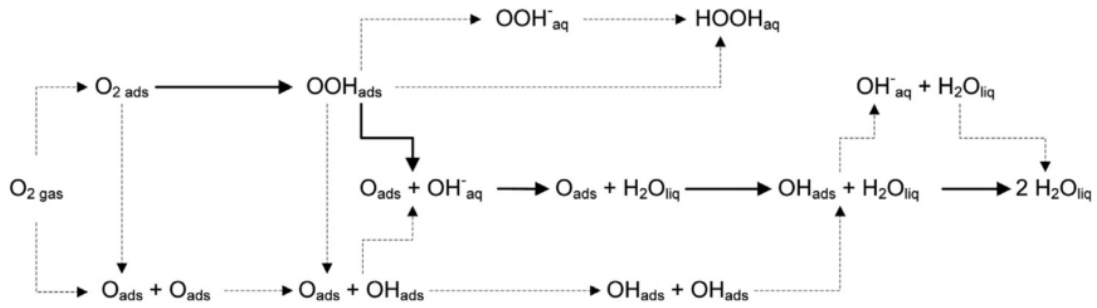

Figure 2.2 Possible oxygen reduction reaction pathways on N-modified carbon supports [4]. Reprinted from International Journal of Hydrogen Energy, 38, W.Y. Wong, W.R.W. Daud, A.B. Mohamad, A.A.H. Kadhum, K.S. Loh, E.H. Majlan, Recent progress in nitrogen-doped carbon and its composites as electrocatalysts for fuel cell applications, 9370–9386, Copyright (2013), with permission from Elsevier.

Bibliography

[1] W.E.I. Xing, G. Yin, ROTATING ELECTRODE METHODS AND OXYGEN REDUCTION, Amsterdam, Elsevier, 2014.

[2] Z. Shi, J. Zhang, Z.-S. Liu, H. Wang, D.P. Wilkinson, Current status of ab initio quantum chemistry study for oxygen electroreduction on fuel cell catalysts, Electrochim. Acta. 51 (2006) 1905–1916. doi:10.1016/j.electacta.2005.07.006.

[3] S. Maldonado, K.J. Stevenson, Influence of nitrogen doping on oxygen reduction electrocatalysis at carbon nanofiber electrodes, J. Phys. Chem. B. 109 (2005) 4707–4716. doi:10.1021/jp044442z.

[4] W.Y. Wong, W.R.W. Daud, A.B. Mohamad, A.A.H. Kadhum, K.S. Loh, E.H. Majlan, Recent progress in nitrogen-doped carbon and its composites as electrocatalysts for fuel cell applications, Int. J. Hydrogen Energy. 38 (2013) 9370–9386. doi:10.1016/j.ijhydene.2012.12.095.

[5] J.P. Paraknowitsch, A. Thomas, Doping carbons beyond nitrogen: an overview of advanced heteroatom doped carbons with boron, sulphur and phosphorus for energy applications, Energy Environ. Sci. 6 (2013) 2839. doi:10.1039/c3ee41444b.

[6] L. Qu, Y. Liu, J.B. Baek, L. Dai, Nitrogen-doped graphene as efficient metal-free electrocatalyst for oxygen reduction in fuel cells, ACS Nano. 4 (2010) 1321–1326. doi:10.1021/nn901850u.

[7] H. Kim, K. Lee, S.I. Woo, Y. Jung, On the mechanism of enhanced oxygen reduction reaction in nitrogen-doped graphene nanoribbons, Phys. Chem. Chem. Phys. 13 (2011) 17505. doi:10.1039/c1cp21665a.

[8] V. Perazzolo, C. Durante, R. Pilot, A. Paduano, J. Zheng, G.A. Rizzi, A. Martucci, G. Granozzi, A. Gennaro, Nitrogen and sulfur doped mesoporous carbon as metal-free electrocatalysts for the in situ production of hydrogen peroxide, Carbon 95 (2015) 949–963. doi:10.1016/j.carbon.2015.09.002.

[9] T. Sharifi, G. Hu, X. Jia, T. Wågberg, Formation of active sites for oxygen reduction reactions by transformation of nitrogen functionalities in nitrogen-doped carbon nanotubes, ACS Nano. 6 (2012) 8904–8912. doi:10.1021/nn302906r

Chapter 3

Experimental Techniques

3.1 Electrochemical techniques

3.1.1 Linear Sweep and Cyclic voltammetry

Linear Sweep Voltammetry (LSV) and Cyclic Voltammetry (CV) are electrochemical techniques in which the potential is varied linearly with time between two potential values E_1 and E_2, and the current response is recorded. The initial potential E_1 is chosen where no redox processes occur, while at E_2 the electrochemical process is diffusion-controlled, i.e. the kinetics is fast and the limiting process is the reactant diffusion to the electrode surface. In LSV the potential scan is stopped at E_2, while in CV an inversion of potential scan is applied at E_2 till the initial potential E_1. In Figure 3.1 a and b the $E - t$ and $i - E$ graphs are reported, respectively. The first one gives information about potential window and scan rate. The second one is the current response associated to redox reactions depending on the applied potential.

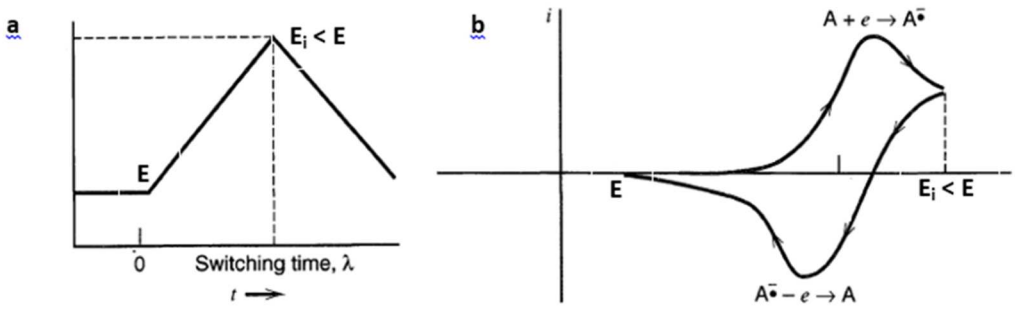

Figure 3.1 a) $E - t$ plot and b) $i - E$ plot for a CV.

In Figure 3.1 the cathodic signal is represented on the right side of the graph with positive current values, while the anodic process is on the left side with negative current values. A second opposite convention might be used for the presentation of CVs: cathodic processes on

the left side with negative current values and anodic processes on the right side with positive current values. This latter convention is used in all the CVs reported in this work.

According the CV reported in Figure 3.2, associated to the process R ⟶ O + e-, where O is a generic oxidised species and R is its reduced form, in the region E_1 – A no electrochemical process occurs. However, the potential-induced change of charge distribution in the double layer, i.e. the solid-liquid interface, is responsible for a capacitive current. This process increase with higher electrode surface area, and in the CVs reported in Chapters 5 and 7 it is used to obtain the capacitance of the mesoporous carbon materials, employed as catalyst and Pt support, respectively. The capacitance is defined according to Eq. 3.1, where Q is the charge and ΔV represents the potential difference. Q can be written as the product of current and time.

$$C = {}^{Q}/_{\Delta V} = {}^{(i \cdot t)}/_{\Delta V} = {}^{i}/_{v_{scan}} \qquad \text{Eq. 3.1}$$

At point A in Figure 3.2 the kinetically controlled oxidation of R species begins. The oxidation rate increases with the potential and the shape of anodic current response is obtained by a balance of reaction rate and diffusion coefficient. In particular the peak E_{pa} arises as oxidation rate becomes faster than the diffusion rate of the species R to the electrode. The region E_{pa} – E_2 is diffusion-limited. Every redox process generates a faradaic current, associated to each electrochemical process in which current is determined by diffusion phenomena. If the process is reversible or quasi-reversible, in the inverse potential scan, from E_2 back to E_1 a signal associated to the inverse reaction O + e- ⇄ R appears.

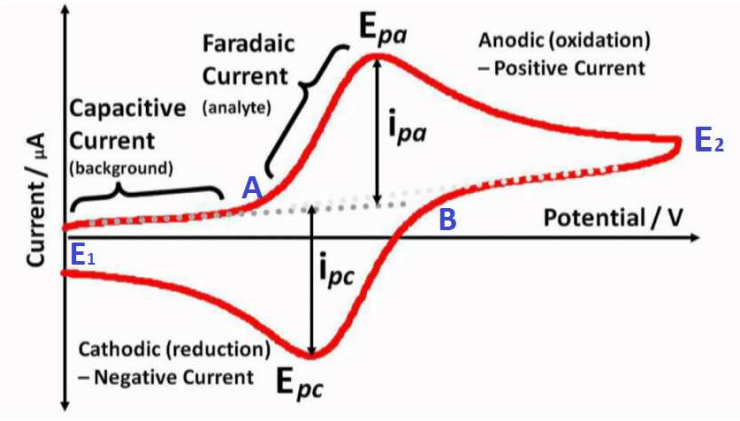

Figure 3.2 Example of reversible CV.

The Randles-Sevcik equation gives the peak current, according Eq. 3.2:

$$I_{\mathrm{p}} = 0.4463\mathrm{n}FAC_0^*\left(\frac{\mathrm{n}F}{RT}\right)^{1/2} D_{\mathrm{R}}^{1/2} v^{1/2} \qquad \text{Eq. 3.2}$$

where n is the number of exchanged electrons, F is the Faraday constant, A (cm^2) is the electrode surface area, C_0^* (mol/cm^3) is the bulk concentration of redox species, R (8.314 J/mol) is the universal gas constant, T (K) is the absolute temperature, D (cm^2/s) is the diffusion coefficient of the reactant and v (V/s) is the scan rate. A reversible electrochemical process shows peculiar features: the peak current I_{p} is directly proportional to $v^{1/2}$, anodic peak current I_{pa} and cathodic peak I_{pc} currents are equal, E_{pa} and E_{pc} are independent of scan rate and separation between E_{pa} and E_{pc} is around 60 mV. A reversible reaction occurs as the standard electrochemical rate constant k^0 is large (in the order of 1 cm/s). If, on the contrary, the k^0 is small (for example 10^{-5} cm/s or lower) the electrochemical process is irreversible. It's worth noting that 'large' and 'small' k^0 are not intended as absolute values, but always in relation to the rate of mass transfer to the electrode. In the case of an irreversible process there is only one electrochemical signal, generally at high overpotential, and the return peak is missing. I_p is directly proportional to $v^{1/2}$ as in the reversible case, E_{p} depends on the potential scan rate, and is shifted toward more positive (anodic scan) or more negative (cathodic scan) potential values for an oxidation or a reduction process, respectively, as v increases. CV technique is employed to characterize electrochemical performance of doped mesoporous carbon towards oxygen reduction in chapter 5, in which a single irreversible peak is present. Reversible and non-reversible redox processes represent two limiting situation. In the case that standard rate constant is not too small, a quasi-reversible process occurs. The key features of this situation are the increased peaks separation as the scan rate is increased and the difference in current intensity between anodic and cathodic signal.

If the peak is not originated by diffusion mechanism toward electrode surface, but from a layer of reactants already adsorbed on electrode surface, a faradaic process with a narrow shape appears. These signals are referred as stripping peaks. Examples of this peak are reported in Chapter 6, where CVs recorded on Pt show the reduction of surface Pt oxides to metallic Pt. Current intensity of a stripping signal is proportional to the scan rate.

3.1.2 Rotating Disk Electrode

Rotating disk electrode (RDE) is the most common tool to investigate electrochemical property under hydrodynamic conditions, in which diffusion and convection are employed to allow reactant to reach the electrode surface. In a typical experiment with RDE a potential sweep (linear or cyclic) at low scan rate is applied to the electrode while the same is in rotation around its axis. The potential scan rate is generally included between 2 and 20 mV/s and the rotation rate varies from 400 to 4000 rotations per minute (rpm). As in the case of voltammetry in stationary conditions, the initial potential is chosen in order to avoid any faradaic processes, then the potential is modified in the direction of the redox process till a limiting current is reached. This value is different for each rotation rate, and depends on the diffusion coefficient of each species. As the reactant concentration is zero at the electrode, the gradient concentration on the thin layer is maximum and the limiting current is reached. A representative experiment is reported in Figure 3.3 a and b, taken from reference [3]. Figure 3.3a represents the fluid velocity and the flow pathway close to the rotating electrode due to convection. The solution that is thrown out radially is replaced by a steam of solution from below, flowing towards the electrode. In a small region over the electrode surface the radial and the axial components of velocity approach zero, and only the azimuthal component remains. This is consistent with the solution being spun around coherently with the electrode surface. It is possible to assess that in this region the reactants reach the electrode surface only by diffusion. The thickness of this layer strictly depends on the rotation rate, and in particular it decreases with the increase of rotation. This is the reason why the current response increases with the rotation rate of electrode. This last statement can be visualized in Figure 3.3b, where LSV at different scan rates are reported. The theory for hydrodynamics at RDE assumes that the electrode is uniformly accessible and affords a precise and reproducible control of the convection and diffusion of reactants to electrode.

The Levich equation describes the limiting current i_l at a RDE (Eq. 3.3):

$$i_l = 0.620 n F A C D_O^{2/3} \nu^{-1/6} \omega^{1/2} \qquad \text{Eq. 3.3}$$

where ν is the kinematic viscosity and ω is the rotation rate, while all the other parameter are the same reported for Randles-Sevcik equation.

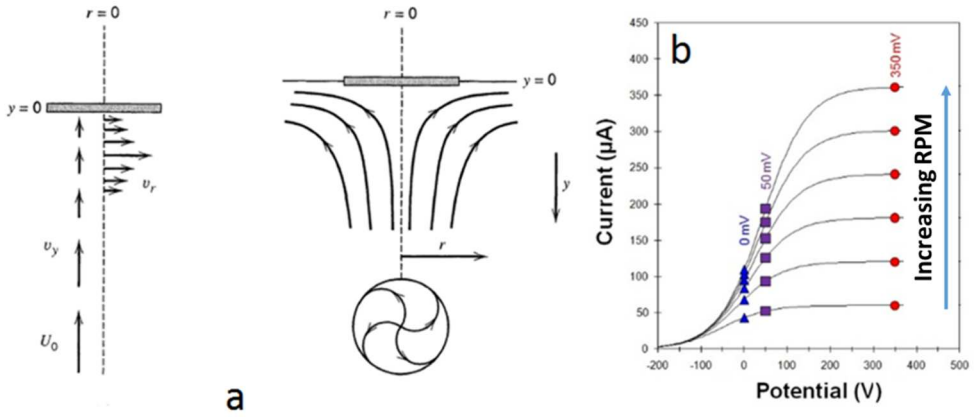

Figure 3.3 a) On the left vector representation of the flow speed near a rotating disk, on the right the flow lines of solution [3]. b) LSV recorded on RDE at different rotation rates. A.J. Bard, L.R. Faulkner, Electrochemical Methods: Fundamentals and Applications (2nd ed), Wiley. 2001, Copyright 2001 © John Wiley & Sons, Inc.

The plot $^1/_j$ versus $^1/_{\omega^{1/2}}$, known as Koutecky-Levich (KL) plot (Eq. 3.4) is used for the determination of the number of exchanged electrons in an electrochemical process, obtained by the slope of the interpolating straight line. In this case j represents the limiting current density, i.e. the limiting current divided by the electrode geometric area. In Eq. 3.4 the term i_k is the current in absence of any mass-transfer effect, that is the current that would flow under kinetic limitation is the mass transfer were efficient enough to maintain the electrode surface concentration equal to the bulk value. The term i_d is the diffusion controlled current, described by Levich equation (3.3):

$$\frac{1}{i} = \frac{1}{i_k} + \frac{1}{i_d} = \frac{1}{nFAkC_{O_2}} + \frac{1}{0.62nFA(D_{O_2})^{2/3}v^{-1/6}C_{O_2}\omega^{1/2}} \qquad \text{Eq. 3.4}$$

Linear sweep voltammetries recorded with RDE could be characterized by: onset potential (E_{onset}), half-wave potential ($E_{1/2}$), Mass Activity (MA) and Specific Acivity (SA). E_{onset} is obtained geometrically with the tangents methods: two straight lines, tangents to the zero current region and the kinetically controlled region of the LSV are drawn, and their intersection represent a good approximation of the potential that trigger the electrochemical process. This value becomes less accurate as the high surface area increases, because of capacitive effects that modify the region in which no electrochemical process occurs. $E_{1/2}$ is defined as the potential at which the current is the half compared to limiting current i_L. This value is representative of electrode kinetic: if it is fast, $E_{1/2}$ is close to E_{onset}, on the contrary if it is slow

and hindered, $E_{1/2}$ is much different than E_{onset}. MA and SA are defined according Equation 3.5 and 3.6 respectively:

$$MA = \frac{I_{k,0.9}}{m_{cat}} \quad \text{(Eq. 3.5)}$$

$$SA = \frac{I_{k,0.9}}{A_{cat}} = \frac{MA}{A_{cat}} \quad \text{(Eq. 3.6)}$$

I_k represents the kinetic current, i.e. the current without any diffusive contribution. This value is very often calculated ad 0.9 V vs RHE in PEM fuel cells. m_{cat} and A_{cat} represent the mass of catalyst (e.g. Pt) for unit of electrode surface and the electrochemical active surface area of the catalyst. In Chapter 6 MA and SA describe the catalytic performance of Pt-based catalyst toward ORR.

3.1.3 Rotating Ring Disk Electrode

Rotating Ring Disk Electrode (RRDE) is made of a disk and a ring electrode, divided by an insulator, as depicted in Figure 3.4.

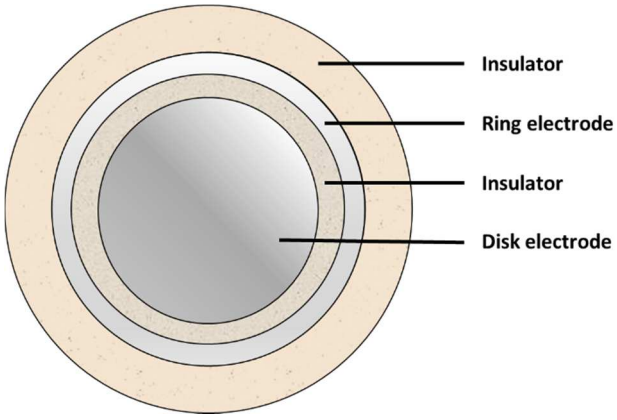

Figure 3.4 Scheme of a RRDE electrode.

RRDE operation is similar to that of a simple RDE, with the advantage of a second working electrode, i.e. the ring, on which it is possible to characterize a second process linked to the main reaction occurring at the disk. RRDE is very useful to detect H_2O_2 produced during oxygen reduction. A linear sweep potential scan at low scan rate (and at a rotation rate included

between 400 and 4000 rpm) is applied at the disk, in order to promote oxygen reduction. A constant potential suitable for hydrogen peroxide oxidation is applied at the ring, in order to detect this species in the case it is produced at the disk. In fact, after ORR, the reaction product are desorbed and thrown away from the disk, according to the flow lines shown in Figure 3.3a on the right, and reach the ring with a certain efficiency, generally much lower than 100%.

Equations 3.7 and 3.8 provide the number of exchanged electrons for each electrochemical process and the yield of hydrogen peroxide, respectively. I_{d} is the current at the disk, I_{r} is the detected current at the ring at the potential applied to the disk. N is the collection efficiency, and it's related to the geometry of the RRDE and indicates the percentage of H_2O_2 produced at the disk that can be detected at the ring.

$$\mathrm{n} = \frac{4I_{\mathrm{d}}}{\mathrm{N}I_{\mathrm{d}} + I_{\mathrm{r}}} \qquad \text{Eq. 3.7}$$

$$\chi_{\mathrm{H_2O_2}} = \frac{2I_{\mathrm{r}}}{\mathrm{N}I_{\mathrm{d}} + I_{\mathrm{r}}} \cdot 100 \qquad \text{Eq. 3.8}$$

The typical response of a RRDE experiment is reported in Figure 3.5. The figure is part of the work of this project.

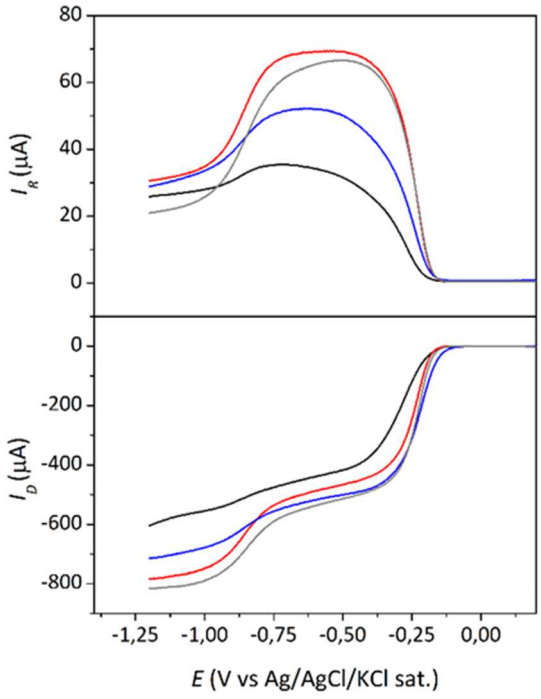

Figure 3.5 RRDE response for a reduction process. LSV recorded at the disk are reported in blue, in red the current recorded at the ring in function of disk applied potential, at different rotation rates, are reported.

3.2 Scanning Electron Microscopy

The scanning electron microscopy (SEM) uses a focused beam of electrons to generate signals at the surface of solid specimens due to interaction of electrons and sample when electrons are decelerated. Signals include secondary electrons, which produce the 2D SEM image, backscattered electrons, diffracted backscattered electrons, photons, visible light and heat. Secondary electrons and backscattered electrons are analysed to obtain SEM image, in particular they show morphology/topography and generate the contrast, respectively. The resolution of a SEM varies between 1 and 20 nm, and it strictly depends on the size of electron spot, which in turn depends on the electron wavelength and on the optical system. In Figure 3.6 it is reported a schematic representation of a SEM. The main components are the electron source, the lenses to focus the electron beam and all the detectors for each kind of signal. The source could be a heated tungsten filament or a field emission cathode. The energy of electrons is included between 100 eV and 30 keV. Secondary electrons are detected by scintillator type detectors, which are charged with a positive voltage in order to attract electrons. Backscattered electrons can be detected with scintillator type detectors as well or solid-state detector. The chamber is kept under vacuum during the measurement in order to avoid obstacles to electrons path. High vacuum (10^{-5} – 10^{-7} torr) is required for high resolution measurement.

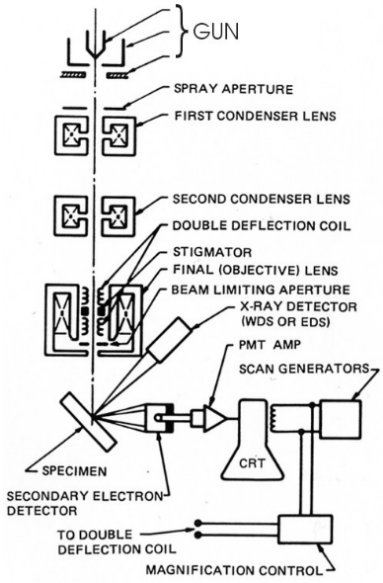

Figure 3.6 Schematic representation of a SEM [6].

3.3 Transmission Electron Microscopy

The Transmission Electron Microscopy (TEM) uses a focused beam of high-energy electrons that is transmitted through the sample to analyse. The operation principles is analogous to the one described for SEM: the source generate via thermo-ionic effect the electron beam that is focused with electromagnetic lenses in a vacuum chamber on the sample. The generated electron beam has higher energy than the one generated in a SEM, and electrons travel through the sample and, depending on its density, some electrons may be scattered. At the bottom of the sample a detector (fluorescent screen) is hit by the electrons and generate the image. The spatial resolution is in the order of few angstrom, so at least ten times higher than the one of SEM. The energy of incident beam could reach 100 keV.

3.4 X-rays Photoelectron Spectroscopy

X-rays photoelectron spectroscopy (XPS) is used to investigate surface of materials, to detect their chemical composition and the state of bonding of each atom. XPS is based on photoelectric effect, i.e. the absorption probability of a photon, with energy hν, by a sample, and the following emission of a core electron. Electronic balance of this process is given by equation 3.9:

$$h\nu = BE + KE + \phi \qquad \text{Eq. 3.9}$$

where hν is the energy of incident radiation, BE (Binding Energy) is the energy of the bond of photoemitted electron with respect to vacuum level, KE is the kinetic energy of photoemitted electron and ϕ is the work function. Emission can happen only if incident radiation is higher than the electron binding energy.

Core electron photoemission generates an electron hole, which is filled by an electron located on an outer orbital. In this case, the electron possess an excess energy, which can be released as fluorescence X or by emission of another electron in an outer orbital (Auger emission).

Binding energy can be determined by kinetic energy of photoemitted electrons, and depends strictly on the chemical species, which can be identified univocally. The position of each

photoemission feature usually varies in a range of few eV, depending on the neighbouring species. This allows the determination of the chemical species but also the species it is linked to and the oxidation state.

The main components of a XPS analyser consist in X-rays source (generally Mg or Al excited by a high energy electron beam), measurement chamber in ultra-high vacuum, electron analyser that can separate their kinetic energy and an electron counter.

3.5 Brunauer-Emmett-Teller (BET) Theory

Gas adsorption is a well-known important tool for the characterization of porous materials and fine powders. Adsorption is defined as the enrichment of ions, molecules or atoms in the vicinity of an interface. This phenomena is used for the determination of surface area and pore size of mesoporous carbons synthesized in this work. In this situation, adsorption occurs close by the solid surface and outside the solid structure. The BET theory concerns multilayer adsorption, and comes from the Langmuir model for monolayer adsorption. According BET model, gas molecules are adsorbed on the the solid surface in non-interacting layers, and the Langmuir theory can be applied to each layer. The BET theory is reported in Equation 3.8:

$$\frac{p/p^0}{n(1-p/p^0)} = \frac{1}{n_m C} + \frac{(C-1)}{n_m C}\,(p/p^0) \qquad \text{Eq. 3.8}$$

where p and p^0 are the equilibrium and the saturation pressure of adsorbate at the selected temperature, n is the specific amount adsorbed at the relative pressure p/p^0, n_m is the specific monolayer capacity and C is the BET constant [7].

The BET model is applied to adsorption/desorption isotherms to obtain the amount of gas creating the layer. Six main types of isotherms are recognized according IUPAC, each one associated to a peculiar structure (Figure 3.7, [8]).

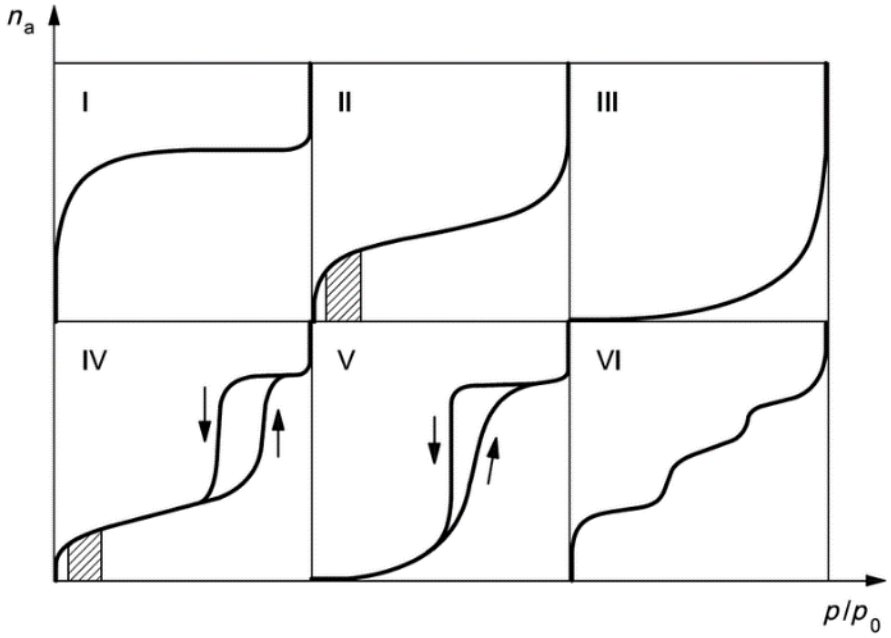

Figure 3.7 Iupac classification of adsorption/desorption isotherms [7].

Reversible Type I isotherm is typical of microporous materials with relatively small external surfaces, such as activated carbons or zeolite. Non porous or macroporous materials originated Reversible Type II isotherm, whose shape is the result of monolayer-multilayer adsorption till high values of p/p^0. The striped region in Isotherm II is associated to the full monolayer formation, especially if the knee is sharp. Type III isotherm doesn't show the monolayer formation, situation in which the adsorbent-adsorbate interaction is weak, so the gas molecules form cluster close by the most energetically favourable sites. Also this isotherm is associated to macroporous or non porous solids. Type IV isotherm is typical for mesoporous adsorbents. Initially, the adsorption is the same as type II, but at high p/p^0 values pore condensation occurs, i.e. gas condenses inside the pores at a pressure p less than the saturation pressure p^0 of the bulk liquid. Type V isotherm is observed for water adsorption on hydrophobic microporous or mesoporous materials. The initial part is similar to Type III isotherm, and it indicates weak interaction between adsorbate and adsorbent. Lastly, stepwise reversible Type VI isotherm indicates layer-by-layer adsorption on a regular non porous material. The step height represents the capacity of each layer [7].

3.6 Elemental Analysis

Elemental analysis consists in the V_2O_5 catalysed combustion of carbonaceous compounds in order to determine their atomic composition. The composition is associated to the whole sample, and not only to the surface as in XPS. In some situations, in fact, the surface composition differs from the bulk one. The sample is located close to a CuO and Cu column, where O_2 is fed and the temperature is raised to 950 °C to promote combustion. This process increases further the temperature till 1900 °C and generate H_2O, CO_2, NO_x and SO_x. The by-products are pushed by He flow till the metallic Cu, which promote the following reduction reactions: $SO_3 \rightarrow SO_2$ and $NO_x \rightarrow N_2$. Molecular-exclusion chromatography is carried out for gas separation, then a Wheatstone bridge is employed as detector.

3.7 Thermogravimetric Analysis

Thermogravimetric Analysis (TGA) involves the continuous weight loss monitoring of the sample in function of temperature, which varies from room temperature to 1000 °C. The measurement can be done under N_2 or O_2 flow, depending on the stability of the sample. O_2 is anyway inserted at the end of the heating, to promote complete degradation of species. The heating is divided in three steps: the first one heat the sample at 100 °C till all the volatile components, i.e. water, are eliminated, then the sample is heated at 10°C/min till 1000 °C, and this temperature is maintained for 20 minutes.

Bibliography

[1] W.E.I. Xing, G. Yin, ROTATING ELECTRODE METHODS AND OXYGEN REDUCTION, Amsterdam, Elsevier. 2014.

[2] R.G. Compton, C.E. Banks, Understanding Voltammetry (2nd ed), London, Imperial College Press. 2010.

[3] A.J. Bard, L.R. Faulkner, Electrochemical Methods: Fundamentals and Applications (2nd ed), Wiley. 2001.

[4] J.F. Moulder, W.F Stickle, P. E. Sobol, K.D. Bomben, Handbook of X-Rays Photoelectron Spectroscopy, Perkin Elmer Corporation. 1992.

[5] J.I. Goldstein, D.E. Newbury, P. Echlin, D.C. Coy, C.E. Lyman, E. Lifshin, L. Sawyer, J.R. Michael, Scanning Electron Microscopy and X-Rays Microanalysis, Kluwer Academy, New York. 2003

[6] http://serc.carleton.edu/research_education/geochemsheets/techniques/SEM.html. Consulted on October 31, 2016.

[7] M. Thommes, K. Kaneko, A.V. Neimark, J.P. Olivier, F. Rodriguez-Reinoso, J. Rouquerol and K. Sing, Physisorption of gases, with special reference to the evaluation of surface area and pore size distribution (IUPAC Technical Report), 87 (2015) 1051-1069.

[8] http://www.see.leeds.ac.uk/business-and-consultation/facilities/techniques-available/bet/a-brief-guide-to-bet/. Consulted on January 15, 2017.

Chapter 4

Synthesis of differently doped Mesoporous Carbons: Hard Template

This chapter includes the synthesis via hard template of differently doped mesoporous carbons and the characterization of their physico-chemical properties via TEM, SEM, BET, XPS, elemental analysis, TGA and Raman. The effect of silica template, pyrolysis temperature and carbon precursor on the final properties of doped carbons is evaluated, in order to select the best synthesis conditions to obtain the desired properties and functionalities of the final mesoporous carbon material.

4.1 Hard template: a simple approach to mesoporous carbons

All the mesoporous carbons (MCs) described in this thesis are synthesized via hard template. This technique involves the pyrolysis of carbon precursor filled templates, and allows to obtain carbon materials that are the exact replica of the templating agent. High control in the final morphology and porosity is possible, but a fine tuning of parameters (i.e. pyrolysis temperature, heating rate, synthesis carrying gas, chemical composition of both carbon precursor and template) involved in the synthesis process is required. For this reason, three series of carbons syntheses were conducted in order to test respectively the effect of:

i. Silica precursor
ii. Pyrolysis temperature
iii. Carbon precursor

This is to find the conditions which allow to have the best properties, i.e. high surface area and pore volume, mesopores dimension, doping amount and degradation temperature.

In this work, all the mesoporous carbons were synthesized from aromatic heterocycles: these molecules give the carbon structure and the doping agent in the same pyrolysis step, so no further post-treatments are required to functionalize the sample. The first investigation concerns the effect of silica template in the final properties of nitrogen doped mesoporous carbons. In this case 1,10-phenanthroline is selected as representative carbon source and is pyrolysed with five different types of mesostructured silica: MCM-41, SBA-15, MSU-H, P200 and P20, as described in Section 4.2. The identification of the silica which provides the best properties to the carbon material was followed by the second investigation that concerns the effect of pyrolysis temperature on the physico-chemical properties of mesoporous carbons. In this experiment, described in Section 4.3, nitrogen doped carbons were synthesized at four different pyrolysis temperatures (750 °C, 850 °C, 950 °C, 1050 °C), again from 1,10-phenanthroline, and the best silica template found in the previous investigation. The last investigation concerns the effect of different carbon precursors on the properties of mesoporous carbons, as described in Section 4.4. Differently doped mesoporous carbons were obtained from the carbon precursors drown in Figure 4.1. The best silica template and pyrolysis temperature were employed for all materials. Phenanthroline and carbazole were used to prepare N doped mesoporous carbons (N-MCs), dibenzothiophene was used to obtain S doped mesoporous carbons (S-MCs), phenothiazine and indigo carmine contain both N and S in their structure, so they gave N and S co-doped mesoporous carbon (N,S-MCs).

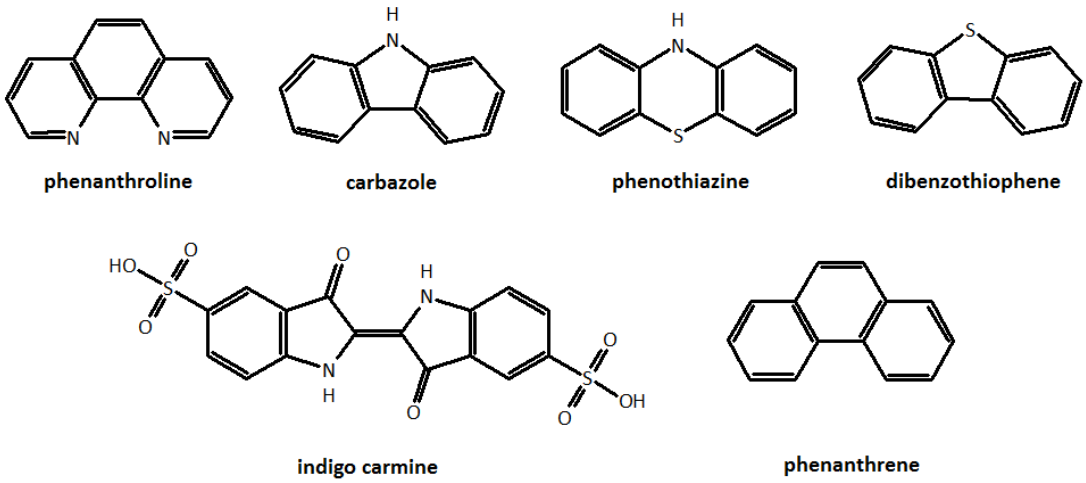

Figure 4.1 Aromatic heterocycles employed for the synthesis of differently doped mesoporous carbons in this Ph.D. project.

4.1.1 Pyrolysis protocol

The standard protocol employed for all the syntheses of carbon materials performed during this work is reported below, and consists of the following steps:

I. MIXING OF PRECURSORS

1 g of silica and 1 g of organic precursor were put together in a small beaker, with 10 mL of a proper solvent. The solvent was chosen according to the solubility of the organic precursor: 1,10-phenanthroline was dissolved in ethanol, while carbazole, dibenzothiophene, phenothiazine, indigo carmine and phenanthrene were dissolved in acetone. The suspension of silica and organic precursor was then mixed for 3 hours in order to let the aromatic heterocycle penetrate in the pore of the template.

II. ADDITION OF CATALYST

Concentrated H_2SO_4 (200 µL) was slowly added in order to catalyse a former reticulation of the organic precursor. The reagents were mixed for 3 hours. In a work published by Y. Shin et al., in which a nitrogen doped carbon was obtained by pyrolysis of 1,10-phenanthroline and silica SBA-15, the fundamental role of an acid catalyst, that allow the reaction to occur, was proved. H_2SO_4 is assumed to protonate part of the 1,10-phenanthroline molecules, so they can act as electrophile and undergo electrophilic substitution on a neutral 1,10-phenanthroline neighbour. On the contrary, no reaction is observed without H_2SO_4 [1].

III. DRYING

The mixture of silica, organic precursor and H_2SO_4 catalyst was dried overnight in an oven. The temperature was selected according to the solvent used to dissolve the carbon precursor: in the case of ethanol, the applied temperature was 110 °C, while wen acetone was used the temperature was set to 80 °C. The purpose of this treatment was to remove completely the organic solvent from the mixture, otherwise it may damage the structure of the mesoporous carbon formed during the pyrolysis step. During this stage the powders change their colour, turning from white to black, brown, pink or violet, depending on carbon precursor.

IV. PYROLYSIS

The dried mixture of silica and organic precursor was moved to a quartz boat and put inside the quartz tube located in the tubular oven for the pyrolysis step under N_2 flow,

which lasts two hours. If the pyrolysis is successful, the final product is black. More details about the pyrolysis treatment are given below.

V. ETCHING OF SILICA

The pyrolysed sample was chemically treated to selectively remove silica, leaving the mesoporous carbon replica of the template. The inorganic-organic composite material was put in a solution made of equal volumes of EtOH and NaOH 1 M, and stirred for 3 days.

VI. FILTERING AND WASHING

The suspension was filtered on a Nylon membrane with 200 nm porosity under vacuum. The obtained carbon material was copiously washed with MilliQ® water, in order to remove all the remaining chemicals from the surface of the carbon, typically salts such as Na^+, OH^-, silicates, EtO^-.

VII. DRYING AND SOFT GRINDING

The mesoporous carbon was removed from the filter, dried at 100 °C for two hours, and then gently grinded in order to obtain a fine powder.

The scheme in Figure 4.2 depicts the mixing of precursors, drying, pyrolysis and silica etching steps.

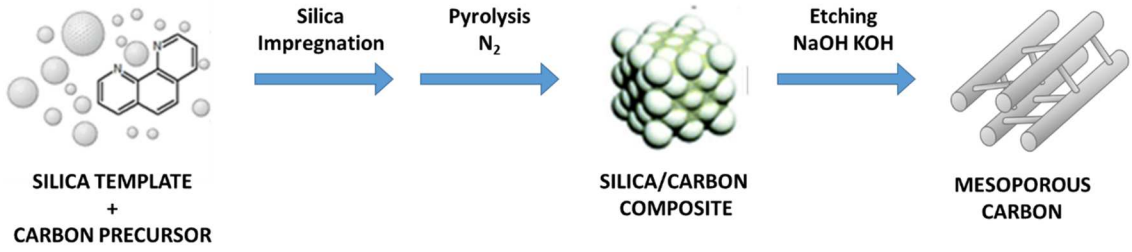

Figure 4.2 Fundamental steps of hard template synthesis procedure: mixing of precursors, pyrolysis and silica etching.

The tubular oven used in the hard template syntheses was provided by Carbolite™ and consists of a furnace filled with a quartz tube and a temperature controller unit. The set temperature is assured only in a 20 cm length zone in the central part of the oven, out of this

section a progressive decrease of the temperature takes place. The quartz tube is isolated from the external environment with two flanges that allow also the inlet and outlet of the carrying gas. The gas flow is monitored with single channel mass flow controller. In Figure 4.3 an image of the tubular oven is reported.

Figure 4.3 Tubular oven used for the pyrolysis step during the synthesis of mesoporous carbons.

The quartz boat containing the mixture of silica and carbon precursor is around 15 cm long, so it can fit perfectly in the constant temperature region located in the middle of the tubular furnace.

The pyrolysis protocol is composed of 4 steps: conditioning, heating, maintaining of pyrolysis temperature and cooling. The conditioning of the quartz tube is the fundamental step to remove as much as possible O_2 from the furnace, to avoid combustion that lowers the yield in mesoporus carbon. In this step 400 sccm N_2 flow was set at room temperature for two hours, to remove completely air. Then the N_2 flow was reduced to 50 sccm, and the temperature was increased with a 5 °C/min constant rate, till the selected pyrolysis temperature. This pyrolysis temperature was maintained for 2 hours, then the heating stopped and the oven started to cool down till room temperature, process that required around 12 hours. In Table 4.1 are listed the parameters for a pyrolysis conducted at a selected temperature, named Tp. When a higher pyrolysis temperature was applied, the heating rate was always 5 °C/min, so the heating treatment step (and the total treatment as well) was longer. It's far more important to keep the same heating rate than the same heating time. In fact, a proper heating rate is fundamental to obtain a regular non-defective mesoporous structure in the carbon material.

Table 4.1 Flow and temperature parameters adopted in a typical pyrolysis protocol at 750 °C.

	Gas	*Flow* (sccm)	T_i (°C)	T_f (°C)	Heating rate (°C/min)	t (min)
Conditioning	N_2	400	r.t.	r.t.	-	120
Heating	N_2	50	r.t	T_p	5	$(T_p - T_i/5)$
Pyrolysis	N_2	50	T_p	T_p	-	120
Cooling	N_2	50	T_p	r.t.	-	720

Figure 4.4 summarizes the heat treatment for all the synthesized samples and their typical morphology in three stages of the synthesis protocol: before the pyrolysis the silica template is filled with the heterocycle carbon precursor, which was pyrolysed giving the carbon matrix during the heat treatment. After silica removal it's possible to appreciate the main mesoporous system interconnected by micropores.

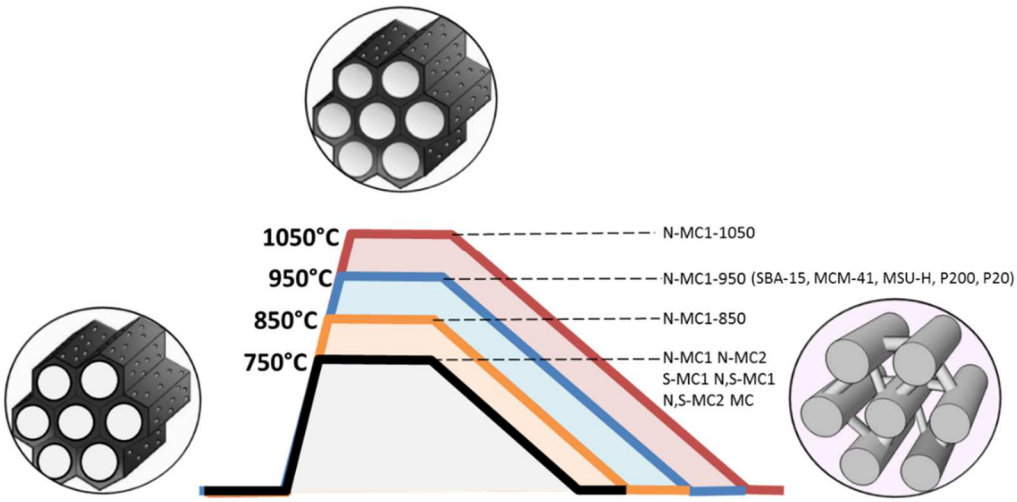

Figure 4.4 Recapitulatory diagram for synthesis and pyrolysis treatment for all the mesoporous carbons synthesized in this work.

4.2 Hard template: effect of silica template

The influence of silica was evaluated by synthesizing five mesoporous carbons from just as many different silica templates. The precursor used was phenanthroline, so the obtained mesoporous carbon is doped with N functionalities, and the pyrolysis temperature was equal to 950 °C. The following silica templates were investigated:

- MCM-41 (Mobil Composition of Matter): is made of cylindrical pores in hexagonal conformation. Pore dimension may be included between 1.5 and 8 nm, and wall

thickness is between 0.5 and 1.5 nm. This silica is synthesized in alkaline soft template conditions with surfactants such as CTAB.

- SBA-15 (Santa Barbara Amorphous): is made as well of cylindrical mesopores in hexagonal configuration. There is a microporous structure connecting the main mesoporous system. The micropores are responsible for an increased surface area and a higher mechanical stability of the carbon structure.
- MSU-H (Michigan State University): the structure is similar to that of SBA-15, but generally has bigger pore diameter.
- P200: mesostructured silica purchased from Sigma Aldrich, made of spherical particles with diameter of 200 nm and mesopores of 4 nm.
- P20: non porous silica spherical particles with mean diameter equal to 20 nm, used for chromatographic applications.

Some kind of silica (i.e. SBA-15, MSU-H and P200) have micropores connecting the main mesoporous system. The presence of connecting micropores is very important and assure a higher mechanical stability and surface area of the carbon material. The obtained mesoporous carbons are labelled NMC-MCM41, NMC-MSUH, NMC-SBA15, NMC-P200 and NMC-P20, so it's clear the type of silica employed to synthesize them.

4.2.1 Morphology: SEM analysis

In **Figure 4.5** the five different kind of silica and the carbon structure they originated are reported. As appears from the images, each carbon structure depends on the morphology of the starting silica. Carbon materials obtained from MCM-41, SBA-15, MSU-H, P200 and P20 silica are called respectively cotton-like, worm-like, arch-like, pinhole-sphere and sponge-like because of their peculiar morphology imprinted by the silica.

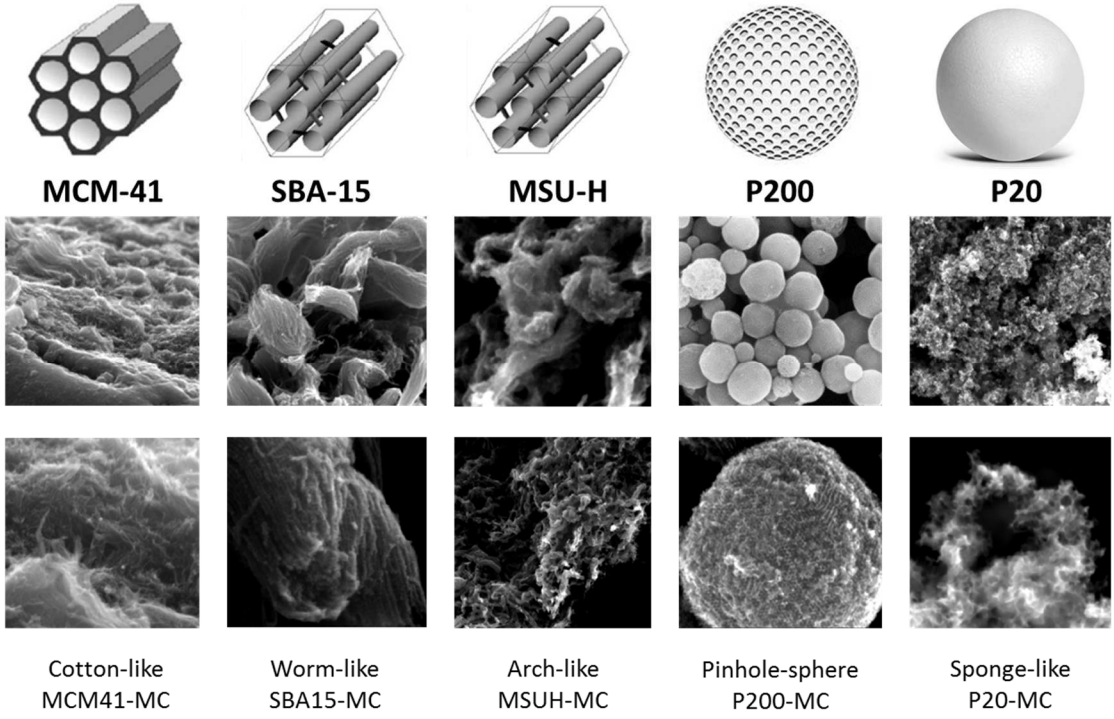

Figure 4.5 On the top the structure of the silica MCM-41, SBA-15, MSU-H, P200 and P20 are reported. Below each picture of silica are reported SEM images at two different magnification of the obtained mesoporous carbons: NMC-MCM41, NMC-MSUH, NMC-SBA15, NMC-P200 and NMC-P20.

4.2.2 Surface Area and Pore Size: BET analysis

BET analysis was conducted in order to highlight the porosity imprinted to the carbon materials by each type of silica analysed. In Figure 4.6 a and b are reported the isotherms for N adsorption and desorption and the pore size distribution respectively. Data are listed in Table 4.2.

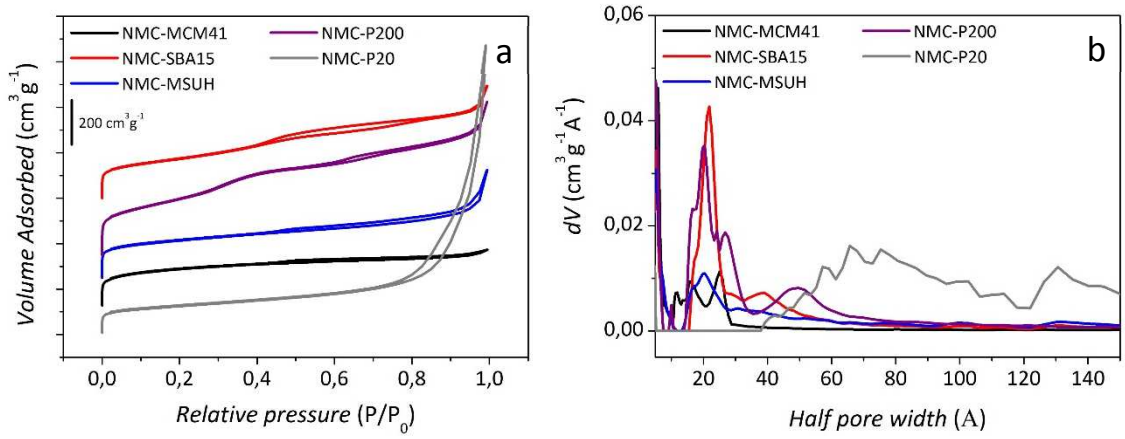

Figure 4.6 a) N_2 adsorption and desorption isotherms and b) pore size distribution for NMC-MCM41, NMC-MSUH, NMC-SBA15, NMC-P200 and NMC-P20.

Table 4.2 BET analysis on NMC-MCM41, NMC-MSUH, NMC-SBA15, NMC-P200 and NMC-P20.

	SBET (m^2/g)	V_p (cm^3/g)	d_{p1} (nm)	d_{p2} (nm)	d_{p3} (nm)
NMC-MCM41	670	0.378	1.16	3.19	5.01
NMC-SBA15	608	0.590	1.01	4.36	7.76
NMC-MSUH	578	0.488	1.02	3.37	4.05
NMC-P200	875	0.804	1.04	4.00	9.78
NMC-P20	437	1.209	0.92	14.57	26.12

All the samples show a type IV isotherm, associated to mesoporous adsorbent. NMC-MCM41 and NMC-MSUH show a type H4 hysteresis loop, associated to micro-mesoporous structure, as confirmed also by the pore size distribution graphs in Figure 4.6b. Main pore system associated to these two samples is in the microporous range, with mean pores diameter equal to 1.16 and 1.02 nm, respectively. NMC-SBA15, NMC-P200 and NMC-P20 exhibit a H2 hysteresis loop, due to a mesoporous structure with a certain degree of complexity in the pores network. In these three samples the main pore system is in the mesoporous range, and in the case of NMC-P20 bigger pore size distributions, centred at 14.75 and 26.12 nm, were obtained.

4.2.3 Chemical composition: elemental analysis

The chemical composition of NMC-MCM41, NMC-MSUH, NMC-SBA15, NMC-P200 and NMC-P20 was obtained by elemental analysis and is reported in Table 4.3. The chemical composition is very similar for all the samples, in particular the amount of nitrogen appears to be independent on the silica precursor. All the samples contain sulphur, which come from the catalyst and probably was incorporated in the carbon matrix during the pyrolysis step. The highest amount of sulphur is found in NMC-MCM41 and NMC-MSUH, in which micropores are predominant, as shown by BET (Figure 4.6b). This peculiar porous structure might hinder the removal of labile sulphur-containing groups from the forming carbon structure, which are trapped inside the pores and are incorporated in the carbon matrix. The amount of oxygen is obtained by subtraction, and for sure its value represents an excess of the real amount. From TGA analysis, reported in the following paragraph, it's clear that each sample is not fully decomposed and the remaining fraction, which varies from few points percent to 25%$_w$ for NMC-P20, might be silica. This is predictable because in the case of P20 silica, the carbon structure grows around the silica particles, and this makes difficult the complete removal of the template with the protocol described in paragraph 4.1.1. Further experiments show that stronger conditions during etching

process, such as ultrasonic treatment in EtOH/NaOH solution, are fundamental to have complete removal of the template.

Table 4.3 Elemental analysis for NMC-MCM41, NMC-MSUH, NMC-SBA15, NMC-P200 and NMC-P20.

	C ($\%_w$)	H ($\%_w$)	N ($\%_w$)	S ($\%_w$)	O[a] ($\%_w$)
NMC-MCM41	63.62	2.22	5.09	2.50	26.57
NMC-SBA15	68.54	1.49	5.66	0.74	23.57
NMC-MSUH	64.51	1.57	4.88	2.16	26.88
NMC-P200	72.40	1.49	5.27	1.62	19.22
NMC-P20	55.15	1.07	4.38	0.94	38.46

[a] Obtained by subtraction. 100 – C($\%_w$) – H($\%_w$) – N($\%_w$) – S($\%_w$) = O($\%_w$).

4.2.4 Thermal stability: TGA

Thermogravimetric analysis was used to investigate the thermal decomposition of each sample. The testing procedure consists in a heating treatment at 10 °C/min under N_2, till 700 or 1000 °C. The degradation temperatures, obtained from the apex of the weight loss derivative, are listed in Table 4.4. In Figure 4.7 the TGA analysis for the series NMC-MCM41, NMC-MSUH, NMC-SBA15, NMC-P200 and NMC-P20 are reported. The most stable sample is NMC-P200, which contains also the lowest amount of oxygen calculated from elemental analysis. NMC-P20 is the less stable material, probably for its non-compact carbon structure.

Table 4.4 Degradation temperature for NMC-MCM41, NMC-MSUH, NMC-SBA15, NMC-P200 and NMC-P20 obtained from TGA analysis.

sample	T_d (°C)	sample	T_d (°C)
NMC-MCM41	626.6	**NMC-P200**	682.0
NMC-SBA15	601.6	**NMC-P20**	591.3
NMC-MSUH	601.4		

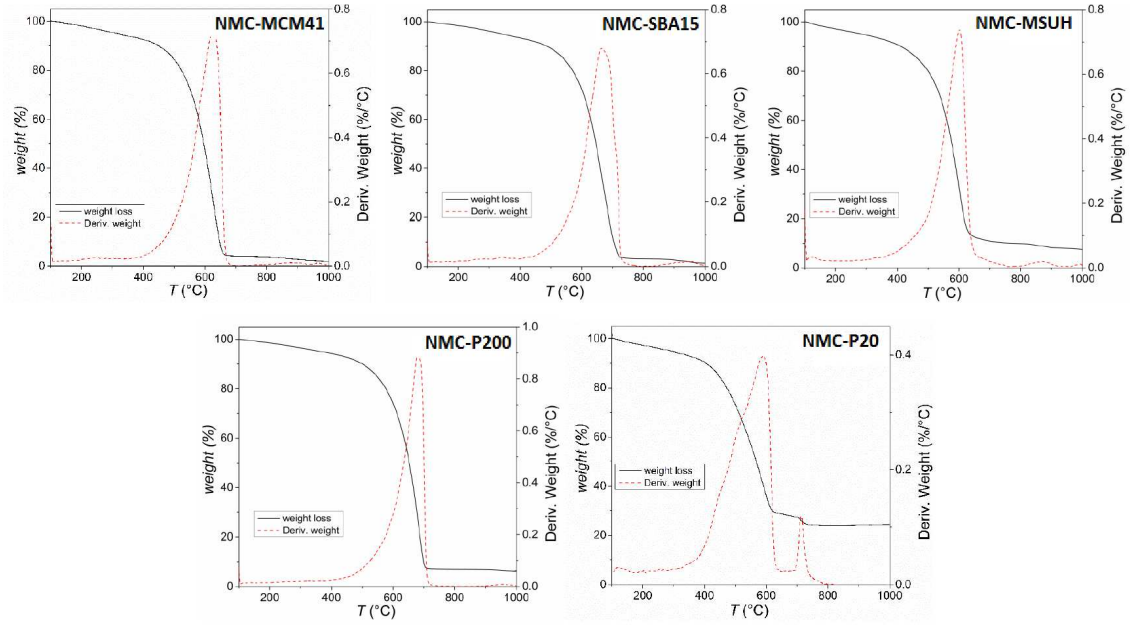

Figure 4.7 TGA curves for NMC-MCM41, NMC-MSUH, NMC-SBA15, NMC-P200 and NMC-P20. In black the percentage weight loss, in red the first derivative of weight loss, which apex gives the degradation temperature.

4.2.5 Electrical conductivity

Electrical conductivity is a very important parameter, which has an important role on the performance of the carbon materials. A too low value of conductivity is indeed responsible for bad electrochemical performance due to ohmic loss.

Electrical conductivity was measured with a home-made instrument composed of a cylindrical polymethilmetacrilate (PMMA) body with a 5 mm cylindrical hole that vertically crosses it. A cylindrical brass piston is inserted in the hole for around 8 mm and close the bottom-end of the cell. Two 1 mm diameter holes are present in the cylindrical central hole, in order to allow the insertion of two copper wire for the conductivity measurement. The copper wire are placed each other to a fixed distance, and are connected to a digital multimeter. The mesoporous carbon powder was inserted in the cylindrical hole, and an increasing force was applied thanks to a 5 mm diameter steel beam and brass cylindrical loads. The system is represented in Figure 4.8.

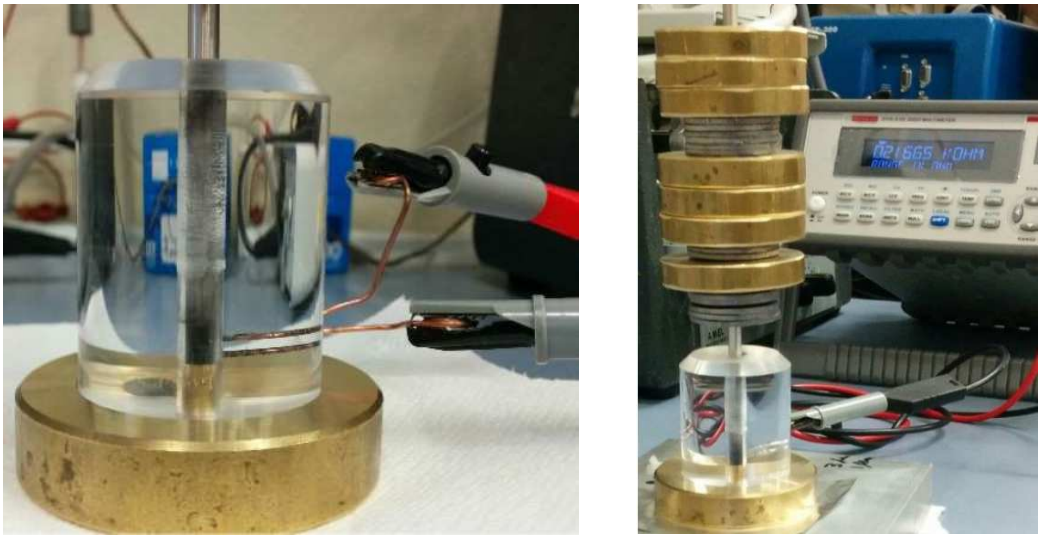

Figure 4.8 Home-made instrument for the determination of electrical conductivity. On the left a close view on the system, on the right a running measurement with many weights applying a compressive force on the carbon material.

Equation 4.1 was used to obtain the electrical conductivity σ. R represent the electrical resistance, d is the distance between the two copper wires and r is the radius of the main hole.

$$\sigma = \frac{d}{RA} = \frac{d}{R\pi r^2} \qquad \text{Eq. 4.1}$$

The electrical conductivity obtained by applying 185 kPa for the mesoporous carbons synthesized from phenanthroline and the different silica templates is reported in Table 4.5. The sample obtained from silica P200 possesses the highest electrical conductivity, among the synthesized ones. On the contrary, NMC-MSUH shows the lowest value of this parameter. The conductivity depends on many factors, i.e. the surface area, the presence of heteroatoms like N or O, the packing and the voids, the hybridization of C atoms. NMC-MCM41, NMC-MSUH, NMC-SBA15, NMC-P200 and NMC-P20 possess similar amount of N functionalities, so this parameter couldn't be responsible for the different electrical conductivity obtained. O atoms are responsible for a decreased conductivity, given that they originate sp3 hybridized C atoms. Also a good packing of the carbon structure, and a proper contact among carbon particles as well, is fundamental for high conductivity. For this reason, it is also predictable that in the case of NMC-P200 the spherical shape of carbon particles allows a better packing of the structure compared to other samples. Rough flat surface of NMC-MCM41 or arch-like and worm-like structures of NMC-SBA15 and NMC-MSUH offer a lower number of contact sites among particles. Similar hypotheses about packaging can be done to justify the dependence of electrical conductivity

from the applied pressure, reported in Figure 4.9. For all the carbon samples conductivity increases along the applied pressure, but in the case of NMC-P200 the increase is the highest, due to a better packaging of carbon spheres.

Table 4.5 Electrical conductivity values for NMC-MCM41, NMC-MSUH, NMC-SBA15, NMC-P200 and NMC-P20, obtained with the instrument shown in Figure 4.7, by applying 185 kPa.

sample	σ (mS/m)	sample	σ (mS/m)
NMC-MCM41	115.9	**NMC-P200**	294.1
NMC-SBA15	217.8	**NMC-P20**	107.5
NMC-MSUH	48.7	**C-MC**	3969.8

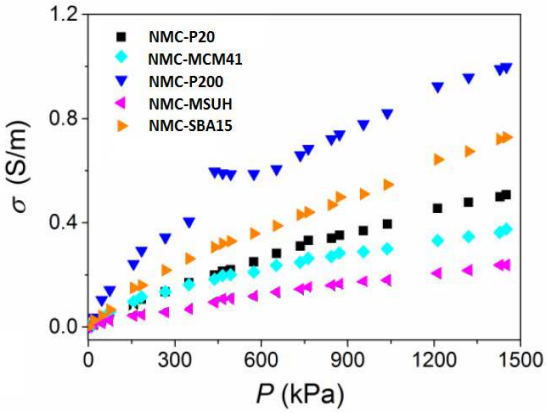

Figure 4.9 Conductivity as a function of applied pressure for NMC-MCM41, NMC-MSUH, NMC-SBA15, NMC-P200 and NMC-P20.

4.2.6 NMC-MCM41, NMC-MSUH, NMC-SBA15, NMC-P200 and NMC-P20: Summary

In **Table 4.6** all the representative properties of NMC-MCM41, NMC-MSUH, NMC-SBA15, NMC-P200 and NMC-P20, obtained from BET, TGA, electrical conductivity and elemental analyses, are reported. The sample prepared from phenanthroline and silica P200 shows the suitable properties to have both a good carbon material and a support for metal nanoparticles to perform ORR. It possesses the highest surface area, proper mesopores distribution, the highest electrical conductivity and degradation temperature. For these reasons Silica P200 was selected as representative template, and it was employed in all the further mesoporous carbons syntheses described in this work. As reminder, this inorganic template consists in 200 nm mean diameter spherical silica particles with interconnected pores of 4 nm diameter (Figure 4.1). The interconnections consist in small micropores connecting the major porous structure, which assure a higher mechanical stability and surface area of the carbon material.

Table 4.6 Summary reporting all the fundamental physico-chemical properties for NMC-MCM41, NMC-MSUH, NMC-SBA15, NMC-P200 and NMC-P20.

	SBET (m^2/g)	V_p (cm^3/g)	d_{p1} (nm)	d_{p2} (nm)	d_{p3} (nm)	σ (mS/m)	***N*** ($‰_w$)	T_{deg} (°C)
NMC-MCM41	670	0.378	1.16	3.19	5.01	115.9	5.09	626.6
NMC-SBA15	608	0.590	1.01	4.36	7.76	217.8	5.27	601.6
NMC-MSUH	578	0.488	1.02	3.37	4.05	48.7	4.88	601.4
NMC-P200	875	0.804	1.04	4.00	9.78	294.1	5.66	682.0
NMC-P20	437	1.209	0.92	14.57	26.12	107.5	4.38	591.3

4.3 Hard template: effect of pyrolysis temperature

The effect of pyrolysis temperature was evaluated by synthesizing a nitrogen doped mesoporous carbon from 1,10-phenanthroline and silica P200, at four different pyrolysis temperatures: 750 °C, 850 °C, 950 °C and 1050 °C. The obtained carbon materials, labelled respecitively N-MC1, N-MC1-850, N-MC1-950 and N-MC1-1050 (Figure 4.10), were characterized via SEM, TEM, BET, elemental analysis and XPS.

Phenanthroline was pyrolysed at four different temperatures to find the better conditions to have high nitrogen content, high graphitization degree and high surface area. The surface area and the graphitization degree improve if the pyrolysis is conducted at high temperature (>1000 °C) and/or for a long time. Unfortunately, these two conditions reduce the amount of nitrogen (and/or sulfur) in the obtained mesoporous carbon. In fact, heteroatoms like N and S are the most labile part of the molecule, and the development of ammonia of sulphide compounds is predictable during the heat treatment. For these reasons it's necessary to optimize pyrolysis temperature and duration, in order to obtain a good balance between nitrogen amount and surface area.

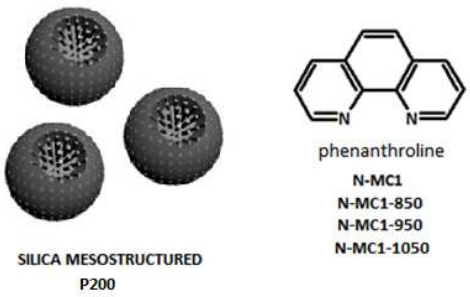

Figure 4.10 On the left is reported the structure of silica P200, on the right there is phenanthroline molecule precursors for the synthesis of N-MC1, N-MC1-850, N-MC1-950 and N-MC1-1050, respectively.

4.3.1 Morphology: SEM and TEM

In Figure 4.11 a and b two SEM images of N-MC1 at different magnifications are reported. The material is made up of spherical carbon spheres, whit mean diameter equal to 300 nm. The dimension distribution of carbon spheres is included between 100 and 400 nm, and corresponds to the one of silica nanoparticles. In Figure 4.11a it's possible to observe two different kinds of particles, according their surface: smooth or rough. The smooth particles are associated to a pyrolysis process occurred completely inside the pore structure of the template. On the contrary, the rough surface is associated to a pyrolysis process that occurred also on the external surface of the silica nanoparticles. The lack of template in this part originate irregular structure with bigger pore size (meso or macropores). In Figure 4.12 a and b two TEM images of N-MC1 at different magnifications are reported. This technique highlights the inner pore structure of the mesoporous carbons, imprinted by the silica template. The channels appear as regular aligned structure.

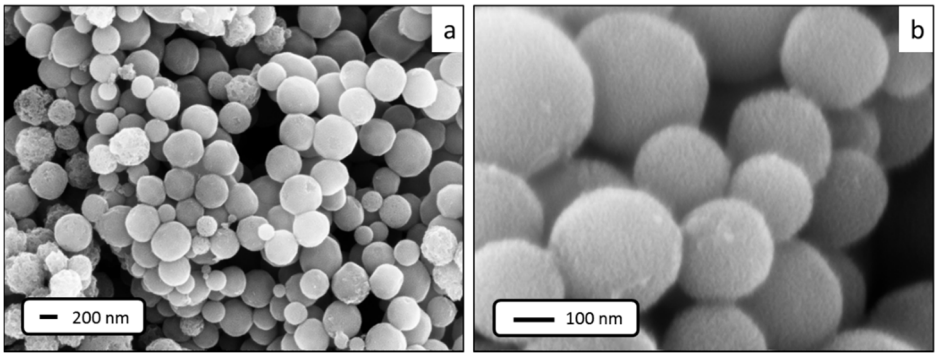

Figure 4.11 SEM images for N-MC1 at a) 200 nm and b) 100 nm magnification.

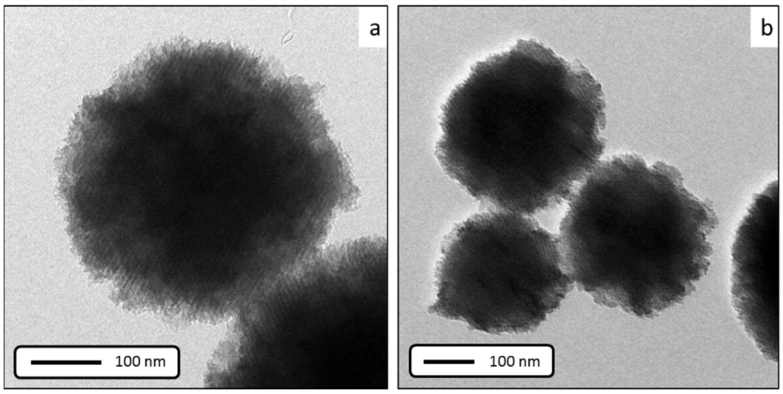

Figure 4.12 TEM images for N-MC1 at a) 200 nm and b) 100 nm magnification.

4.3.2 Surface area and pore dimension: BET

In this paragraph the results from BET analysis conducted on N-MC1, N-MC1-850, N-MC1-950 and N-MC1-1050 are described. In Figure 4.13a the nitrogen-adsorption isotherms of N-MC1 prepared at different temperatures are reported. N-MC1 follows a type IV isotherm, while the samples prepared at higher temperatures (N-MC1-850, N-MC1-950 and N-MC1-1050) follow a type II isotherm, according to IUPAC classification. Type IV isotherm is representative of materials with pores in the range between 1.5 and 100 nm. At higher pressures an increase in nitrogen adsorption occurs due to filling of pores, the inflection point corresponds typically to the complete adsorption of nitrogen on the first monolayer of carbon. Type II isotherm is associated to non-porous or macroporous materials [2]. In Figure 4.13b the pore size distribution for N-MC1, N-MC1-850, N-MC1-950 and N-MC1-1050 are reported.

In Table 4.7 specific surface area obtained from Brunauer-Emmett-Teller (BET) analysis, pore volume and pore diameter, are listed. The computational DFT model consistently fits the experimental data considering cylindrical and spherical pore geometry. There is no influence of pyrolysis temperature on SBET, which is maintained basically constant in N-MC1, N-MC1-850, N-MC1-950 and N-MC1-1050. On the contrary, both pore volume and pore diameter decrease with increased pyrolysis temperature. This might indicate a collapse of the carbon structure along with the increasing of temperature.

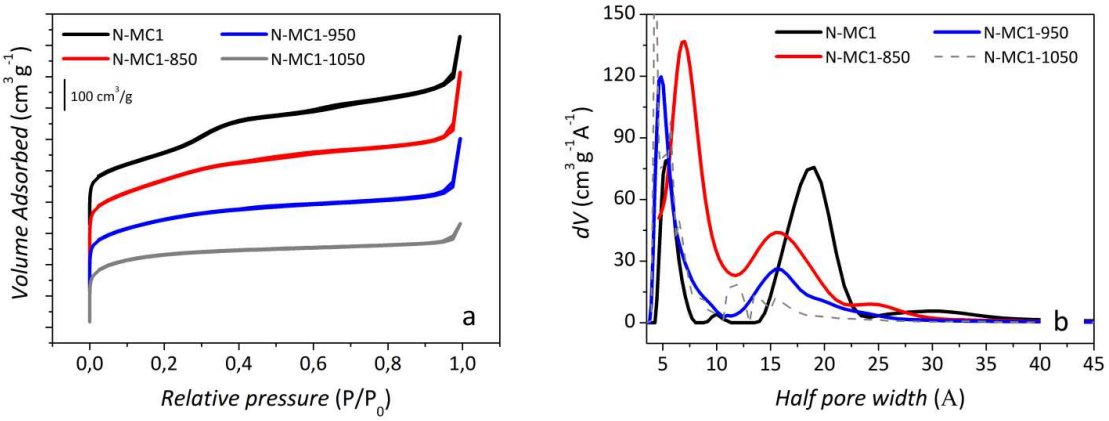

Figure 4.13 a) Nitrogen adsorption and desorption isotherms and b) pore size distribution for N-MC1 (black), N-MC1-850 (red), N-MC1-950 (blue) and N-MC1-1050 (gray).

Table 4.7 BET surface are and pore structure for N-MC1 synthesized at different temperatures.

	SBET (m^2/g)	V_p (cm^3/g)	d_{p1} (nm)	d_{p2} (nm)	d_{p3} (nm)
N-MC1	881	0.689	1.0	3.6	-
N-MC1-850	972	0.622	1.4	3.2	5
N-MC1-950	840	0.489	0.9	3.1	-
N-MC1-1050	850	0.401	0.9	1.1	2.2

4.3.3 Chemical composition and functional groups: elemental analysis and XPS

Elemental analysis and XPS are employed for the quantitative determination of atomic composition and relative state of bonding of all the elements which compose the mesoporous carbons.

In Table 4.8 the chemical compositions of N-MC1, N-MC1-850, N-MC1-950 and N-MC1-1050 obtained from elemental analysis is reported. The amount of nitrogen in the mesoporous carbons decrease with the increasing of the pyrolysis temperature: N-MC1 contains the higher amount of nitrogen, equal to 7.32 $\%_w$, N-MC1-850 and N-MC1-950 have similar amount of nitrogen (5.62 and 5.25$\%_w$, respectively) and N-MC1-1050 has the lowest amount of heteroatom, equal to 3.54 $\%_w$.

XPS analysis was carried out for all the samples in order to quantify the difference in chemical composition and state of bonding. In the large range measurements (surveys) reported in Figure 4.14, three main peaks are observed for all N-MC1s, associated to photoemission from orbital 1s of carbon, nitrogen and oxygen.

Table 4.8 Elemental analysis for N-MC1, N-MC1-850, N-MC1-950 and N-MC1-1050.

	C ($\%_w$)	**N** ($\%_w$)	**O**[a] ($\%_w$)	**H** ($\%_w$)
N-MC1	64.42	7.32	26.49	1.77
N-MC1-850	57.26	5.62	34.63	2.49
N-MC1-950	63.50	5.25	29.49	1.76
N-MC1-1050	50.44	3.54	43.45	2.57

[a] Obtained by subtraction. 100 – C($\%_w$) – H($\%_w$) – N($\%_w$) = O($\%_w$).

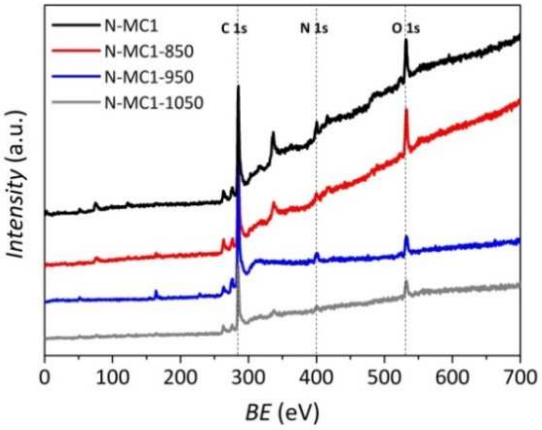

Figure 4.14 XPS surveys for N-MC1 (black), N-MC1-850 (red), N-MC1-950 (blue) and N-MC1-1050 (grey).

High resolution analysis of N-MC1 highlights the following components: C 1s region (Figure 4.15a) shows a broad peak that can be fitted with four main components assigned to [3][4][5]:

- C sp^2 species: C-C, B.E. 284.4 eV
- C sp^3 species bound to H and C: B.E. 284.9 eV
- C sp^3 species bound to N and O: B.E. 286.5 eV
- In the higher BE tail some components from C=O bond can be identified

The broad O 1s peak (Figure 4.15c) can be fitted with four components corresponding to [6]:

- Carbonyl oxygen in esters or amides, B.E. 530.8 eV
- Oxygen atoms in hydroxyl or ethers, B.E. 531.6 eV
- Ether oxygen atoms in esters, B.E. 532.6 eV
- Carboxyl groups, B.E. 533.7 eV

The N 1s signal (Figure 4.15b) is fitted with four components [3][7]:

- Pyridinic nitrogen B.E. 398.4 eV
- Pyrrolic nitrogen B.E. 399.6 eV
- Graphitic nitrogen B.E. 400.7 eV
- Oxidized nitrogen B.E. 401.6 eV

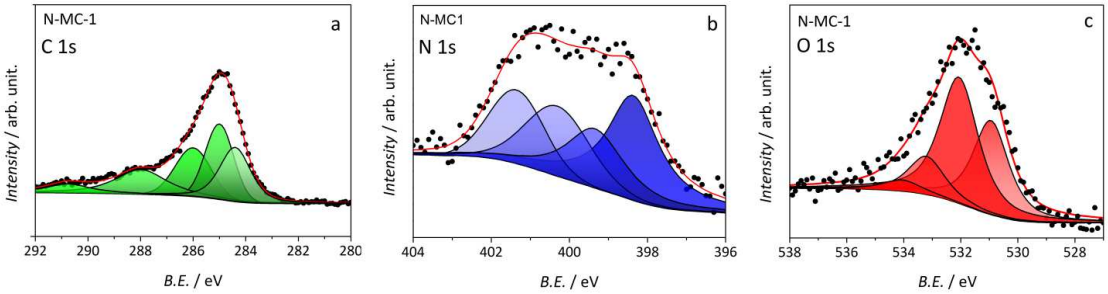

Figure 4.15 High resolution XPS characterization of N-MC1: a) C 1s signal deconvolution, b) N 1s signal deconvolution and c) O 1s signal deconvolution.

The X-rays induced photoemission from a core orbital is governed by the local structure of the examined atom, in particular the electron density is the key parameter that influence the probed binding energy, which basically is related to the chemical states of the same atom. In the case of N, four kind of functionalities were found in the carbon materials, but in literature many examples with more than four N groups are present. The different N groups are characterized by different electron density, higher in the case of pyridinic N, and progressively decreasing in the pyrrolic, graphitic and oxidized N. The types of N functionality found in N-MC1 are consistent with the findings reported in a previous paper [8], in which a nitrogen doped porous carbon was obtained from a partially oxidized carbon treated with NH_3 at different temperatures. Below 300 °C nitrile, lactam, imide and amine-type functional groups are formed. Pyridine-type N (i.e. pyridine oxide or protonated pyridine) is formed between 300 °C and 500 °C, while pyridinic, pyrrolic and quaternary-type N are obtained and are the major species at temperature higher than 500 °C.

In Figure 4.16 N defects on a graphene sheet are represented. This situation could ideally describe the surface of the synthesized mesoporous carbon. The pyridinic site is the least positively charged, represented at XPS by the component at lower B.E. in the N 1s signal. This group is part of the π-system of the carbon structure, and contributes to it with one p electron. The pyrrolic N contributes to the π-system with two p electrons and hence has a higher B.E., equal to 398.8 eV. The pyridinic N at the edges of a graphene sheet originates via substitution of a C-H group with N, while substitution of C with N in a five-membered ring gives rise to pyrrolic N. The graphitic N originates as a substitution of a C atom in the hexagonal arrangement of a graphene layer with a N atom [9]. The oxidized N signal has been identified in literature with many functional groups: Wang et al. suggested a quaternary site in which N is incorporated in a different site than pyridinic N [10]; Buckley suggested a protonated or oxide form of pyridinic-N [11].

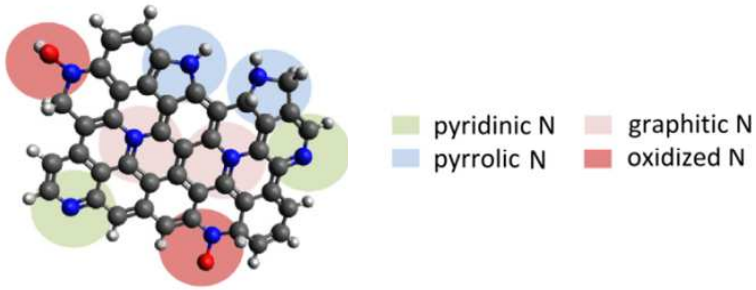

Figure 4.16 Model of the surface of a nitrogen doped mesoporous carbon in which the N functional groups highlighted with XPS are represented.

Spectra associated to photoemission from orbital 1s of nitrogen of N-MC1-850, N-MC1-950 and N-MC1-1050, are reported in Figure 4.17 a, b and c, respectively. These materials contain the same pyridinic, pyrrolic and graphitic N functionalities described for N-MC1. On the contrary, oxidized N is present only in very low amount and this component can be excluded in the deconvolution procedure of N-MC1 without decreasing the accuracy of the fitting. This is predictable, given that high temperature heat treatments are responsible for a higher degree of graphitization, and facilitate the removal of labile heteroatoms-containing groups and oxidized species. Since the precursor used is phenanthroline, the N 1s component associated to pyridinic N is the most abundant in N-MC1, decreasing at higher temperature along with oxidized N, which can be ignored in the fitting procedure. On the contrary, graphitic and pyrrolic N increase as the pyrolysis temperature is increased. This can be easily visualized in Figure 4.18, where the normalized area of each N component in every sample is shown.

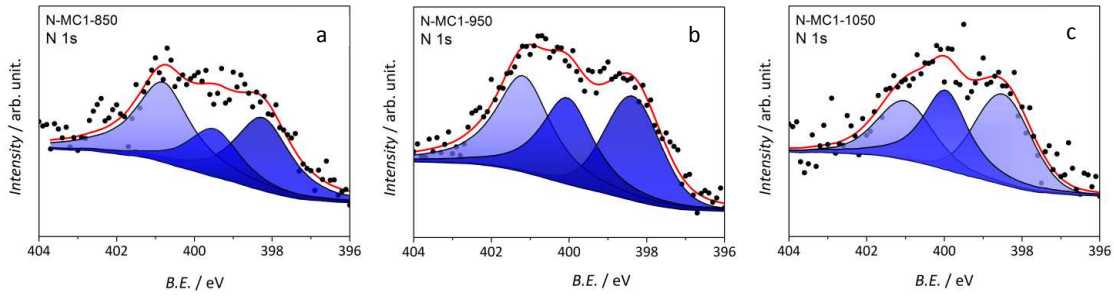

Figure 4.17 High resolution XPS characterization of N 1s of: a) N-MC1-850, b) N-MC1-950 and c) N-MC1-1050.

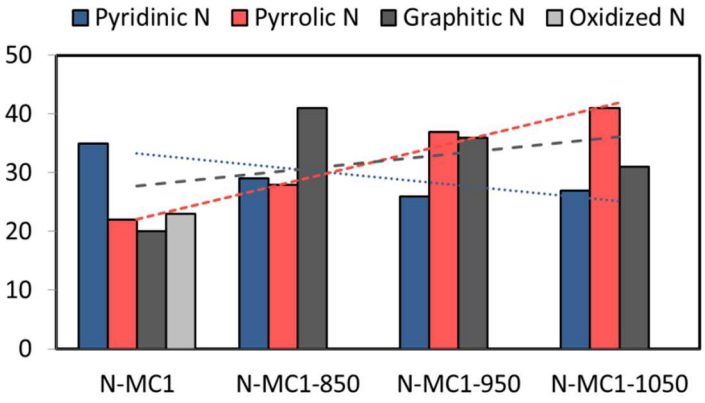

Figure 4.18 Evolution of pyridinic, pyrrolic, graphitic and oxidized N species as the pyrolysis temperature is increased.

The higher thermal stability of graphitic N has been observed by temperature-programmed desorption (TPD) investigation on several carbon materials such as HOPG, carbon nanotubes and amorphous carbon. In particular the thermal treatment of N-doped HOPG seems to highlight a greater thermodynamic stability of these defects [9][12]. This can be easily inferred by considering that, in this case, the N atoms exploit the highest coordination with other C atoms. Previous findings highlight the conversion to pyridinic N of protonated and oxide pyridine under mild pyrolysis conditions [8]. The pyrrolic N is converted to pyridinic-N during the carbon structural development, or in severe pyrolysis conditions [13]. In fact, pyridinic-N located at the edge of the graphene layer and quaternary graphitic N are the major functionalities obtained during pyrolysis and they also show good thermal stability. The thermal stability follows the order: graphitic (quaternary) N > pyridinic N > pyrrolic N > oxidized N [8]. This is consistent with the absence of oxidized N groups in N-MC1-850, N-MC1-950 and N-MC1-1050 highlighted with high resolution XPS spectra of N 1s in Figure 4.17. Data reported in Figure 4.18 and Table 4.9 highlight an opposite trend compared to literature: an overall decrease in pyridinic N and a net increase in pyrrolic N is found when N-MC1 is synthesized at increasing pyrolysis temperatures. Apparently, this situation is in contrast with the thermal stability pointed out for N species, but a similar situation was found also by Schmiers et al. [14], who performed the pyrolysis of different polymeric-N-heterociclic compounds in order to characterize the evolution of chemical bonding due to the pyrolysis itself. In detail, the pyrolysis of polyvinylpyridine was performed at 600 °C and 900 °C, after a cross-link pre-treatment and the formation of pyrrolic N along with increasing temperature was detected. C-NMR and FT-IR highlighted that the transformation of pyridinic N in pyrrolic N via pyridone compound might be plausible, according to the mechanism depicted in Figure 4.19. The pyridone group is formed at low temperatures, and it is not stable

in the considered range of pyrolysis temperatures. The protocol employed for the synthesis of N-MC1, N-MC1-850, N-MC1-950 and N-MC1-1050 includes also an overnight drying procedure under air that promote a former reticulation of the 1,10-phenanthroline. In this process oxygen might be trapped and facilitate the cross-link of the carbon precursor.

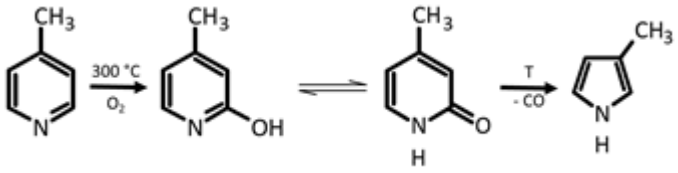

Figure 4.19 Explicative mechanism for the formation of pyrrolic N during pyrolysis at different temperatures.

Table 4.9 Type of nitrogen functionalities and relative amount for N-MC1, N-MC1-850, N-MC1-950 and N-MC-1050.

	N 1s			
N functional group	Pyridinic N	Pyrrolic N	Graphitic N	Oxidized N
B.E. (eV)	398.4	399.6	400.7	401.6
N-MC1	35	22	20	23
N-MC1-850	31	28	41	0
N-MC1-950	27	37	36	0
N-MC1-1050	28	41	31	0

4.3.4 Thermal stability: TGA

Thermogravimetric analysis was carried out by a Q5000IR TGA instrument (TA Waters) on N-MC1, N-MC1-850, N-MC1-950 and N-MC1-1050, to evaluate their thermal stability. The determination was carried out under N_2, the temperature is increased from 25 °C to 700 °C, at 10 °C/min. In the case of N-MC1-1050 a heat treatment till 1000 °C was necessary, and O_2 was inserted instead of N_2 at 900 °C.

In Figure 4.20 a and b the TGA curves and the first derivatives of the weight loss are reported, respectively. The decomposition temperature, as convention, is the apex of the first derivative. N-MC1 starts to decompose at 500 °C in N_2. The derivative of the TGA shows one pronounced weight loss at 609 °C and another of a lower intensity at 586 °C, visible as a shoulder of the main peak, due to different functionalities of the sample. The weight loss increases rapidly

with further increase of temperature, till the temperature of 640 °C, where all the mesoporous carbon spheres are decomposed. N-MC-850 and N-MC-950 show similar TGA curve as N-MC1, but they have lower decomposition temperature, equal to 558 °C and 566 °C, respectively. Also in this case a shoulder of the main decomposition peak is present at lower temperature. N-MC1-1050 has the highest thermal stability, the derivative shows two overlapping signals at 624 °C and 660 °C. The main contribution to this property might arise from the high pyrolysis temperature, responsible for the creation of a high graphitic structure with a lower amount of defects (i.e. oxygen-containing species).

The significant weight loss is due to the thermal degradation of carbon powder, involving breakage of C-C and C-N bonds. In particular, the N functionalities such as pyrrolic and pyridinic groups decompose and react with surface species to give NH_3, HCN, and N_2 as desorption products [8]. The oxygen-containing species, identified by XPS, produce mainly CO, CO_2 and H_2O during heat treatment. TDP characterization of oxidized carbon nanotubes in helium clarified how the signal were originated: H_2O is supposed to come from the dehydration of adjacent carboxyl groups, which form anhydrides, or to the dehydration of phenolic hydroxyl groups at low temperature, around 280 °C. The CO_2 may be formed by decomposition of carboxylic groups at around 340 °C, by degradation of carboxylic anhydrides at 470 °C and lactones at 650 °C, more stable than carboxylic groups. CO originates probably by degradation of ketones at 280 °C, of carboxylic anhydrides around 470 °C and of phenols, quinones and ethers at 700 °C.

Comparison with a commercial mesoporous carbon (C-MC) was also done. TGA of C-MC is reported in Figure 4.20a, and shows higher thermal stability than all N-MC1 family. The higher graphitization degree of C-MC plays for sure an important role in increasing thermal stability. Also the high amount of oxygen-containing groups could generate the same of the previous described decomposition pathways, and this is in agreement with the progressive mass decrease for synthesized N-MC, highlighted at lower temperature than T_d, that is absent in the C-MC curve. Furthermore, N incorporated in the carbon matrix is responsible for a higher degree of defects, and this might lower the thermal stability of the material as well. Anyway, in the case of N-MC1, N-MC1-850 and N-MC1-950 there seem to be a positive effect of nitrogen on the thermal stability, because this property decreases as the N decreases. Different situation occurs for N-MC1-1050, because it's the most stable material, even if the N content is the lowest. In this case a higher graphitization degree realised thanks to the high pyrolysis temperature, might play an important role in the thermal stability of the material.

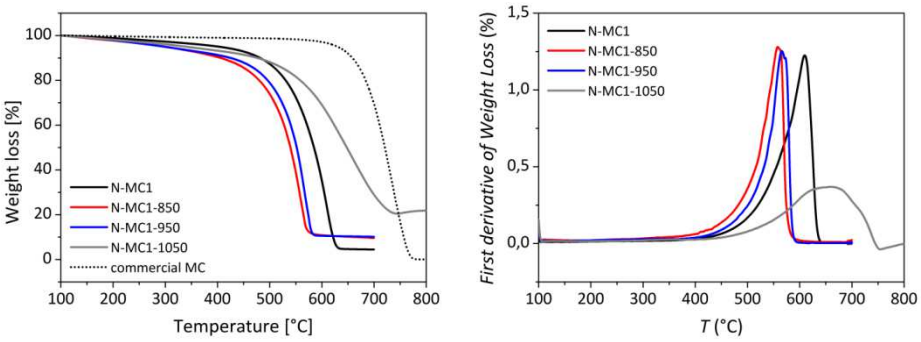

Figure 4.20 a) Termogravimetric analysis carried out under N_2 and b) first derivative for N-MC1 (black), N-MC1-850 (red), N-MC1-950 (blue) and N-MC1-1050 (grey). The black dotted line is associated to commercial mesoporous carbon.

4.3.5 N-MC1, N-MC1-850, N-MC1-950 and N-MC1-1050: Summary

In Table 4.10 are reported the fundamental physico-chemical properties of N-MC1, N-MC1-850, N-MC1-950 and N-MC1-1050. N-MC1 synthesized at 750 °C is the material with the highest amount of nitrogen, highest pore volume and more interesting pore structure, with a high fraction of pores with 3.6 nm mean diameter. For these reasons the pyrolysis protocol applied to synthesize it was replied also to synthesize mesoporous materials from the other carbon precursors listed in Figure 4.1. Carbazole, phenothiazine, dibenzothiophene, indigo carmine and phenanthrene were all pyrolysed at 750 °C, in order to obtain differently doped mesoporous carbons. In the following chapter the physico-chemical properties of these samples are described.

Table 4.10 Summary reporting all the fundamental physico-chemical properties for N-MC1-750, N-MC1-850, N-MC1-950 and N-MC1-1050

	SBET (m^2/g)	V_p (cm^3/g)	d_{p1} (nm)	d_{p2} (nm)	d_{p3} (nm)	***N*** ($\%_w$)	T_{deg} (°C)
N-MC1-750	881	0.689	1.0	3.6	-	7.32	609
N-MC1-850	972	0.622	1.4	3.2	5	5.62	558
N-MC1-950	840	0.489	0.9	3.1	-	5.25	566
N-MC1-1050	850	0.401	0.9	1.1	2.2	3.54	624

4.4 Hard template: effect of carbon precursor

The effect of carbon precursor was investigated by synthesizing differently doped mesoporous carbons from all the precursors listed in Figure 4.21. Carbazole gave a nitrogen doped mesoporous carbon (N-MC2), dibenzothiophene gave a sulphur doped mesoporous carbon (S-MC1), phenothiazine and indigo carmine gave nitrogen and sulphur co-doped mesoporous carbons (N,S-MC1 and N,S-MC2, respectively), phenanthrene gave an undoped mesoporous carbon (MC). The sample obtained from phenanthroline is labelled N-MC1 and is the same sample described in the previous Section. All the synthesized samples were characterized by SEM, TEM, BET, elemental analysis, XPS and TGA.

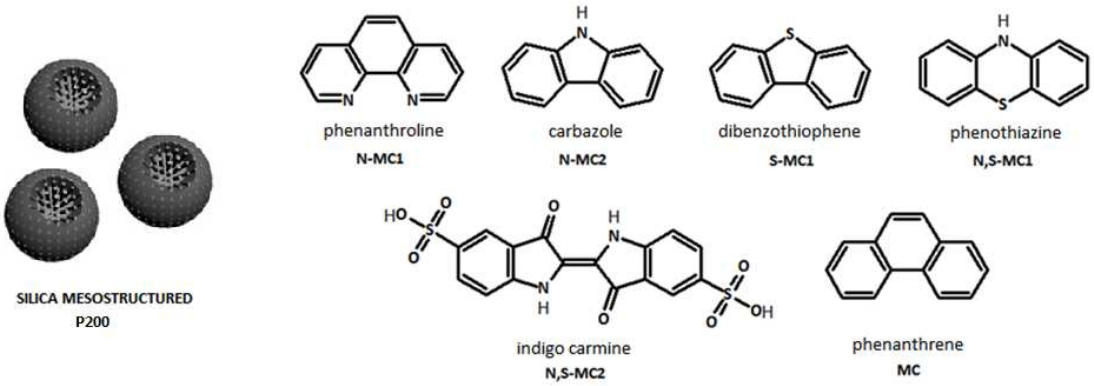

Figure 4.21 On the left the structure of silica P200 is reported, on the right all the aromatic heterocycles employed for the synthesis of N-MC1, N-MC2, N,S-MC1, N,S-MC2, S-MC1 and MC are listed.

4.4.1 Morphology: SEM analysis

In the following figures representative SEM images obtained from N-MC2 (Figure 4.22a,b), N,S-MC1 (Figure 4.22c,d), N,S-MC2 (Figure 4.22e,f) and S-MC1 (Figure 4.22g,h), each at two different magnification, are reported. Their structure remind the one observed for N-MC1 in Figure 4.11: mesoporous carbons are made up of spherical nanoparticles with mean radius equal to 150 nm, as the silica template. N-MC2 and N,S-MC1 are made of both smooth and rough carbon particles, S-MC1 is made totally of rough particles. N,S-MC2 shows a peculiar structure, made of rough spherical carbon particles and irregular structure. In this case, it can be assumed that the pyrolysis of indigo carmine, the carbon precursors, doesn't occur totally inside the pore structure, but also on the external surface of silica template. In this case irregular planar structures were obtained.

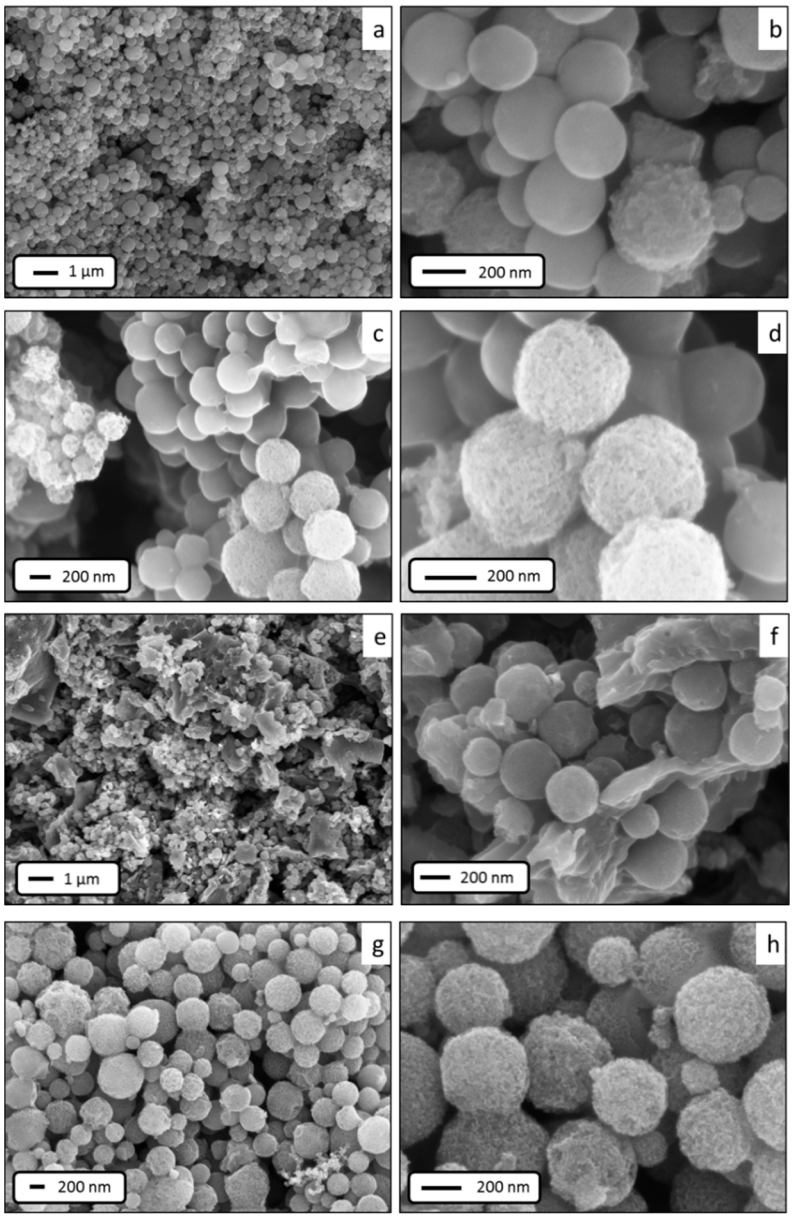

Figure 4.22 SEM images obtained at two different magnification a, b) N-MC2; c, d) N,S-MC1; e, f) N,S-MC2; and g, h) S-MC1.

4.4.2 Surface area and pore dimensions: BET

BET analysis was carried out on all the synthesized samples, and the results are reported in Table 4.11 and Figure 4.23. All the samples have high BET surface areas, included between 800 m^2/g and 1100 m^2/g, and high pore volume, except N,S-MC2, which has the lowest BET area equal to 409 m^2/g and the lowest pore volume. This sample also highlighted a peculiar morphology at SEM analysis, because it's made up of both carbon mesoporous spheres and lamellar structures. The pore size distribution is narrow for all samples, both micropores and mesopores with mean diameter equal to 1 nm and 4 nm, respectively are present.

Table 4.11 BET surface area, pore volume and pore diameter of N-MC1, N-MC2, N,S-MC1, N,S-MC2, S-MC1 and MC.

	SBET (m^2/g)	**V_p** (cm^3/g)	**d_{p1}** (nm)	**d_{p2}** (nm)	**d_{p3}** (nm)	**d_{p4}** (nm)
N-MC1	881	0.689	1.1	3.8	6.2	-
N-MC2	810	0.625	1.7	3.2	4.0	5.4
N,S-MC1	855	0.681	1.1	4.0	6.4	-
N,S-MC2	409	0.313	0.9	4.0	-	-
S-MC1	1103	0.864	1.1	4.0	5.5	8.4
MC	953	0.881	1.1	4.0	6.2	-

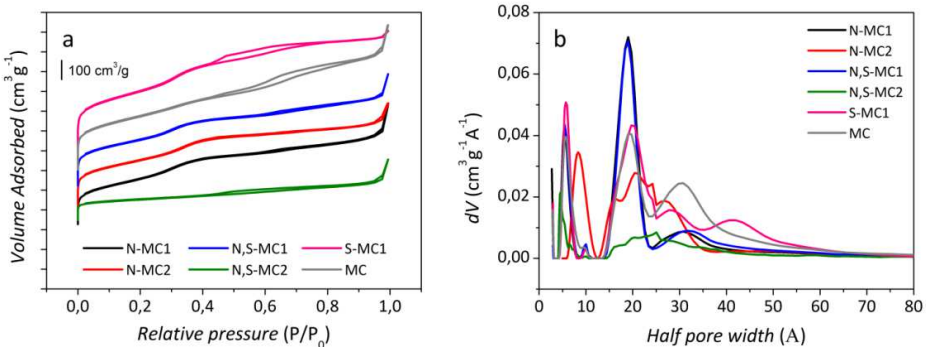

Figure 4.23 a) Nitrogen adsorption and desorption isotherms and b) pore size distribution for N-MC1 (black), N-MC2 (red), N,S-MC1 (blue), N,S-MC2 (green), S-MC1 (pink) and MC (grey).

4.4.3 Elemental analysis and XPS

Elemental analysis and XPS were carried out in order to determine the chemical composition and the state of bonding of the mesoporous carbon materials. In Table 4.12 the chemical composition obtained by elemental analysis is reported. Both XPS and elemental analysis confirm the presence of nitrogen in N-MC1, N-MC2, N,S-MC1 and N,S-MC2, and sulphur in N,S-MC1, N,S-MC2 and S-MC1. Sulphur is found in small amount also in N-MC1 and N-MC2, probably as a consequence of acid treatment with concentrated H_2SO_4, described at point II in paragraph 4.1. N-MC1 contains the highest nitrogen content, equal to 7.32%$_w$, and such a content decreases gradually in the order N,S-MC2, N,S-MC1 and N-MC2. This behaviour highlights a correlation between the C/N ratio in the initial carbon precursor and in the final mesoporous carbon. S-MC1 has the highest amount of S, equal to 13.79%$_w$, and this is remarkable because sulphur-containing groups are usually thermolabile and it's difficult to find in literature many examples of carbon supports containing such a high level of covalently-bonded sulphur. The

amount of sulphur in N,S-MC1 and N,S-MC2 is equal to 4.12%$_w$ and 6.38%$_w$, respectively, lower than S-MC2, but anyway high compared to other carbon material described in literature.

Table 4.12 Elemental analysis for N-MC1, N-MC2, N,S-MC1, N,S-MC2, S-MC1 and MC.

	C (%$_w$)	N (%$_w$)	S (%$_w$)	O (%$_w$)	H (%$_w$)
N-MC1	64.42	7.32	1.16	25.33	1.77
N-MC2	53.79	3.06	0.65	39.19	3.31
N,S-MC1	72.07	4.51	4.12	17.83	1.47
N,S-MC2	55.22	6.38	6.38	30.25	1.77
S-MC1	69.11	0.10	13.79	15.81	1.19

In Figure 4.24a, b and c the high resolution signals associated to photoemission from orbital 1s of nitrogen of N-MC2, N,S-MC1 and N,S-MC2, respectively, are reported. In Table 4.13 the relative amount of each component is reported. The pyridinic and graphitic components are present in all the samples under examination, while N,S-MC1 and N,S-MC2 contain also a small fraction of pyrrolic nitrogen. The graphitic and pyridinic components are the most abundant N functionalities: graphitic N prevails in N-MC2 and N,S-MC1, while pyridinic N is the main component in N-MC1 and N,S-MC2. The pyrrolic group is totally absent in N-MC2, even if this sample was synthesized starting from a pyrrolic N-containing precursor. The same result is described by J.R. Pels et al. in their work [13]: carbazole was pyrolysed as well to obtain carbonaceous material, but N was found totally as pyrrolic group only in the sample prepared at 600 °C and it was reduced to 10% and 0% for pyrolysis temperature equal to 800 °C and 1000 °C, respectively, while pyrrolic and graphitic N were formed. So it is possible to exclude a 'chemical memory effect', given that the predominant N functionality in the organic precursor is not transferred to the mesoporous carbon material, due do the different thermal stability of N functionalities ad side reactions, which involve decomposition of pyridone species, as described in Figure 4.19. It's curious to notice that carbazole (which contains pyrrolic N) generates N-MC2 with only pyridinic and graphitic N, while phenanthroline (which contains pyridinic N) gives N-MC1 with a high percentage of pyrrolic N functionality.

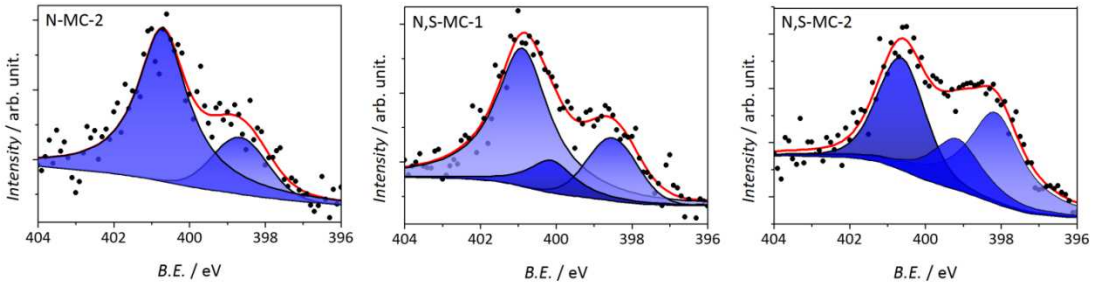

Figure 4.24 High resolution spectra associated to photoemission from orbital 1s of N for a) N-MC2, b) N,S-MC1 and c) N,S-MC2 and deconvolution in pyridinic, pyrrolic and graphitic components.

Table 4.13 Amount of all N species found with XPS in each N-doped mesoporous carbon.

	N 1s			
N functional group	Pyridinic N	Pyrrolic N	Graphitic N	Oxidized N
B.E. (eV)	398.4	399.6	400.7	401.6
N-MC1	35	22	20	23
N-MC2	21	0	79	0
N,S-MC1	20	13	68	0
N,S-MC2	43	21	36	0

In Figure 4.25 a, b and c the high resolution signals associated to photoemission from orbital 2p of sulphur of N,S-MC1, N,S-MC2 and S-MC1, respectively, are reported. Only thiophenic groups are present in N,S-MC1 and S-MC1, while N,S-MC2 is more complex and thiophenic, sulphynil and oxidized sulphur groups are present (Table 4.14).

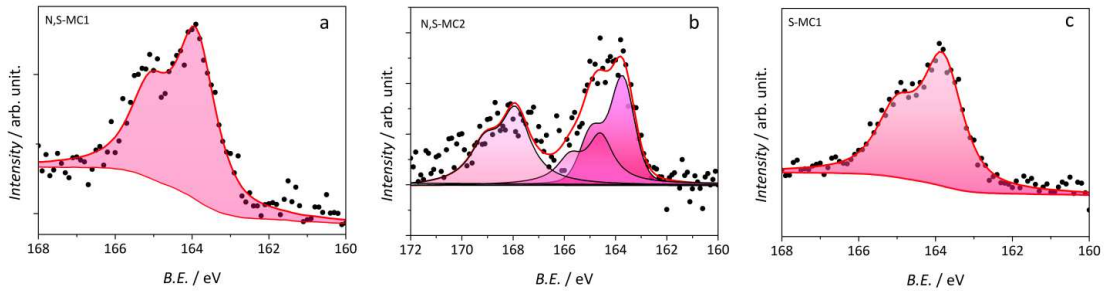

Figure 4.25 High resolution spectra associated to photoemission from orbital 2p of S for a) N,S-MC1, b) N,S-MC1 and c) S-MC1 and deconvolution in thiophenic, sulfynil and oxidized S groups.

Table 4.14 Amount of all S species found with XPS in each N-doped mesoporous carbon.

	S 2p		
N functional group	Thiophenic S	Sulfynil S	Oxidized S
B.E. (eV)	163.9	164.6	167.9
N,S-MC1	100	0	0
N,S-MC2	36	23	41
S-MC1	100	0	0

In Figure 4.26, as explicative example, the photoemission from C 1s and O 1s orbitals for S-MC1 are reported. In all the MCs synthesized the carbon and the oxygen signals can be deconvoluted in the same way as N-MC1 described in Section 4.2.3. Three main components are identified in the C 1s signal, associated to C sp^2 species, C sp^3 species bound to H and C and C sp^3 species bound to N and O. The C 1s signal contains also low intensity components at high B.E., between 288 and 292 eV, not included in the determination of the relative amount of each C functional group. The deconvolution of O 1s high resolution signal shows four components, associated to carbonyl oxygen in esters or amides, oxygen atoms in hydroxyl or ethers, ether oxygen atoms in esters and carboxyl groups. In the case of N,S-MC2 a component at higher B.E. is present.

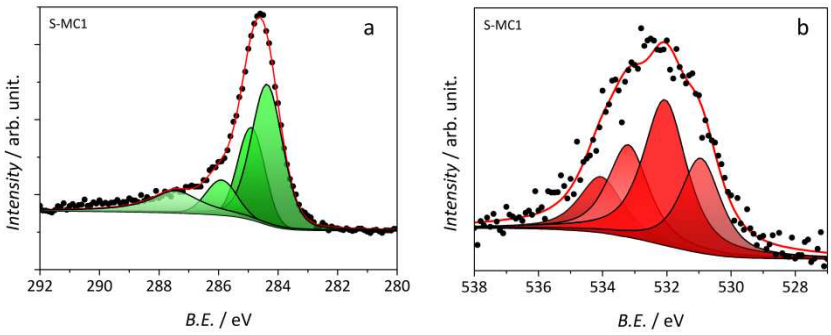

Figure 4.26 High resolution spectra associated to photoemission from a) orbital C 1s and b) orbital O 1s of S-MC1 and deconvolution in constituent functional groups.

Table 4.15 Amount of all C species found with XPS in each N-doped mesoporous carbon.

	C 1s		
N functional group	C=C, graphitic	C-C, C-H	C-O-C, CN, C-OH
B.E. (eV)	284.4	285.5	286.5
N-MC1	35	36	29
N-MC2	44	34	22
N,S-MC1	33	42	26
N,S-MC2	37	34	29
S-MC1	58	29	13
MC	23	36	41

Table 4.16 Amount of all O species found with XPS in each N-doped mesoporous carbon.

	O 1s			
N functional group	R(C=**O**)OR	C-O-C, C-OH	C-O-C	R(C=**O**)OH
B.E. (eV)	530.8	531.6	532.6	533.7
N-MC1	34	48	14	4
N-MC2	31	42	21	5
N,S-MC1	19	37	23	20
N,S-MC2	30	43	18	10
S-MC1	24	39	23	15
MC	24	34	29	14

In Table 4.15 and Table 4.16 the percentage of C and O functionalities in all the MCs synthesized are reported, respectively. Regarding C, the graphitic component is the most important, because it improves properties of carbon materials such as electrical conductivity, thermal and chemical stability, resistance to corrosion. On the contrary, these same properties are worsen if oxidised carbon groups are present in the carbon materials. Unfortunately, the percentage of graphitic C is low, and only in the case of S-MC1 exceeds the 50%$_{at}$. S-MC1 shows also the lowest amount of oxidized C and sp^3 C. In the other doped mesoporous carbons the amount of each C species is basically constant. On the contrary, the un-doped MC has the highest amount of oxidized C species (41%$_{at.}$) and the lowest amount of graphitic C (23%$_{at.}$). All the components present in the C 1s photoemission spectra are shifted by 0.1 – 0.3 eV to higher B.E compared to the ones in C1s spectrum of MC, probably due to the higher electronegativity of N and S compared to C, responsible for an electron withdrawing effect on carbon. In the case of oxygen, the most abundant functional groups are the hydroxyls and ethers, centred at 531.6 eV. The presence of N, and partially also S, prevent a further oxidation of the carbon structure: O 1s signal of MC shows a higher degree of oxidation compared to the same signal of doped MC, especially N-MC1 and N-MC2.

4.4.4 Thermal stability: TGA

The thermal stability was evaluated by TGA to clarify the effect on the thermal stability of the differently doped mesoporous carbons, and is compared to the stability of a commercial high-graphitic mesoporous carbon. The thermogravimetric curves are reported in Figure 4.27a, together with the first derivative (Figure 4.27b) to identify the degradation temperature.

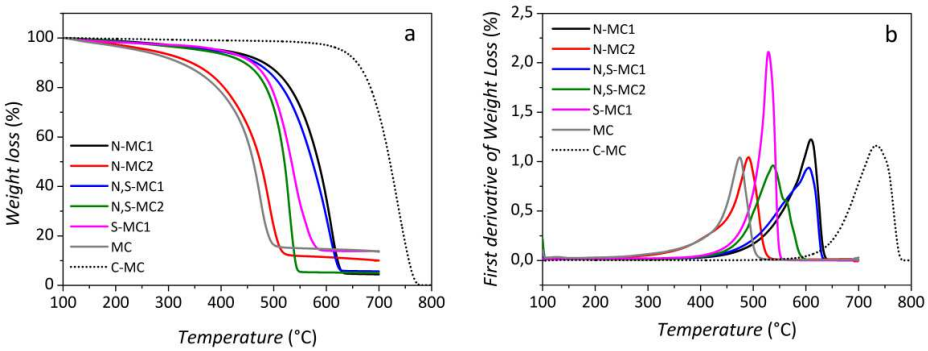

Figure 4.27 a) Termogravimetric analysis carried out under N_2 and b) first derivative of weight loss for N-MC1 (black), N-MC2 (red), N,S-MC1 (blue) N,S-MC2 (green), S-MC1 (pink) and MC (grey). The black dotted line is associated to commercial mesoporous carbon.

The thermal stability follows the trend: N-MC1 ≈ N,S-MC1 > N,S-MC2 > S-MC1 > N-MC2 > MC, and all the samples are less stable than the commercial reference material (C-MC). All the doped mesoporous carbon are more stable than the non-doped support MC, so clearly there is a stabilizing effect by heteroatoms in the thermal stability. But N and S heteroatoms seem to determine an opposite effect on the degradation temperature: from Figure 4.28 it's possible to observe a decrease in thermal stability associated to a decrease in N content. This effect is described also in literature, and is associated to non-crystalline or disordered carbon structure [15], while a decrease in thermal stability due to increasing nitrogen content is highlighted as well for ordered carbon support, like carbon nanotubes [16]. A detrimental effect on thermal stability seems to be determined by sulphur, given that the higher is its amount on the material, the lower is its thermal stability. In this case a clear relation among stability and amount of heteroatoms is not obtained, but it's fundamental to take into account that oxygen-containing groups are present, and as described in Section 4.2.4, their decomposition starts at very low temperature.

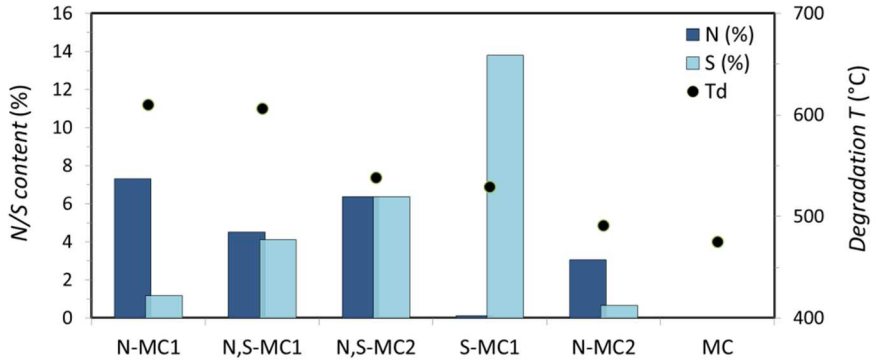

Figure 4.28 Correlation between amount of N, S and degradation temperature in the differenlty doped MCs.

At present, it is not clear if this improvement in thermal stability is due to the insertion of heteroatoms in the carbon matrix, or to the lower oxygen content, depicted by elemental analysis.

4.4.5 N-MC1, N-MC2, N,S-MC1, N,S-MC2, S-MC1, MC: Summary

In Table 4.17 are reported the fundamental physico-chemical properties of N-MC1, N-MC2, N,S-MC1, N,S-MC2, S-MC1 and MC.

Table 4.17 Summary reporting all the fundamental physico-chemical properties for N-MC1, N-MC2, N,S-MC1, N,S-MC2, S-MC1 and MC.

	SBET (m^2/g)	V_p (cm^3/g)	d_{p1} (nm)	d_{p2} (nm)	d_{p3} (nm)	d_{p4} (nm)	N ($\%_w$)	T_{deg} (°C)
N-MC1	881	0.689	1.1	3.8	6.2	-	7.32	610
N-MC2	810	0.625	1.7	3.2	4.0	5.4	3.06	491
N,S-MC1	855	0.681	1.1	4.0	6.4	-	4.51	606
N,S-MC2	409	0.313	0.9	4.0	-	-	6.38	538
S-MC1	1103	0.864	1.1	4.0	5.5	8.4	0.10	529
MC	953	0.881	1.1	4.0	6.2	-	-	473

4.5 Raman Characterization

Carbon has several allotropes, the most famous being diamond and graphite. In the last years other structures have been recognised as carbon allotropes, among these it's possible to find graphene and nanotubes. Diamond is a crystalline lattice of C sp^3 atoms, while graphite is an overlapping of graphene layers, each made of hexagonal ring made up of C sp^2 atoms.

Raman investigation of MCs was carried out in order to achieve some information about their structural composition, that influence their catalytic activity. In fact, papers in which catalytic activity of carbon based electrodes is related to their structure can be found. Raman, together with XPS and elemental analysis, is a very useful tool to investigate chemical and structural properties of the synthesized mesoporous carbons such as defects, stacking of the graphene layers and the finite site of the crystallites. The most important signals obtained by Raman scattering from a carbon-based material are the so called *G band* at 1582 cm^{-1}, the *D1 band* at 1350 cm^{-1}. The *G band* is associated to graphitic structures, in which the C is present as sp^2 hybridization. Diamond like C (sp^3) and linear carbon chains (sp) have typical Raman features respectively at 1333 cm^{-1} and between 1850 and 2100 cm^{-1}. The *D1* and *D' band* are caused by defect in the carbon structure, so they don't appear in high-graphitic materials. The *G' band* corresponds to an overtone of *D band* [17]. An important parameter is the ratio between *D1 band* and *G band* (I_D/I_G), which gives information about the defective degree of the analysed carbon structure. This ratio is also correlated to the crystallite size, according a relation found by Tuinstra and Koenig, first, and Knight and White, later [18][19].

Figure 4.29a shows the Raman spectra of the newly prepared doped mesoporous carbons and the commercial mesoporous carbon (C-MC). All spectra are normalized to the maximum of the *G band* and vertically shifted for clarity. The two intense bands observed at 1600 cm^{-1} and at 1350 cm^{-1} are the *G* (graphitic, E2g) and the *D1* band (defect, A1g). Raman spectra can be interpreted on the basis of a phenomenological three-stage model, that shows the evolution of the *G band* position and of the *D1*/*G* ratio along an amorphization trajectory going from graphite to tetrahedral amorphous carbon (see for example ion implantation in glassy carbon) [20][21]. In the first stage of this model, graphite transforms into nanocrystalline graphite (NC-graphite), where the three-dimensional order is lost due to the formation of nano-sized graphite crystallites. The Raman spectra accompanying this process exhibit a shift of the *G band* peak from about 1580 cm^{-1} to about 1600 cm^{-1} and a rise of the *D1*/*G* ratio from 0 to 2. In the second stage NC-graphite coverts into amorphous carbon (*G band* around 1500 cm^{-1}, *D1*/*G* ratio around 0.2), that consists of mainly sp^2 sites in puckered ring-like configurations (five-to

eight-fold disordered rings) and in the third stage, amorphous carbon converts into tetrahedral amorphous carbon (*G band* around 1560 cm^{-1}, *D1*/*G* = 0), in which sp^2 sites gradually converts from rings to olefin chains. It is also possible to follow an ordering pathway (for example by annealing an amorphous carbon after synthesis) [22]: in this case the literature shows that hysteresis effects can occur leading, in general, to a non-unique relation among the *G band* position, the *D1*/*G* ratio and the sp^3 content in stages 2 and 3.

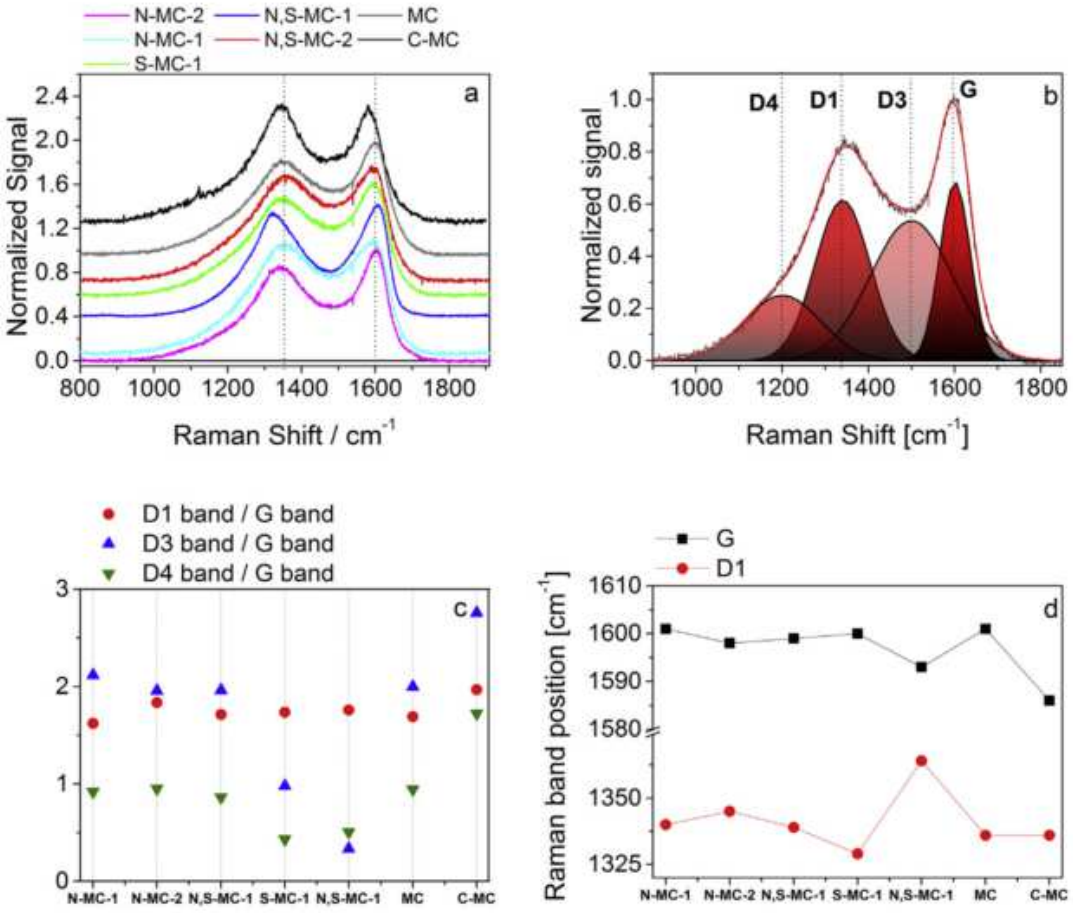

Figure 4.29 (a) Raman spectra for the synthetized MCs, (b) example of a deconvoluted N-MC-1 spectrum, (c) band areas normalized to the G band area for the investigated MCs and d) D1 and G band position for MCs.

In order to recognize individual components in the Raman spectra, deconvolution analysis has been carried out. In the literature, commercial carbon blacks have been fitted with three bands [17] and other carbon materials with four or even five bands [23]. We found that in our case four bands were necessary to achieve a good fit: however, letting all parameters free, the fit became ambiguous, and depending on the starting values and on the band shape

adopted, the fit reached several minima, all with a very good and similar adjusted R^2 but corresponding to different band combinations. This probably arises from the overlap of the bands used to deconvolute the spectrum. Therefore, we finally fitted our experimental data on the basis of the bands already known from the literature: the frequency of the two bands corresponding to D1 and G were constrained between 1300 and 1400 cm^{-1} and between 1550 and 1650 cm^{-1} respectively. The frequency of the other two bands were fixed at 1500 cm^{-1} (D3 band) and 1200 (D4 band). In the literature, the D3 band is assigned to amorphous carbon and the D4 one has been tentatively related to the presence of polyenes or ionic impurities [23]. All band shapes were chosen Gaussian and FWHMs let free. Figure 4.29 an example of the fit for N-MC-1 is reported. In Figure 4.29c the D1, D3 and D4 band areas, normalized to the G band area, are shown for all MCs. Their G-band position is reported in Figure 4.29d. The results in the figure suggest that D1/G band ratio is very similar for all MCs: the spectral differences among the MCs seem to arise from the presence of other types of defects (D3 and D4). The D3/G band ratio seems to be the same for all MCs except for S-MC1 and N,S-MC2 for which it is lower. The D4/G band ratio is significantly lower in MCs than in C-MC. Since all synthesized MCs show a G-band peak at ~1600 cm^{-1} they can be assigned to a NC-graphite structure. The expected D1/G ratio is 2 and it coincides with the D1/G area ratio calculated from the fits for all synthesized MCs [21]. In the case of C-MC, the G band lies at 1586 cm^{-1} and the D1/G ratio around 2: these parameters would place C-MC between the middle of stage 1 and the middle of stage 2. It is worth noting that no clear relation between the type of precursor and the Raman spectra emerges: for example N-MC-2, N,S-MC-1, MC have very similar spectra but N-MC-2 contains N, N,S-MC-1 N and S, MC none of the two.

The Raman analysis performed on N-MC1 samples prepared at different temperature of pyrolysis (T = 750 (a), 850 (b), 950 (c), 1050 (d) °C) is shown in Figure 4.30, where spectra are normalized to the maximum of the G band. A coarse visual comparison of the spectra suggests that the D1/G band ratio is almost independent of the T and that the amount of amorphous carbon slightly decreases at higher temperature. The spectra are fitted following the same method previously described (Figure 4.30c); Figure 4.30b shows the D1/G, D3/G, D4/G dependence on the T. Consistently with the observations previously, the trends indicate a small variation of the D1/G ratio and a moderate reduction of the D3/G ratio for sample N-MC1-1050 compared to the others. This analysis indicates that the amorphous carbon content slightly diminishes at higher pyrolysis temperature. Finally, this Raman analysis suggests that, being the D1/G ratio similar for all MCs, they should be characterized by the same density of edge plane defects and size of nano-crystallites.

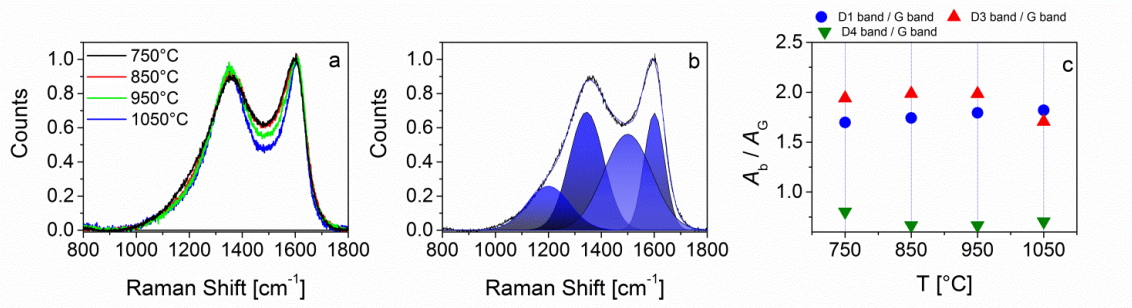

Figure 4.30 (a) Raman spectra for the N-MC1s synthetized at different temperatures, (b) example of a deconvoluted N-MC1 spectra and (C) band areas normalized to the G band area for the investigated MCs.

The work described in this chapter can be found in reference [24].

Bibliography

[1] Y. Shin, G.E. Fryxell, M.H. Engelhard, G.J. Exarhos, Functional mesoporous carbon built from the 1,10-phenanthroline building block: A new class of catalyst support, Inorg. Chem. Commun. 10 (2007) 1541–1544. doi:10.1016/j.inoche.2007.09.021.

[2] M. Thommes, K. Kaneko, A. V. Neimark, J.P. Olivier, F. Rodriguez-Reinoso, J. Rouquerol, K.S.W. Sing, Physisorption of gases, with special reference to the evaluation of surface area and pore size distribution (IUPAC Technical Report), Pure Appl. Chem. 87 (2015) 1051–1069. doi:10.1515/pac-2014-1117.

[3] M. Favaro, L. Perini, S. Agnoli, C. Durante, G. Granozzi, A. Gennaro, Electrochemical behavior of N and Ar implanted highly oriented pyrolytic graphite substrates and activity toward oxygen reduction reaction, Electrochim. Acta 88 (2013) 477–487. doi:10.1016/j.electacta.2012.10.100.

[4] L. Perini, C. Durante, M. Favaro, V. Perazzolo, S. Agnoli, O. Schneider, G. Granozzi, A. Gennaro, Metal–Support Interaction in Platinum and Palladium Nanoparticles Loaded on Nitrogen-Doped Mesoporous Carbon for Oxygen Reduction Reaction, ACS Appl. Mater. Interfaces. 7 (2015) 1170–1179. doi:10.1021/am506916y.

[5] Y. Wang, Y. Shao, D.W. Matson, J. Li, Y. Lin, Nitrogen-Doped Graphene and Its Biosensing, ACS Nano 4 (2010) 1790–1798. doi:10.1063/1.4870424.

[6] S. Kundu, T.C. Nagaiah, W. Xia, Y. Wang, M. Bron, W. Schuhmman, M. Muhler, Thermal Stability and Reducibility of Surface Oxygen-Containing Functional Groups on Multiwalled Carbon Nanotubes Surfaces: a Quantitative High-Resolution XPS and TPD/TPR Study, J. Phys. Chem. 112 (2008) 16869–16869.

[7] X. Liu, H. Zhu, X. Yang, One-step synthesis of dopamine-derived micro/mesoporous nitrogen-doped carbon materials for highly efficient oxygen-reduction catalysts, J. Power Sources. 262 (2014) 414–420. doi:10.1016/j.jpowsour.2014.04.023.

[8] W. Shen, W. Fan, Nitrogen-containing porous carbons: synthesis and application, J. Mater. Chem. A 1 (2013) 999–1013. doi:10.1039/C2TA00028H.

[9] R. Arrigo, M. Hävecker, R. Schlögl, D.S. Su, Dynamic surface rearrangement and thermal stability of nitrogen functional groups on carbon nanotubes, Chem. Commun. (2008) 4891–4893. doi:10.1039/b812769g.

[10] T. Sharifi, G. Hu, X. Jia, T. Wågberg, Formation of active sites for oxygen reduction reactions by transformation of nitrogen functionalities in nitrogen-doped carbon nanotubes, ACS Nano 6 (2012) 8904–8912. doi:10.1021/nn302906r.

[11] A.N. Buckley, Nitrogen functionality in coals and coal-tar pitch determined by X-ray photoelectron spectroscopy, Fuel Process. Technol. 38 (1994) 165–179. doi:10.1016/0378-3820(94)90046-9.

[12] K. Stańczyk, R. Dziembaj, Z. Piwowarska, S. Witkowski, Transformation of nitrogen structures in carbonization of model compounds determined by XPS, Carbon 33 (1995) 1383–1392. doi:10.1016/0008-6223(95)00084-Q.

[13] J.R. Pels, F. Kapteijn, J.A. Moulijn, Q. Zhu, K.M. Thomas, Evolution of nitrogen functionalities in carbonaceous materials during pyrolysis, Carbon 33 (1995) 1641–1653. doi:10.1016/0008-6223(95)00154-6.

[14] H. Schmiers, J. Friebel, P. Streubel, R. Hesse, R. Köpsel, Change of chemical bonding of nitrogen of polymeric N-heterocyclic compounds during pyrolysis, Carbon 37 (1999) 1965–1978. doi:10.1016/S0008-6223(99)00071-8.

[15] P. Kichambare, J. Kumar, S. Rodrigues, B. Kumar, Electrochemical performance of highly mesoporous nitrogen doped carbon cathode in lithium-oxygen batteries, J. Power Sources 196 (2011) 3310–3316. doi:10.1016/j.jpowsour.2010.11.112.

[16] E.N. Nxumalo, V.O. Nyamori, N.J. Coville, CVD synthesis of nitrogen doped carbon nanotubes using ferrocene/aniline mixtures, J. Organomet. Chem. 693 (2008) 2942–2948. doi:10.1016/j.jorganchem.2008.06.015.

[17] T. Jawhari, A. Roid, J. Casado, Raman spectroscopic characterization of some commercially available carbon black materials, Carbon 33 (1995) 1561–1565. doi:10.1016/0008-6223(95)00117-V.

[18] F. Tuinstra, L. Koenig, Raman Spectrum of Graphite, J. Chem. Phys. 53 (1970) 1126–1130. doi:10.1063/1.1674108.

[19] M.A. Pimenta, G. Dresselhaus, M.S. Dresselhaus, L.G. Cançado, A. Jorio, R. Saito, Studying disorder in graphite-based systems by Raman spectroscopy, Phys. Chem. Chem. Phys. 9 (2007) 1276–1291. doi:10.1039/b613962k.

[20] D.G. McCulloch, S. Prawer, A. Hoffman, Structural investigation of xenon-ion-beam-irradiated glassy carbon, Phys. Rev. B 50 (1994) 5905–5917. doi:10.1103/PhysRevB.50.5905.

[21] A. Ferrari, J. Robertson, Interpretation of Raman spectra of disordered and amorphous carbon, Phys. Rev. B 61 (2000) 14095–14107. doi:10.1103/PhysRevB.61.14095.

[22] A.C. Ferrari, B. Kleinsorge, N.A. Morrison, A. Hart, V. Stolojan, J. Robertson, Stress reduction and bond stability during thermal annealing of tetrahedral amorphous carbon, J. Appl. Phys. 85 (1999) 7191. doi:10.1063/1.370531.

[23] A. Sadezky, H. Muckenhuber, H. Grothe, R. Niessner, U. Pöschl, Raman microspectroscopy of soot and related carbonaceous materials: Spectral analysis and structural information, Carbon 43 (2005) 1731–1742. doi:10.1016/j.carbon.2005.02.018.

[24] V. Perazzolo, C. Durante, R. Pilot, A. Paduano, J. Zheng, G.A. Rizzi, A. Martucci, G. Granozzi, A. Gennaro, Nitrogen and sulfur doped mesoporous carbon as metal-free electrocatalysts for the in situ production of hydrogen peroxide, Carbon, 95 (2015) 949-963.

Chapter 5

Doped Mesoporous Carbons: Oxygen Reduction Reaction and Electrochemical Stability

In this chapter is described the electrochemical characterization toward oxygen reduction reaction (ORR) carried out with the differently doped mesoporous carbons described in chapter 4 obtained with different silica and carbon precursors, at several pyrolysis temperatures. The techniques employed were cyclic voltammetry (CV) and linear sweep voltammetry (LSV) with rotating disk electrode (RDE) and rotating ring disk electrode (RRDE). The measurement were carried out in both 0.5 M H_2SO_4 and 0.5 M KOH. The electrochemical stability of mesoporous carbons obtained from silica P200 and different carbon precursors at pyrolysis temperature of 750 °C was evaluated. The potential-induced chemical modification were detected by Raman and X-rays photoelectron spectroscopies while the structural changes are highlighted with SEM.

5.1 Electrochemical Oxygen Reduction Reaction

All the electrochemical measurement described in this chapter were carried out with doped mesoporous carbons in 0.5 M H_2SO_4 or 0.5 M KOH. The solution was saturated with Ar for the blank measurement and with O_2 for the performance determination, each one being bubbled in the cell for at least half an hour before the measurement. The CV in static condition were recorded at 0.05, 0.1, 0.2, 0.3, 0.4, 0.5, 0.8, 1 and 2 V/s, the LSV with RDE were recorded at 5 mV/s with at 800, 1100, 1400, 1600, 1700, 2000, 2300, 2600, 2900, 3200 and 3500 rpm. All the CVs reported here were taken at 200 mV/s in the case of static condition, and at 5 mV/s and at

1600 or 2000 rpm in the case of LSV with RDE. The ink for the deposition of the mesoporous carbon on the surface of an inert electrode was made of 1.25 mg of catalyst in 1.25 mL of a solution of MilliQ® H_2O containing 6%$_{vol}$ of nafion polymer. The inert WE was a GC disk with diameter of 3 mm, the CE is a Pt ring and the RE was a SCE ($Hg|Hg_2Cl_2|KCl$ sat.) or a Ag/AgCl/KCl electrode. Potentials in the tables are referred to SHE, and all the curves have been shifted by + 0.241 V, theoretical value corresponding to the difference between SCE and SHE.1600 or 2000 rpm in the case of LSV with RDE. The ink for the deposition of the mesoporous carbon on the surface of an inert electrode was made of 1.25 mg of catalyst in 1.25 mL of a solution of MilliQ® H_2O containing 6%$_{vol}$ of nafion polymer. The inert WE was a GC disk with diameter of 3 mm, the CE is a Pt ring and the RE was a SCE ($Hg|Hg_2Cl_2|KCl$ sat.) or a Ag/AgCl/KCl electrode. Potentials in the tables are referred to SHE, and all the curves have been shifted by + 0.241 V, theoretical value corresponding to the difference between SCE and SHE.

5.1.1 Oxygen reduction reaction with nitrogen doped mesoporous carbons synthesized with different silica templates: NMC-MCM41, NMC-SBA15, NMC-MSUH, NMC-P200 and NMC-P20.

All the nitrogen doped mesoporous carbons synthesized with different silica template were characterized in Ar sat. 0.5 M H_2SO_4 and 0.5 M KOH. These measurements allow to obtain the capacitive current of each material, which depends on surface area and on modification of carbon structure with nitrogen and oxygen functionalities. In Figure 5.1 a and b the CVs recorded in Ar sat. 0.5 M H_2SO_4 and 0.5 M KOH, respectively, are reported. Given that the amount of nitrogen is almost the same for all the samples, around 5%$_w$, it's predictable that the difference in capacitive currents arises mainly from the different surface areas and surface oxygen amount. According to literature, N containing groups induce a pseudo-capacitive effect due to the increase of intrinsic charges and to the adsorption of protons and electrolyte in the double layer region. Furthermore, a quasi-reversible redox signal in the 0.2-0.6 V range, associated to a proton-coupled redox reaction involving quinone/hydroquinone appears. In alkaline environment these two processes are hindered because of the low concentration of H^+ ions, so the capacitive current is lower.

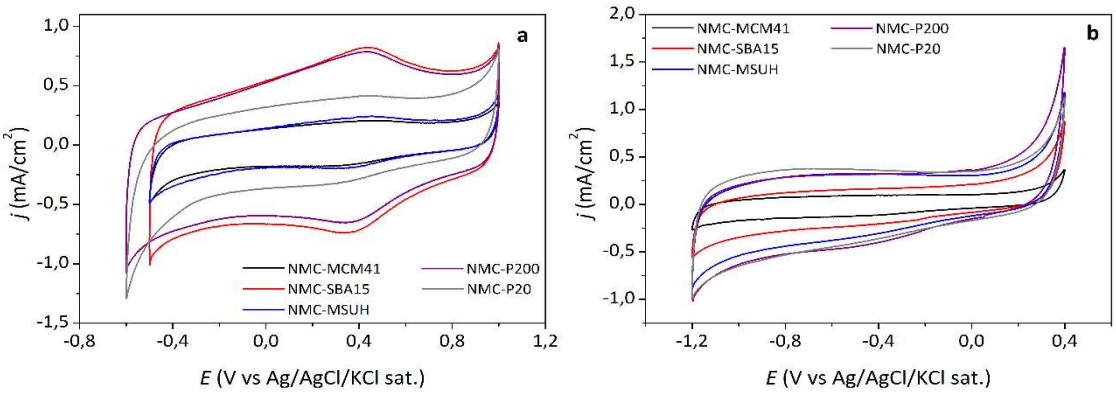

Figure 5.1 CVs recorded with NMC-MCM41 (black), NMC-SBA15 (red), NMC-MSUH (blue), NMC-P200 (purple) and NMC-P20 (grey) in Ar sat. a) 0.5 M H_2SO_4 and b) 0.5 M KOH. Scan rate 50 mV/s.

Histograms in Figure 5.2 report the specific capacitance for the samples in 0.5 M H_2SO_4 (black bars) and 0.5 M in KOH (grey bars). Capacitance was calculated by equation 5.2, which highlights that this property is the linear regression slope of I_{cap} (defined as the mean value of anodic and cathodic current taken at the same potential, eq. 5.1) versus the scan rate. So, a typical experiment for capacitance determination consists in recording CV at least at four different scan rates, calculating I_{cap} at a selected potential for each CV and plotting it versus the scan rate itself.

$$I_{cap} = \frac{|I_{cat}| + I_{an}}{2} \qquad \text{Eq. 5.1}$$

$$I_{cap} = C\frac{dE}{dt} = Cv \qquad \text{Eq. 5.2}$$

Capacitances reported in Figure 5.2 were calculated at 0.0 V (vs Ag/AgCl/KCl sat.), corresponding to a potential region in which no process occurs. Black bars correspond to capacitance in 0.5 M H_2SO_4, grey bars to capacitance in 0.5 M KOH and they are correlated with surface area (Figure 5.2a), nitrogen content (Figure 5.2b) and total nitrogen and oxygen amount (Figure 5.2c). It's clear that capacitance is higher in acid solution, due to the above specified statements. NMC-SBA15 shows the highest specific capacitance in this environment, followed by NMC-P200, NMC-P20, NMC-MSUH and NMC-MCM41. A good correlation between these values and the amount of N in each sample is highlighted, as can be seen in Figure 5.2b. Differences in surface area turns out to be not so relevant in the determination of capacitance, and a correlation between these two parameters was highlighted only in the case of NMC-MSUH, NMC-SBA15 and NMC-P20, symptom that not only one parameter is relevant in determining the capacitance. On the contrary, in alkaline environment the capacitance

decreases in the order NMC-P200, NMC-P20, NMC-MSUH, NMC-SBA15 and NMC-MCM4, so it's higher for the sample characterized by the highest surface area. Probably other parameters are involved, such as surface chemistry: as can be seen in Figure 5.2c, the total amount of nitrogen and oxygen and the capacitance in alkaline environment appears to be inversely proportional. The obtained amount of oxygen is an over-estimation, because it was calculated from the residual percentage not identified by elemental analysis, and it's modulated with the residual that appears in each TGA associated to silica.

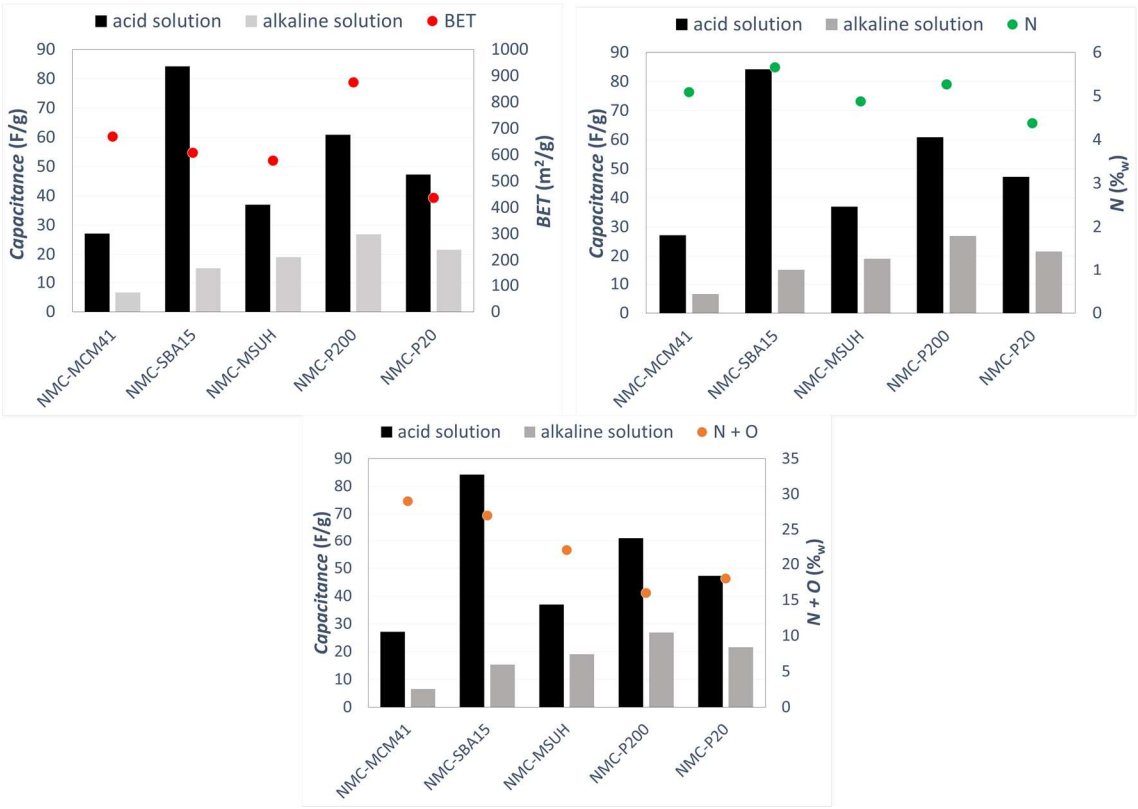

Figure 5.2 Histograms report the capacitance in 0.5 M H2SO4 (black bars) and 0.5 M KOH (gray bars). a) red dots represent the BET surface area; b) the green dots represent the nitrogen content obtained from elemental analysis; c) the orange dots represent the oxygen content obtained from elemental analysis and TGA.

All the materials were characterized toward oxygen reduction reaction. CVs in steady conditions were recorded to identify peak potential, LSVs with rotating disk electrode were employed for the determination of onset potential (E_{onset}), half-wave potential ($E_{1/2}$) and limiting current (i_{lim}), while LSV with rotating ring disk electrode are employed to determine the oxygen reduction pathway. In Figure 5.3 is reported the electrochemical characterization for NMC-P200, selected as representative sample. Figure 5.3 a and c show CVs in steady state condition and LSVs with RDE in O_2 sat 0.5 M H_2SO_4, respectively , while in Figure 5.3 b and d the same analysis

in O_2 sat 0.5 M KOH is reported, for NMC-P200. In Table 5.1 all the data obtained from electrochemical characterization toward ORR in both acid and alkaline solution, are reported and different behaviours are highlighted. In 0.5 M H_2SO_4 the samples have different electrocatalytic properties toward ORR, in particular NMC-MSUH results the most active material, followed by NMC-P20, NMC-MCM41, NMC-P200 and NMC-SBA15. On the contrary, in alkaline solution all the materials show very similar performance, worse than that in acid solution.

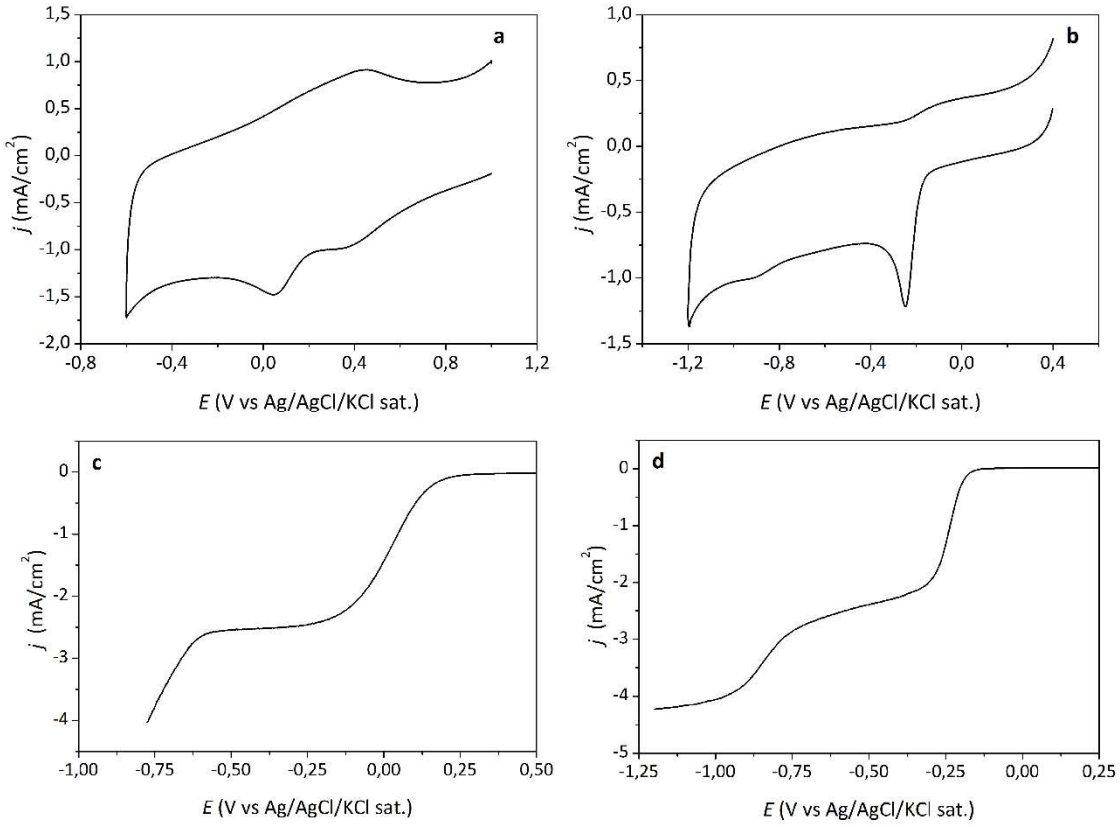

Figure 5.3 Electrochemical characterization toward ORR of NMC-P200. CV in steady state conditions in O_2 sat. a) 0.5 M H_2SO_4 and b) 0.5 M KOH. Scan rate 50 mV/s. LSVs with RDE in O_2 sat. c) 0.5 M H_2SO_4 and d) 0.5 M KOH. Scan rate: 5 mV/s, rotation rate: 1600 rpm.

As will be explained in Paragraph 5.1.4, ORR is a proton-electron coupled reduction reaction, so its activity is pH dependent. In particular, in alkaline environment, the limiting process is the protonation of the $O_2^{\bullet-}$ [1]. In the case of acid environment, a structural effect might be fundamental in discriminating the different performances toward oxygen reduction. In particular, pore dimensions and geometry could help or hinder the diffusion to and from the electrochemical active sites of oxygen and reaction products. From literature it is known that pore diameter lower than 5 nm hinders the diffusion of all species to and from the electrode.

This has a strong impact on the half-wave potential: as can be seen from Table 5.1 NMC-MCM41, NMC-MSUH and NMC-P20 represent the most active materials, but their half-wave potential are the same as NMC-P200 and NMC-SBA15, which have much lower activity. This results in a stretched LSV for NMC-MCM41, NMC-MSUH and NMC-P20, which corresponds to a hindered reduction process due to a bad oxygen diffusion toward active sites (**Figure 5.4**). The onset potential, on the contrary, is not affected by diffusion issues to and from active sites, because the surface is already completely covered as the reduction starts. The onset potential is determined mainly by surface chemistry of carbon material, so it's predictable that the most active carbon materials possess a higher amount of pyridinic N, or a coordination of more defects which turns out to be favourable to the oxygen reduction process. In this case, a full XPS characterization was not carried out because the main interest was focused on the physical properties of materials, such as surface area, pore volume and diameter. So, in this case, it's possible to justify the different behaviour only by comparison with literature previous findings.

Table 5.1 Electrochemical data for ORR in O_2 sat 0.5 M H_2SO_4 and 0.5 M KOH

		E_p[a,b] (V)	E_{onset}[b,d] (V)	$E_{1/2}$[b,d] (V)	j_{lim}[d] (mA/cm^2)	n_1[e]	X_{H2O2} (%)	n_2[e]
NMC-MCM41	H_2SO_4	0.113	0.314	0.157	2.18	2.7	65	-
NMC-SBA15	H_2SO_4	0.203	0.272	0.198	2.10	2.4	80	-
NMC-MSUH	H_2SO_4	0.286	0.388	0.219	2.46	2.8	60	-
NMC-P200	H_2SO_4	0.238	0.292	0.214	2.35	2.5	75	-
NMC-P20	H_2SO_4	0.099	0.344	0.194	2.97	4.3	-	-
NMC-MCM41	KOH	-0.108	-0.015	-0.092	1.86	2.2/3	50	3.2
NMC-SBA15	KOH	-0.069	-0.012	-0.066	2.22	2.0	76	3.7
NMC-MSUH	KOH	-0.052	0.016	-0.063	2.05	2.2	61	3.3
NMC-P200	KOH	-0.050	0.005	-0.048	2.38	2.4	71	4.0
NMC-P20	KOH	-0.055	0.008	-0.061	2.60	2.4	-	3.9

[a] Data obtained by cyclic voltammetry

[b] All potential are referred to SHE

[c] $\Delta E_p = E_p^{MCs} - E_p^{C\text{-}MC}$, where $E_p^{C\text{-}MC}$ is -0.201 V/SHE in 0.5 M H_2SO_4 and -0.198 V/SHE in 0.5 M KOH

[d] Data obtained by RDE voltammetry

[e] number of electrons exchanged. n_1 is associated to the first electrochemical reduction step and is calculated at -0.5 V vs Ag/AgCl/KCl sat. in acid solution and at -0.7 V vs. Ag/AgCl/KCl in alkaline solution. n_2 is associated to the second electrochemical reduction step, visible only in alkaline solution, and is calculated at -1.2 V vs. Ag/AgCl/KCl.

The number of exchanged electrons, which gives information about the oxygen reduction mechanism, can be obtained in two different ways: Koutecky-Levich analysis of LSV obtained with RDE, or RRDE experiments (explained in Chapter 3). RRDE is a very useful tool for

the determination of exchanged electrons and selectivity toward two or four reaction pathways, according to equations 5.3 and 5.4, respectively. In this case the mesoporous carbon-containing ink was drop-casted on a 5 mm diameter GC disk, surrounded by a Pt ring. O_2 is reduced at the disk, which has a potential which varies linearly with time. The reaction products are pushed toward the Pt ring, kept at a fixed potential for proper oxidation of eventually formed H2O2 to O2. When H2O2 reaches the ring an increasing oxidative current is recorded, corresponding to the kinetic controlled region for ORR (i, Figure 5.4), then a steady state is reached at the same time as the ORR at the disk is diffusion-controlled (ii, Figure 5.4).

$$n = \frac{4I_d}{I_d + I_r/N} \qquad \text{Eq. 5.3}$$

$$\chi_{H_2O_2}(\%) = (2 - {}^{n}/_{2})100 \qquad \text{Eq. 5.4}$$

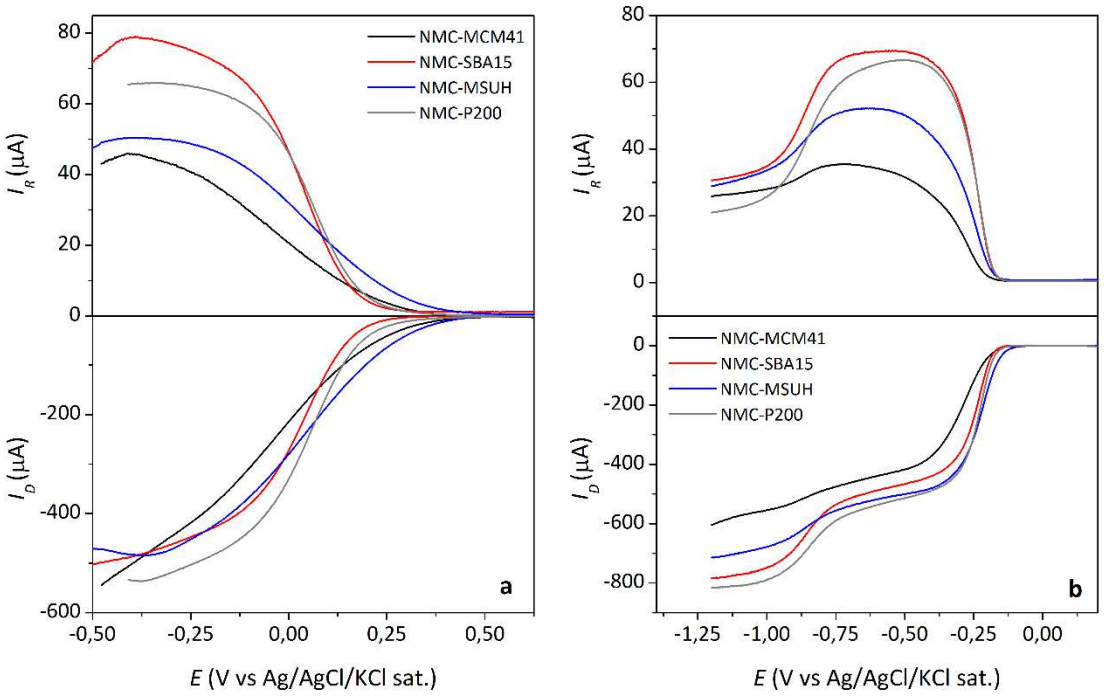

Figure 5.4 RRDE analysis for oxygen reduction on NMC-MCM41 (black), NMC-SBA15 (red), NMC-MSUH (blue) and NMC-P200 (grey). The upper graphs show ring currents, the below graph disk currents. a) Measurements in 0.5 M H_2SO_4. E_r = 0.9 V, scan rate (disk) = 5 mV/s, rotation rate: 1600 rpm. b) Measurements in 0.5 M KOH. E_r = 0.45 V, scan rate (disk) = 5 mV/s, rotation rate: 1600 rpm. Potentials are reported versus Ag/AgCl/KCl sat.

The number of exchanged electrons reported in Table 5.1 was, in fact, obtained via RRDE. The typical method for the determination of exchanged electrons, i.e. the Koutecky-Levich equation, in this case gives misleading results: the slope of the linear regression of the

graph j^{-1} versus $\omega^{-1/2}$ is close to the value for an ideal four electron reduction, but this is surprising in the case of carbon materials, known to promote H_2O_2 formation. This error is due to the absence of a clear plateau for diffusion-limited current, because this process is mixed with solvent reduction. On the contrary, the ratio of I_d and I_r, as reported in eq. 5.3, gives the exact number of exchanged electrons, which can be used to calculate the selectivity toward hydrogen peroxide with equation 5.4. RRDE confirms that the mechanism for oxygen reduction is in fact a two electron pathway, which leads to the formation of hydrogen peroxide. The number of electrons is different than 2, in particular it is a bit higher, because the selectivity toward H_2O_2 is not equal to 100%. This means that part of the molecules that reach the electrode are not reduced to H_2O_2, but follows other pathways such as the four electron reduction to H_2O. In the case on NMC-MCM41, data obtained from K-L analysis and by RRDE are not in agreement. In particular, K-L shows a two electron pathway, while RRDE indicates a selectivity for H_2O_2 equal to only 50%. In this case it is possible to suppose also an incorrect response of the RRDE methodology. In fact, the LSV (recorded at the disk) shows that E_{onset} and $E_{1/2}$ are clearly more negative with respect to the other carbon materials, and this is not in agreement with the results obtained from RRDE analysis reported in Table 5.1.

5.1.2 Oxygen reduction reaction with nitrogen doped mesoporous carbons synthesized at different pyrolysis temperatures: N-MC1, N-MC1-850, N-MC1-950 and N-MC1-1050.

In this Section the electrochemical results for ORR obtained with N-MC1, N-MC1-850, N-MC1-950 and N-MC1-1050, are described.

N-MC1 prepared at different temperatures were tested toward ORR by cyclic voltammetry and by linear sweep voltammetry with RDE in 0.5 M H_2SO_4 and 0.5 M KOH. CVs in Ar sat. 0.5 M H_2SO_4 and 0.5 M KOH are reported in Figure 5.5: N-MC1 synthesized at 750 °C shows the highest capacitive current among the N-MC1 family. First of all, the intensity of capacitive current depends on the surface area of the electrode material, but, in this case, this cannot be the only contribution, given that surface area for N-MC1, N-MC1-850, N-MC1-950 and N-MC1-1050 are almost the same. A second important parameter is the modification of the carbon structure with N: according to literature, N containing groups induce a pseudo-capacitive effect due to the increase of intrinsic charges and to the adsorption of protons and electrolyte in the double layer region [2][3]. In fact, the capacitive current decreases as the nitrogen content becomes lower. All the CVs recorded in acidic solution exhibit a quasi-reversible signal in the range 0 – 0.50 V/SCE, associated to the quinone/hydroquinone redox couple, which undergoes

proton-electron coupled transfer. This redox reaction is disadvantaged in 0.5 M KOH, due to the low concentration of H^+ species, and, in fact, the redox signal is absent in all the CVs shown in Figure 5.5 [4]. The presence of quinone/hydroquinone species is also confirmed by XPS from O 1s, shown in Figure 4.9c. This signal becomes less intense as the pyrolysis temperature is increased, because this situation promotes the elimination of oxygen-containing species in the carbon materials, and facilitates the formation of more stable structures.

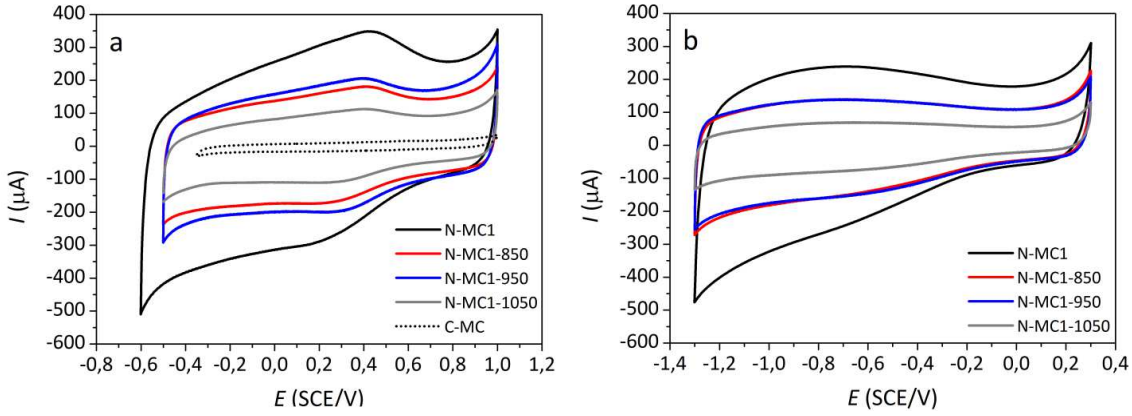

Figure 5.5 Cyclic voltammetries recorded on N-MC1 (black), N-MC1-850 (red), N-MC1-950 (blue) and N-MC1-1050 (grey) in Ar. sat a) 0.5 M H_2SO_4 and b) 0.5 M KOH. Scan rate: 200 mV/s.

In Figure 5.6 linear sweep voltammetry in O_2 sat. 0.5 M H_2SO_4 (a) and O_2 sat. 0.5 M KOH (b) and linear sweep voltammetry with rotating disk electrode in O_2 sat. 0.5 M H_2SO_4 (c) and O_2 sat. 0.5 M KOH (d) are reported. In Table 5.2 data obtained by these analyses are reported. The electrochemical activity toward ORR is compared to the performance obtained on a commercial mesoporous carbon (C-MC). C-MCs are not catalytic toward ORR, so the difference in peak potential (Ep) obtained by LSV or onset potential (Eonset) obtained with RDE are indicative of the catalytic properties of N-MC1 family with respect to the non-active material taken as reference.

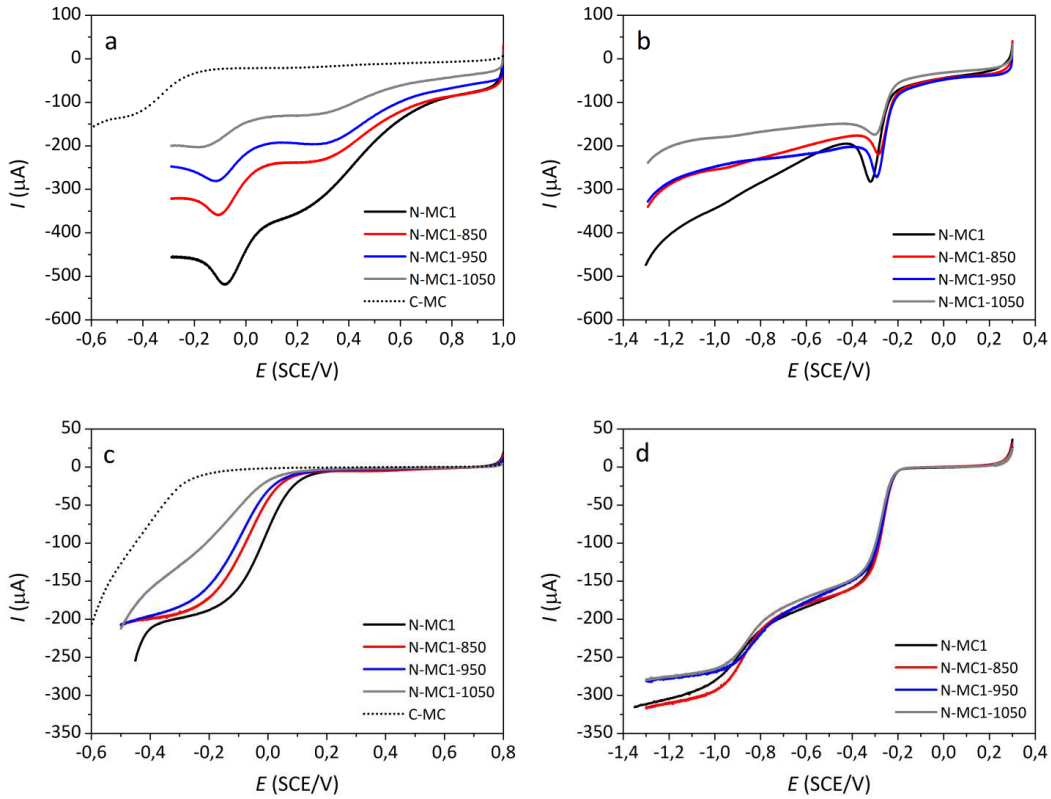

Figure 5.6 Electrochemical measurements for oxygen reduction at N-MC1 (black), N-MC1-850 (blue), N-MC1-950 (red) and N-MC1-1050 (grey). Cathodic scan of cyclic voltammetry in O_2 sat. a) 0.5 M H_2SO_4, b) 0.5 M KOH; Scan rate: 200 mV/s. Linear sweep voltammetry with RDE in O_2 sat. c) 0.5 M H_2SO_4, d) 0.5 M KOH; Scan rate 5 mV/s, rotation rate: 2000 rpm.

Electrochemical behaviour in O_2 sat. 0.5 M H_2SO_4 and O_2 sat. 0.5 M KOH is different. In the case of acidic environment there is a clear difference in the performance toward ORR, in particular N-MC1 has the highest catalytic activity among the N-MC1 family. N-MC1-850 and N-MC1-950 have comparable activity, in both cases lower than N-MC1, and N-MC1-1050 is the least active. N-MC1, N-MC1-850 and N-MC1-950 show a plateau in the diffusion limited region at RDE analysis; on the contrary, N-MC1-1050 highlights a high overpotential and a sluggish oxygen reduction kinetics. This implicates the absence of plateau and the shift of onset potential to more negative values, and simultaneous oxygen reduction and hydrogen evolution occur. The improved catalytic activity of nitrogen doped carbon based electrodes towards ORR is a well-established effect [5][6], generally ascribed to electron-accepting nitrogen atoms. In particular N graphitic and pyridinic groups generate a highly positive charge density on the adjacent carbon atoms, where oxygen molecules can adsorb more easily. In this case, it is possible to assert that the discriminant effect is mainly played by the nitrogen content rather than the type of N functional groups, since, as reported in the previous Section, the additional percentage of

graphitic N and pyridinic groups is almost constant in all N-MC-1 samples, whereas the total nitrogen content change drastically passing from 750 to 1050 °C.

Table 5.2 Electrochemical data obtained from cyclic and linear sweep voltammetries in O_2 sat. 0.5 M H_2SO_4 and 0.5 M KOH, for oxygen reduction for N-MC1 pyrolysed at different temperatures.

		E_p[a,b] (V)	ΔE_p[a,c] (V)	E_{onset}[b,d] (V)	$E_{1/2}$[b,d] (V)	j_{lim} (mA/cm^2)	n_1[e]	n_2[e]
N-MC1	H_2SO_4	0.197	0.398	0.324	0.218	2.694	2.56	-
N-MC1-850	H_2SO_4	0.164	0.365	0.283	0.165	2.748	3.14	-
N-MC1-950	H_2SO_4	0.136	0.337	0.269	0.149	2.748	2.98	-
N-MC1-1050	H_2SO_4	0.066	0.267	0.262	n.a.	n.a.	2.01	-
N-MC1	KOH	-0.057	0.141	0.011	-0.049	2.660	2.22	3.49
N-MC1-850	KOH	-0.040	0.148	0.031	-0.055	2.052	2.15	3.46
N-MC1-950	KOH	-0.046	0.152	0.023	-0.041	2.214	2.52	3.20
N-MC1-1050	KOH	-0.059	0.139	0.015	-0.049	2.450	2.40	3.07

[a] Data obtained by cyclic voltammetry

[b] All potential are referred to SHE

[c] $\Delta E_p = E_p^{MCs} - E_p^{C\text{-}MC}$, where $E_p^{C\text{-}MC}$ is -0.201 V/SHE in 0.5 M H_2SO_4 and -0.198 V/SHE in 0.5 M KOH

[d] Data obtained by RDE voltammetry

[e] number of electrons exchanged. n_1 is associated to the first electrochemical reduction step and is calculated at -0.3 V/SCE in acid solution and -0.6 V/SCE in alkaline solution. n_2 is associated to the second electrochemical reduction step, visible only in alkaline solution, and is calculated at -1.2 V/SCE.

The characterization toward ORR in 0.5 M KOH gives different results. In this medium it is still evident the higher capacitance for N-MC1 with respect to N-MC1s prepared at higher temperatures. However, the reversible peak due to the oxidation/reduction of quinone groups is missing, since the proton-electron coupled transfer is hindered at alkaline pHs. Figure 5.6c reports the cyclic voltammetries in O_2 saturated 0.5 M KOH; it is worth noting that a catalytic effect is present, but the O_2 reduction occurs approximately at the same potential for all N-MC1s. In fact, the E_p ranges between -0.040 to -0.059 V vs. SHE, and this is also confirmed by onset and half wave potentials recorded at RDE (Table 5.2). Figure 5.6 reports the RDE voltammetries for O2 reduction. The LSVs are composed of two reduction steps of almost the same height, and the current features are superimposable for all four N-MC-1s, thus confirming comparable electrocatalytic activity for all N-MC-1 carbons, notwithstanding the pyrolysis temperature.

The number of exchanged electrons in the process was evaluated with the Koutecky-Levich (K-L) equation, applied to the linear sweep voltammetries recorded with rotating disk

electrode, and it's reported for each catalysts in Table 5.2. Also in this case, as expected for a non-noble metal containing material, the oxygen reduction proceeds via hydrogen peroxide intermediate, that is further reduced to water at a more negative potential. In the experiment carried out in acidic environment, only a single step is present in the LSV, which corresponds to hydrogen peroxide formation, but the H_2 formation from the aqueous solvent is evolved before the further reduction of H_2O_2 to H_2O. In alkaline environment two steps are present: the first one corresponds to the bi-electronic reduction of O_2 to H_2O_2, which is further reduced to H_2O with a successive bi-electronic reaction. This is clear in the K-L plots reported in Figure 5.7: in the first and second graphs, corresponding to H_2O_2 formation, the obtained slope is similar to that of an ideal two-electron process, while the slope in the third graph, associated to the reduction of H_2O_2, is close to that of an ideal four-electron process. The K-L equation was applied at -0.3 V/SCE for the reaction occurring in acid environment, while it was applied at -0.6 and -1.2 V/SCE for the first and the second reduction steps in alkaline environment, respectively. The number of exchanged electrons during the two-electron reduction of O_2 to H_2O_2 is never equal exactly to 2, but it changes and usually is higher than two. So, also in this case, it means that the reaction is not completely selective for the 2 electron pathway, but also the 4 electron pathway occurs at the same time.

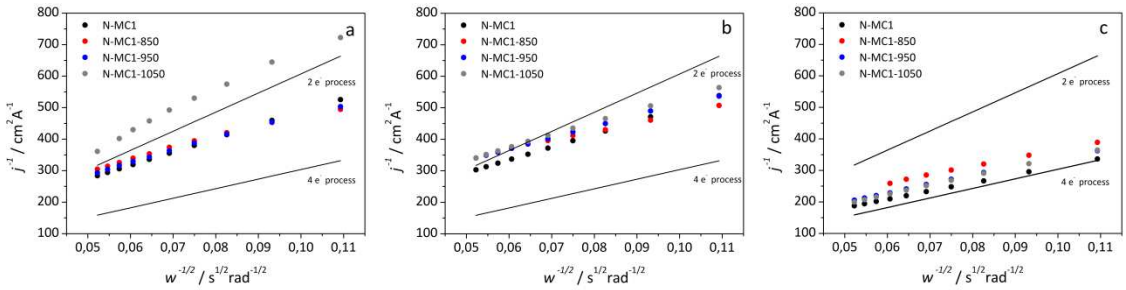

Figure 5.7 Koutecky-Levich plots for (a) O_2 sat. 0.5 M H_2SO_4 at -0.3 V/SCE and (b) O_2 sat. 0.5 M KOH at -0.6 V/SCE and (c) -1.2 V/SCE.

5.1.3 Oxygen reduction reaction with nitrogen doped mesoporous carbons synthesized from different carbon precursors

In this Section the electrochemical results for ORR obtained with N-MC1, N-MC2, N,S-MC1, N,S-MC2, S-MC1 and MC, are described. In Figure 5.8 a, b and c the CVs in Ar sat. 0.5 M H_2SO_4, LSVs in O_2 sat. 0.5 M H_2SO_4 and the LSVs recorded with RDE in O_2 sat. 0.5 M H_2SO_4, respectively, are reported In the presence of oxygen all doped and co-doped MCs show higher current density polarization curves and a very lower overpotential (i.e., the electrochemical activation energy)

with respect to the commercial carbon C-MC (Table 5.3). The capacitive current (Figure 5.8 a) is higher for N-MC1, and decreases for all the other samples: also in this case it is true what stated for N-MC1s synthesized at different pyrolysis temperatures: the higher the amount of N, the higher the capacitive current thanks to the pseudocapacitve effect induced by N groups in acid solution. There is also a quasi-reversible signal, associated as well to quinone/hydroquinone redox couple, which is quite intense in S-MC1 and MC. The LSVs (Figure 5.8b) are useful to compare at first sight the catalytic activity of all the MCs: according to the peak potential determined by cyclic voltammetry in steady condition, N-MC1 is the most active material followed by N,S-MC1, N-MC2 and N,S-MC2. On the contrary, the S-doped S-MC1 shows the lowest electrocatalytic activity toward ORR, and it's similar to the un-doped MC. The LSVs recorded with RDE (Figure 5.8c) highlight the same activity trend: N-MC1 and N,S-MC1 are the most active materials, their Eonset is the highest and the kinetic is faster than the other samples. This is clear also because the kinetic-controlled region is not 'stretched' as in S-MC1, N,S-MC2 and MC, but the current increases quickly with the potential.

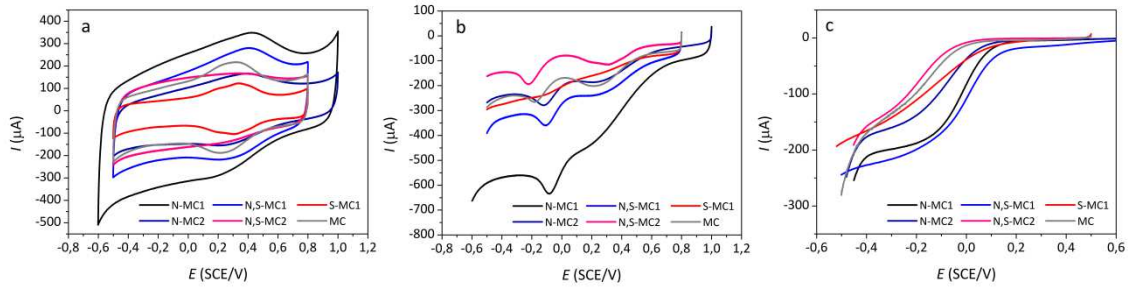

Figure 5.8 a) CVs in Ar sat 0.5 M H2SO4, scan rate 200 mV/s; b) LSV (scan rate 200 mV/s and c) LSV with RDE (scan rate 5 mV/s, rotation rate: 1600 rpm) in O2 sat. 0.5 M H2SO4 for N-MC1, N-MC2, S-MC1, N,S-MC1, N,S-MC2 and MC.

Figure 5.9a shows the variation of the E_p as function of the weight percentage of sulphur determined by elemental analysis, whereas Figure 5.9b reports the same quantity as function of the nitrogen weight percentage. The positive slope of the interpolating line in Figure 5.9b, which correlates the catalytic activity to the nitrogen content, indicates that the catalytic activity increases linearly with the nitrogen content. On the contrary, the negative slope of the interpolating line of Figure 5.9a points out that, even though S-doped MCs have relevant catalytic activity, the increasing percentage of sulphur is detriment for the O_2 reduction kinetics, i.e. the higher the sulphur content, the lower the catalytic activity. LSVs with RDE confirm the activity trend obtained by CVs.

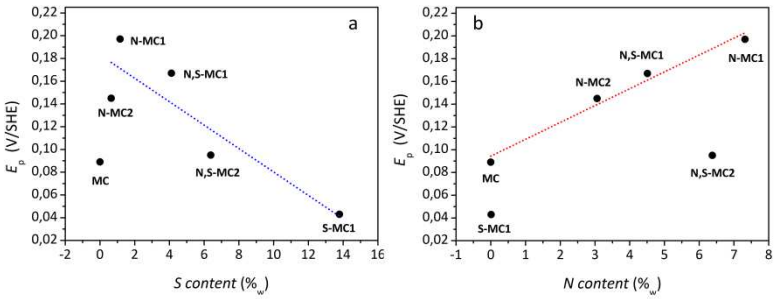

Figure 5.9 Peak potential versus a) S content ($\%_w$) and b) N content ($\%_w$) for all doped MCs.

The number of transferred electrons in correspondence of plateau in LSV recorded with RDE (Figure 5.8c) was obtained via K-L analysis. In this case the plateau is well defined for N-MC1 and N,S-MC1, while in the other measurements an increase of current till the H_2 evolution region is present. Anyway, a fixed potential of -0.3 V/SCE for all the materials was selected for the K-L analysis, reported in Figure 5.10b, which confirms a two-electron reduction of O_2 to H_2O_2. The reduction pathway was investigated with RRDE (explained in Chapter 3) as well, according to equations 5.3 and 5.4. The analysis is reported in Figure 5.10a.

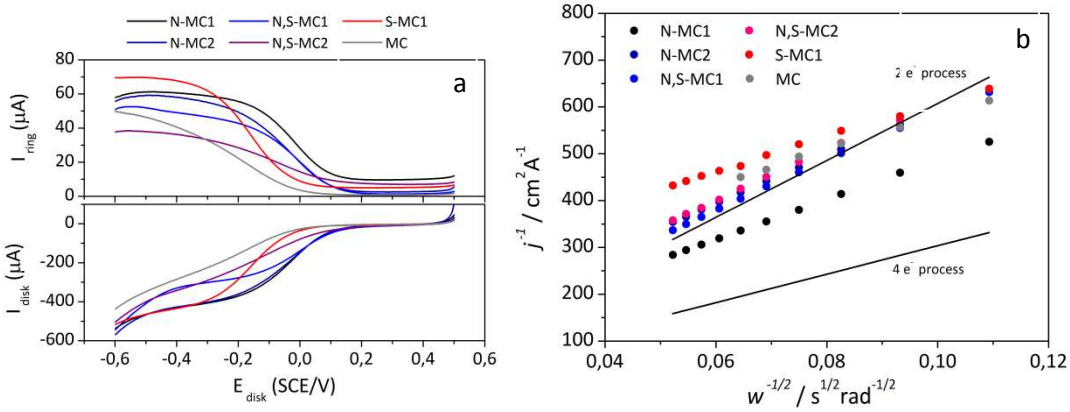

Figure 5.10 a) RRDE analysis in O2 sat. 0.5 M H2SO4, scan rate (disk): 5 mV/s, rotation rate: 1600 rpm, Ering: 1.0 V/SCE and b) K-L analysis for N-MC1, N-MC2, S-MC1, N,S-MC1, N,S-MC2 and MC.

In Table 5.3 all data obtained from electrochemical analysis carried out on differently doped MC in acid solution are summarized. Also in this case the selectivity for H_2O_2 is equal to around 70%, except for N,S-MC2 that is much lower.

Table 5.3 Electrochemical data obtained from cyclic and linear sweep voltammetries in O_2 sat. 0.5 M H_2SO_4 for oxygen reduction for all the differently doped MCs pyrolysed at 750 °C

	E_p[a,b] (V)	ΔE_p[a,c] (V)	E_{onset}[b,d] (V)	$E_{1/2}$[b,d] (V)	$\Delta E_{1/2}$[a,c] (V)	j_{lim} (mA/cm^2)	n_1[e]	X_{H2O2} (%)
N-MC1	0.197	0.398	0.324	0.218	0.353	2.694	2.56	68
N-MC2	0.145	0.346	0.277	0.148	0.283	2.339	2.6	71
N,S-MC1	0.167	0.368	0.318	0.198	0.333	2.725	2.5	76
N,S-MC2	0.095	0.296	0.349	0.142	0.277	-	2.9	56
S-MC1	0.043	0.244	0.305	0.179	0.314	2.486	2.5	77
MC	0.089	0.290	0.216	0.085	0.220	2.125	2.5	74
C-MC	-0.201	-	-0.033	-0.135	-	-	-	

To investigate the electrode kinetics under catalytic production of hydrogen peroxide EIS experiments were carried out at RDE in O_2 saturated 0.5M H_2SO_4 for all the prepared MCs. The potential was set at $E_{1/2}$ for each MCs with a superimposed perturbing signal of 5 mV; the EIS results are shown in Figure 5.11.

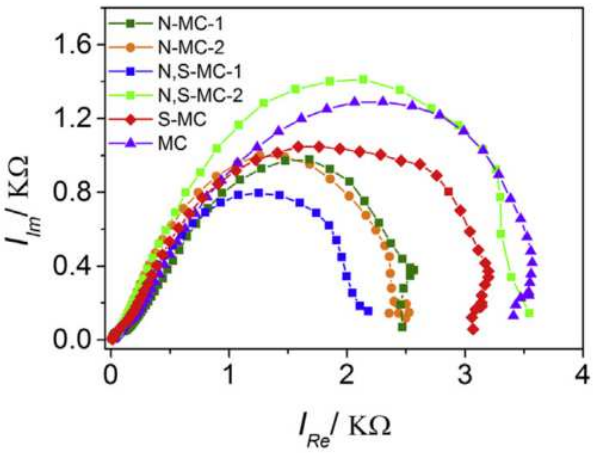

Figure 5.11 Nyquist plots of EIS for ORR on doped MC in O_2 saturated 0.5 M H_2SO_4 at $E_{1/2}$, rotation rate 1600 rpm. The frequencies range from 100 kHz to 10 mHz.

The charge transfer resistance R_{ct}, as measured by the diameter of the semicircle in the plot, is related to the charge transfer reaction kinetics according to Eq. 5.5:

$$R_{ct} = RT/nFj_0 \qquad \text{(Eq. 5.5)}$$

where j_0 is a kinetic parameter (the exchange current), whereas the other terms of the equation assume the usual meaning. Considering that the semicircle in EIS curves represents the R_{ct} of ORR, it can be clearly seen from Figure 5.11 that the corresponding R_{ct} in the case of N-MC1, N-

MC2 and N,S-MC1 are the smallest among the doped catalysts. This indicates that the ORR at nitrogen doped MCs is more favourable compared to the other S-doped MCs or the un-doped MC, due to the enhanced reaction kinetics. It is worth noting that the co-doped N,S-MC2 has the highest R_{ct}, this is in good agreement with what already observed at RDE. In fact, even though the onset potential is not as negative as for MC, the disk current curve reported in Figure 5.10a is stretched, indicating a kinetic hindrance possible arising from the deactivation of the electrode

Many papers report that sulphur doped electrocatalysts possess excellent ORR activity, but generally the sulphur content is restricted to low percentage (1 or 2%) [7] [8]. Sulphur has similar electronegativity to carbon but larger atomic radius, differently from nitrogen, which has similar dimension to carbon but higher electronegativity. Therefore, the catalytic activity induced by the two different types of doping must arise from different grounds. The thiophenic groups increase the surface hydrophobicity [9] and induce more strain and defect sites in the carbon material, furthermore, it is claimed that sulphur facilitates the proton transfer during the reduction process [8]. Therefore, we may infer that when sulphur content increases above few percentage points, the proton transfer slows down and so the whole reaction, because of the lower electrode wettability, which limits the effective three-phase interface area.

The catalytic activity toward ORR was evaluated also in 0.5 M KOH. Cyclic voltammetry in Ar sat. 0.5 M KOH and linear sweep voltammetry in steady state and with RDE in O_2 sat 0.5 M KOH are reported in Figure 5.12 a, b and c, respectively. All the synthesized MCs show a reduction peak potential more positive with respect to C-MC, indicating the presence of a catalytic activity. However, the E_p, $E_{1/2}$ and E_{onset} are very similar for the different MCs, with the only exception of N,S-MC1 and N,S-MC2, where the ORR occurs at more negative values (Table 5.4). The observed catalytic activities are comparable to or even better than those of nitrogen doped carbon nanotubes reported in literature [10][11]. So, also in this case, the catalytic activity toward ORR in alkaline media is similar, due to a different reduction mechanism than the acid solution, which will be described in Paragraph 5.1.4. The K-L analysis of the plateau currents in Figure 5.12c for the first step at -0.6 V/SCE and the second step at -1.2 V/SCE show slopes coherent with a bi-electronic and tetra-electronic reduction process, respectively (Figure 5.13a and b). The same behaviour was confirmed for all the investigated materials. Therefore, it can be assumed that in alkaline environment the O_2 is at first reduced to H_2O_2, and then further reduced in the second step, at far more negative potentials, to H_2O. To confirm this mechanism H_2O_2 was purposely added into the solution and immediately after the LSV at RDE was acquired (Figure 5.13c). It is clear that the addition of H_2O_2 causes the increase of the limiting current only of the second step, confirming the two electron pathway mechanism for the first one. In this

analysis an anodic current is present at potential higher than -0.2 V/SCE, corresponding to the oxidation of H_2O_2.

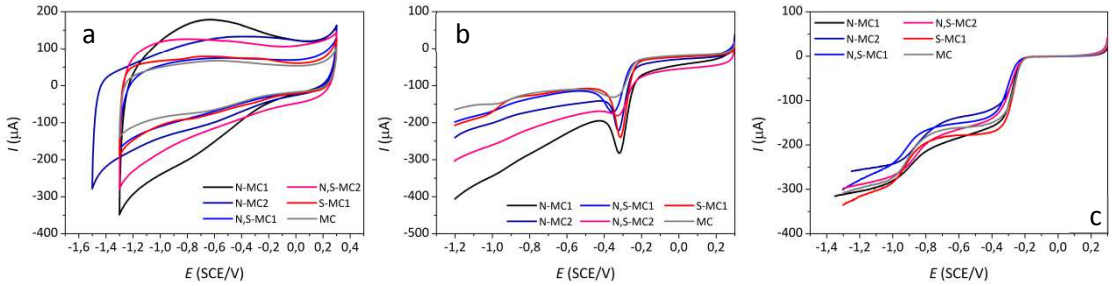

Figure 5.12 a) CVs in Ar sat 0.5 M KOH, scan rate 200 mV/s; b) LSV (scan rate 200 mV/s) and c) LSV with RDE (scan rate 5 mV/s, rotation rate: 1600 rpm) in O_2 sat. 0.5 M KOH for N-MC1, N-MC2, S-MC1, N,S-MC1, N,S-MC2 and MC.

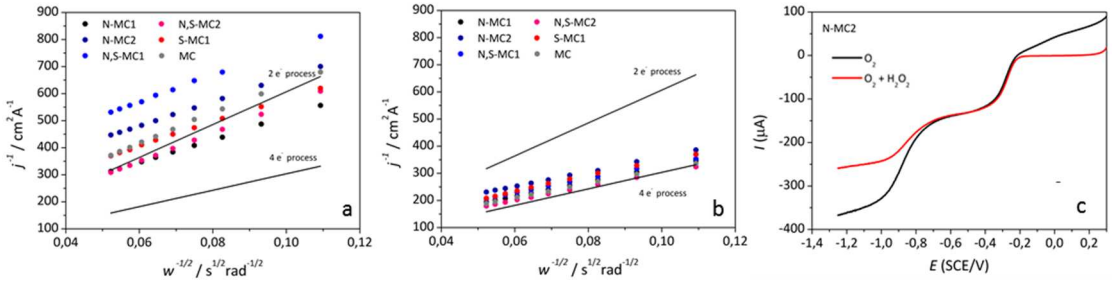

Figure 5.13 a) K-L analysis of the first reduction step for ORR at -0.6 V/SCE; b) K-L analysis of the second reduction step for ORR at -1.2 V/SCE and c) ORR response obtained with RDE on N-MC2 after the addition of 2 mM H_2O_2 in 0.5 M KOH solution (scan rate: 5 mV/s, rotation rate: 1600 rpm).

The RRDE analysis confirmed the double step reduction mechanism for all the prepared MC. The ring electrode potential in alkaline media was set at 0.45 V for the determination the H_2O_2 produced at the disk electrode. It is clear that the ring current increases and then assumes a constant value along the first diffusion-controlled O_2 reduction step, whereas at the second O_2 reduction step the ring current decreases reaching an almost steady value. The number of electrons determined according to Equation 5.3 is in agreement with the preferential production of H_2O_2 in the first step and H_2O in the second one (Table 5.5). In particular N,S-MC-1, S-MC-1 and N-MC-1 show a plateau region of more than 300 mV between the reduction of O_2 to H_2O_2 and the following reduction of H_2O_2 to H_2O, suggesting the possibility to selectively stop the reduction process to H_2O_2 without further reduction to H_2O. The selectivity toward H_2O_2

production (Equation 5.4) [12] was found to be higher than 70% for all MCs when the ring potential was set between 0.15 and 0.45 V. The X_{H2O} value reported in Table 5.5 has not the same meaning of the value X_{H2O2}, because it depends on a chemical specie generated at the electrode, and it's associated to a consecutive reaction to the main process. So, basically, it express the amount of generated H_2O_2 that desorb from the disk and reach the ring in the time scale of a RRDE analysis.

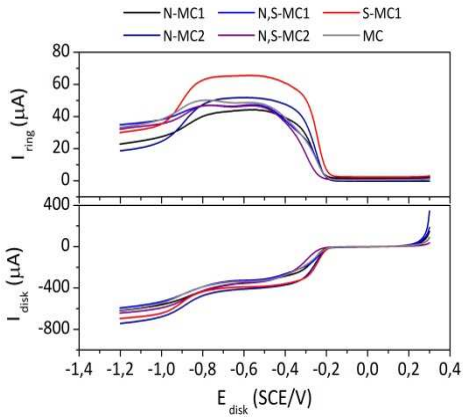

Figure 5.14 RRDE analysis in O_2 sat. 0.5 M KOH, scan rate (disk): 5 mV/s, rotation rate: 1600 rpm, E_{ring}: 1.0 V/SCE for N-MC1, N-MC2, S-MC1, N,S-MC1, N,S-MC2 and MC.

Table 5.4 Electrochemical data obtained from cyclic and linear sweep voltammetries in O_2 sat. 0.5 M KOH for oxygen reduction for all the differently doped MCs pyrolysed at 750 °C

	E_p[a,b] (V)	ΔE_p[a,c] (V)	E_{onset}[b,d] (V)	$E_{1/2}$[b,d] (V)	$\Delta E_{1/2}$[a,c] (V)	j_{lim}[d] (mA/cm^2)
N-MC1	-0.057	0.141	0.011	-0.049	0.100	-2.600
N-MC2	-0.064	0.134	0.015	-0.047	0.102	-1.870
N,S-MC1	-0.116	0.082	0.032	-0.084	0.065	-1.898
N,S-MC2	-0.073	0.125	0.022	-0.084	0.065	-2.078
S-MC1	-0.056	0.142	0.017	-0.037	0.112	-2.373
MC	-0.109	0.089	-0.033	0.018	0.167	-2.277
C-MC	-0.198	-	-0.075	-0.149	-	-2.281

[a] Data obtained from cyclic voltammetry
[b] All potentials are referred to SHE
[c] $\Delta E_p = E_{p,MCs} - E_{p,CMC}$
[d] Data obtained from RDE voltammetry.

Table 5.5 Number of electrons and selectivity for the two oxygen reduction steps in O_2 sat. 0.5 M KOH. Data obtained from LSV with RRDE .

	n_1[a]	X_{H2O2} (%)	n_1[b]	X_{H2O} (%)
N-MC1	2.6	69	3.5	74
N-MC2	2.6	67	3.6	81
N,S-MC1	2.5	75	3.2	60
N,S-MC2	2.6	70	3.3	66
S-MC1	2.4	80	3.4	70
MC	2.5	74	3.2	62

[a] Calculated at -0.3 V/SHE
[b] Calculated at -0.9 V/SHE

5.1.4 Mechanism for oxygen reduction in acid and alkaline solution

Given that ORR is an electron-proton coupled reaction, the change in O_2 reduction potential switching from acid to alkaline solution depends from a thermodynamic contribution due to H^+ concentrations, which involves a shift of almost 60 mV by unit of pH, and from a kinetic contribution, which depends on the chemical and morphological nature of the catalyst. The morphological nature of the carbon such as pore dimension and ramification was recently appointed to be responsible for promoting the 2e pathway to H_2O_2 [12], whereas the surface chemistry is responsible for the catalytic activity of the material [10]. Concerning the surface chemistry of the MCs prepared in this work, it may be asserted that both nitrogen and oxygen functional groups are determinant for the catalytic activity, in particular in acidic environment. In fact, even MC shows to be active towards ORR, although to a lesser extent with respect to N-MC-1 and N-MC-2. In literature it is reported that the presence of quinone [13] [14] and carboxyl groups [15] in the carbon material can promote ORR, at alkaline and acid pH, respectively. The commercial standard C-MC shows very similar O_2 reduction potential notwithstanding the pH; on the contrary, the O_2 reduction with the MCs prepared in this work show different performances, when the electrolyte is switched from acid to alkaline condition. In fact, at low pH all doped MCs show a peculiar catalytic activity where the nitrogen functional groups seem to play a pivotal role in determining the catalytic effect, and this is confirmed by the dependence of E_p with the nitrogen content. Conversely, at high pH, the catalytic activity is still present, but the performances of the different MCs become almost superimposable, notwithstanding the content of nitrogen or sulphur dopant, indicating a possible deactivation of the effects promoted by the functional groups (electron transfer mediation or electronic effect on the catalytic sites). With reference to N functional groups, it's demonstrated that pyridinic and graphitic N are the

most abundant ones in the doped material, but only the pyridinic groups, which lay at the step edges of the material, follows a pH chemistry. Therefore we may speculate that protonation/deprotonation of the pyridinic N may switch on and off the nitrogen doping contribution to the whole catalytic effect, possibly by influencing the adsorption/desorption of O_2 and its intermediates on the electrode surface. This may be in part explained on the basis of O_2 reduction mechanism: in fact, according to what reported by McCreery [1], when O_2 is not adsorbed on the electrode surface, the rate determining step (rds) is always the electron transfer (Eq. 5.6), notwithstanding the pH, this would be the case of C-MC:

$$O_2 + e^- \leftrightarrow O_2^{\bullet -}{}_{(ads)} \qquad \text{(Eq. 5.6)}$$

Conversely, when O_2 is adsorbed on the electrode surface, it get more easily reduced to $O_2^{\bullet -}$, which in turn remains adsorbed on the electrode surface and can be protonated by H_2O or H_3O^+. However, $HO_2^{\bullet -}{}_{(ads)}$ has a pK_a higher than $HO_2^{\bullet -}{}_{(aq)}$, so the protonation reaction is hindered at very basic pH (Eq. 5.7)[1]:

$$O_2^{\bullet -}{}_{(ads)} + H_2O \leftrightarrow HO_2^{\bullet -}{}_{(ads)} + OH^- \qquad \text{(Eq.5.7)}$$

In conclusion, doped MCs do not show different catalytic behaviour at basic pH because in this case (pH > 12) Eq. 5.6 is the rds; on the contrary at pH < 10 Equation 5.5 is the rds, and a different catalytic behaviour among each MCs can be observed

5.2 Electrochemical stability of N-MC1, S-MC1 and N,S-MC1

Electrochemical stability was evaluated in order to understand the chemical and structural modification occurring at three selected doped mesoporous carbon, i.e. N-MC1, N,S-MC1 and S-MC1, after an accelerated stress test (AST) was applied. The stability was evaluated with four different protocols, described in detail below, followed by ORR, SEM, XPS or Raman analysis in order to quantify the degradation of the materials.

5.2.1 AST1: 10000 potential cycles in Ar sat. 0.5 M H_2SO_4 or 0.5 M KOH solution

The first stress test protocol consists in applying 10000 potential cycles at 1 V/s in either 0.5 M H_2SO_4 or 0.5 M KOH. The cycling was carried out between -0.25 V/SCE and 1.0 V/SCE in the case of acid environment, and between -1.2 and 0.4 V/SCE in alkaline solution, that in both cases was saturated with Ar. Screening CVs were recorded before, during and after the test, to check the electrode response, at 200 or 100 mV/s. The measurements in H_2SO_4 and KOH were carried out in a three electrode system, in which the RE was a SCE, the CE was a Pt ring and the WE was a 1 cm^2 GC piece with a controlled-size exposed surface, usually equal to 0.8 cm^2, supported with conductive tweezers. A copper sheet assured proper electrical contact between tweezers and GC, and the total resistance of the system was measured to be comparable to a commercial GC electrode. This procedure was done in order to transfer the square GC into a XPS or SEM vacuum chamber, for the post degradation analysis. The ink used for this determination was prepared with 1.25 mg of catalyst and 1.25 mL of MilliQ H_2O, and it doesn't contain nafion, because this oligomer interferes with the XPS signal of the elements that have to be detected. For this reason, the GC was not polished to a mirror finish as in ORR characterization, but it was treated only with silicon carbide papers (P800 and P2000), in order to keep a rough surface which can maintain the mesoporous carbon attached to its surface.

In Figure 5.15 the CVs recorded before and after the AST1, at 200 mV/s, for N-MC1 (a), N,S-MC1 (b) S-MC1 (c) and MC (d) are reported. Two kinds of qualitative analysis are possible by simply observing their shape, regarding oxidation of carbon materials and the capacitive currents. In all the CVs a reversible signal associated to quinone/hydroquinone couple, is present, proportional to the degree of oxidation of the sample. In the case of S-MC1 it's made of two contributions, probably associated to different configuration of carbonyl groups. The increase of quinone groups is gradual during the AST, and is consistent with an increase of oxidation for all N-MC1, N,S-MC1, S-MC1 and MC. The MC shows a higher increase of this signal, and this is agreement with previous findings about increased resistance to oxidation caused by the N and S doping. The capacitive currents (background current) result almost unchanged before and after AST, indicating a substantial invariance of the electrochemical active area, which it is not strictly superimposable with the geometric or effective surface area. This might also be consistent with an unchanged pore structure of the samples, which means that no collapse phenomena occurred.

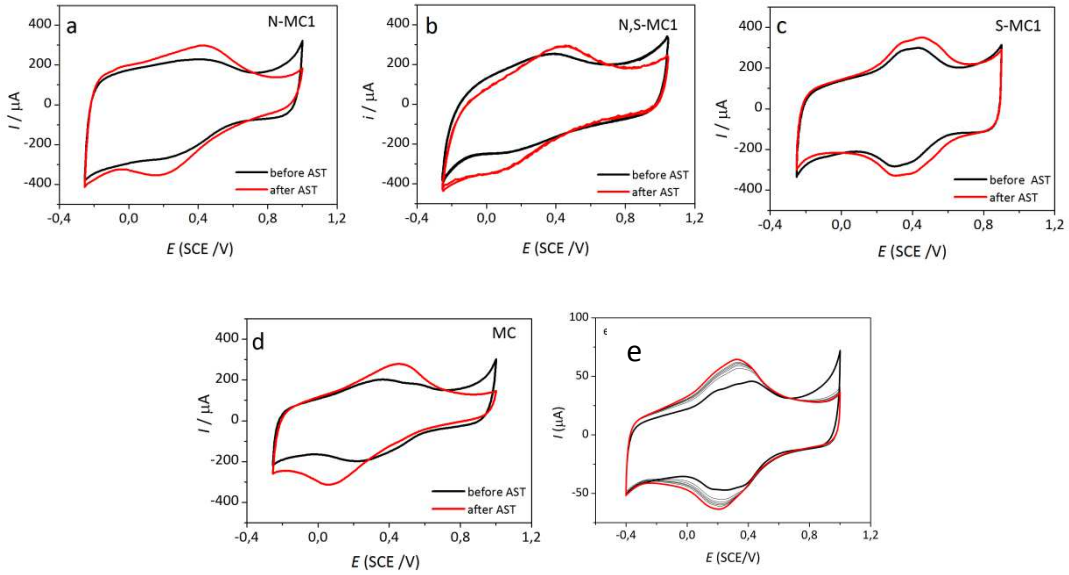

Figure 5.15 CVs recorded before (black) and after (red) the AST1, at 200 mV/s, for N-MC1 (a), N,S-MC1 (b) S-MC1 (c) and MC (d) in Ar sat. 0.5 M H_2SO_4

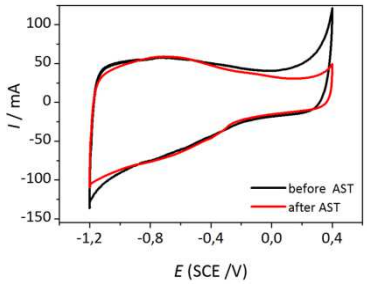

Figure 5.16 CVs recorded before (black) and after (red) the AST1, at 200 mV/s, for S-MC1 in 0.5 M KOH.

The AST tests in 0.5 M KOH in a potential window between -1.2 and 0.4 V/SCE were also performed. In this medium the reversible peak due to the oxidation/reduction of quinonic groups is missing, since the proton-electron coupled transfer is hindered at alkaline pH. Cyclic voltammetry for S-MC1 is reported as an example (Figure 5.16). After the AST, beside a different behaviour for hydrogen and oxygen discharge, there are no new visible peaks due to oxidation, and the capacitive current remains unchanged.

SEM investigations were carried out after AST to highlight changes in the electrode morphology due to carbon corrosion and pore collapse. After the AST (Figure 5.17 d, e and f), the MCs spheres apparently keep the same morphology and size distribution without evidences

of structure collapse, even though a slightly higher surface roughness may be observed (Figure 5.17f).

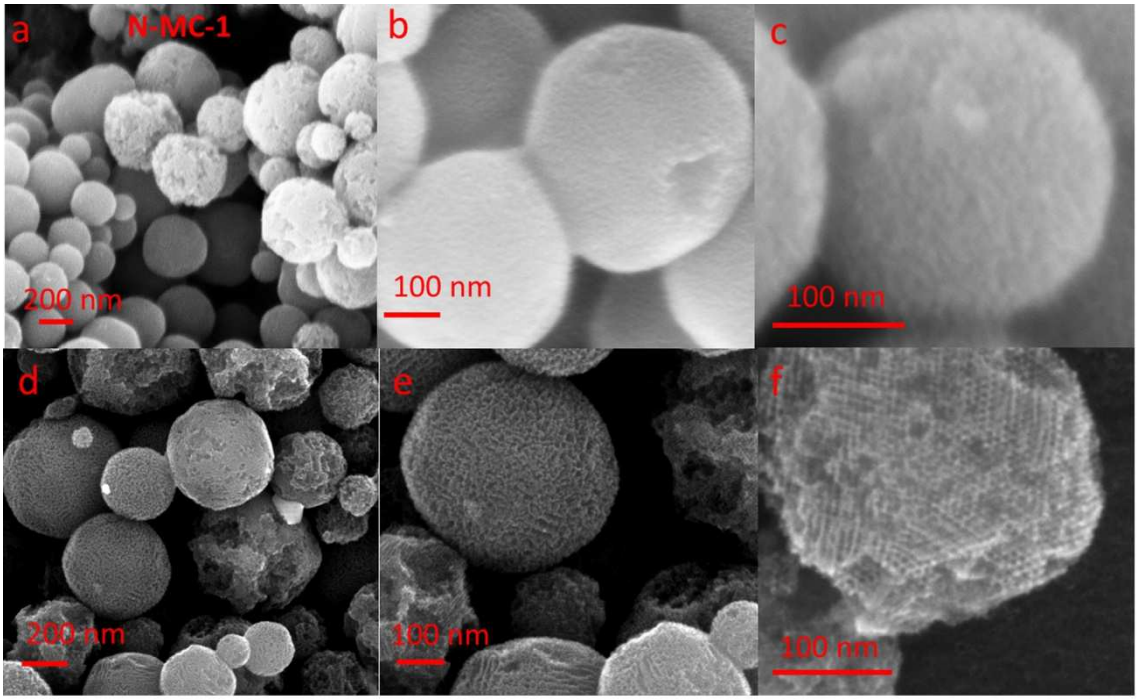

Figure 5.17 SEM analyses before (a, b, c) and after (d, e, f) AST1 in in Ar sat. 0.5 M H2SO4 for 1-NMC, 1-N,SMC and 1-SMC, respectively.

The collapse of the electrode structure is a well-established cause for increased mass-transport losses of cathodes suffering from carbon corrosion. However, a decrease of the electrodes porosity was not observed, even if this is not confirmed by BET, and this was confirmed by the presence of carved particles, where ordered pore structure becomes more exposed (Figure 5.17f). The determination of pore dimensions, performed after AST by graphical evaluation, confirmed a mean diameter of 3.5 nm as in the pristine sample.

In order to characterize the chemical modifications induced by the electrochemical oxidation process, XPS measurements for N-MC1, N,S-MC1 and S-MC1 after the AST were carried out. In the large range measurements, three main peaks were observed for N-MC1 and N,S-MC1 (i.e. C 1s, N 1s and O 1s), S-MC1 and N,S-MC1 show also the presence of the S 2p peak. The XPS analysis and signal identification were already exhaustively described in Chapter 4. In the C 1s and O 1s regions relative to N-MC1, N,S-MC1 or S-MC1 there are only slightly appreciable differences between the as prepared MCs and those after AST. XPS peaks and their deconvolution for N-MC1, before and after electrochemical cycles, are reported in Figure 5.18. In the cycled samples (Figure 5.18b) C sp^2 species seems to decrease, whereas at higher BE some

components from C=O bonds (BE = 289.8 eV) can also be singled out [16]. Similarly, the broad O 1s peak can be fitted with three components corresponding to carbonyl oxygen in esters or amides (531.1 eV); oxygen atoms in hydroxyls or ethers (532.4 eV) and carboxyl groups (533.9 eV) (Figure 5.18c)[17]. After the AST small changes in components ratios (carbonyl oxygen in esters or amides (531.1 eV); oxygen atoms in hydroxyls or ethers (532.4 eV) and carboxyl groups (533.9 eV)) where observed (Figure 5.18d); these findings are in agreement with the results obtained by Jarvi's group, which performed a systematic identification of the different oxidized groups generated on the carbon surface, through XPS investigation [18] and confirmed the outcomes from cyclic voltammetry, which state the increase of hydroquinonic groups.

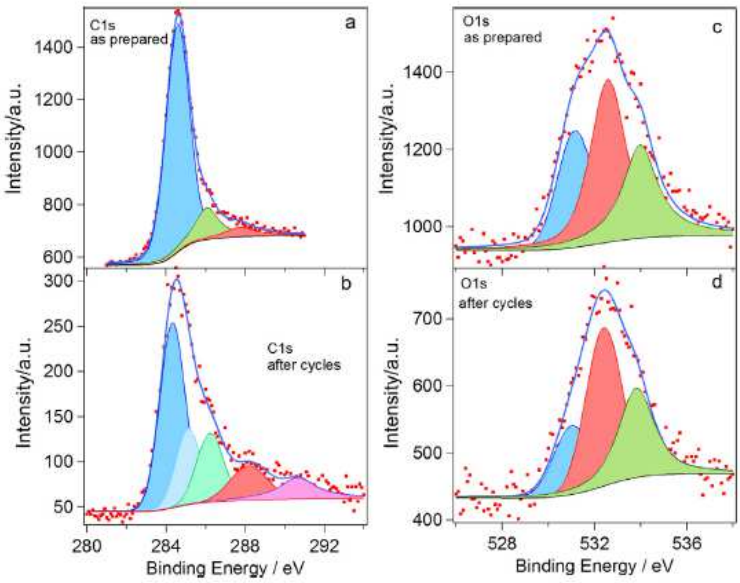

Figure 5.18 XPS detailed study of N-MC1 and signal deconvolution of (a) C 1s as prepared, (b) C 1s after 10000 cycles in 0.5 M H_2SO_4; (c) O 1s as prepared, and (d) O 1s after 10000 cycles in 0.5 M H_2SO_4. All spectra were recorded on nafion free samples.

In Figure 5.19 the XPS data in the N 1s region are reported. The fitting of the N 1s peak after normalization and a Shirley background subtraction was performed. In this way, a simple visual inspection of the figure allows to see the composition trend after the AST process in H2SO4 or KOH solutions with reference to the different N species. The N 1s XPS region of the as prepared N-MC1 is reported in Figure 5.19b; where the pyridinic, pyrrolic, graphitic and oxidized N species are indicated. In Figure 5.19 a and a' the N1s peaks acquired after the AST in H2SO4 for N-MC1 drop-casted on a GC support, in the presence and in the absence of nafion, as binder agent, are reported. After the AST, the pyridinic component strongly decreases, the pyrrolic one completely disappears, whereas there is a strong enhancement of the graphitic and oxidized N

components indicated as -NOx. It is worth noting that the presence of nafion leads to an enlargement of the N 1s peak, as can be clearly seen in Figure 5.19a, and leads to a shift of the graphitic component to about 400.0 eV. This effect has already been observed by other authors in the case of fluorinated, nitrogen doped, carbon nanotubes [19]. The higher value of the FWHM and slightly different shape of the peak can be caused by an inhomogeneous charging of the surface after impregnation with nafion, which is not an electronic conductor. Figure 5.19c reports the N 1s XPS region of N-MC-1 after ten thousands of voltammetric cycles in a 0.5 M KOH solution. Unlike what already observed in acidic solution, the nitrogen species appear to be more stable, so that pyridinic and pyrrolic components decrease, but much less, than in acidic solution. In addition, N-graphitic group component slightly increases along with oxidized nitrogen. These findings are in agreement to what already observed from CV after AST in alkaline electrolyte. In Figure 5.19h the effect of the AST process for the nitrogen functional groups in both alkaline and acidic electrolyte are easily sketched. In the histograms, three columns for each electrolyte and the as prepared are considered: one for N graphitic groups (green dense horizontal lines), the second for pyridinic + pyrrolic groups (red dense vertical lines) and a third for all oxidized nitrogen species (blue solid). It is clear that oxidized nitrogen species column increases sensitively when AST was performed in H_2SO_4 solution, whereas it remains almost unchanged when AST was carried out in KOH. A similar conclusion can be drawn for pyridinic + pyrrolic group columns, since the percentage value of pyridinic + pyrrolic groups meagrely decreases when the sample was treated in alkaline solution, but evidently decreases when the AST was performed in acidic solution (Figure 5.19h, red dense vertical lines). Therefore, it is evident that the pyridinic and pyrrolic groups are electrochemically unstable at least in acidic electrolyte, where graphitic and oxidized nitrogen groups are formed in place of pyridinic and pyrrolic ones. It is worth noting, that the N-graphitic component is the only N-species that is virtually unchanged or even increased after electrochemical cycles showing an incomparable electrochemical stability with respect to the other nitrogen groups (Figure 5.19h, green dense horizontal lines). To the best of our knowledge, the superior electrochemical stability of graphitic functional groups was never observed in literature, however, the superior thermal stability of N-graphitic groups with respect to other N groups was already observed in the case of N-doped HOPG after surface thermal treatment in UHV conditions up to 750 °C [16]. Furthermore, similar evidences were observed in doped graphene [20], carbon nanotubes [21] and amorphous carbon [22], where the superior thermal stability of N-graphitic functional groups was ascribed to a greater thermodynamic stability as it can be deduced by considering that in graphitic defects, N atoms can coordinate the highest number of other C atoms.

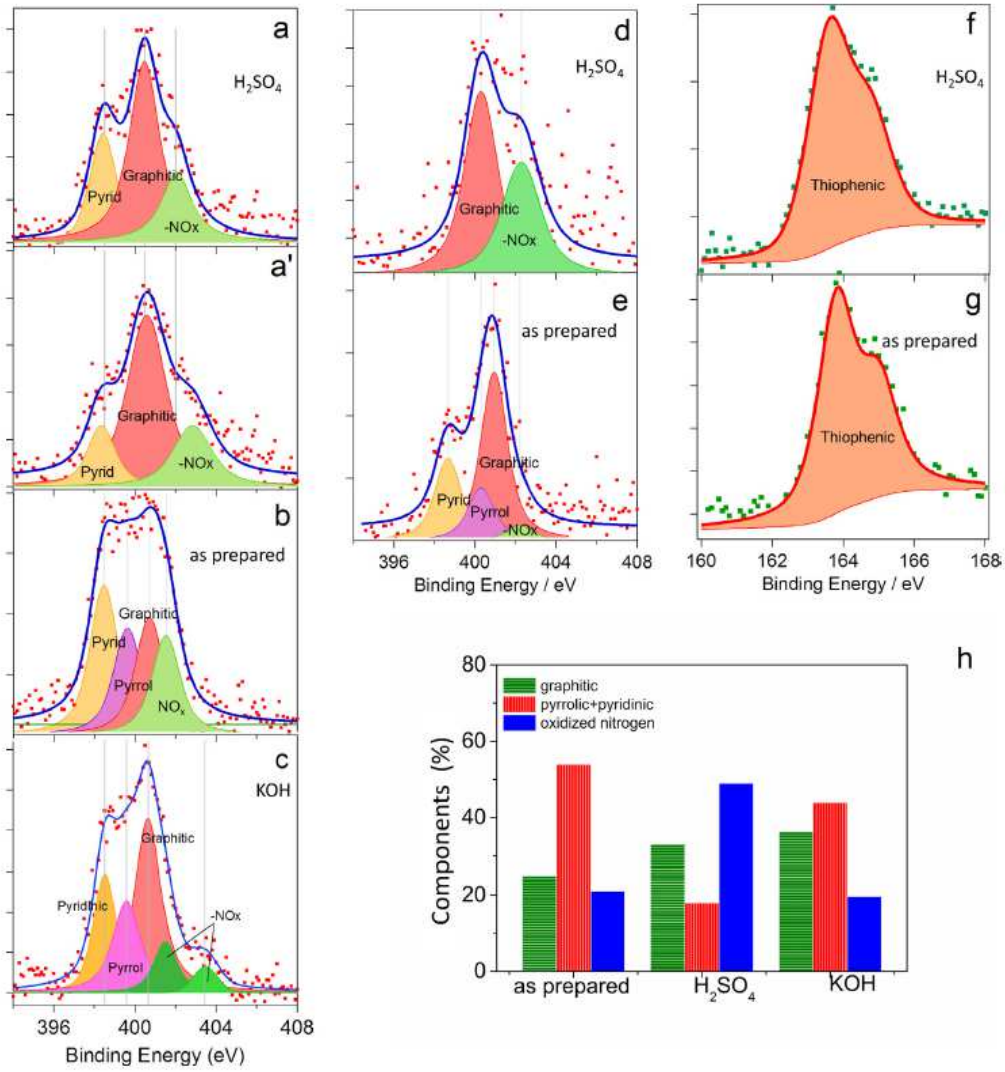

Figure 5.19 N 1s XPS region of (a,a') N-MC1 after 10000 cycles in 0.5 M H2SO4 (b) N-MC1 as prepared, (c) N-MC1 after 10000 cycles in 0.5 M KOH, (d) N,S-MC1 after 10000 cycles in 0.5 M H2SO4, (e) N,S-MC-1 as prepared. S 2p XPS region of S-MC-1 (f) after 10000 cycles in 0.5 M H2SO4 and (g) as prepared. (h) Comparison of nitrogen component changes in N-MC-1 before and after AST in different environments.

A very similar behaviour was observed in the case of N,S-MC1 sample (cycles performed in 0.5 M H2SO4 solution), Figure 5.19d. If we compare the N 1s XPS region between the as prepared N,S-MC-1 (Figure 5.19e) and the oxidized one (Figure 5.19d), it is evident that the pyridinic and the pyrrolic components completely disappear, whereas the graphitic component shifts at 400.0 eV. Also in this case strong components accounting for N oxidized species (NOx) are present. The S 2p photoemission region of the as prepared S-MC-1 (Figure 5.19g) and N,S-MC1 (not reported here) can be fitted by a single component centred at 163.9 eV, which represents the sulphide -C-S-C, often referred as thiophenic-like units [7]. A very similar S 2p XPS was recorded for S-MC1 after AST (cycles performed in 0.5 M H_2SO_4 solution), attesting a

substantial resistance of thiophenic like groups to degradation, at least in the adopted operational conditions (Figure 5.19f). In fact, oxidized sulphur was not detected, probably because of low thermodynamic stability of such species, as observed in literature.

5.2.2 AST2: 4000 potential cycles in Ar sat. 0.5 M H_2SO_4 and 0.5 M KOH solution

This procedure was applied in order to check the electrode performance after a less strong test than the previous one. In this case the ink was made of mesoporous carbon suspended in a solution of nafion and MilliQ H_2O, and was drop-casted on the surface of a commercial GC electrode, 3 mm diameter. The test was carried in either 0.5 M H_2SO_4 or 0.5 M KOH, and the performances toward ORR were checked before and after the test.

Figure 5.20 reports the background LSVs at RDE before and after the AST for N-MC1 and S-MC1, (Figure 5.20 a and b, respectively). It is worth noting that background currents of both doped MCs normalized by the geometric surface area, show a lower overvoltage versus hydrogen evolution with respect to the as prepared catalysts (Figure 5.20 a and b, dashed lines). This behaviour is also observed when a carbon electrode is exposed to Ar ion sputtering, laser ablation or plasma treatments [16]. The reduction of the working potential window is caused by microstructural damages (exposure of clean edge plane sites) and surface oxidation [23][24]. In this case, the effect is plainer for N-MC1, where the H2 discharge shift is 250 mV toward more positive potential, i.e. five times with respect to what observed for S-MC1. Figure 5.20 c and d report the LSVs recorded at RDE in the presence of O2 before (solid line) and after (dashed line) the AST for N-MC1 and S-MC1 modified GC electrodes, respectively. It may be observed that, after the AST, there is a shift of the onset reduction potential toward more negative values with respect to the as prepared catalyst, but also a decrease of the limiting current, and this is particularly evident in N-MC1 (Figure 5.20c). Figure 5.20 e and f report also the LSVs recorded at RDE in the presence of O2 before (solid line) and after (dashed line) the AST for N-MC1 and S-MC1 modified GC electrodes in 0.5 M KOH, respectively. In alkaline electrolyte, the LSVs for all the investigated MCs are composed of two reduction steps of almost the same height, where at first step O_2 is reduced to H_2O_2, which is further reduced to H_2O in the second step at far more negative potentials [25]. In the case of S-MC1 the loss in term of limiting current and catalytic activity is negligible after the AST. Conversely, for N-MC1 the LSV is slightly shifted toward more negative potentials, but the limiting currents remain almost unchanged after AST (Figure 5.20e).

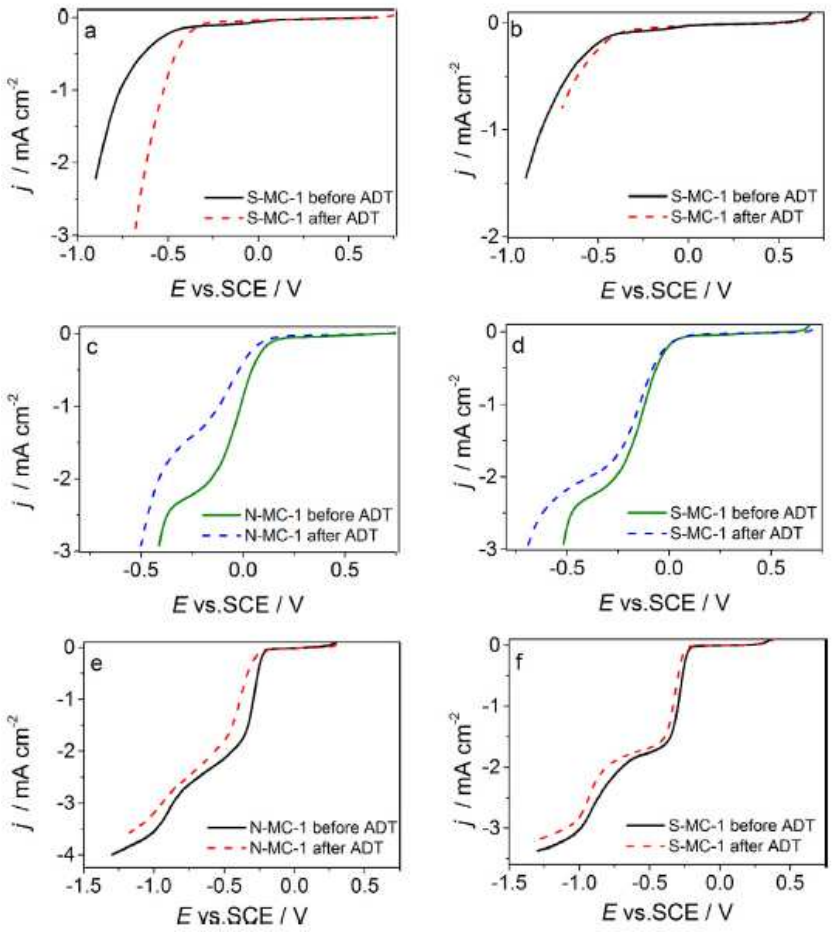

Figure 5.20 LSV at RDE before (solid lines) and after (dashed lines) AST of: (a) N-MC-1 and (b) S-MC-1 modified GC electrode in 0.5 M H_2SO_4, (c) N-MC-1 and (d) S-MC-1 modified GC electrode in O_2 saturated 0.5 M H_2SO_4, (e) N-MC-1 and (f) S-MC-1 modified GC electrode in O_2 saturated 0.5 M KOH. ω = 1600 rpm, v = 5 mV/s.

The SEM and Raman measurements pointed out the increase of the MC surface after AST, which was appointed to surface carbon corrosion and small carbon fragment detachment. However, the morphology and the porosity of the carbon substrate were observed to be substantially preserved. It must be stressed, that the increase of carbon surface does not correspond directly to the increase of the electrochemical active surface or, in any case, to the increase of the sites active toward ORR. Therefore, the observed decrease of limiting currents in Figure 5.20 c-f should be related to a decrease of the ORR active sites. In fact, the findings in both 0.5 M H2SO4 and KOH appear to be totally in agreement to what observed by XPS analysis, where it was highlighted that nitrogen functional groups are more labile than thiophenic groups and undergo electrochemical oxidation to a different extent in both electrolytes, resulting in a decrease of catalytic performances and surface active sites. In particular, pyridinic groups,

usually appointed as the most active sites for ORR, were observed to decrease after AST. In 0.5 M KOH S-MC1 and, to a lesser extent, N-MC1 show to mostly preserve their catalytic performances, in line with the higher stability of the N and S functional groups in alkaline electrolyte with respect to acidic electrolyte during AST. However, it is clear that even though N-MC1 is more active to ORR with respect to S-MC1, it suffers higher catalytic performances loss than the sulphur doped one.

5.2.3 AST3: 3 hours chronoamperometry with RDE in O_2 sat 0.5 M H_2SO_4 and 0.09 M Na_2SO_4 + 0.01 M H_2SO_4

In this test a three hours long chronoamperometry was carried out with RDE at 1600 rpm in O_2 sat. 0.5 M H_2SO_4 in order to evaluate the degradation during operation. A constant potential was applied to the WE, and it was selected for all the measurements from the CV in steady condition, exactly 500 mV after the ORR peak. In this situation the current recorded at the RDE should be constant during the whole test, so a progressive decrease in its value corresponds to a degradation of the catalyst. The ink in this case was made by suspending the catalyst in a solution of MilliQ H_2O and nafion. The polymer in this test is fundamental, because of the stress experimented by the catalyst which can determine its untimely detachment from GC surface under dynamic conditions.

In Figure 5.21 the chronoamperometries recorded on N-MC1, N,S-MC1 and S-MC1 are reported. The degradation is evaluated by the current profile slope versus time: the higher the slope (i.e. the current decrease), the higher the degradation. In 0.5 M H_2SO_4 the most stable catalyst is N-MC1, given that it shows the least current decrease. On the contrary, the highest degradation occurred for S-MC1. The stability of N,S-MC1 is between N-MC1 and N,S-MC1. So, in operating conditions, the stability has an opposite trend compared to what observed in Ar sat. solution. XPS analyses were not carried out after the stability test, but it's predictable that sulphur groups are less stable and tend to give oxidized species that reduce the overall stability and/or the activity. The same test was repeated also in higher pH solution, O_2 sat. 0.09 M Na_2SO_4 + 0.01 M H_2SO_4 and the same stability trend was highlighted (N-MC1>N,S-MC1>S-MC1), but the currents were much lower.

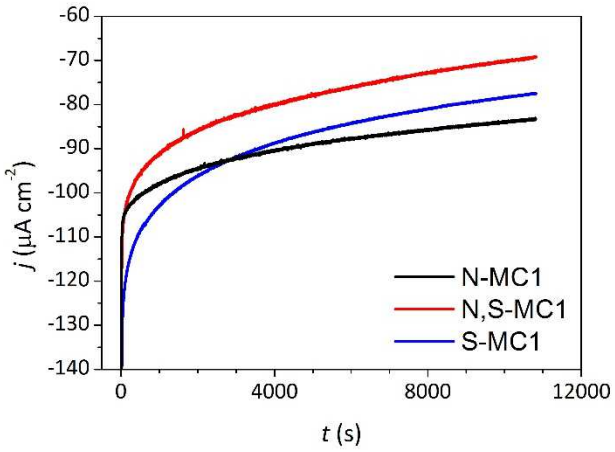

Figure 5.21 Chronoamperometry in O_2 sat 0.5 M H_2SO_4 for N-MC1 (black), N,S-MC2 (red) and S-MC1 (blue). Rotation rate: 1600 rpm.

5.2.4 AST4: 10000 potential cycles in Ar sat. 0.1 M $HClO_4$ solution. A Raman-Electrochemistry coupled examination

The in-situ Raman experiments were carried out in a homemade spectroelectrochemical cell, which consists of a teflon cell body inserted in a quartz containing electrolyte cuvette, reported in Figure 5.22. The teflon body is properly manufactured in order to assure a tight sealing from the cuvette to avoid any loose between the two parts. The working electrode was a 6 mm diameter GC disk embedded in the teflon support; a copper wire and a silver conducting resin assured the electric conduction out of the cell. The counter electrode was a Pt ring positioned in front of the GC electrode. The reference electrode was a silver/silver chloride wire inserted in a saturated KCl solution, which is contained in a small teflon cannula ($Ø_{int}$ = 0.8 mm) ending with a small ceramic septum. The homemade Ag/AgCl/KCl electrode was calibrated before each experiment versus a commercial SCE. Two small holes on the top side on the Teflon body allow the insertion of two tiny Teflon or steel cannula, which assured the inlet and the outlet of the cell. The electrolyte solution was refilled and removed by means of a syringe connected to the inlet cannula through a suitable adapter. The same system can be employed for bubbling Ar or O_2 depending on the type of experiment. Raman scattering experiments were carried out with a home-built Macro-Raman setup, already described in previous publications [26][27]. The excitation wavelength was 514 nm. The size of the laser spot at the sample was about 3 mm by 80 mm and the power at the sample about 12 mW (Intensity = 5 W/cm^2). Cyclohexane was used as a frequency standard for the calibration of the Raman shift. Every spectrum was acquired as the average of 10 spectra with 10 second integration time and on the same point of the sample throughout the AST procedure. Macro-Raman configuration is preferable to Micro-Raman

configuration for this type of studies, since it provides a much larger spatial average. However, test measurements were recorded also with a home-built Micro-Raman setup [28][29][30] operating at 514 nm with a 20x objective and showed that also in this configuration the spectra do not depend on the sampled area. In the *in situ* Raman-AST experiments, ten thousand voltammetric cycles were performed between -0.25 and 1.00 V vs. SCE at a scan rate of 1 V/s, in 0.1 M $HClO_4$. The Raman spectra were recorded every five hundred electrochemical cycles. $HClO_4$ was preferred to H_2SO_4, since the latter has Raman bands superimposed to the MCs spectra; moreover H_2SO_4 bands are sensitive to possible pH variation of the solution during AST. For controlling the modification in the voltammetric behaviour, a cyclic voltammetry was recorded every 500 cycles in the same range, but at a lower scan rate of 100 mV/s.

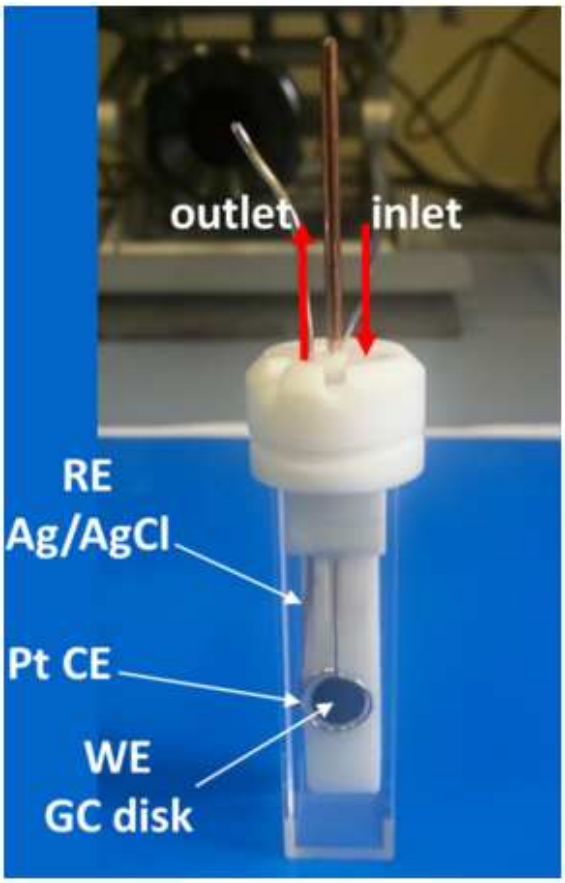

Figure 5.22 Spectroelectrochemical cell employed in Raman-electrochemistry coupled examination.

Figure 5.23a shows the spectrum of the empty Quartz cuvette with the typical band at 807 cm^{-1} (green line); the spectrum of the Quartz cuvette filled with the 0.1 M $HClO_4$ electrolyte solution (red line), with the characteristic band at 930 cm^{-1} and the spectrum of N-MC1 acquired in situ (black line).

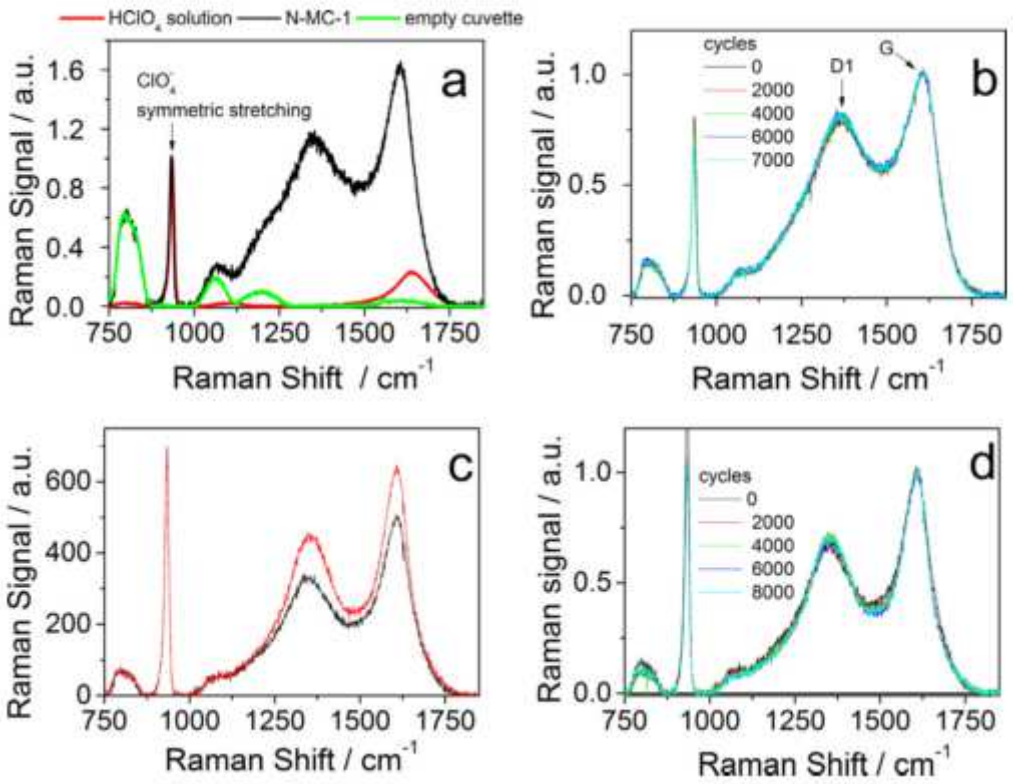

Figure 5.23 a) Raman spectra for N-MC1 (black), 0.1 M $HClO_4$ (red) and empty quartz cuvette (green); b) N-MC1 spectra normalised to the G band; c) MC non-normalized spectra evolution during AST; d) MC spectra normalized to the G band during AST.

The in situ Raman acquisitions were performed during the AST tests, by drop-casting the MC inks over the working electrode of the spectroelectrochemical cell in Figure 5.22. Therefore, N-MC1 spectra in Figure 5.23a contains also the feature due to the electrolyte and the quartz cuvette. All the spectra were normalized to the 930 cm^{-1} band for better comparing changes in band intensity. In the case of the quartz cuvette spectra acquired in the absence of $HClO_4$ electrolyte, the normalization was performed with respect to the 807 cm^{-1} band in the N-MC1 spectrum. All spectra baseline have been corrected prior to normalization. In the spectrum of $HClO_4$, the band at 930 cm^{-1} corresponds to the symmetric stretching of the ClO_4^- and the band at 1640 cm^{-1} is the OH bending of water [31]. The Raman spectrum of quartz is discussed in Ref [32][33]. The spectrum of N-MC1 is mainly characterized by the D1 (disorder) and G (graphitic) bands located at approximately 1350 and 1600 cm^{-1}, respectively. The spectrum is superimposed to the bands of quartz, that originates the shoulders at 1064 and 1180 cm^{-1}, and to the solution bands: in particular, note that the spectrum of water is superimposed to the G band, influencing its intensity and/or its spectral position (Figure 5.23). A detailed analysis of the structural information that can be deduced from the Raman spectra of MCs has been already carried out

in another paper [25]: it revealed that MCs are mainly composed by a mixture of nano-crystalline graphite and amorphous Carbon. Figure 5.23b shows the variation of the Raman spectra of N-MC-1 during AST, normalized to the G band; the normalization is necessary to better distinguish the changes in the spectrum shape. Even without further elaboration to remove the quartz and solution contributions, it is clear that the Raman spectrum does not change shape after AST. This is true for all MCs. Further information can be achieved by looking at non-normalized spectra: the spectra of MC, before and after AST are shown in Figure 5.23c. In this case, the perchlorate band exhibits only a very low intensity variation (around 4%) during AST; on the other hand the MC Raman spectrum rises in intensity by about 35% and its shape does not change (see Figure 5.23d where data are normalized to the G band). It was checked as well that the electrode used as support (glassy carbon) does not exhibit this effect and that the spectrum of the $HClO_4$ solution was the same before and after the AST: this rules out modifications of perchlorate concentration and the possible effect of pH changes either on the perchlorate or on the water Raman bands. The previous considerations indicate that the increase of the MC spectrum signal is not due to experimental artefacts. This effect is present also in other MCs, in particular S-MC1. The fact that the shape of Raman spectra of MCs does not show significant changes during AST suggests that the structural composition is not influenced by the durability tests: therefore we expect the amorphous to graphitic ratio to be very similar before and after the electrochemical cycles. It's mentioned that Raman studies of carbon electrode durability have been performed in the literature by Zana and Hara [34]: they showed that in some cases, the degradation produces significant effects on Raman spectra. A comparison with the literature is, however, rather difficult due the different experimental conditions adopted. Finally, the second effect we mentioned, that is, the rise in the intensity of the Raman spectrum during AST, can be interpreted as an increase in the surface area, without structural modifications detectable by Raman spectroscopy: we speculate that this might be due to swelling or corrugation of the sample. The increased corrugation of the sample after AST was also observed by SEM images, and may be the results of surface carbon corrosion and detachment of small carbon fragments, which lead to a carved structure. In fact, in the presence of water, carbon can be consumed through the electrochemical oxidation to carbon dioxide (eq. 5.8) or the heterogeneous water–gas reaction (eq. 5.9):

$$C + 2H_2O \rightarrow CO_2 + 4H^+ + 4e^- \qquad \text{(Eq. 5.8)}$$

$$C + H_2O \rightarrow CO + H_2 \qquad \text{(Eq. 5.9)}$$

The electrochemical properties of differently doped mesoporous carbons (Sections 5.1.2 and 5.1.3) are described in reference [25]. The chemical and electrochemical stability of the same materials is described in reference [35].

Bibliography

[1] H.-H. Yang, R.L. McCreery, Elucidation of the Mechanism of Dioxygen Reduction on Metal-Free Carbon Electrodes, J. Electrochem. Soc. 147 (2000) 3420. doi:10.1149/1.1393915.

[2] M. Seredych, D. Hulicova-Jurcakova, G.Q. Lu, T.J. Bandosz, Surface functional groups of carbons and the effects of their chemical character, density and accessibility to ions on electrochemical performance, Carbon N. Y. 46 (2008) 1475–1488. doi:10.1016/j.carbon.2008.06.027.

[3] G. Lota, B. Grzyb, H. Machnikowska, J. Machnikowski, E. Frackowiak, Effect of nitrogen in carbon electrode on the supercapacitor performance, Chem. Phys. Lett. 404 (2005) 53–58. doi:10.1016/j.cplett.2005.01.074.

[4] M.H. V Huynh, T.J. Meyer, Proton-coupled electron transfer, Chem. Rev. 107 (2007) 5004–5064. doi:10.1021/cr0500030.

[5] X. Liu, H. Zhu, X. Yang, One-step synthesis of dopamine-derived micro/mesoporous nitrogen-doped carbon materials for highly efficient oxygen-reduction catalysts, J. Power Sources. 262 (2014) 414–420. doi:10.1016/j.jpowsour.2014.04.023.

[6] L. Qu, Y. Liu, J.B. Baek, L. Dai, Nitrogen-doped graphene as efficient metal-free electrocatalyst for oxygen reduction in fuel cells, ACS Nano. 4 (2010) 1321–1326. doi:10.1021/nn901850u.

[7] H. Wang, X. Bo, Y. Zhang, L. Guo, Sulfur-doped ordered mesoporous carbon with high electrocatalytic activity for oxygen reduction, Electrochim. Acta. 108 (2013) 404–411. doi:10.1016/j.electacta.2013.06.133.

[8] S.-A.A. Wohlgemuth, R.J. White, M.-G.G. Willinger, M.-M.M. Titirici, M. Antonietti, A one-pot hydrothermal synthesis of sulfur and nitrogen doped carbon aerogels with enhanced electrocatalytic activity in the oxygen reduction reaction, Green Chem. 14 (2012) 1515–1523. doi:10.1039/c2gc35309a.

[9] M. Seredych, K. Lászlõ, T.J. Bandosz, Sulfur-Doped Carbon Aerogel as a Metal-Free Oxygen Reduction Catalyst, ChemCatChem. 7 (2015) 2924–2931. doi:10.1002/cctc.201500192.

[10] G. Tuci, C. Za, A. Rossin, A. Milella, L. Luconi, M. Innocenti, L.T. Phuoc, C. Duong-viet, C. Pham-huu, G. Giambastiani, Chemically Functionalized Carbon Nanotubes with Pyridine Groups as Easily Tunable N - Decorated Nanomaterials for the Oxygen Reduction Reaction in Alkaline Medium, (2014).

[11] C. Domínguez, F.J. Pérez-Alonso, S.A. Al-Thabaiti, S.N. Basahel, A.Y. Obaid, A.O. Alyoubi, J.L. Gómez De La Fuente, S. Rojas, Effect of N and S co-doping of multiwalled carbon nanotubes for the oxygen reduction, Electrochim. Acta. 157 (2015) 158–165. doi:10.1016/j.electacta.2015.01.031.

[12] J. Park, Y. Nabae, T. Hayakawa, M. Kakimoto, Highly Selective Two-Electron Oxygen Reduction Catalyzed by Mesoporous Nitrogen-Doped Carbon, (2014).

[13] N. Alexeyeva, E. Shulga, V. Kisand, I. Kink, K. Tammeveski, Electroreduction of oxygen on nitrogen-doped carbon nanotube modified glassy carbon electrodes in acid and alkaline solutions, J. Electroanal. Chem. 648 (2010) 169–175.

doi:10.1016/j.jelechem.2010.07.014.

[14] I. Kruusenberg, N. Alexeyeva, K. Tammeveski, The pH-dependence of oxygen reduction on multi-walled carbon nanotube modified glassy carbon electrodes, Carbon N. Y. 47 (2009) 651–658. doi:10.1016/j.carbon.2008.10.032.

[15] H.-J. Zhang, H. Li, X. Li, B. Zhao, J. Yang, Electrocatalysis of oxygen reduction on carbon nanotubes with different surface functional groups in acid and alkaline solutions, Int. J. Hydrogen Energy. 39 (2014) 16964–16975. doi:10.1016/j.ijhydene.2014.08.093.

[16] M. Favaro, L. Perini, S. Agnoli, C. Durante, G. Granozzi, A. Gennaro, Electrochemical behavior of N and Ar implanted highly oriented pyrolytic graphite substrates and activity toward oxygen reduction reaction, Electrochim. Acta. 88 (2013) 477–487. doi:10.1016/j.electacta.2012.10.100.

[17] S. Kundu, T.C. Nagaiah, W. Xia, Y. Wang, M. Bron, W. Schuhmman, M. Muhler, Thermal Stability and Reducibility of Surface Oxygen and Nitrogen Functional Groups on Carbon Nanotubes and Their Application in, 481 (2008) 16869–16869.

[18] K.H. Kangasniemi, D.A. Condit, T.D. Jarvi, Characterization of Vulcan Electrochemically Oxidized under Simulated PEM Fuel Cell Conditions, J. Electrochem. Soc. 151 (2004) E125. doi:10.1149/1.1649756.

[19] L.G. Bulusheva, A.V. Okotrub, A.G. Kudashov, N.F. Yudanov, E.M. Pazhetnov, A.I. Boronin, O.G. Abrosimov, N.A. Rudina, Fluorination of multiwall nitrogen-doped carbon nanotubes, Russ. J. Inorg. Chem. 51 (2006) 613–618. doi:10.1134/S0036023606040176.

[20] W. Ding, Z. Wei, S. Chen, X. Qi, T. Yang, J. Hu, D. Wang, L.J. Wan, S.F. Alvi, L. Li, Space-confinement-induced synthesis of pyridinic- and pyrrolic-nitrogen- doped graphene for the catalysis of oxygen reduction, Angew. Chemie - Int. Ed. 52 (2013) 11755–11759. doi:10.1002/anie.201303924.

[21] R. Arrigo, M. Hävecker, R. Schlögl, D.S. Su, Dynamic surface rearrangement and thermal stability of nitrogen functional groups on carbon nanotubes, Chem. Commun. (2008) 4891–4893. doi:10.1039/b812769g.

[22] K. Stańczyk, R. Dziembaj, Z. Piwowarska, S. Witkowski, Transformation of nitrogen structures in carbonization of model compounds determined by XPS, Carbon 33 (1995) 1383–1392. doi:10.1016/0008-6223(95)00084-Q.

[23] Q. Chen, G.M. Swain, Structural Characterization, Electrochemical Reactivity, and Response Stability of Hydrogenated Glassy Carbon Electrodes, Langmuir 14 (1998) 7017–7026. doi:10.1021/la980907z.

[24] O. Dumanli, A.N. Onar, Activation of glassy carbon electrodes by photocatalytic pretreatment, Electrochim. Acta 54 (2009) 6438–6444. doi:10.1016/j.electacta.2009.05.096.

[25] V. Perazzolo, C. Durante, R. Pilot, A. Paduano, J. Zheng, G.A. Rizzi, A. Martucci, G. Granozzi, A. Gennaro, Nitrogen and sulfur doped mesoporous carbon as metal-free electrocatalysts for the in situ production of hydrogen peroxide, Carbon 95 (2015) 949–963. doi:10.1016/j.carbon.2015.09.002.

[26] R. Pilot, A. Zoppi, S. Trigari, F.L. Deepak, E. Giorgetti, R. Bozio, Wavelength dispersion of the local field intensity in silver-gold nanocages., Phys. Chem. Chem. Phys. 17 (2015)

7355–65. doi:10.1039/c4cp04453c.

[27] V. Weber, A. Feis, C. Gellini, R. Pilot, P.R. Salvi, R. Signorini, Far- and near-field properties of gold nanoshells studied by photoacoustic and surface-enhanced Raman spectroscopies, Phys. Chem. Chem. Phys. 17 (2015) 21190–21197. doi:10.1039/C4CP05054A.

[28] I. Ros, T. Placido, V. Amendola, C. Marinzi, N. Manfredi, R. Comparelli, M. Striccoli, A. Agostiano, A. Abbotto, D. Pedron, R. Pilot, R. Bozio, SERS Properties of Gold Nanorods at Resonance with Molecular, Transverse, and Longitudinal Plasmon Excitations, Plasmonics. (2014) 1–13. doi:10.1007/s11468-014-9669-4.

[29] G. Giallongo, R. Pilot, C. Durante, G.A. Rizzi, R. Signorini, R. Bozio, A. Gennaro, G. Granozzi, Silver Nanoparticle Arrays on a DVD-Derived Template: An easy&cheap SERS Substrate, Plasmonics. 6 (2011) 725–733. doi:10.1007/s11468-011-9256-x.

[30] G. Giallongo, C. Durante, R. Pilot, D. Garoli, R. Bozio, F. Romanato, A. Gennaro, G.A. Rizzi, G. Granozzi, Growth and optical properties of silver nanostructures obtained on connected anodic aluminum oxide templates., Nanotechnology. 23 (2012) 325604. doi:10.1088/0957-4484/23/32/325604.

[31] C.I. Ratcliffe, D.E. Irish, Vibrational spectral studies of solutions at elevated temperatures and pressures. 5. Raman studies of liquid water up to 300.degree.C, J. Phys. Chem. 86 (1982) 4897–4905. doi:10.1021/j100222a013.

[32] R.J. Piffath, S. Sass, An Infrared and Raman Study of Benzylidenemalononitriles, Appl. Spectrosc. 26 (1972) 256–261. doi:10.1366/000370272774352344.

[33] J.D. Masso, C.Y. She, D.F. Edwards, Effects of inherent electric and anisotropic forces on raman spectra in ??-quartz, Phys. Rev. B. 1 (1970) 4179–4181. doi:10.1103/PhysRevB.1.4179.

[34] M. Hara, M. Lee, C.H. Liu, B.H. Chen, Y. Yamashita, M. Uchida, H. Uchida, M. Watanabe, Electrochemical and Raman spectroscopic evaluation of Pt/graphitized carbon black catalyst durability for the start/stop operating condition of polymer electrolyte fuel cells, Electrochim. Acta. 70 (2012) 171–181. doi:10.1016/j.electacta.2012.03.043.

[35] V. Perazzolo, E. Grądzka, C. Durante, R. Pilot, N. Vicentini, G.A. Rizzi, G. Granozzi, A. Gennaro, Chemical and Electrochemical Stability of Nitrogen and Sulphur Doped Mesoporous Carbons, Electrochim. Acta, 197 (2016) 251-262.

Chapter 6

Pt Nanoparticles on N- and S-doped Mesoporous Carbon

In this chapter three representative mesoporous carbon samples are selected and modified with Pt Nanoparticles (NPs). Different Pt NPs deposition protocols are tested and the obtained catalysts are characterized via TEM and XPS. Electrochemical performance toward oxygen reduction is evaluated in 0.5 M H_2SO_4 and 0.1 M $HClO_4$. Electrochemical stability is evaluated with two different stress tests: one specific for Pt stability, and the other for both C and Pt degradation.

6.1 Platinum Nanoparticles on N-MC

An investigation of Pt Nanoparticles deposition on nitrogen doped mesoporous carbon obtained from pyrolysis of phenanthroline and silica P200 at 750 °C was conducted. This sample was labelled N-MC1 in the previous chapters, in the following description it will be referred simply as N-MC, given that the sample N-MC2 obtained from carbazole is not used in this part of the research.

6.1.1 Experimental conditions

Preliminary electrochemical results were obtained with a non-optimized protocol. The glassware was cleaned with Aqua Regia solution for three hours, then well rinsed with bi-distilled water. The ink was prepared suspending 1.25 mg of catalyst in 1.25 mL of MilliQ H_2O containing 6%$_{vol}$ of Nafion, sonicated in ultrasonic bath for 20 minutes. The catalyst layer was prepared by

drop-casting the ink on a clean 3 mm diameter GC surface, in order to realize a Pt loading equal to 40 μg/cm^2 and dried overnight in static condition. The electrochemical measurements were conducted in 0.5 M H_2SO_4 in Ar sat. or O_2 sat. solutions in the case of ECSA and performance determination, respectively. The WE was a clean GC disk modified with catalyst layer, the RE was a sat. SCE inserted in a jacket filled with sat. KNO_3 to hinder chloride contamination, the CE was a Pt ring. The ECSA was obtained by CV in Ar sat. 0.5 M H_2SO_4, from H adsorption and desorption signals. ORR performance were evaluated with LSV in the potential range between 0.74 and -0.25 V/SCE in the cathodic direction, at 5 mV/s and 1600 rpm.

6.1.2 Deposition investigation: chemical and solid state reduction of Pt on N-MC

Pt nanoparticles were deposited on N-MC from different Pt salts and by two different ways: chemical deposition and solid state deposition. Initially around 40 mg of N-MC were suspended in 15 mL of a proper solvent (Milli Q water in the case of chemical reduction and acetone in the case of solid state reduction) and a 2 mL solution of a Pt salt was added and stirred for 6 hours. In the chemical deposition the Pt salt was reduced by adding dropwise a solution of $NaBH_4$ (10 times molar excess), stirred overnight to complete the reaction, then filtered on a nylon membrane (0.22 μm, 46 mm diameter), abundantly washed with Milli Q water and dried at 100 °C for 2 hours. In the solid state deposition the mixture of N-MC and Pt salt was dried in an oven at 80 °C for 2 hours, then the mixture was transferred in a quartz boat inside a tubular oven under H_2/N_2 8%/92% atmosphere. The first hour the temperature was kept constant at 25 °C for conditioning the tube, then was quickly raised to 300 °C for 3 hours. In both protocols, the amount of Pt salt was established in order to realize a 23%$_w$ Pt loading. The chemical deposition was performed three times with $PtCl_2$, K_2PtCl_6 and H_2PtCl_6, and the catalysts obtained were named respectively 2Pt@N-MC, 3Pt@N-MC and 4Pt@N-MC. Solid state deposition was performed only with $Pt(acac)_2$, and the material was named 1Pt@N-MC. Many Pt depositions on N-MC were tested, in order to discover which one produced the best results in terms of Pt nanoparticles diameter, dispersion on MC support and activity towards ORR. The best deposition was repeated also on S-MC and N,S-MC.

The nature of Pt precursor salt is very important to obtain nanoparticles with a small mean radius, a narrow distribution and good dispersion on the surface of mesoporous carbon, because of the interaction between the Pt salt and the support. It is known from literature that π complexes of Pt(II) precursor salt interact with unsaturated carbon (C=C) in the formation of Pt nanoparticles [1]. So Pt (II) salts could produce finely and homogeneously dispersed Pt

nanoparticles, at least if the loading of Pt is lower than a certain value, i.e. 5.4 μg cm^{-2} for Glassy Carbon (GC). On the contrary, Pt salts in different oxidation states, as Pt(IV), are not able to generate this interaction with unsaturated carbon, so nanoparticles don't have a narrow distribution of dimensions and form agglomerates, big structure undefined in term of shape and activity [2].

6.1.3 TEM, ICP and TGA characterizations

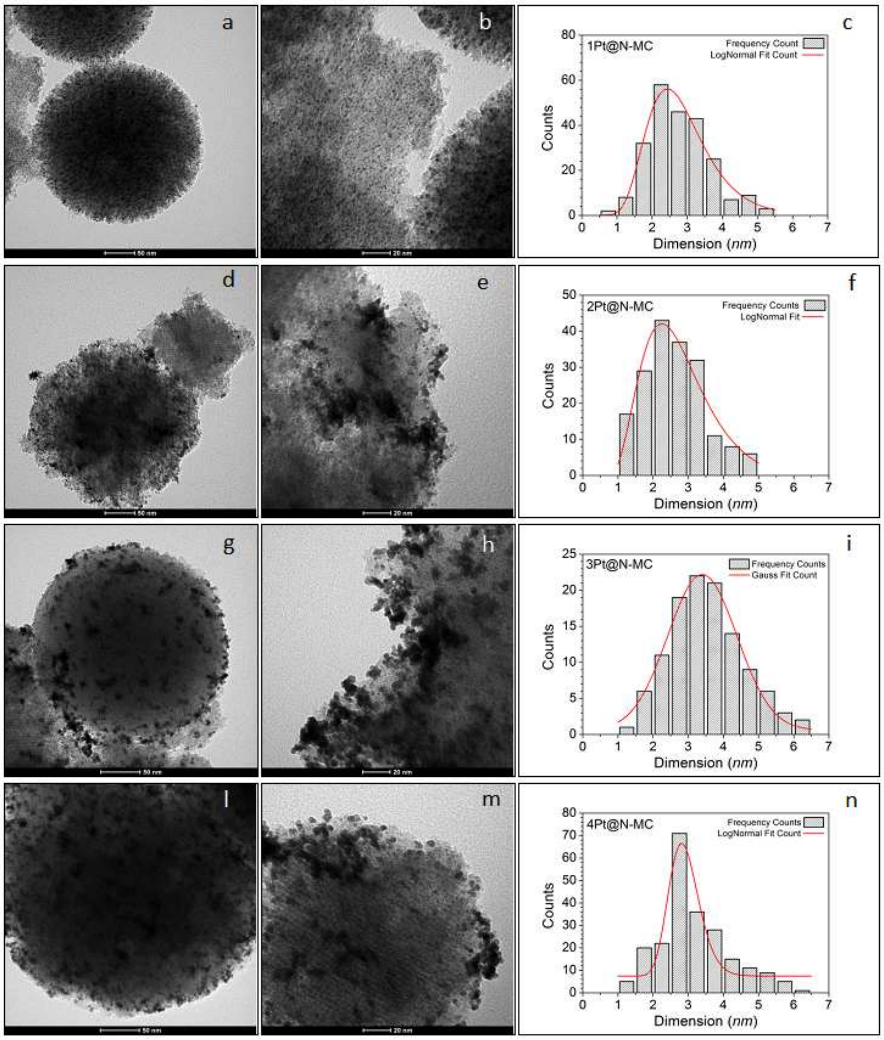

Figure 6.1 a,b) TEM images of 1Pt@N-MC and c) dimensional distribution of NPs; d,e) TEM images of 2Pt@N-MC and f) dimensional distribution of NPs; g,h) TEM images of 3Pt@N-MC and i) dimensional distribution of NPs; l,m) TEM images of 4Pt@N-MC and n) dimensional distribution of NPs.

In Figure 6.1a-n TEM images for 1Pt@N-MC, 2Pt@N-MC, 3Pt@N-MC and 4Pt@N-MC are reported. For each catalyst there are two TEM images at different magnification (50 and 20 nm), plus the dimensional distribution of the radii of Pt nanoparticles, calculated at least in three different regions of each catalyst. Statistical data obtained from dimensional analysis are reported in Table 6.1. As can be seen from TEM images, the main difference between chemical and solid state deposition is related to the morphology of the metallic phase: in the first case, when H_2PtCl_6, K_2PtCl_6 or $PtCl_2$ were used, small nanoparticles which form big aggregates were obtained, while, in the second case, with $Pt(acac)_2$, small spherical nanoparticles, with mean diameter equal to 2.80 nm and homogeneously dispersed on N-MC support were produced. The chemical deposition from K_2PtCl_6 and H_2PtCl_6 gave the biggest mean diameter of NPs, equal to 3.16 nm and 3.54 nm, respectively, while that from $PtCl_2$ gave the smallest one, equal to 2.60 nm. However, the calculation of parameters reported in Table 6.1 doesn't consider aggregates, so, actually, the active metallic phase of 2Pt@N-MC, 3Pt@N-MC and 4Pt@N-MC is made of big aggregates undefined in terms of dimensions and morphology, and this situation is quite relevant in voltammetric analysis.

The deposition investigation allowed to confirm what already observed in literature, i.e. that Pt(IV) salts generate aggregates of NPs, while Pt(II) provides small and finely dispersed NPs. The exception was 2Pt@N-MC: despite it was obtained from $PtCl_2$, it gave rise to aggregates of NPs. This is probably due to two factors: a limited amount of C sp^2 on the surface respect to the loading of Pt precursor salt [2][3], and the insolubility of $PtCl_2$ in water. Probably, the latter is the main factor that prevent the interaction between Pt(II) and the N-MC by π complex.

ICP allows the determination of the exact amount of Pt in the carbon matrix, and its weight percentage is reported in Table 6.1. The theoretical loading set in the synthesis procedure was equal to 23%$_w$, but the chemical treatment is responsible for small losses in Pt precursor by precursor salt sublimation or incomplete chemical reduction. 4Pt@NMC shows the lowest amount of Pt, and this is predictable because of the high hygroscopicity of H_2PtCl_6, that makes it difficult to be exactly weighted. TGA were recorded to check the carbon degradation temperature and the residual weight. The residual should be comparable with the amount of Pt obtained by ICP.

Table 6.1 Mean Pt NPs diameter for 1Pt@N-MC, 2Pt@N-MC, 3Pt@N-MC and 4Pt@N-MC. Pt amount (percentage in the catalysts) and degradation temperature.

	N[a]	Mean (nm)	Std. Dev. (nm)	Median (nm)	Pt loading ($\%_w$)	T_{deg} (°C)
1Pt@N-MC	236	2.80	0.93	2.78	24.1	370
2Pt@N-MC	183	2.60	0.86	2.57	22.9	-
3Pt@N-MC	114	3.54	1.04	3.48	27.4	358
4Pt@N-MC	223	3.16	0.99	2.99	21.2	378

[a] number of Pt nanoparticles measured for the determination of mean diameter

6.1.5 ECSA determination

The electrochemical surface area (ECSA), i.e. the Pt area participating at the electrochemical reaction, of 1Pt@N-MC, 2Pt@N-MC, 3Pt@N-MC and 4Pt@N-MC can be obtained by hydrogen adsorption and desorption peaks and by carbon monoxide stripping [4][5][6][7]. This two methods give different results; generally, the value obtained from CO stripping is higher than the one obtained from hydrogen adsorption/desorption, and their ratio depends on the dimension and morphology of NPs. K.J.J. Mayrhofer et al. found that the ratio of CO-stripping on H adsorption-desorption decreases with increasing particle size, and in particular is equal to 1.4 when the mean radius of Pt NPs on high surface area carbon is 1 nm, and decrease to 1.1 when the mean diameter of Pt NPs is equal to 5 nm [8].

In a typical cyclic voltammetry of Pt in 0.5 M H_2SO_4, two signal appears in the region between 0 and -0.25 V vs. SCE, as depicted in Figure 6.2. The one in the cathodic direction is due to hydrogen adsorption on Pt, whereas that in the anodic scan is due to hydrogen desorption. The determination of ECSA from these two signals can be done by equation 6.1, in which Q_{ads} and Q_{des} are the charge associated to adsorption and desorption of hydrogen, respectively, and their mean value is divided by 210 µC cm^{-2}, which corresponds to a full monolayer of hydrogen that covers Pt surface. The integration was effectuated after double layer correction, and the baseline is a straight line connecting the first and the last point of integration. The value obtained from each integral in the anodic and cathodic direction was divided by the scan rate, that in this experiment was equal to 200 mV/s, in order to obtain Q_{ads} and Q_{des}. ECSA obtained with this technique are reported in Table 6.2.

$$ECSA = \frac{Q_{ads} + Q_{des}}{2 \cdot 210} \qquad \text{Eq. 6.1}$$

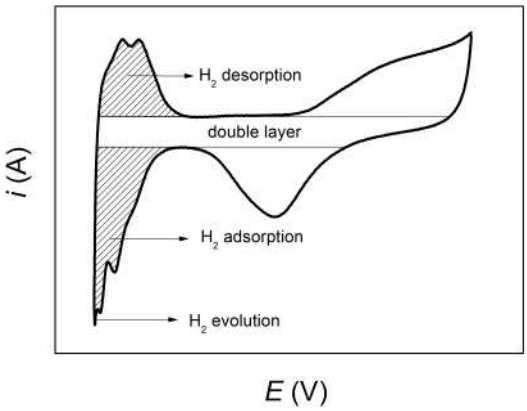

Figure 6.2 CV in Ar sat 0.5 M H_2SO_4 on Pt@N-MC, *v* = 200 mV/s

Determination of ECSA was done also by stripping of CO. In this case Pt-based electrodes were first activated in Ar saturated 0.1 M $HClO_4$ by 150 potential cycles between -0.25 and 0.74 V/SCE at 500 mV/s. Then CO was bubbled inside the solution for 5 minutes, while applying on working electrodes a constant potential, equal to -0.20 V/SCE, corresponding to the CO adsorption potential. Then the CO was removed by bubbling pure Ar inside the solution for 25 min, while applying the same adsorption potential of -0.20 V/SCE. Two consecutive CV at scan rate equal to 10 mV/s were recorded in the potential range between -0.25 and 0.74 V/SCE, in the first scan a narrow peak appears, corresponding to CO oxidation to CO_2; the second scan was used as baseline to integrate the stripping signal. An explicative experiment is reported in Figure 6.3b, in which during the first cycle the CO oxidation signal appears. This signal can be called also CO stripping, and is associated to an oxidative process involving a full monolayer adsorbed on the Pt surface, excluding diffusive processes. For this reason, the intensity of this signal is directly proportional to the applied scan rate. The second cycle is the baseline for the integration of the oxidation peak: in this case the integral is calculated in the same potential window and subtracted to the area obtained from integration of the stripping peak (Figure 6.3b).

The determination of ECSA was done according to equation 6.2:

$$ECSA = \frac{A_{CO}}{v_{scan} \cdot 420} \qquad \text{Eq. 6.2}$$

in which A_{CO} is the area corresponding to the oxidation of CO after baseline correction, v_{scan} is the scan rate used to record the CV and 420 µC cm^{-2} is the charge associated to the oxidation of a monolayer of CO on Pt surface. In Figure 6.3a the CO stripping curves for 1Pt@NMC, 2Pt@NMC, 3Pt@NMC and 4Pt@NMC are superimposed. The shape and the position

of the CO oxidation are associated to the morphology of Pt NPs, and the following effects are described in literature. First of all, a negative shift of the CO oxidation signal, as the Pt particle size increases from 1.8 to 3.3 nm, occurs. As the diameter increases further, the signal is comparable to the one obtained with bulk Pt. The second effect concerns the Pt NPs agglomerates, responsible for the splitting of CO oxidation peak due to inter-particles heterogeneity [2]. Lastly, a splitting in the stripping signal could be due also to Pt sites interacting with graphitized and disordered carbon structures, and the relative intensity are just related to the ratio of two carbon forms [9]. Analyzing Figure 6.3a , 1Pt@NMC and 3Pt@NMC show a single intense CO oxidation peak, while 2Pt@NMC and 4Pt@NMC show its splitting and low intensity. Comparison with TEM measurements in Figure 6.1 and data in Table 6.1, it's clear that 2Pt@NMC and 4Pt@NMC show the most inhomogeneous Pt NPs distribution on the surface of N-MC, and this could justify the splitting of CO oxidation peak. The more negative signal is at the same potential for the two compounds, but the second peak is found at higher potential for 2Pt@NMC. Keeping in mind that the more positive signal is associated to non-agglomerated and smaller particles, this is in agreement with the mean diameter found in Table 6.1 for 2Pt@NMC, the smallest among these four catalysts. 1Pt@NMC shows a single oxidation peak, and this is in agreement with TEM analysis that highlights small, non-agglomerated Pt nanoparticles. 3Pt@NMC represents an anomaly, because of the narrow CO stripping signal appearing even in case of Pt agglomerates. The mean diameter of Pt NPs, without taking into account the agglomerates, is the biggest so it's justified also the negative shift of the stripping process.

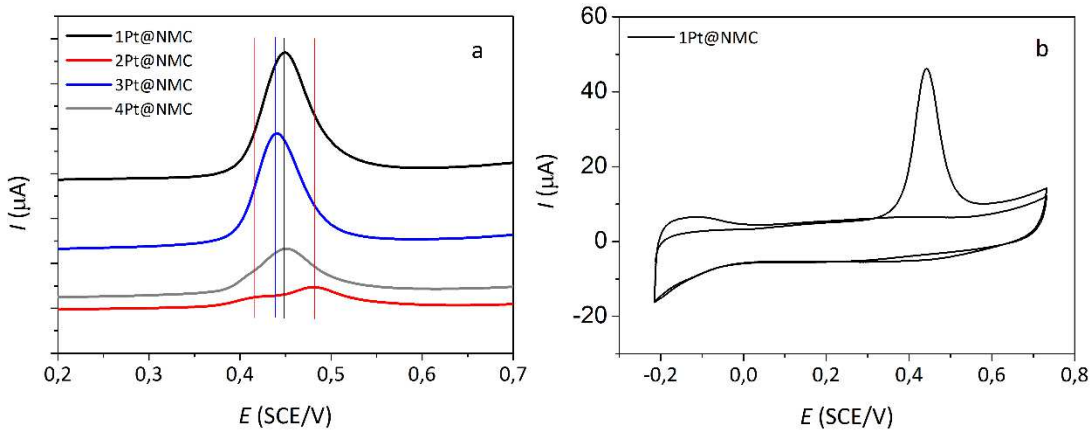

Figure 6.3 a) Magnification of the CO oxidation signal on 1Pt@NMC, 2Pt@NMC, 3Pt@NMC and 4Pt@NMC and b) CO stripping CV for 1Pt@NMC used for integration and baseline subtraction.

In Table 6.2 the ECSA values obtained from H adsorption/desorption and CO oxidation are reported. The ECSA are referred to unit of mass: this value is obtained dividing the ECSA

from Equations 6.1 and 6.2 by the Pt loading on the electrode surface. ECSA obtained by the two different methods, as already stated, is usually different, in particular when Pt nanoparticles are small [8]. The highest CO/H ratio was obtained for 1Pt@NMC, the only sample which possesses well defined Pt NPs. For the other samples there is a decrease of the CO/H ratio, probably for both effect of bigger particle size and agglomeration. Both techniques of fixing the surface area of Pt catalysts, can be considered equally beneficial and important, but one should always be aware of the systematic errors of either approach. For the investigation of the correct H adsorption/desorption and CO-stripping charge of high surface area catalysts, a background correction for the carbon support must always be implemented.

Table 6.2 ECSA values obtained from H adsorption/desorption and CO oxidation for Pt@NMC, 2Pt@NMC, 3Pt@NMC and 4Pt@NMC

	Pt on GC (μgcm^{-2})	**ECSA** $H_{ads/des}$ (m^2/g)	**ECSA** $CO_{oxidation}$ (m^2/g)	**Ratio** $ECSA_{CO/H}$
1Pt@N-MC	2.41	17.98	31.44	1.7
2Pt@N-MC	2.29	6.99	10.32	1.4
3Pt@N-MC	2.74	16.64	23.09	1.4
4Pt@N-MC	2.12	23.49	21.75	0.9

6.1.6 ORR on 1Pt@NMC, 2Pt@NMC, 3Pt@NMC and 4Pt@NMC

Electrochemical activity toward oxygen reduction was evaluated by CVs and LSV with RDE in O_2 sat. 0.5 M H_2SO_4 solution. In **Figure 6.4** a, b and c CVs in steady condition and LSV with RDE, with the K-L analysis for the exchanged electrons determination, are reported. The CVs (**Figure 6.4**a) show typical features of both Pt catalyst and high surface area carbon support. The signal associated to oxygen reduction on Pt active sites is the cathodic peak at around 0.5 V/SCE, while the two signals in the cathodic and anodic direction between 0 and -0.25 V/SCE are associated to H adsorption and desorption, the same peaks used for the surface area determination. The high capacitive current, on the contrary, is due to the mesoporous carbon support, as highlighted in the previous chapters. The LSVs (**Figure 6.4**c) are recorded at 5 mV/s and 1600 rpm, and such rate is low enough to remove or make the capacitive contribution irrelevant. The current is almost equal to zero till the potential in which the oxygen reduction starts. The K-L analysis (**Figure 6.4**b) of RDE measurement confirms the 4 electron reduction of oxygen to H_2O

on Pt supported on Carbon materials. This is predictable, given that Pt, the commercial material employed in real systems, is known to promote the direct formation of water.

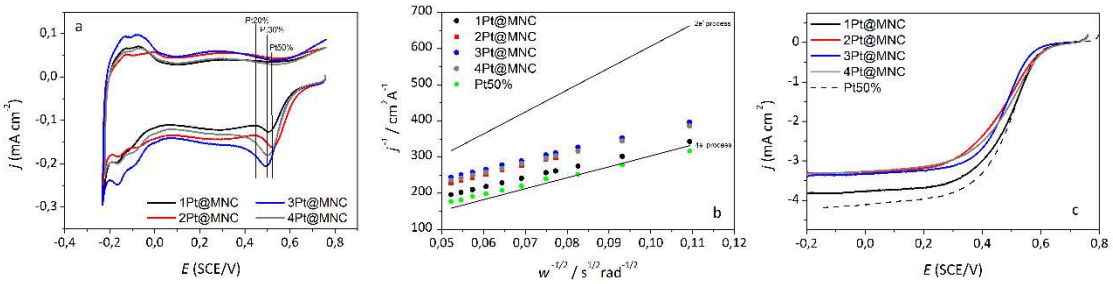

Figure 6.4 Electrochemical activity toward ORR in 0.5 M H_2SO_4 on 1Pt@NMC, 2Pt@NMC, 3Pt@NMC and 4Pt@NMC. a) CVs recorded at 200 mV/s; b) K-L analyis of RDE measurement c) LSV with RDE recorded at 5 mV/s and 1600 rpm.

In Table 6.3 the data obtained by electrochemical analysis are reported. Peak potential and current (E_p and I_p) were obtained via CVs (Figure 6.4a), while onset and half-wave potentials and limiting current densities (E_{onset}, $E_{1/2}$ and j_{lim}) were obtained via RDE analysis. The performance are compared to that of two commercial materials, made of Pt NPs (50 and 30 $\%_w$ loading) on high surface area carbon. As can be seen from both figures and data, the activity of 1Pt@NMC, 2Pt@NMC, 3Pt@NMC and 4Pt@NMC is different, in particular 1Pt@NMC and 2Pt@NMC are the most active materials toward ORR, followed by 4Pt@NMC and 3Pt@NMC. Given that all the materials are made of the same components, i.e. Pt NPs and nitrogen doped mesoporous support, the different electrochemical activity should arise in the metal phase. The morphology is for sure relevant: many papers in literature state that the most active Pt NPs possess a diameter between 2 and 6 nm [10][11][12][13][14], so this might be the main reason why 1Pt@NMC is the most active material. The aggregate of NPs probably have an effect in decreasing the catalytic activity because of the lower electrochemical surface area, as reported in Table 6.2. In the case of 2Pt@NMC, 3Pt@NMC and 4Pt@NMC, all made of Pt aggregates, the most active is the one prepared from $PtCl_2$. In this case it is possible to infer the importance of π interaction between Pt(II) and graphitic carbon, as reported in Section 6.3.1. Furthermore, Alonso-Vante reports that the Pt interacting with graphitic domains has better performance, due to the strong metal-support interaction [15]. The commercial references show catalytic performance directly proportional to the amount of Pt they possess, in particular, the higher the amount, the higher the activity toward ORR. The activity comparison among the commercial references and the synthesized materials shows a slightly higher activity of 1Pt@NMC and 2Pt@NMC compared to Pt50%. Furthermore, the amount of Pt in the catalyst layer in the case

of Pt50% is double with respect to the catalysts made of Pt on doped mesoporous carbons. This improvement of performance might be ascribed to the nitrogen doping of support, which modify the electronic structure of Pt metal phase, enhancing ORR [16][17]. In particular, X. Ning et al. highlighted that interaction of Pt with graphitic N promote catalytic performance towards ORR.

Table 6.3 Electrochemical data for ORR in 0.5 M H_2SO_4 on 1Pt@NMC, 2Pt@NMC, 3Pt@NMC and 4Pt@NMC. All potentials are referred to SCE.

MC	E_p[a] (V)	I_p[a] (μA)	J_{lim}[b] (mA/cm^2)	E_{onset}[b] (V)	$E_{1/2}$[b] (V)	n[c]
1Pt@NMC	0.502	-112	-2488	0.594	0.450	4.73
2Pt@NMC	0.500	-81	-3162	0.592	0.463	4.25
3Pt@NMC	0.453	-92	-3109	0.565	0.450	4.53
4Pt@NMC	0.487	-131	-3564	0.585	0.474	4.59
Pt50%	0.494	-98	-3593	0.583	0.466	4.93
Pt30%	0.486	-114	-4422	0.573	0.465	5.36
Pt20%	0.458	-116	-4726	0.565	0.454	6.04

[a] obtained from CVs in steady conditions
[b] obtained from RDE analysis
[c] obtained from Koutecky-Levich analysis of RDE data

6.2 Platinum nanoparticles on S-MC and N,S-MC

In this Section the characterization and the activity toward ORR of two families of catalyst made of Pt NPs on N- and S-doped and on N,S-co-doped mesoporous carbons are described. The carbon supports employed in these syntheses were prepared from phenantroline (N-MC), dibenzothiophene (S-MC) and phenothiazine (N,S-MC) with silica P200 as template at 750 °C. The very same mesoporous carbon were labelled N-MC1, N,S-MC1 and S-MC1 in Chapter 4.

Pt NPs were deposited on N,S-MC and S-MC via solid state reduction of $Pt(acac)_2$ and chemical reduction of $PtCl_2$, with the same protocols described in Section 6.1.2. The samples are labelled 1Pt@N,SMC and 1Pt@SMC when obtained via solid state reduction, and 2Pt@N,SMC and 2Pt@SMC when obtained via chemical reduction. Their properties and activity toward ORR are compared to 1Pt@NMC and 2Pt@NMC.

6.2.1 TEM, ICP and TGA characterizations

In Figure 6.5 the TEM images obtained for 1Pt@NMC (Figure 6.5a, b, c), 1Pt@N,SMC (Figure 6.5d, e, f) and 1Pt@SMC (Figure 6.5g, h, i) are reported. TEM images of 1Pt@NMC are reported again just to have a direct comparison with the same deposition on 1Pt@N,SMC and 1Pt@SMC. From this comparison it's clear (Table 6.4) that the mean diameter for Pt deposited by solid state reduction of $Pt(acac)_2$ is the smallest, and its value is equal to 1.82 nm. In the case of the other samples, the mean diameter is bigger, around 2.5 and 3.5 nm. This is consistent with an interaction between Pt NPs and sulphur doped support, which leads to the formation of smaller NPs. TEM analysis of 2Pt@NMC, 2Pt@N,SMC and 2Pt@SMC is reported in Figure 6.6. From the distribution of dimensions graphs it's clear that the mean diameter of nanoparticles is almost constant in the three samples, symptom that in this case there is no specific interaction between carbon support and Pt NPs, as realised in the case of 1Pt@SMC.

In Figure 6.7 the TGA analyses carried out on 1Pt@NMC, 1Pt@N,SMC, 1Pt@SMC, 2Pt@NMC, 2Pt@N,SMC and 2Pt@SMC, and, as comparison, the TGA measurement of the bate mesoporous carbon supports, are reported. There is a clear decrease in the degradation temperature for all the Pt-containing samples with respect to the bare support. This is probably due to the Pt reducing treatment in both aqueous solution with $NaBH_4$ and H_2 treatment at high temperature, which chemically react with the carbon surface creating thermo labile surface groups.

Table 6.4 Mean diameter of Pt NPs, Pt loading and degradation temperature for 1Pt@NMC, 1Pt@N,SMC, 1Pt@SMC, 2Pt@NMC, 2Pt@N,SMC and 2Pt@SMC.

	N[a]	Mean[b] (nm)	Std. Dev. (nm)	Median (nm)	Pt loading[c] ($\%_w$)	T_{deg}[d] (°C)
1Pt@N-MC	236	2.80	0.93	2.78	24.1	370
1Pt@N,S-MC	266	3.54	1.05	3.43	35.7	380
1Pt@S-MC	234	1.82	0.49	1.79	29.4	347
2Pt@N-MC	183	2.59	0.86	2.57	22.4	-
2Pt@N,S-MC	139	2.41	0.90	2.30	25.7	395
2Pt@S-MC	181	2.49	0.81	2.42	23.5	416

[a] number of Pt nanoparticles measured for the determination of mean diameter
[b] obtained obtained by measuring with ImageJ the diameter of Pt NPs represented in different region of the sample
[c] Pt loading on mesoporous carbon, obtained by ICP analysis
[d] degradation temperature, obtained by TGA analysis

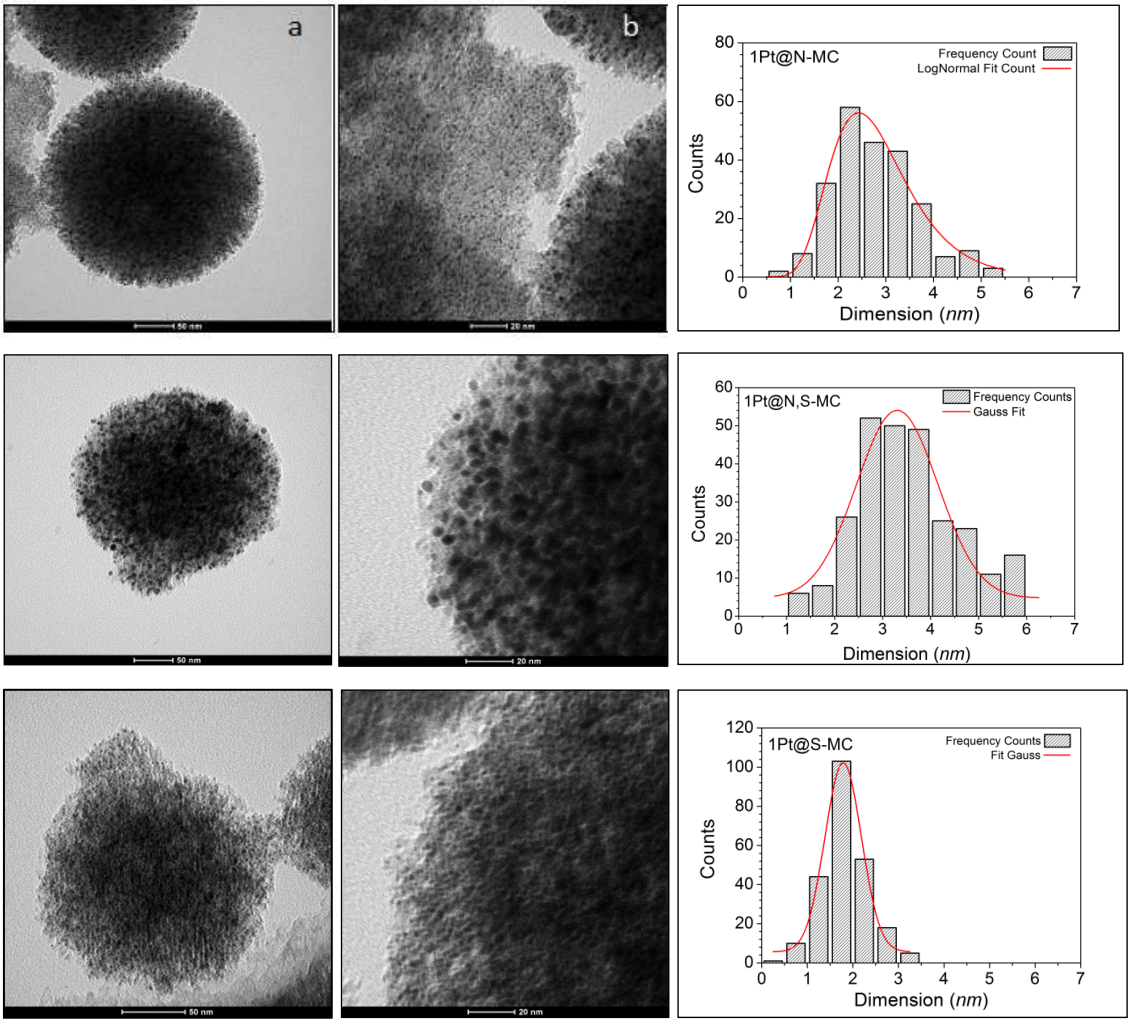

Figure 6.5 TEM analysis at two different magnifications and Pt dimension distribution for 1Pt@NMC (a, b, c), 1Pt@N,SMC (d, e, f) and 1Pt@SMC (g, h, i).

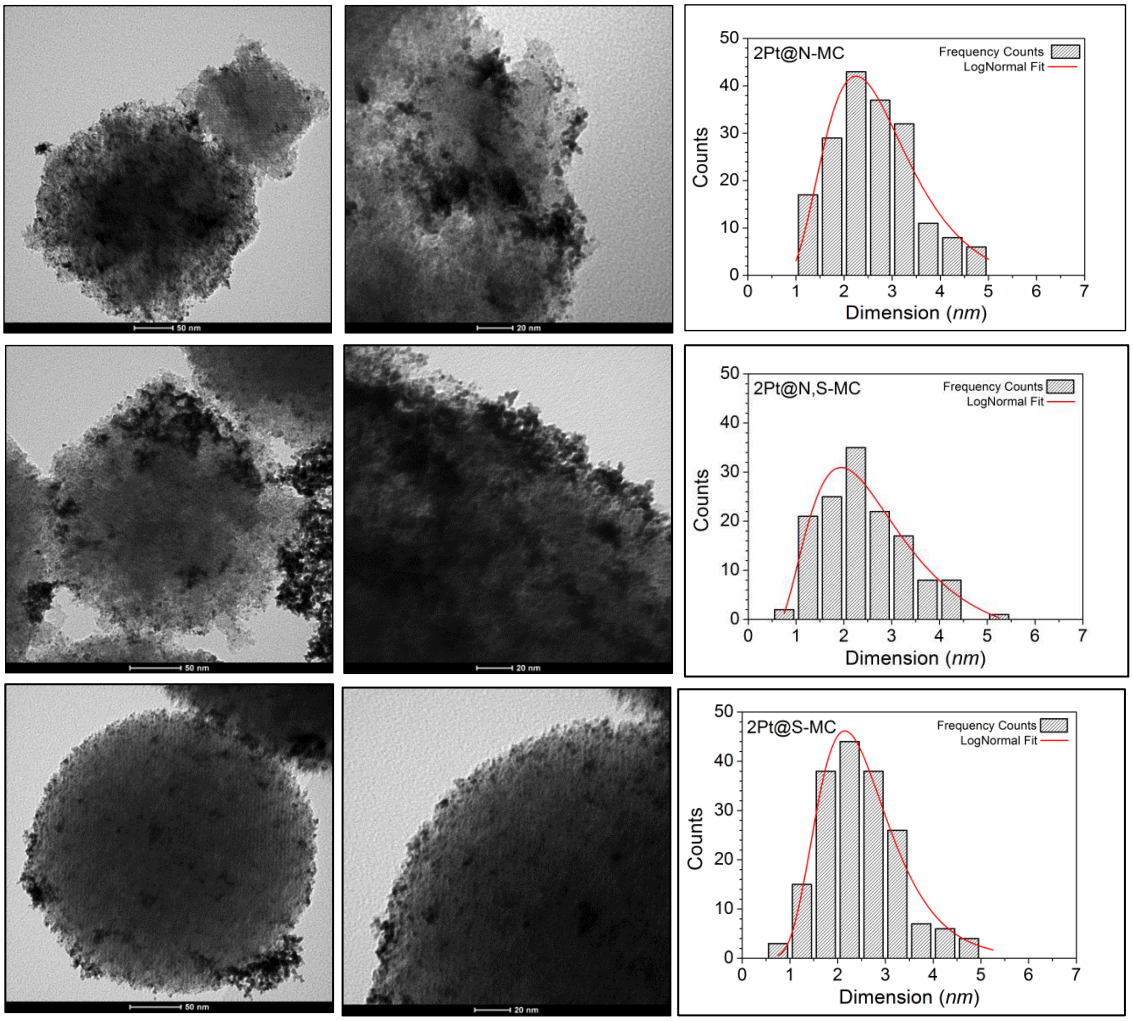

Figure 6.6 TEM analysis at two different magnifications and Pt dimension distribution for 2Pt@NMC (a, b, c), 2Pt@N,SMC (d, e, f) and 2Pt@SMC (g, h, i).

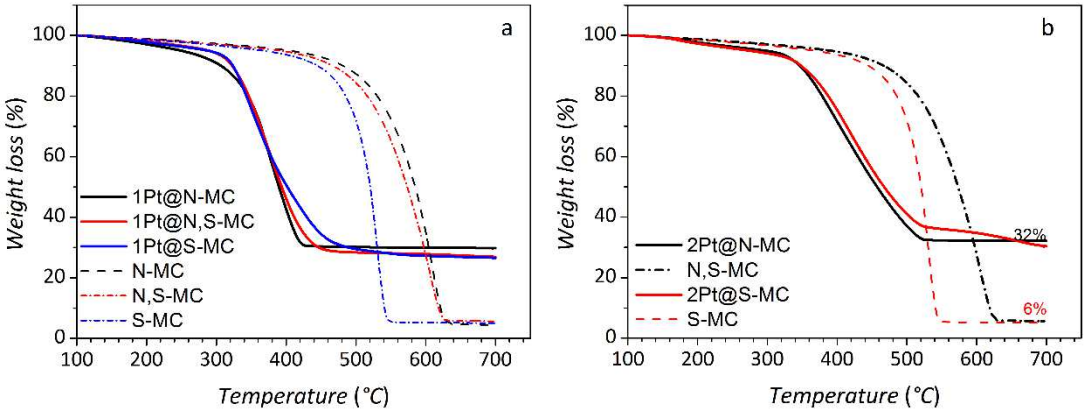

Figure 6.7 TGA analysis for a) 1Pt@NMC, 1Pt@N,SMC, 1Pt@SMC, compared to NMC, SMC and N,SMC and b) 2Pt@N,SMC, 2Pt@SMC compared to SMC and N,SMC.

6.2.2 XPS characterization

XPS analysis was carried out on 1Pt@NMC, 1Pt@SMC and Pt50% on high surface area carbon in order to highlight specific interaction between the metal phase and the doped support, that can justify as well the different growth of Pt NPs on S-MC support. **Figure 6.8** shows the photoemission from orbital 4f of Pt for Pt50%, 1Pt@NMC and1Pt@SMC. The three appearing signals are associated to Pt(0), Pt(II) and Pt(IV), the most common oxidation states of Pt, characterized by an increasing B.E. Each signal is split because of two energetic levels in which d orbitals are distributed.

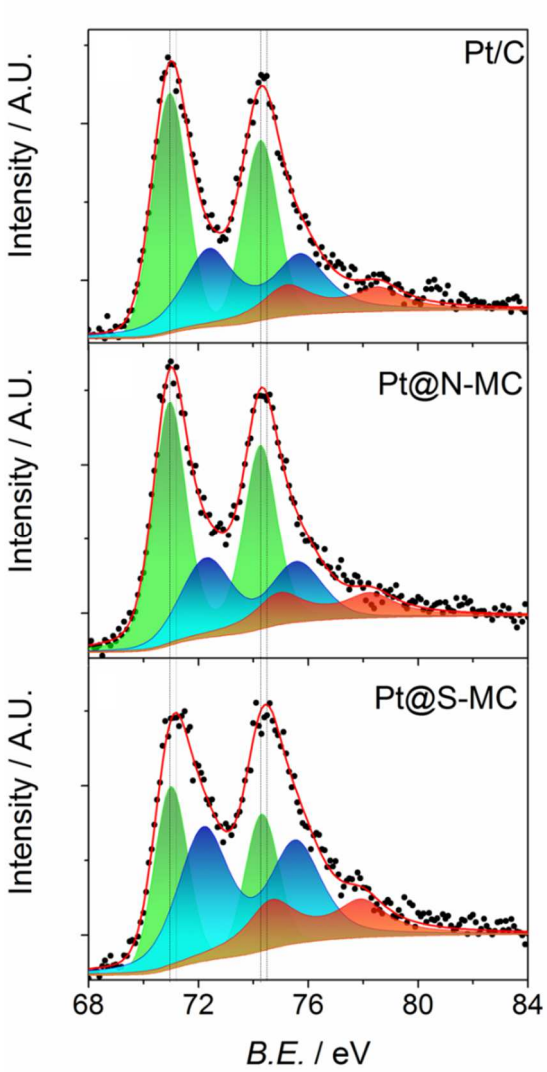

Figure 6.8 Photoemission from orbital 4f od Pt for Pt50%/C, 1Pt@NMC and 1Pt@SMC

A peculiar behavior is highlighted for 1Pt@SMC, given that the Pt photoemission is shifted by 0.2 eV toward higher B.E. compared to Pt@NMC and Pt50%. This corresponds to an interaction, consisting in charge transfer from Pt orbitals to S doped support, which determines

the smaller particle size of Pt nanoparticles on S-MC, which in turn results more easily oxidized. This last statement is in agreement with data reported in Table 6.5, associated to the amount of each Pt oxidation state in the samples.

Table 6.5 Pt oxidation stated found in 1Pt@NMC, 1Pt@SMC and Pt50% and relative amount.

MC	Pt(0) (%at.)	Pt(II) (%at.)	Pt(IV) (%at.)
1Pt@NMC	37.1	32.6	30.3
1Pt@SMC	33.8	35.3	30.9
Pt50%	37.0	33.0	30.0

6.2.3 ORR characterization

1Pt@N,S-MC, 1Pt@SMC, 2Pt@N,S-MC and 2Pt@SMC were tested toward ORR and their activity was compared to 1Pt@NMC and 2Pt@NMC described in Paragraph 6.1.6, respectively. In **Figure 6.9**a the LSVs recorded with RDE on 1Pt@N,S-MC, 1Pt@SMC, together with the activity of 1Pt@NMC descried in Paragraph 6.1.6 are reported, while in Figure 6.9b there is the Koutecky-Levich plot calculated from RDE measurements for the three electrodes. In Figure 6.10a and b there are the same analyses for 2Pt@N,SMC and 2Pt@SMC, compared to 2Pt@NMC as well. Pt50% on high surface area commercial carbon is selected as reference material.

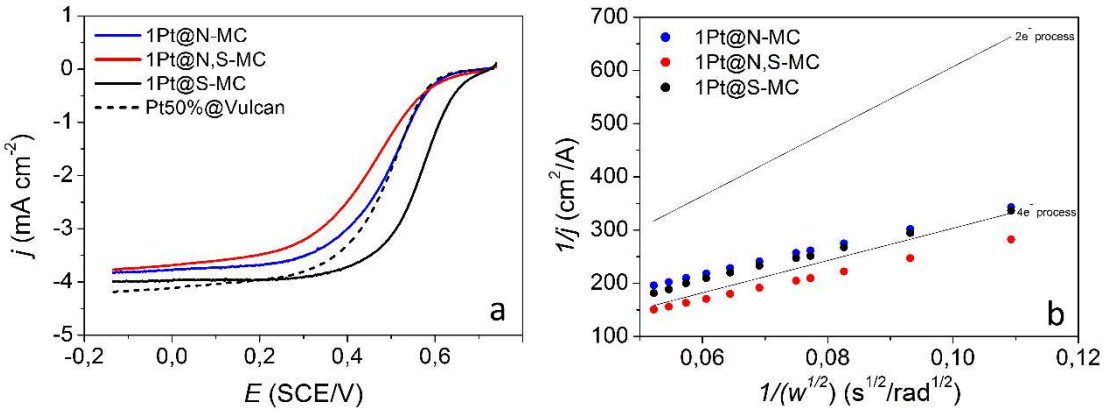

Figure 6.9 a) RDE analysis for ORR on 1Pt@NMC (blue), 1Pt@N,SMC (red) and 1Pt@SMC (black) in 0.5 M H_2SO_4, *v* = 5 mV/s, rotation rate 1600 rpm; b) Koutecky-Levich plots.

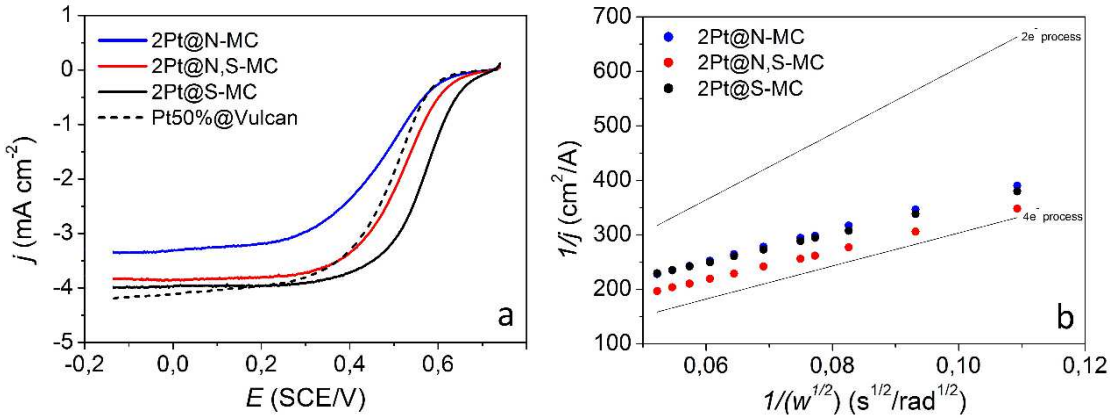

Figure 6.10 a) RDE analysis for ORR on 2Pt@NMC (blue), 2Pt@N,SMC (red) and 2Pt@SMC (black) in 0.5 M H_2SO_4, *v* = 5 mV/s, rotation rate 1600 rpm; b) Koutecky-Levich plots.

Table 6.6 Electrochemical data for ORR in 0.5 M H_2SO_4 on 1Pt@NMC, 2Pt@NMC, 1Pt@NSMC, 2Pt@NSMC, 1Pt@SMC and 2Pt@SMC. All potential are referred to SCE.

MC	E_p[a] (V)	I_p[a] (μA)	J_{lim}[b] (mA/cm^2)	E_{onset}[b] (V)	$E_{1/2}$[b] (V)	n[c]
1Pt@NMC	0.502	-112	-2488	0.594	0.450	4.73
1Pt@NSMC	0.430	-188	-4264	0.606	0.506	4.75
1Pt@SMC	0.534	-245	-3968	0.640	0.566	4.55
2Pt@NMC	0.471	-87	-3162	0.592	0.463	4.25
2Pt@NSMC	0.500	-81	-2564	0.614	0.510	4.59
2Pt@SMC	0.505	-115	-3096	0.636	0.528	4.58
Pt50%	0.494	-98	-3593	0.583	0.466	4.93

[a] obtained from CVs in steady conditions
[b] obtained from RDE analysis
[c] obtained from Koutecky-Levich analysis of RDE data

Figure 6.9 and Figure 6.10 highlight that the activity of Pt on N-MC, N,S-MC and S-MC is different, and in particular the catalyst made of Pt NPs on sulphur doped mesoporous carbon supports, prepared by both chemical reduction of $PtCl_2$ ad $Pt(acac)_2$, is the most active material toward ORR, among the synthesized ones. Moreover, this catalyst shows higher catalytic activity than the reference material, Pt50% on high surface area carbon. In Table 6.6 the electrochemical data obtained from ORR analysis on the catalysts made of Pt on differently doped MC are reported. This table clearly shows the increase of performance, calculated with both onset and half-wave potentials, when the employed support is sulphur doped mesoporous carbon. This effect is not well described in literature, because nowadays sulphur doped carbons are not extensively employed as catalyst support, but preferably as metal-free catalysts. The key parameter involved in the enhancing of performance toward ORR might be the charge transport

from Pt to the support highlighted by XPS, described in Section 6.2.2. In this case, Pt possesses a lower electronic density on S-MC with respect to other supports, and this for sure facilitates the interaction and the adsorption of oxygen, with higher electronic density, on the support itself. Some examples of sulphur doped graphene as Pt NPs support are present in literature. In these cases thiophenic sulphur is inserted in the carbon lattice of graphene, and this structure might be considered as the ideal system of the sulphur doped mesoporous carbon, in which sulphur is present as well as thiophenic units. An enhancing of oxygen reduction performance of Pt NPs on S-doped graphene was highlighted by R. Wang et al. [18] and by D. Higgins et al. [19]. In this last paper, a computational study was carried out in order to establish how the metal phase interacts with the support and to highlight the factors responsible for the catalytic enhancement. First of all, Pt adsorbs on a C-S bridge site, and a higher adsorption energy on thiophenic and graphitic S is found with respect to un-modified graphene (value equal to -2.68 eV, -3.27 eV and -2.01 eV, respectively). So, the adsorption of Pt on S sites is stronger than on C site in graphene. This, at least in graphene, increases the stability of Pt NPs on the S-doped surface of graphene. Then the d-band position of Pt on graphene and on S-doped graphene is evaluated. In the case of S-doped material it is downward shifted, and this is directly connected to the increased catalytic performance toward ORR. The same behaviour is found also for Pt NPs on thiol-modified carbon nanotubes, described by L. Li et al. [20].

6.2.4 Electrochemical Stability test in 0.5 M H_2SO_4: 1Pt@NMC, 1Pt@SMC, 1Pt@N,SMC

Two kinds of electrochemical stability test were carried out on representative samples 1Pt@NMC, 1Pt@SMC and 1Pt@N,SMC. The first protocol consists in applying 3500 cycles between -0.25 and 0.75 V/SCE at 500 mV/s in Ar sat. 0.5 M H_2SO_4, followed by TEM analysis of the catalyst in order to define the final morphology of the Pt NPs. The ink, made of 1.25 mg of Pt@doped carbon and 1.25 mL of a 6%$_v$ of nafion in MilliQ H_2O, was homogenized in ultrasound bath and drop-casted on a 5 cm^2 GC on both side. The powder was gently washed with MilliQ H_2O and collected after the stability test in a small vial with 2 mL of H2O, in order to be directly employed during TEM analysis. In Figure 6.11 the characterization of 1Pt@SMC is reported: it's pretty clear by TEM image that the surface diffusion of Pt NPs occurs to give bigger metal nanoparticles via Ostwald ripening. In Figure 6.11b the Pt NPs dimensions distribution is reported, which clearly shows an increase of mean diameter from 1.8 nm (Figure 6.5 g, h and i) to 14.2 nm. The same results were obtained also with 1Pt@NMC (TEM image and dimension distribution not shown), where the NPs with an initial mean diameter equal to 2.80 nm growth

till the mean value of 15.3 nm. Furthermore CVs at 50 mV/s before and after the stability test were collected in order to quantify the decrease in ECSA by H adsorption and desorption signals. In this case the working electrode has a very big geometrical area so the percentage decrease in ECSA and not its absolute value is given, just to give an idea of the degradation extent.

Table 6.7 Mean Pt NPs diameter on N-MC and S-MC before and after the electrochemical stability test consisting of 3500 potential cycles in Ar sat. 0.5 M H_2SO_4, and ECSA loss.

	d_m before test	d_m after test	ECSA loss
Pt@NMC	2.4 nm	15.3 nm	50 %
Pt@SMC	1.9 nm	14.2 nm	70 %

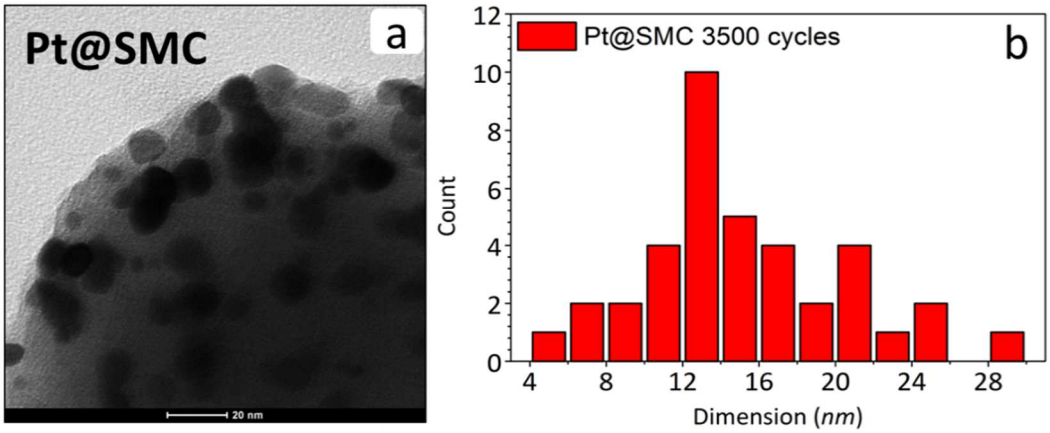

Figure 6.11 a) TEM analysis of 1Pt@SMC after 3500 potential cycles in 0.5 M H_2SO_4 and b) dimension distribution of Pt NPs after electrochemical operations.

The second stability protocol applied on 1Pt@NMC, 1Pt@N,SMC and 1Pt@SMC consists in 10000 cycles at 500 mV/s between 0.6 and 1.0 V/RHE in O_2 sat 0.5 M H_2SO_4, in order to quantify the activity toward oxygen reduction after the test. Potential cycles in this window is responsible mainly for Pt degradation, on the contrary C shouldn't be affected in large extent by this test.

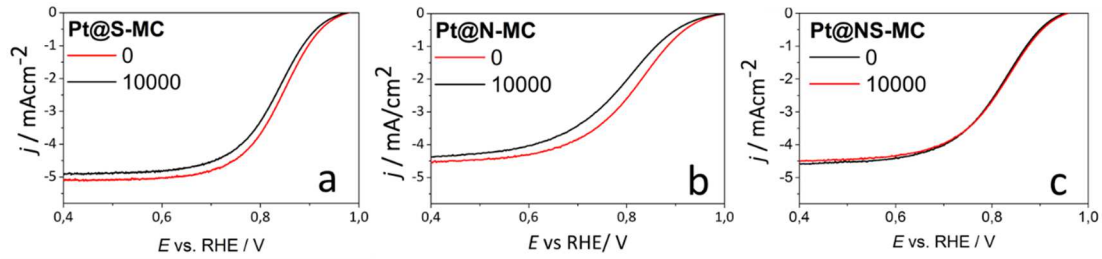

Figure 6.12 LSVs with RDE in O_2 sat. 0.5 M H_2SO_4 for a) 1Pt@SMC, b) 1Pt@NMC and c) 1Pt@N,SMC. Scan rate. 5 mV/s; rotation rate: 1600 rpm.

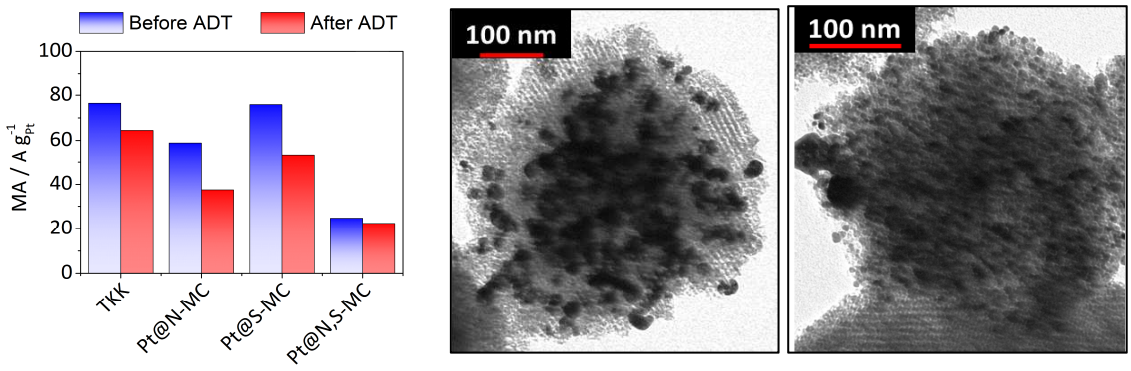

Figure 6.13 a) Mass Activity before and after the test for 1Pt@NMC, 1Pt@N,SMC and 1Pt@SMC and the reference Pt50% on high surface area carbon; TEM images after the stability test of b) 1Pt@SMC and c) 1Pt@NMC.

In Figure 6.13 histograms of MA calculated before and after the electrochemical test are reported the. All the materials show a higher decrease of its value than the reference material, except 1Pt@N,SMC. This sample, even if the Pt loading on the GC surface is the same as 1Pt@NMC and 1Pt@SMC, shows a lower ECSA and a lower MA. In this case the main problem might involve Pt site inactive for ORR, because they are located in a region not in touch with electrolyte solution and/or reactants.

6.3 Improving ORR testing protocol

An exhaustive research intended to improve all the experimental conditions employed during ORR analysis was carried out, from catalyst layer preparation, to experimental protocols and data processing. This work was carried out at Toyota Motor Europe, in Zaventem, Belgium. The

following statements are highlighted in several works published by Shyam Kocha and Yannick Garsany, in which all the parameters involved in performance determination toward ORR are evaluated [21][22][23][24][25][26][27].

6.3.1 Methods for cleaning glassware

The cleanliness of the glassware employed during experiments is the first fundamental step: in literature several procedures regarding soaking in Aqua Regia, hot concentrated nitric or sulphuric acid, acidified potassium permanganate, piranha solution (mix of concentrated sulphuric acid and hydrogen peroxide), mix of concentrated sulphuric acid nochromix®, are described. After cleaning, the glassware has to be soaked in boiling MilliQ water for at least 3 times. In Figure 6.14 the increase of SA along the number of soaking in boiling water is reported.

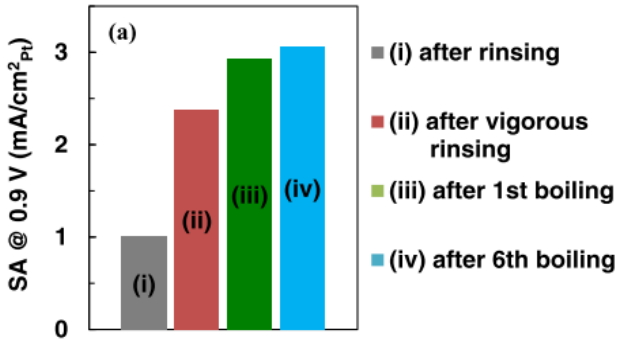

Figure 6.14 SA calculated at 0.9 V/RHE for ORR on poly-Pt. Effect of number of soaking in boiling water. K. Shinozaki, J.W. Zack, R.M. Richards, B.S. Pivovar, S.S. Kocha, Oxygen Reduction Reaction Measurements on Platinum Electrocatalysts Utilizing Rotating Disk Electrode Technique: I. Impact of Impurities, Measurement Protocols and Applied Corrections, J. Electrochem. Soc. 162 (2015) F1144–F1158. Creative Commons Attribution 4.0 Licence (CC BY, http://creativecommons.org/licenses/by/4.0/).

6.3.2 Supporting electrolyte

The typical electrolyte employed for ORR characterization is 0.1 M $HClO_4$, while in older papers the activity was evaluated in 0.5 M H_2SO_4 as well. H_2SO_4 should be avoided because of high adsorption of sulphate species on Pt. Cons of $HClO_4$ are due to Cl^- impurities, but their negative effect could be restricted using low concentration of this electrolyte, such as 0.1 M. The ECSA is not affected by different electrolyte, on the contrary the MA is around 5 times lower in H_2SO_4, as reported in Figure 6.15 [28]. In this figure also the behaviour of 0.1 M KOH is reported.

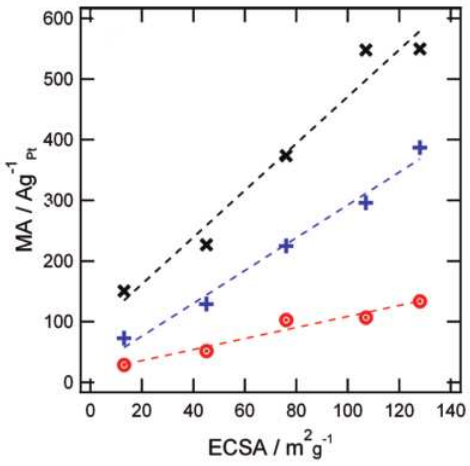

Figure 6.15 MAs versus ECSA in 0.1 M $HClO_4$ (black dots), 0.05 M H_2SO_4 (red dots) and 0.1 M KOH (blue dots). Adapted with permission from M. Nesselberger, S. Ashton, J.C. Meier, I. Katsounaros, K.J.J. Mayrhofer, M. Arenz, The particle size effect on the oxygen reduction reaction activity of Pt catalysts: influence of electrolyte and relation to single crystal models, J. Am. Chem. Soc. 133 (2011) 17428–33. Copyright 2011 American Chemical Society.

6.3.3 Purity grade of supporting electrolyte

The choice of purity grade of the electrolyte for the electrochemical performances determination is fundamental. When perchloric acid is employed, the effect of purity grade on the SA of a polycrystalline Pt toward ORR is shown in Figure 6.16. Basically all reagents superior than ACS and Trace Metal Basis can be used without considerably reducing the performances.

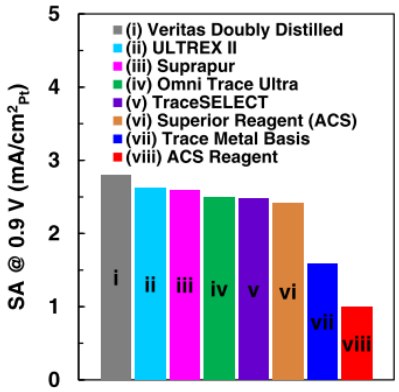

Figure 6.16 SA calculated at 0.9 V/RHE for ORR on poly-Pt. Effect of purity grade of electrolyte. K. Shinozaki, J.W. Zack, R.M. Richards, B.S. Pivovar, S.S. Kocha, Oxygen Reduction Reaction Measurements on Platinum Electrocatalysts Utilizing Rotating Disk Electrode Technique: I. Impact of Impurities, Measurement Protocols and Applied Corrections, J. Electrochem. Soc. 162 (2015) F1144–F1158. Creative Commons Attribution 4.0 Licence (CC BY, http://creativecommons.org/licenses/by/4.0/).

6.3.4 Catalyst layer

The catalyst layer preparation is another key parameter for succeeding in ORR testing. This is realized suspending the catalyst in an optimized ink, and a certain amount of which is drop-casted on a clean GC surface and dried. First of all, ink composition is fundamental for the obtaining of higher ECSA value. As reported by Kocha in Figure 6.17, the higher ECSA are obtained with inks made of water, isopropanol (IPA) and nafion, and generally, if isopropanol is absent or its content is not optimized, the resulting ECSA is lower.

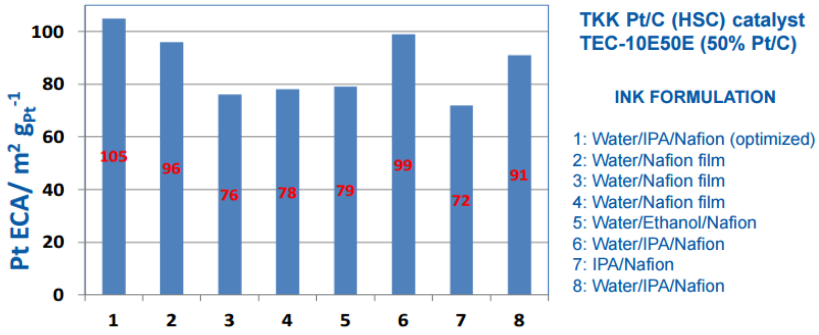

Figure 6.17 ECSA for the same Pt/C catalyst obtained with different ink compositions [30].

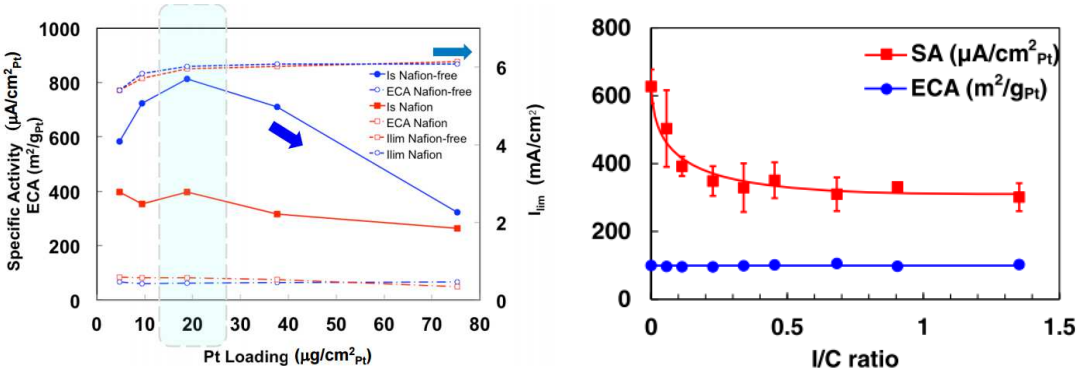

Figure 6.18 On the left the effects of Pt loading on the surface of the GC on SA, limiting current and ECSA of an ink with and without nafion are reported [30]. On the right there is the dependence of SA and ECSA on Ionomer/Carbon ratio K. Shinozaki, J.W. Zack, S. Pylypenko, B.S. Pivovar, S.S. Kocha, Oxygen Reduction Reaction Measurements on Platinum Electrocatalysts Utilizing Rotating Disk Electrode Technique: ii Influence Of Ink Formulation, Catalyst Layer Uniformity and Thikness, J. Electrochem. Soc. 162 (2015) F1384-F1396. Creative Commons Attribution 4.0 Licence (CC BY http://creativecommons.org/licenses/by/4.0/).

The sonication of the ink should be carried out in ice-cooled ultrasonic bath or horn-sonicator, in the latter case for a shorter time. Pt loading on GC should be included between 15

and 25 μg/cm^2, in order to maintain higher SA and limiting currents, which can increase further in absence of Nafion (Figure 6.18, left). Furthermore, it's important to maintain a low Ionomer/Carbon (I/C) ratio in order to obtain higher specific activities (Figure 6.18, right) [31], while ECSA seems to be not affected by this parameter.

The drying of the ink on the GC surface is a fundamental step for a good film deposition. Static drying or rotational drying are usually employed. The first case is the traditional catalyst layer fabrication technique, and consists simply in the dropping of the ink on a GC surface; in the second procedure the ink is drop-casted on a GC tip mounted on inverted rotator shaft and dried at 700 rpm. Several methods are available to determine the qualitative degree of catalyst layer uniformity. Pictures of the same catalyst layers prepared with these two different protocols show the higher homogeneity of the catalyst layers obtained via rotational drying. In particular, static drying are responsible for the generation of the so called 'coffee ring' structure, corresponding to inhomogeneity of the catalyst layer, which agglomerate preferably on the border of the GC. This structure is to be avoided because it determines a lowering and a non-reproducibility of the ORR performance as well [27].

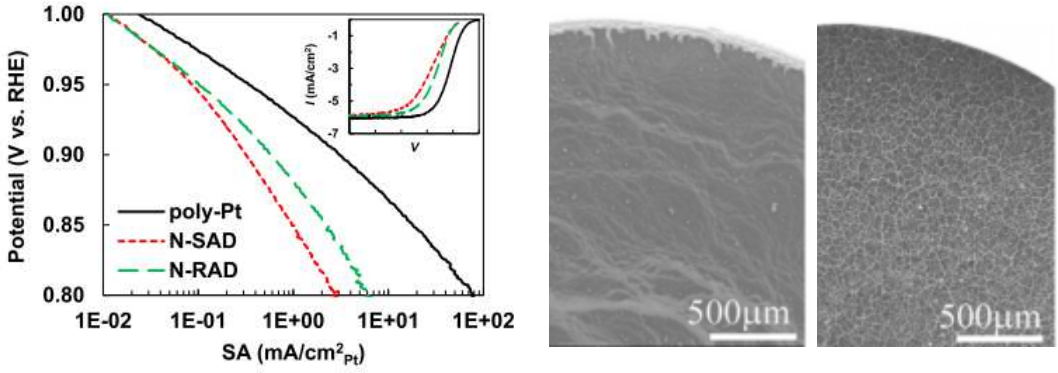

Figure 6.19 a) effect of drying method on the ORR performance of poly-Pt (black) and 46.4%Pt/C catalyst layers prepared using static drying (red) and rotational drying (green) reprinted from International Journal of Hydrogen Energy, 40, K. Shinozaki, J.W. Zack, S. Pylypenko, R.M. Richards, B.S. Pivovar, S.S. Kocha, Benchmarking the oxygen reduction reaction activity of Pt-based catalysts using standardized rotating disk electrode methods, 16820–16830., Copyright 2015, with permission from Elsevier. b and c) SEM images of GC disk with Pt/C distributed by static drying and rotational drying, respectively, reprinted from Electrochimica Acta, 72, K. Ke, K. Hiroshima, Y. Kamitaka, T. Hatanaka, Y. Morimoto, An accurate evaluation for the activity of nano-sized electrocatalysts by a thin-film rotating disk electrode: Oxygen reduction on Pt/C, 120–128, Copyright 2012, with permission from Elsevier.

6.3.5 Electrochemical measurement

Each Pt NPs on high surface area catalyst has to be electrochemically activated before the performance test. The conditioning, called also break in, consists in potential cycles in the range between 0.05 and 1.2 V/RHE. This in an approximate range that might vary according the sample. Usually the number of cycles is not fixed, but the conditioning can be stopped as the consecutive CVs are stable. Generally, upper potential around 1 V/RHE is not enough for a complete activation of Pt, but attention is needed in increasing it till 1.3 or 1.4 V/RHE, because these potentials might damage the catalyst layer. So, an evaluation of the final MA and SA values is necessary to understand if the applied conditioning was correct. The most important parameter seems to be the time of conditioning, and not the total number of cycles.

Electrochemical surface area (ECSA) was evaluated by H adsorption and desorption signals present in CVs recorded in steady state conditions under inert atmosphere (Ar or N_2 sat 0.1 M $HClO_4$). Low scan rate, such as 50 mV/s, are recommended in order to keep the capacitive current low.

The activity toward oxygen reduction is given as current density per Pt surface area or mass at 0.9 V/RHE and 100 kPa O_2. The potential equal to 0.9 V/RHE is selected because the OCV of Pt in acid electrolytes is about 1 V; the ORR currents at 0.9 V are small enough that they may be expected to have negligible resistance due to solution and to catalyst layer as well as complete participation of all the active sites; the ORR currents are large enough in comparison to the reverse currents (i.e. Pt dissolution, carbon corrosion and impurities). It's important to select scan and a rotation rates for all the experiments, to allow comparison among different measurements. In fact, Pt oxide suppresses ORR kinetics, and it is formed at high potential, as well as other mixed surface oxide species (PtOH, PtO), and the coverage is function of both potential and time. Anodic scan for ORR shows higher performance than the cathodic one, because in this situation a free Pt surface (not covered with oxides species) is assured. The scan rate should be included between 5 and 20 mV/s. If 5 mV/s are applied there is a high contribution of surface oxides and impurities in suppressing ORR activity, on the contrary a high capacitive current appears if the scan rate is increased. For this reason, background currents need to be measured in every experiment, and subtracted to the ORR measurements. Ohmic drop has to be determined before each experiment and compensate during the measurement of ECSA and performance [23] [24].

6.4 Determination of ORR performance with optimized experimental protocol: 1Pt@NMC, 1Pt@N,SMC, 1Pt@SMC and 1Pt@MC

In Table 6.8 all the experimental parameter set during the evaluation of oxygen reduction activity for all the catalysts are listed. The selected electrolyte was 0.1 M $HClO_4$. The ohmic drop was calculated after the conditioning with a single point impedance measurement, and the correction was automatically applied to all the following electrochemical measurements. N_2 and O_2 were bubbled in solution for 30 min. The WE was a 5 mm diameter GC disk, the CE was a Pt wire and the RE was a Reversible Hydrogen Electrode (RHE). RHE consists in a high surface area Pt grid, immersed in the same solution employed for the electrochemical measurement (0.1 M $HClO_4$). In this case the impurity level was minimum, for example chloride contamination due to SCE was suppressed. The ink was prepared by dissolving a proper amount of catalyst in a solution made of 2%$_v$ of nafion and 98%$_v$ of H_2O:IPA (80:20). The amount of polymer is higher than that used in several papers, in which a concentration of 0.4%$_v$ is suggested to keep as low as possible the I/C ratio [26]. The carbon particle size of the supports synthesized in this work is bigger than the one of commercial catalysts, so for this reason a higher amount of polymer is required to produce a homogeneous catalyst layer on the GC. Bigger particles create in fact a worse coating on the GC, and requires a higher amount of nafion to remain strongly adhered with the GC support and among themselves. The ink was set in an ice-cooled ultrasonic bath for 60 mins, and then treated with horn sonicator for 3 mins, prior to the drop-casting. The amount of catalyst in the ink was set in order to realize a 15 μg/cm^2 Pt loading on GC surface and drop-casting around 8-10 μL of ink. In fact, this is the proper amount to be deposited on the electrode to have a proper drying and no splitting of the drop on the teflon support around the GC. The rotational drying was conducted overnight at 700 rpm.

Table 6.8 Experimental protocol for the determination of ORR activity.

EXPERIMENTAL PROTOCOL						
Gas	***T***	***E range*** [a]	**Scan direction** [b]	υ_{scan} [a]	***Cycles*** [c]	***Rotation rate***
	(°C)	(V)		(mV/s)		(rpm)
Conditioning						
N_2	27	0.05-1.20	-	500	150	0
ECSA						
N_2	27	0.05-1.05	-	50	6	0
ORR background						
N_2	27	0.05-1.05	Anodic	20	5	1600 400 900 2500
ORR performance						
O_2	27	0.05-1.05	anodic	20	5	1600 400 900 2500

[a] all potentials are referred to RHE
[b] CV is performed in all determinations, but in the case of ORR background and performance only the anodic scan is analysed
[c] this is the number of cyclic voltammograms. In the case of ORR the first rotation speed analysed was 1600 rpm, performed twice to assure a proper activation of the surface, especially after bubbling O_2 in the cell.

6.4.1 ORR in 0.5 M H_2SO_4: 1Pt@NMC, 1Pt@SMC, 1Pt@N,SMC

Electrochemical characterization toward ORR on 1Pt@NMC, 1Pt@N,S-MC and 1Pt@SMC was repeated with the optimized protocol. In **Figure 6.20** the anodic scans for oxygen reduction in 0.1 M H_2SO_4 on 1Pt@NMC, 1Pt@N,S-MC, 1Pt@SMC and Pt/C as commercial reference, are reported. The obtained data are reported in Table 6.9.

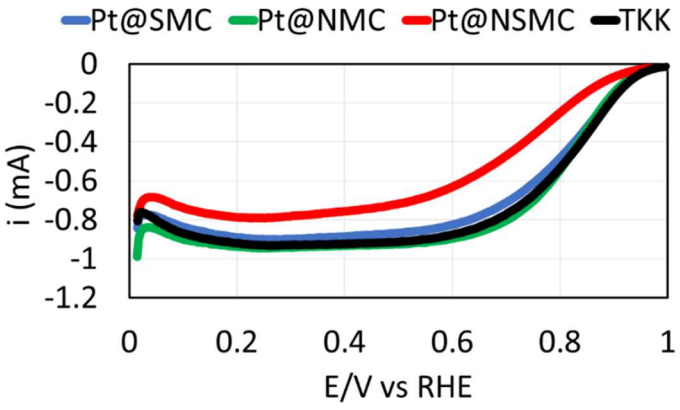

Figure 6.20 RDE analysis for ORR on 1Pt@NMC (blue), 1Pt@N,SMC (red) and 1Pt@SMC (black) in 0.5 M H_2SO_4, scan rate: 20 mV/s, rotation rate 1600 rpm, with optimised protocol conditions.

Table 6.9 Electrochemical data for ORR in 0.5 M H_2SO_4 on 1Pt@NMC, 1Pt@NSMC, 1Pt@SMC, TKK obtained with optimized protocol.

MC	Pt load[a] ($\mu g/cm^2$)	ECSA[b,f] (m^2/g_{Pt})	MA@0.9[c,e,f] (A/g)	MA'@0.9[c,d] (A/g)	SA@0.9[c,e,f] ($\mu A/cm^2$)
1Pt@NMC	15	69.1 ± 2.1	59.2±4.4	3	86.1 ± 4.53
1Pt@NSMC	15	28.8 ± 3.5	24.3 ± 0.2	3	85.9 ± 10.99
1Pt@SMC	15	64.0 ± 1.6	77.4 ± 1.7	16	120.9 ± 0.4
Pt50%	15	79.8 ± 1.9	76.4 ± 3.7	2	95.8 ± 6.9

[a] Pt loading on the GC electrode surface
[b] determined by H adsorption and desorption signals
[c] all potentials are referred to RHE
[d] values obtained with non-optimized measurement protocol
[e] values obtained with optimized measurement protocol
[f] standard deviation obtained from the square root of sum of square variations from the mean value, divided by the number of data analysed.

The performance for ORR obtained with an optimized protocol are much better than the values obtained in non-optimized conditions (Figure 6.21), and the increase of MA varies from 5 to 40 times with respect to previous determination. The MA is higher for 1Pt@SMC and decrease for 1Pt@NMC and 1Pt@NSMC. The catalytic activity of reference material is comparable to the performance of 1Pt@SMC. All the experiment are repeated at least four times and they show a good reproducibility, also in the cases in which the ink was prepared ex novo (i.e. every day). The differences in ECSA and MA arise presumably in the ionic impurities introduced with the non-optimized protocol which adsorb on Pt active sites and make them not

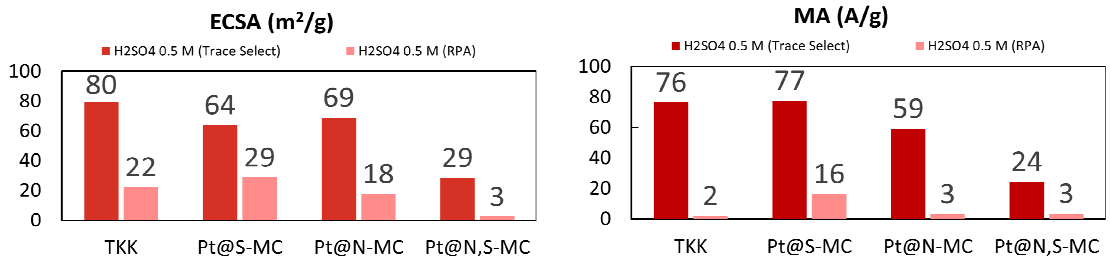

Figure 6.21 Histograms illustrating ECSA and MA values for 1Pt@NMC, 1Pt@NSMC, 1Pt@SMC and TKK with non-optimized (pink) and optimized (red) protocols.

accessible to oxygen, i.e. Aqua Regia residual due to lack of boiling steps in the cleaning procedure, KNO_3 released from the salt bridge of SCE jacket, and the cathodic scan as well, which doesn't consider the Pt oxides formation. In this work the importance of experimental protocol in the determination of electrochemical activity is highlighted. It's clear that Pt is very sensitive to passivation due to impurities, so the protocol has to be evaluated carefully in order to eliminate all phenomena which can determine abatement of ORR performance.

6.4.2 Solid State deposition on undoped MC

The solid state deposition of Pt from $Pt(acac)_2$ at 300 °C under H_2/N_2 flow was repeated also on MC, a mesoporous carbon described in Chapter 4 synthesized from phenanthrene. This material represent the reference material for the evaluation of catalytic activity obtained with Pt NPs on differently doped mesoporous carbons. In fact, the material possesses the same morphology as the Pt on differently doped catalyst, but it's not doped and allows to quantify the effect of heteroatoms in the ORR performance of Pt.

In Figure 6.22 TEM images at two different magnifications of 1Pt@MC show that the Pt NPs on that carbon support don't have a controlled and narrow dimension distribution: some region of the carbon surface are covered with very small particles, while others have big aggregates of mean diameter equal to 20 nm. The comparison with the morphology obtained in the case of 1Pt@NMC, 1Pt@SMC and 1Pt@NSMC highlights the strong effect of N and S doping of carbon support in creating narrow and homogeneous NPs distribution on the mesoporous carbon support.

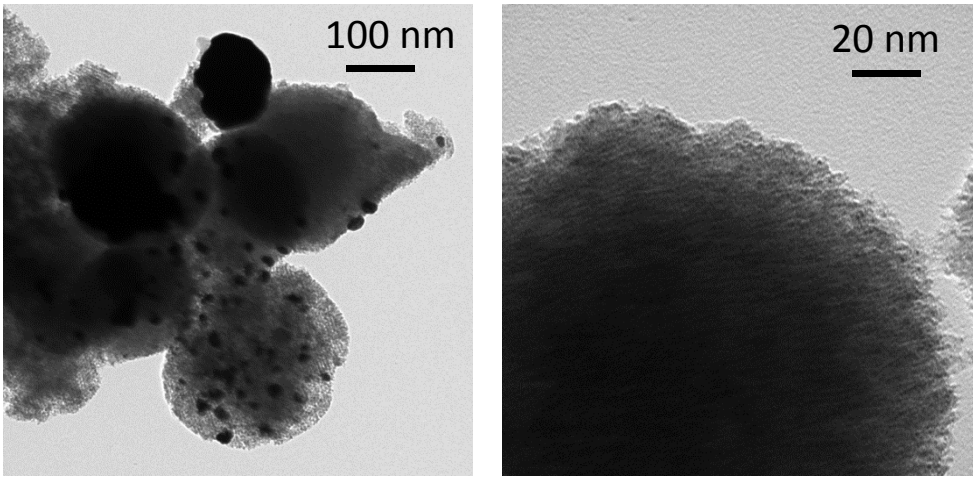

Figure 6.22 TEM images of Pt@MC obtained via solid state deposition of $Pt(acac)_2$ at two different magnifications.

6.4.3 ORR in 0.1 M $HClO_4$: 1Pt@NMC, 1Pt@SMC, 1Pt@MC

Oxygen reduction performance was evaluated in 0.1 M $HClO_4$ with the optimized protocol described in Paragraph 6.4. The anodic scans recorded on 1Pt@NMC, 1Pt@SMC and 1Pt@MC are reported in **Figure 6.23**, along with the comparison with the commercial Pt/C catalyst (TKK).

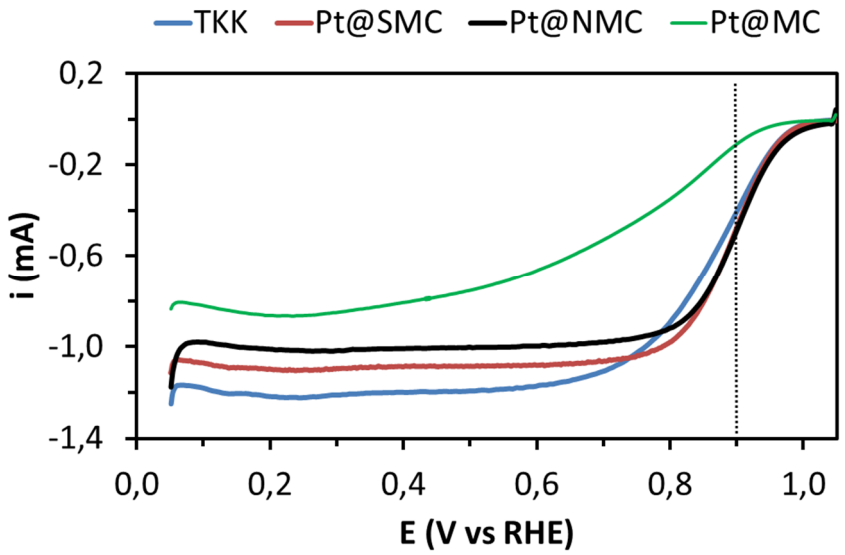

Figure 6.23 RDE analysis for ORR on 1Pt@NMC (black), 1Pt@SMC (red) and 1Pt@MC (green) and commercial Pt/C (TKK, blue) in 0.1 M $HClO_4$, scan rate: 20 mV/s, rotation rate 1600 rpm, anodic scan, with optimised protocol conditions.

In Table 6.10 the electrochemical data for ORR are reported, while in **Figure 6.24** there are two histogram graphs reporting the values of MA and ECSA for 1Pt@NMC, 1Pt@NSMC, 1Pt@SMC and TKK. It can be clearly seen that the most active catalyst toward ORR is 1Pt@SMC, with a MA equal to 271 A/g, followed by 1Pt@NMC with a MA of 255 A/g. Pt/C commercial reference shows lower performance than 1Pt@SMC and 1Pt@NMC, equal to 222 A/g. 1Pt@MC is the least active catalyst, showing a MA equal to 44 A/g. Its CV shows sluggish kinetics for oxygen reduction, as appears from the stretched shape of the mixed kinetic-diffusion controlled region, and a lower limiting current as well. The ECSA values are probably consistent with an incomplete Pt utilization: the amount of Pt on the GC support is the same in all the catalysts (15 $\mu g/cm^2$) and from TEM images the dimension of Pt NPs on 1Pt@NMC and 1Pt@SMC are similar to that of TKK. Nevertheless the ECSA for the home-made samples is lower than the TKK, and given also the bigger size of carbon particles, it is reasonable that the Pt NPs in the core of the carbon sphere are not in touch with electrolyte. This is because Pt NPs closer to the pore entrance block the access to the inner part of the carbon structure.

Table 6.10 Electrochemical data for ORR in 0.1 M $HClO_4$ on 1Pt@NMC, 1Pt@NSMC, 1Pt@SMC, TKK obtained with optimized protocol.

MC	Pt loading[a] ($\mu g/cm^2$)	ECSA[b,e,f] (m^2/g_{Pt})	MA@0.9[c,e,f] (A/g)	SA@0.9[c,e,f] ($\mu A/cm^2$)
1Pt@NMC	15	75 ± 1	255 ± 37	337 ± 50
1Pt@SMC	15	55 ± 9	271 ± 24	501 ± 67
1Pt@MC	15	9 ± 1	44 ± 3	520 ± 68
Pt50% (TKK)	15	79 ± 4	222 ± 15	282 ± 23

[a] Pt loading on the GC electrode surface
[b] determined by H adsorption and desorption signals
[c] all potentials are referred to RHE
[e] values obtained with optimized measurement protocol
[f] standard deviation obtained from the square root of sum of square variations from the mean value, divided by the number of data analysed

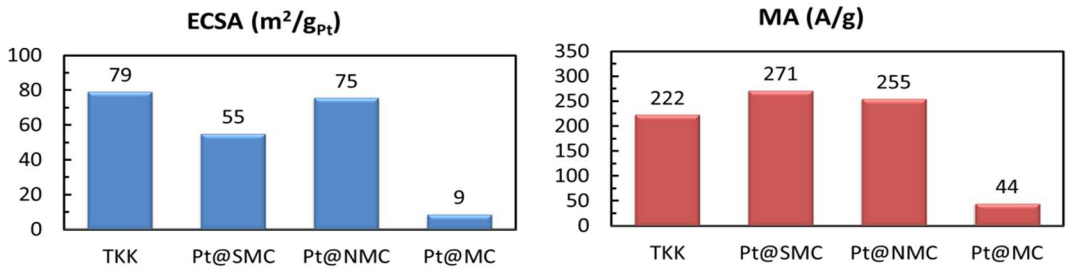

Figure 6.24 Histograms illustrating ECSA and MA values for 1Pt@NMC, 1Pt@NMC, 1Pt@MC and TKK determined with optimized protocol.

6.4.4 Electrochemical stability test in 0.1 M $HClO_4$: 1Pt@NMC, 1Pt@SMC, 1Pt@MC. Protocol 1.

The first electrochemical stability test consists in applying 10000 cycles between 0.6 and 0.9 V/RHE at 0.5 V/s in 0.1 M $HClO_4$. In this conditions the main degradation is due to Pt oxidation and migration, so the process determines an increase in the mean particle size, corresponding to a decrease in surface area, and loss of Pt due to dissolution [29]. CVs at 50 mV/s were recorded before and after the test in the range 0.05 – 1.05 V/RHE in order to calculate ECSA, and are reported in **Figure 6.25** a and b for 1Pt@SMC and 1Pt@NMC, respectively. The test highlights that the Pt on NMC is more stable than the SMC: a smaller decrease in H adsorption and desorption signals is present in the CVs reported. This is clear also from the data reported in Table 6.11, where the final ECSA is reported. 1Pt@MC is the less stable material, and has a final ECSA equal to only 45% of the initial value. 1Pt@SMC shows an ECSA loss equal to 25%. The smaller Pt NPs size of 1Pt@SMC might be responsible for its lower stability compared 1Pt@NMC.

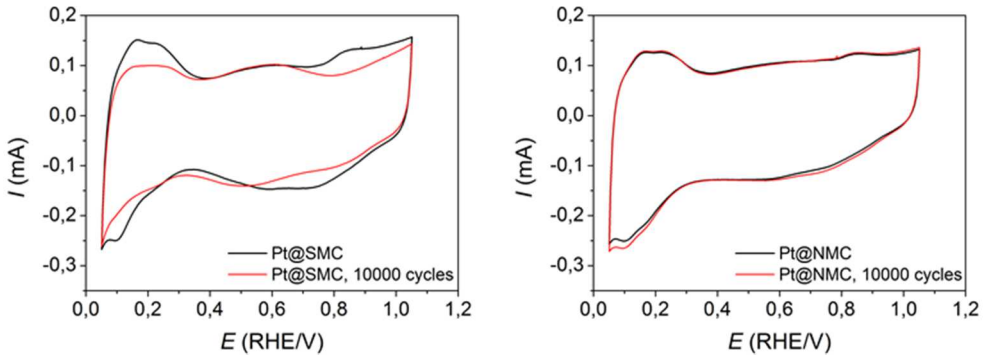

Figure 6.25 CVs for ECSA determination in N_2 sat. 0.1 M $HClO_4$ before (black) and after (red) the stability test for a) 1Pt@SMC and b) 1Pt@NMC. Scan rate: 50 mV/s.

Table 6.11 ECSA value before and after the stability test in N_2 0.1 M $HClO_4$ consisting in 10000 potential cycles between 0.6 and 0.9 V/RHE.

Catalyst	Pt loading ($\mu g/cm^2$)	ECSA (m^2/g_{Pt})	FINAL ECSA (m^2/g_{Pt})	FINAL ECSA (%)
1Pt@NMC	15	75	69	92
1Pt@SMC	15	55	41	75
1Pt@MC	15	9	4	45
Pt50% (TKK)	15	79	70	89

Commercial Pt/C catalyst shows a slightly lower stability than 1Pt@NMC, but anyway it is more stable than the Pt on S-MC and on un-doped MC.

6.4.5 Electrochemical stability test in 0.1 M $HClO_4$: 1Pt@NMC, 1Pt@SMC, 1Pt@MC. Protocol 2.

The second electrochemical stability test consists in applying 3600 potential cycles between 0.4 and 1.4 V/RHE at 0.5 V/s in 0.1 M $HClO_4$. This conditions are stronger than the previous experiment, and the degradation is due to both Pt and C corrosion. Pt, as in the previous case, can agglomerate and dissolve, and C is oxidized to quinone species or CO_2. The Pt ECSA is determined at the beginning, at the end and each 1200 potential cycles of the stability test, and its values are reported in **Figure 6.26** and in **Table 6.12**. The main degradation for all samples occurs in the first part of the test, after 1200 cycles a stabilization of the system seems to occur. This is consistent with predominant Pt Ostwald ripening in the first 1200 cycles, followed by oxidation phenomena involving both Pt and C in the last part of the test.

Table 6.12 ECSA values before and after the stability test in N_2 0.1 M $HClO_4$ consisting in 3600 potential cycles between 0.4 and 1.4 V/RHE at 500 mV/s.

MC	Pt loading ($\mu g/cm^2$)	ECSA (m^2/g_{Pt})	FINAL ECSA (%)
1Pt@NMC	15	75	28
1Pt@SMC	15	55	36
1Pt@MC	15	9	23
Pt50% (TKK)	15	79	57

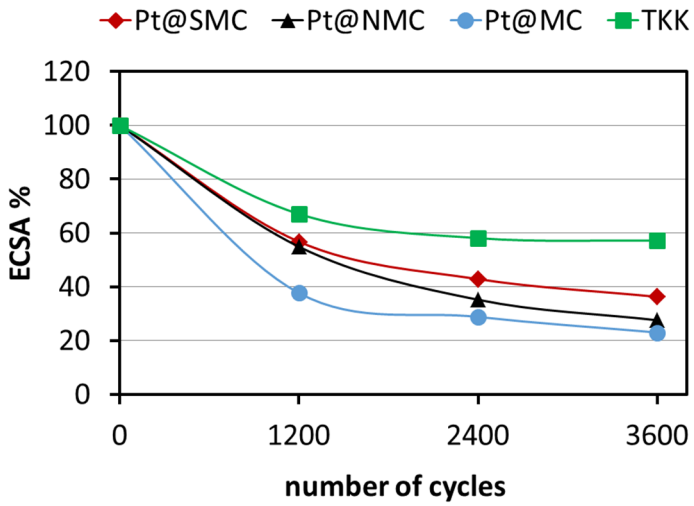

Figure 6.26 ECSA values before, during and after the stability test in N_2 0.1 M $HClO_4$ consisting in 3600 potential cycles between 0.4 and 1.4 V/RHE at 500 mV/s.

The commercial Pt/C (TKK) catalyst shows superior stability in this electrochemical stress test, and the main reason might be connected with the higher degree of graphitization of the commercial carbon support of Pt/C. Oxygen containing groups, present as well in the mesoporous carbons N-MC, S-MC and MC, are responsible for a lower resistance to oxidation.

Bibliography

[1] O. Cherstiouk, P. Simonov, E. Savinova, Model approach to evaluate particle size effects in electrocatalysis: preparation and properties of Pt nanoparticles supported on GC and HOPG, Electrochim. Acta 48 (2003) 3851–3860. doi:10.1016/S0013-4686(03)00519-X.

[2] F. Maillard, S. Schreier, M. Hanzlik, E.R. Savinova, S. Weinkauf, U. Stimming, Influence of particle agglomeration on the catalytic activity of carbon-supported Pt nanoparticles in CO monolayer oxidation, Phys. Chem. Chem. Phys. 7 (2005) 385–393. doi:10.1039/b411377b.

[3] F. Maillard, E.R. Savinova, U. Stimming, CO monolayer oxidation on Pt nanoparticles: Further insights into the particle size effects, J. Electroanal. Chem. 599 (2007) 221–232. doi:10.1016/j.jelechem.2006.02.024.

[4] M.J. Watt-Smith, J.M. Friedrich, S. Rigby, T.R. Ralph, F.C. Walsh, Determination of the electrochemically active surface area of Pt/C PEM fuel cell electrodes using different adsorbates, J. Phys. D. Appl. Phys. 41 (2008) 174004. doi:10.1088/0022-3727/41/17/174004.

[5] B. Fang, B.N. Wanjala, J. Yin, R. Loukrakpam, J. Luo, X. Hu, J. Last, C.J. Zhong, Electrocatalytic performance of Pt-based trimetallic alloy nanoparticle catalysts in proton exchange membrane fuel cells, Int. J. Hydrogen Energy 37 (2012) 4627–4632. doi:10.1016/j.ijhydene.2011.05.066.

[6] T. Vidaković, M. Christov, K. Sundmacher, The use of CO stripping for in situ fuel cell catalyst characterization, Electrochim. Acta 52 (2007) 5606–5613. doi:10.1016/j.electacta.2006.12.057.

[7] C.M. Pedersen, M. Escudero-Escribano, A. Velázquez-Palenzuela, L.H. Christensen, I. Chorkendorff, I.E.L. Stephens, Benchmarking Pt-based electrocatalysts for low temperature fuel cell reactions with the rotating disk electrode: oxygen reduction and hydrogen oxidation in the presence of CO (review article), Electrochim. Acta 179 (2015) 1–11. doi:10.1016/j.electacta.2015.03.176.

[8] K.J.J. Mayrhofer, D. Strmcnik, B.B. Blizanac, V. Stamenkovic, M. Arenz, N.M. Markovic, Measurement of oxygen reduction activities via the rotating disc electrode method: From Pt model surfaces to carbon-supported high surface area catalysts, Electrochim. Acta 53 (2008) 3181–3188. doi:10.1016/j.electacta.2007.11.057.

[9] J. Ma, A. Habrioux, C. Morais, A. Lewera, W. Vogel, Y. Verde-Gómez, G. Ramos-Sanchez, P.B. Balbuena, N. Alonso-Vante, Spectroelectrochemical probing of the strong interaction between platinum nanoparticles and graphitic domains of carbon, ACS Catal. 3 (2013) 1940–1950. doi:10.1021/cs4003222.

[10] S. Mukerjee, Particle size and structural effects in platinum electrocatalysis, J. Appl. Electrochem. 20 (1990) 537–548. doi:10.1007/BF01008861.

[11] L. Su, W. Jia, C.-M. Li, Y. Lei, Mechanisms for enhanced performance of platinum-based electrocatalysts in proton exchange membrane fuel cells, ChemSusChem. 7 (2014) 361–78. doi:10.1002/cssc.201300823.

[12] Y. Liu, L. Zhang, B.G. Willis, W.E. Mustain, Importance of Particle Size and Distribution in Achieving High-Activity, High-Stability Oxygen Reduction Catalysts, ACS Catal. 5 (2015)

1560–1567. doi:10.1021/cs501556j.

[13] M. Shao, A. Peles, K. Shoemaker, Electrocatalysis on Platinum Nanoparticles : Particle Size Effect on oxygen reduction reaction activity, Nano Lett. 11 (2011) 3714–3719. doi:10.1021/nl2017459.

[14] F.J. Perez-Alonso, D.N. McCarthy, A. Nierhoff, P. Hernandez-Fernandez, C. Strebel, I.E.L. Stephens, J.H. Nielsen, I. Chorkendorff, The Effect of Size on the Oxygen Electroreduction Activity of Mass-Selected Platinum Nanoparticles, Angew. Chemie 51 (2012) 4641–4643. doi:10.1002/anie.201200586.

[15] Y. Luo, N. Alonso-Vante, The Effect of Support on Advanced Pt-based Cathodes towards the Oxygen Reduction Reaction. State of the Art, Electrochim. Acta (2015). doi:10.1016/j.electacta.2015.04.098.

[16] L. Perini, C. Durante, M. Favaro, V. Perazzolo, S. Agnoli, O. Schneider, G. Granozzi, A. Gennaro, Metal–Support Interaction in Platinum and Palladium Nanoparticles Loaded on Nitrogen-Doped Mesoporous Carbon for Oxygen Reduction Reaction, ACS Appl. Mater. Interfaces. 7 (2015) 1170–1179. doi:10.1021/am506916y.

[17] X. Ning, H. Yu, F. Peng, H. Wang, Pt nanoparticles interacting with graphitic nitrogen of N-doped carbon nanotubes: Effect of electronic properties on activity for aerobic oxidation of glycerol and electro-oxidation of CO, J. Catal. 325 (2015) 136–144. doi:10.1016/j.jcat.2015.02.010.

[18] R. Wang, D.C. Higgins, M.A. Hoque, D. Lee, F. Hassan, Z. Chen, Controlled growth of platinum nanowire arrays on sulfur doped graphene as high performance electrocatalyst, Sci. Rep. 3 (2013) 2431. doi:10.1038/srep02431.

[19] D. Higgins, M.A. Hoque, M.H. Seo, R. Wang, F. Hassan, J.-Y. Choi, M. Pritzker, A. Yu, J. Zhang, Z. Chen, Development and Simulation of Sulfur-doped Graphene Supported Platinum with Exemplary Stability and Activity Towards Oxygen Reduction, Adv. Funct. Mater. 24 (2014) 4325–4336. doi:10.1002/adfm.201400161.

[20] L. Li, S.G. Chen, Z.D. Wei, X.Q. Qi, M.R. Xia, Y.Q. Wang, Experimental and DFT study of thiol-stabilized Pt/CNTs catalysts, Phys. Chem. Chem. Phys. 14 (2012) 16581–16587. doi:10.1039/C2CP41346A.

[21] P.J. Ferreira, G.J. la O', Y. Shao-Horn, D. Morgan, R. Makharia, S. Kocha, H. Gasteiger, Instability of Pt⁄C Electrocatalysts in Proton Exchange Membrane Fuel Cells, J. Electrochem. Soc. 152 (2005) A2256. doi:10.1149/1.2050347.

[22] K. Shinozaki, J.W. Zack, S. Pylypenko, R.M. Richards, B.S. Pivovar, S.S. Kocha, Effect of measurement protocol and impurity levels on the oxygen reduction reaction activity of Pt/C using rotating disk electrode, Abstr. Pap. 249th ACS Natl. Meet. Expo. Denver, CO, United States, March 22-26, 2015. (2015) CATL-70. doi:10.1016/j.ijhydene.2015.08.024.

[23] K. Shinozaki, J.W. Zack, R.M. Richards, B.S. Pivovar, S.S. Kocha, Oxygen Reduction Reaction Measurements on Platinum Electrocatalysts Utilizing Rotating Disk Electrode Technique: I. Impact of Impurities, Measurement Protocols and Applied Corrections, J. Electrochem. Soc. 162 (2015) F1144–F1158. doi:10.1149/2.1071509jes.

[24] Y. Garsany, O. Baturina, K.E. Swider-Lyons, S.S. Kocha, Experimental Methods for Quantifying the Activity of Platinum Electrocatalysts for the Oxygen Reduction Reaction, Anal. Chem. 82 (2010) 6321–6328. doi:10.1021/ac100306c.

[25] K. Shinozaki, B.S. Pivovara, S.S. Kocha, Enhanced Oxygen Reduction Activity on Pt/C for Nafion-free, Thin, Uniform Films in Rotating Disk Electrode Studies, ECS Trans. 58 (2013) 15–26. doi:10.1149/05801.0015ecst.

[26] K. Shinozaki, J.W. Zack, S. Pylypenko, R.M. Richards, B.S. Pivovar, S.S. Kocha, Benchmarking the oxygen reduction reaction activity of Pt-based catalysts using standardized rotating disk electrode methods, Int. J. Hydrogen Energy 40 (2015) 16820–16830. doi:10.1016/j.ijhydene.2015.08.024.

[27] K. Ke, K. Hiroshima, Y. Kamitaka, T. Hatanaka, Y. Morimoto, An accurate evaluation for the activity of nano-sized electrocatalysts by a thin-film rotating disk electrode: Oxygen reduction on Pt/C, Electrochim. Acta 72 (2012) 120–128. doi:10.1016/j.electacta.2012.04.004.

[28] M. Nesselberger, S. Ashton, J.C. Meier, I. Katsounaros, K.J.J. Mayrhofer, M. Arenz, The particle size effect on the oxygen reduction reaction activity of Pt catalysts: influence of electrolyte and relation to single crystal models, J. Am. Chem. Soc. 133 (2011) 17428–33. doi:10.1021/ja207016u.

[29] A. Zana, C. Rüdiger, J. Kunze-Liebhäuser, G. Granozzi, N.E. Reeler, T. Vosch, J.J.K. Kirkensgaard, M. Arenz, Core-shell TiO_2@C: Towards alternative supports as replacement for high surface area carbon for PEMFC catalysts, Electrochim. Acta 139 (2014) 21–28. doi:10.1016/j.electacta.2014.07.002.

[30] https://energy.gov/sites/prod/files/2014/03/f12/webinarslides_rde_technique_03121 3.pdf. Consulted on September 28, 2016.

[31] K. Shinozaki, J.W. Zack, S. Pylypenko, B.S. Pivovar, S.S. Kocha, Oxygen Reduction Reaction Measurements on Platinum Electrocatalysts Utilizing Rotating Disk Electrode Technique: ii Influence Of Ink Formulation, Catalyst Layer Uniformity and Thikness, J. Electrochem. Soc. 162 (2015) F1384-F1396

Chapter 7

Industrial Applications

In this chapter two potentially useful industrial application of the materials synthesized and tested in this Ph.D work are described. Differently doped mesoporous carbons were employed as catalysts for in situ hydrogen peroxide production for the degradation of organic pollutants. The catalysts made of Pt NPs on differently doped mesoporous carbons were incorporated in a membrane electrode assembly (MEA) and tested as cathode materials in proton exchange membrane fuel cells.

7.1 1Pt@N-MC and 1Pt@S-MC: cathode side of a PEMFC

The catalysts 1Pt@N-MC and 1Pt@S-MC were incorporated in a MEA in order to be tested as cathode in a PEM fuel cell. The preparation of the MEAs was done by IonPower (New Castle, DE) according to in-house protocols. The MEAs possess a Pt loading equal to 0.1 mg/cm^2 at the anode and 0.3 mg/cm^2 at the cathode. The different loading is due to the different kinetics for oxygen reduction (cathodic reaction) and hydrogen oxidation (anodic reaction). In fact, hydrogen oxidation shows low overpotential and its kinetics is quite fast. On the contrary, oxygen reduction is hindered and requires a high overpotential to occur. The MEA consists in a 50 µm thick nafion membrane, supporting the commercial Pt/C catalyst on the anodic side and the 1Pt@N-MC or 1Pt@SMC on the cathodic side. A commercial material (TKK = Pt/C) was incorporated in a MEA, with the same properties, in order to realise a comparison between home-made catalysts and a commercial material. The MEA was assembled in a system such as the one reported in Figure 7.1, in which it occupies the central position. The cells has a symmetric configuration and consists in the following components, already fully described in Chapter 1:

- Anode and Cathode End Plates, in the outer part of the cell, used for regulation of entrance and exit of gases, reaction products and coolant.

- Current collectors
- Plates for gas spreading and directing homogeneously on the whole surface. Sometimes this part and the current collectors are built together.
- Gas diffusion layers (GDL). This is a very important supporting material, usually made of porous carbon fibers which allows electrical connection between the collectors and the electrode. The essential function of a GDL consists in the passage for reactants transport, heat and water removal, mechanical support to the MEA and protection of catalyst layers.
- MEA.

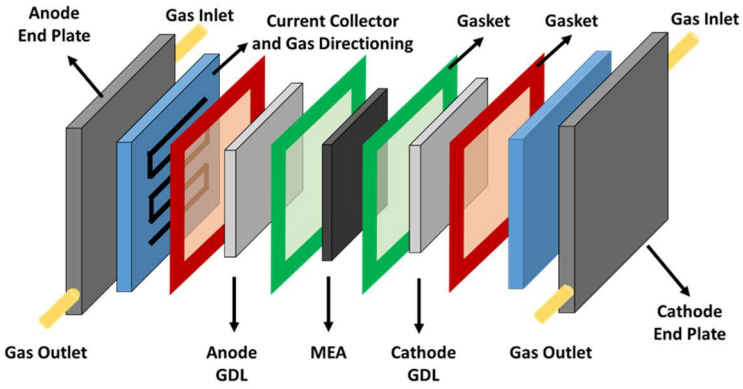

Figure 7.1 Cell for MEAs characterization. It is possible to appreciate all the components in the following order: end plates, current collectors, plates for gas directing, gas diffusion layers, gaskets and MEA.

The analysis of a MEA includes the measure of polarization curves, capacitance, impedance, ECSA and Tafel slope.

Polarization curves, power densities and impedance were obtained at three different relative humidity (RH): 30%, 80% and 160%. The RH was obtained by balancing the temperature of the coolant and of the inlet gas. The inlet gas at a fixed temperature passes through a humidifier with a fixed dew point, while the coolant temperature was varied according the desired RH. ECSA and capacitance were obtained at 100% RH, while the Tafel slope were calculated at 90% RH. Actually, a relative humidity of 160% indicates that the gas contains also liquid water. This value is obtained by the ratio of dew point temperature and coolant temperature.

In Figure 7.2 a and b the polarization curves and the power density curves for 1Pt@S-MC at three different relative humidity are respectively reported. Humidity has a strong influence over the nafion membrane: in fact, this property determines its degree of hydration, and, as a consequence, the performance of the catalyst. Low humidity value is deleterious for

the performance, because membrane is not completely hydrated and the migration of protons is hindered. The same effect is present also when the relative humidity is too high, because in this case the amount of water could determine clogging problems that prevent diffusion toward Pt catalyst or removal of formed water. These effects appear clearly in the curves in **Figure 7.2**, and the best performance were obtained when relative humidity is equal to 80%.

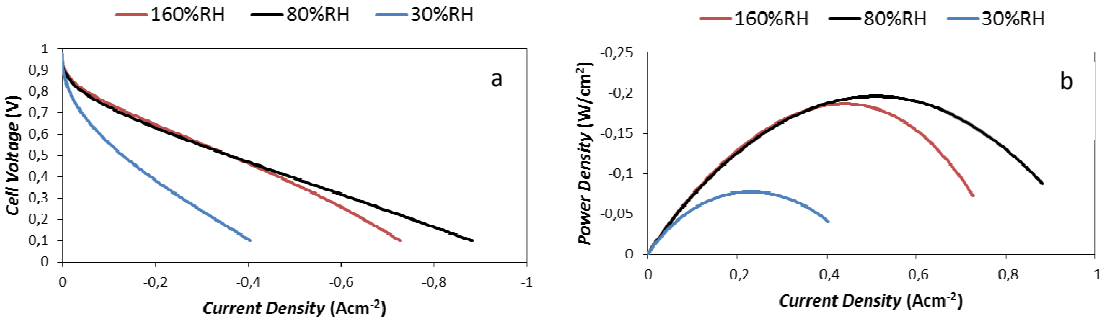

Figure 7.2 Polarization curves for 1Pt@SMC at three different relative humidity degrees: 160% (red), 80% (black) and 30% (blue). Scan rate: 5 mV/s

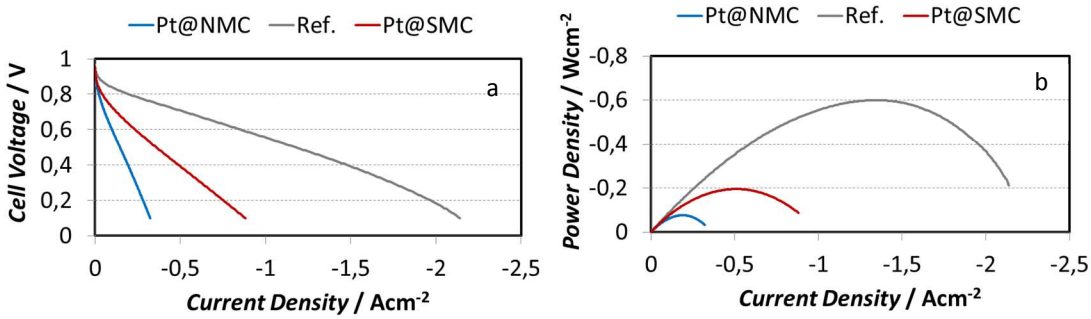

Figure 7.3 Polarization curves for 1Pt@SMC, 1Pt@NMC and Pt/C reference at 80% relative humidity.

Figure 7.3 a and b show current and power densities for 1Pt@NMC, 1Pt@SMC and the reference catalyst. 1Pt@S-MC has better performance than Pt@N-MC, but both materials show lower performance compared to the commercial Pt/C (Figure 7.3a). The current density for the Pt/C reference is double compared to 1Pt@S-MC.

In Table 7.1 all the data obtained by measuring MEAs with 1Pt@N-MC, 1Pt@S-MC and commercial Pt/C as cathode, are reported, with Pt loading equal to 0.3 mg/cm^2. Current densities obtained from polarization curves at 0.6 and 0.4 V (labelled *I*@0.6 and *I*@0.4), oxygen transport resistance and ohmic resistance are obtained from polarization curves reported in **Figure 7.2**, cyclic voltammetry at low scan rate and impedance spectroscopy, respectively, and in all cases Air was fed into the cathode and H_2 to the anode. ECSA and capacitance were obtained

via CVs under N_2 and H_2 at the anode and at the cathode, respectively, and at 100% relative humidity.

Table 7.1 Data obtained by testing the MEAs made of 1Pt@N-MC, 1Pt@SMC and Pt/C as cathode, Pt loading 0.3 mg/cm^2. In all cases anode is made of commercial Pt/C with 0.1 mg$_{Pt}$/cm^2.

	RH	***I*@0.6**[a]	***I*@0.4**[a]	***O*$_2$ res.**[b]	***R***[c]	***C***[d]		***ECSA***[e]	
	(%)	(mA/cm^2)	(mA/cm^2)	(S/m)	(mΩ)	(mF)		(m^2/g)	
						cat	an	1 nlpm	0 nlpm
	160	59.3	138.3	808.5	247.0				
1Pt@NMC	80	72.5	167.0	496.0	378.8	42.8	47.2	26.5	19.8
	30	43.3	80.1	571.2	2411				
	160	199.8	403.0	368.0	215.5				
1Pt@SMC	80	195.0	427.0	104.3	316.3	51.9	56.9	60.0	27.9
	30	61.2	146.3	176.0	940.0				
Pt/C ref.	80	856	1480	70	82	20		-	58

[a] obtained from polarization curves. Air was fed to the cathode.
[b] obtained from CVs at low scan rate. Air was fed to the cathode.
[c] obtained from impedance spectroscopy. Air was fed to the cathode.
[d] obtained from CVs at four different scan rates. 'An' refers to the anodic scans, 'Cat' to the cathodic scans. Relative humidity: 100%. N_2 was fed to the cathode.
[e] obtained by CV at low scan rate. The measurement was ususally carried out at reactant flow equal to 0, but in this case the CVs are better if the reactant flow is kept at 1nlpm. Relative humidity: 100%. N_2 was fed to the cathode.

The performances of Pt@N-MC and Pt@S-MC as cathode materials of a PEM fuel cell are not so good compared to the activity of commercial Pt/C. The conditions experimented in this analysis are much stronger than that in a RDE experiment. Generally, RDE gives important information regarding the electrochemical activity of a catalyst for ORR, but in a fuel cells several parameter contribute to the performance, such as higher temperature and pressure, gas flows, mass transport trough the GDL and in the catalyst layer, the nafion membrane. In fact, while in RDE measurements nafion simply act as a binder to keep nanoparticles attached among them and to the GC support, in a fuel cells it represents the fundamental material to keep in contact metal active sites and reagents.

Table 7.1 shows clearly a high O_2 transport and ohmic resistance for 1Pt@N-MC and 1Pt@SMC compared to commercial Pt/C. The O_2 transport resistance is deleterious especially for 1Pt@N-MC: in this case, as highlighted by BET analysis reported in Table 4.11 and Figure 4.23b, the pore size is smaller than 1Pt@SMC, in particular both carbon supports have a pore distribution centred at around 3.8 nm, but S-MC shows a significant fraction of bigger pores with mean diameter around 8.4 nm. In literature such pore dimension is reported to be good for fuel diffusion. On the contrary, Pt inside pore with diameter between 3 and 8 nm is considered not to contribute to the electrochemical reaction, because nafion polymer units are too big to enter

these pores, and as a consequence there is no contact among them and Pt NPs [1]. This might be the reason why the performance of 1Pt@NMC are even worse than that of 1Pt@SMC.

Ohmic resistance of 1Pt@NMC and 1Pt@SMC is much higher than that of the commercial Pt/C, and this is due probably for the carbon support. Mesoporous carbons usually possess lower electrical conductivity than commercial high-graphitized carbon support. This statement is reported in several papers, and was also confirmed in this work by the determination of electrical conductivity in several carbon materials obtained from different kind of silica (Section 4.2.5). The obtained data show a one-time fold decrease in electrical conductivity of N-MC (prepared with P200 silica) with respect to commercial MC.

The capacitance of 1Pt@N-MC and 1Pt@S-MC is higher than that of the commercial reference, and this is due for sure to the N and S functionalities that, as highlighted in Chapter 4, are responsible for pseudo-capacitive effect. The values reported in Table 7.1 are labelled '*cat*' and '*an*' obtained by integrating the current values in the cathodic scan and anodic scan direction, respectively.

The ECSA is lower for 1Pt@N-MC and 1Pt@S-MC with respect to commercial Pt/C. This might indicate as well that a low fraction of the whole Pt NPs on the carbon support is active, and this may be linked to the small pores, as described before. ECSA, in fact, is lowest for the sample with the smallest pore size (1Pt@NMC).

So, to briefly comment the obtained results, the MEA analysis of 1Pt@N-MC and 1Pt@S-MC highlights few problems associated with the nitrogen and sulphur doped mesoporous carbon as Pt support in PEM fuel cells. The different conditions in which the MEAs were investigated compared to that experimented in RDE analysis show that the electrical conductivity and the pores size were still not optimized for the employment of 1Pt@N-MC and 1Pt@S-MC in PEM fuel cells. In particular, the smallest pore sizes make the nafion distribution non homogeneous in the whole surface of the catalyst and leave several Pt structure non connected to the nafion membrane and, as a consequence, not in touch with reactants. Anyway, making MEAs is not so easy because of dispersion and agglomeration issue occurring during the manufacturing.

7.2 N-MC, S-MC and N,S-MC: organic pollutants degradation

Differently doped mesoporous carbons described in Chapters 4 and 5 promote two electrons reduction of O_2 with high selectivity for H_2O_2 production that can reach up 80%. Their ability to promote this reaction pathway was employed for the *in situ* generation of H_2O_2 for water treatment and pollutant degradation. At present, the anthraquinone process is the only economically feasible process for H_2O_2 production on an industrial scale, but it is expensive and generates hazardous waste. Thus, novel, safer and cleaner methods for the production of H_2O_2 are being explored and particularly appealing is the development of electrolysers for the in situ generation of H_2O_2 [2][3].

This experiment consisted in a controlled electrolysis of O_2 bubbled continuously inside the electrochemical cell. Hydrogen peroxide or equivalent radicals species formed during the process react with the organic pollutant and decompose it. H_2O_2 formed at the electrode surface has a good oxidant power, with a $E^{\ominus}$ = 1.78 V [4]. Furthermore, when an undivided electrolytic cell is used, H_2O_2 can be oxidized to O_2 at the anode with formation of hydroperoxyl radical ($^{\bullet}HO_2$) as intermediate, a much weaker oxidant than both H_2O_2 and $^{\bullet}HO$ (eq. 7) [5], in the so-called advanced oxidation with electrogenerated H_2O_2 (AO-H_2O_2). The selected organic pollutant was methyl orange. The experiment was carried out in 0.01 M H_2SO_4 + 0.1 M Na_2SO_4 + 0.25 mM methyl orange in MilliQ H_2O (pH around 2.4). The working electrode was a MC modified GC, which was prepared by drop-casting 100 µL of ink made up of MilliQ H_2O, doped MC catalyst and nafion solution, sonicated for 30 min. The realized carbon loading was 0.6 mg/cm^2. Graphite rod and SCE were employed as counter and reference electrode, respectively. Electrolysis was performed with constant magnetic stirring and temperature equal to 25 °C. Methyl orange degradation was followed by UV-vis spectroscopy and total organic carbon (TOC) analysis. The applied electrolysis potential was equal to -0.5 V/SCE for all electrolyses.

7.2.1 RRDE characterization of N-MC, S-MC and N,S-MC in 0.01 M H_2SO_4 + 0.1 M Na_2SO_4

Electrocatalytic properties toward ORR were tested in O_2 sat. 0.01 M H_2SO_4 + 0.1 M Na_2SO_4 with RRDE configuration, reported in **Figure 7.4**b. The same catalytic effect highlighted in 0.5 M H_2SO_4 (section 5.1.3) is present also in a higher pH solution, since that the oxygen reduction on doped carbon starts 440-570 mV more positive than the bare GC. The activity of these doped carbons was compared to that of a bare glassy carbon. The disk potential (E_d) was varied at 5 mV/s between 0.5 and -1.0 V/SCE at a rotation rate of 1600 rpm. The ring potential (E_r) was kept

constant at 1 V/SCE. The catalytic activity is defined as the variation of the onset potential: $\Delta E_{onset} = E_{onset}^{MCs} - E_{onset}^{GC}$. The E_{onset} for the doped MCs decreases in the order N-MC > N,S-MC > S-MC. In Table 7.2 the data obtained from RRDE for catalytic activity, exchanged electrons and selectivity toward ORR are reported. In **Figure 7.4**a the CVs for ORR in O_2 sat. 0.01 M H_2SO_4 + 0.1 M Na_2SO_4, are reported, in which it is possible to observe the peak potentials for ORR decreasing in the order N-MC > N,S-MC ≈ S-MC, and the capacitive current decreases in the same order. The capacitive current is the highest for N-MC because of N heteroatom. In **Figure 7.4**c a CV of 0.25 mM of methyl orange in O_2 sat. 0.01 M H_2SO_4 + 0.1 M Na_2SO_4 is reported: a reversible peak is present around to 0.4 V/SCE, followed by an irreversible peak at around -0.7 V/SCE, associated probably to electrochemical reductions of aromatic system.

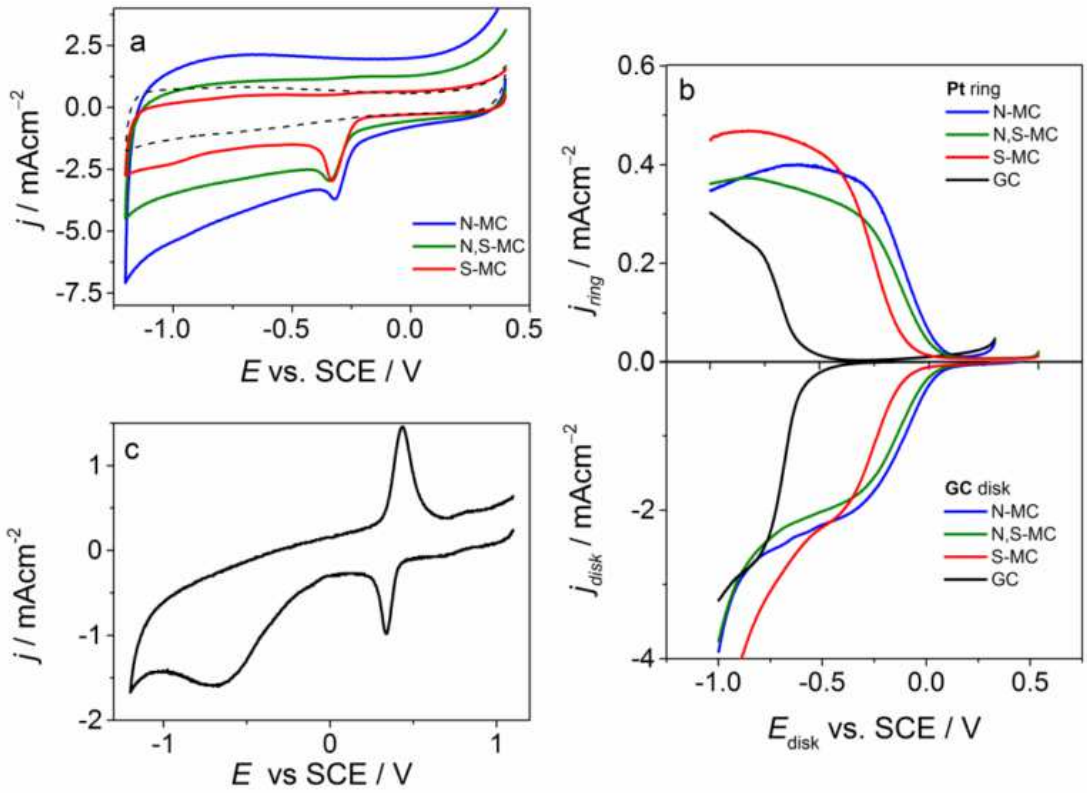

Figure 7.4 a) Cyclic voltammetries at N-MC, S-MC and N,S-MC in O_2 saturated 0.01 M H_2SO_4 + 0.1 M Na_2SO_4; υ = 200 mV/s; b) RRDE (Pt ring and GC disk) LSV at N-MC, S-MC and N,S-MC in O_2 saturated 0.01 M H_2SO_4 + 0.1 M Na_2SO_4; υ = 5 mV/s, rotation rate 1600 rpm, E_{ring} = 1.0 V/SCE; c) MO CV in 0.01 M H_2SO_4 + 0.1 M Na_2SO_4 at N-MC modified electrode, υ = 200 mV/s.

Table 7.2 Electrochemical data obtained from linear sweep voltammetry at RRDE in O_2 saturated 0.01 M H_2SO_4 + 0.1 M Na_2SO_4 solutions.

	E_{onset}[a] (V)	ΔE_{onset}[b] (V)	n[c]	χ_{H2O2}[d] (%)
GC	-0.489	-	2.93	53.5
N-MC1	0.087	0.576	2.31	84.5
S-MC1	-0.046	0.443	2.29	85.5
N,S-MC1	0.054	0.543	2.37	81.5
MC	-0.021	0.468	2.49	74.5

[a] potentials are referred to SCE
[b] $\Delta E_{onset} = E_{onset}^{MCs} - E_{onset}^{GC}$
[c] number of transferred electrons calculated from RRDE
[d] selectivity toward H_2O_2 calculated with RRDE experiment

7.2.2 Methyl Orange Degradation Characterization

Figure 7.5 and Figure 7.6 report the results of the electrochemical treatment of Methyl Orange (MO) in O2 saturated 0.01 M H2SO4 + 0.1 M Na2SO4 solution, where the working electrode was a N doped MC modified GC electrode. The O2 solution saturation can be accomplished by insufflating either pure O2 or a standard air mixture. The degradation was carried out at pH = 2.4. The electrolysis was carried out at a fixed potential (E = -0.5 V/SCE) in order to generate H2O2 for the dye degradation. When N-MC was used as cathode, the dye solution was completely decolourized after the passage of 150 C, with a mean current density observed of 0.783 mA/cm2 (Figure 7.5a and b). Since the solution colour is pH dependent, the solution pH was monitored during the treatment confirming a slight pH change after the treatment, passing from 2.4 to 3.1 (Table 7.3). The bleaching of the solution was confirmed by the decrease of the absorption band centred at 507 nm associated with the –N=N– bond (Figure 7.5c), whereas the mineralization of the dye was evaluated by TOC analysis, which pointed out the incineration of the 67% of the organic fraction (Table 7.3). The degradation can be associated with the homogeneous oxidation of the dye by the H2O2 generated in situ. At the same time new absorption bands grow in the UV region, indicating the formation of lower molecular weight species, resulting from the degradation of MO. The cleavage of the azo-bond is responsible of the chromophore characteristic loss and generates intermediates which, according to literature, absorb in the spectral range 260– 300 nm and can be referred as multi-substituted aromatic species as phenol, catechol or hydroquinone [6]. To verify whether the N-MC is effectively responsible for the production of the bleaching agent H2O2 and that the MO degradation is not the consequence of its direct reduction at the electrode surface or its direct and indirect oxidation at graphite counter electrode, two more experiments were implemented: one

employing GC as working electrode (at *E* = -0.5 V vs. SCE) in the presence of O2, and a second one using a N-MC modified GC, but in the absence of oxygen. The results reported in Figure 7.6a clearly point out that the dye degradation is less effective when H2O2 is generated by O2 reduction at bare GC or when MO is degraded at the N-MC electrode, without the homogeneous mediation of H2O2. Furthermore, it may be observed that the sample was not mineralized since TOC values remains unchanged during the electrolysis (Table 7.3). In fact, the recorded current density at GC electrode is far lower than at N-MC (0.197 mA/cm2), due to the scarce catalytic activity of GC with respect to the doped MC, so that also the production of H2O2 is hindered. Furthermore, when N-MC modified GC is used and O2 is not purposely inflated in solution the only electrochemical process that may occur, at E = -0.5 V vs. SCE, is the direct reduction of the dye at the working electrode, as confirmed by the voltammetric behaviour of MO reported in Figure 7.4. These outcomes allow to exclude the contribution of the direct oxidation of the dye at the graphite counter electrode (CE), whereas its indirect oxidation by oxidant species generated at CE can be considered not substantial. In fact, it is reasonable that if the CE has an active role in the dye oxidation or in the generation of •HO2 radicals, this would occur notwithstanding the nature of the working electrode or the presence of O2 in solution. However, the generation of •HO2 cannot be excluded at present, even though its oxidant power is lower than H2O2 itself. The degradation tests were carried out also at S-MC and N,S-MC coated GC electrode (Figure 7.4a). An un-doped MC (u-MC), with similar surface area and morphology of N-MC, was also considered for sake of comparison. Figure 7.6 b and c show the MO concentration and the current density variation during the electrolyses. It is clear from Figure 7.6b that u-MC coated GC electrode performs better than the naked GC, but worsen than N-MC. In fact, the final MO degradation is higher than 90%, but the TOC abatement is only slightly higher than 32% (Table 7.3). u-MC showed to improve the MO and TOC abatement with respect to the naked GC, because of a higher surface area and a more intimate contact between O_2, electrolyte and electrode surface. On the other hand, the superior activity of N-MC is easily appointable to a better catalytic activity towards ORR that nitrogen doped material showed with respect to u-MC [7]. In the case of S-MC the degradation efficiency is slightly lower than at N-MC (Figure 7.6b) and this may be referred to the lower catalytic activity at S-MC with respect to N-MC and to the sideway H2 evolution, which accounts for the higher mean current density recorded (0.867 mA/cm2). When N,S-MC is used, the degradation is initially faster than at both N-MC and S-MC (Figure 7.6e), but after two hours the degradation kinetics slows down as confirmed by the rapid slope change in the experimental point trend. This type of behaviour may be due to a loss of activity during the experiments possibly triggered by the same H_2O_2 generated at the electrode. However, deeper investigations on optimized as diffusion electrodes

are needed for better addressing the material stability. The lower performances of S-MC and N,S-MC with respect to N-MC were confirmed also by TOC analysis which established a mineralization of 53% and 2% of the organic dye, respectively.

Table 7.3 Electrolysis data in O_2 sat. 0.01 M H_2SO_4 + 0.1 M Na_2SO_4 + 0.25 mM MO solution at different electrodes at *E* = -0.5 V/SCE.

	pH_{in}	pHf_{in}	j_0[a] (mA/cm^2)	J[b] (mA/cm^2)	Q_{tot} (C)	$[MO]_{fin}$[c] (%)	TOC (mg/L)	TOC[d] (%)
N-MC1	2.4	3.1	1.350	0.783	150	0.5	13.86	33
N-MC1[e]	2.4	2.5	0.025	0.023	5.5	87.8	42.6	100
S-MC1	2.4	3.1	1.433	0.948	150	0.5	19.74	47
N,S-MC1	2.4	3.0	0.917	0.607	150	6.5	41.16	98
MC	2.4	2.9	0.783	0.627	150	7.9	28.56	68
GC	2.4	2.6	0.205	0.161	28.9	60.3	41.9	100

[a] starting current density with respect to geometric area
[b] calculated mean current density
[c] MO concentration at the end of electrolysis
[d] TOC measured at the end of the electrolysis
[e] in absence of O_2

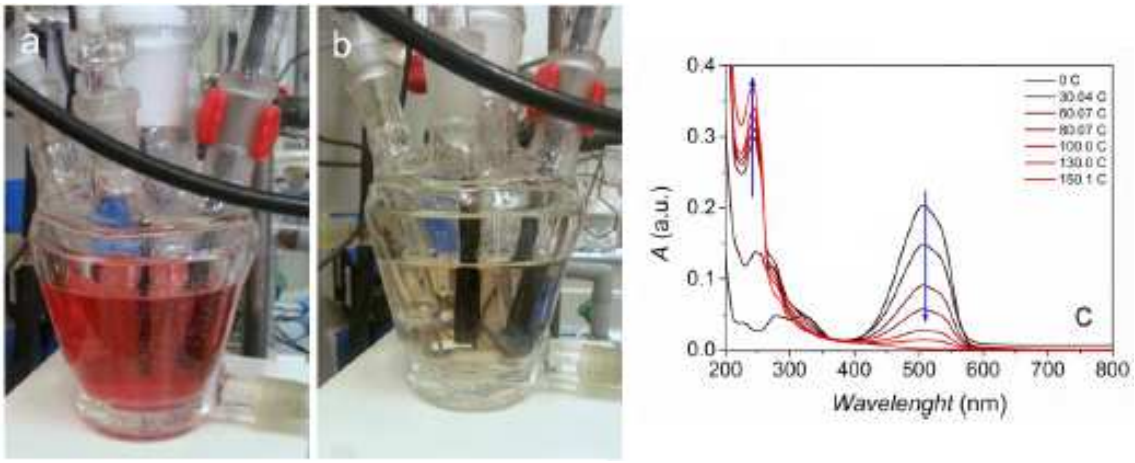

Figure 7.5 Methyl Orange solution before (a) and after (b) the electrochemical treatment; c) evolution of the absorbance spectrum for methyl orange during the electrolysis.

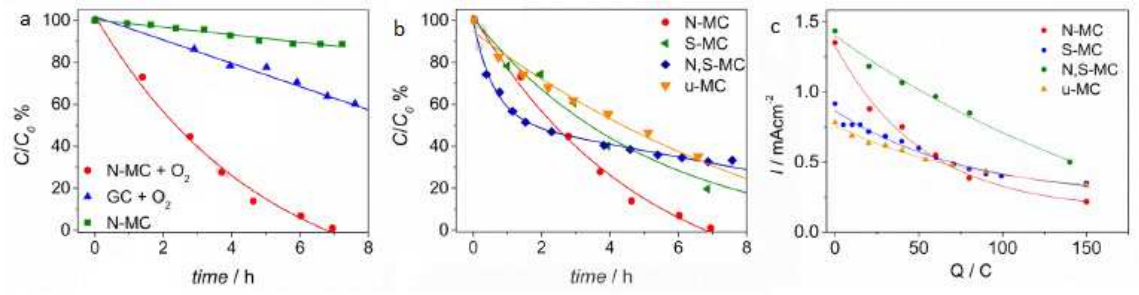

Figure 7.6 a) Methyl orange degradation in 0.01 M H_2SO_4 + 0.1 M Na_2SO_4 at N-MC in O_2 sat. solution (red), GC in O_2 sat. solution (blue) and N-MC in a free O_2 solution (green); b) Methyl orange degradation in O_2 sat. 0.01 M H_2SO_4 + 0.1 M Na_2SO_4 at N-MC (red), N,S-MC (blue), S-MC (green) and un-doped MC (yellow); c) Variation of current density with the charge.

The work described in Section 7.2 originated a publication [8].

Bibliography

[1] E. Antolini, Carbon supports for low-temperature fuel cell catalysts, Appl. Catal. B Environ. 88 (2009) 1–24. doi:10.1016/j.apcatb.2008.09.030.

[2] J.M. Campos-Martin, G. Blanco-Brieva, J.L.G. Fierro, Hydrogen peroxide synthesis: An outlook beyond the anthraquinone process, Angew. Chemie - Int. Ed. 45 (2006) 6962–6984. doi:10.1002/anie.200503779.

[3] J.K. Edwards, B. Solsona, E.N. N, A.F. Carley, A. a Herzing, C.J. Kiely, G.J. Hutchings, Switching Off Hydrogen Peroxide Hydrogenation in the Direct Synthesis Process, Science 323 (2009) 1037–1041.

[4] M. Giomo, A. Buso, P. Fier, G. Sandonà, B. Boye, G. Farnia, A small-scale pilot plant using an oxygen-reducing gas-diffusion electrode for hydrogen peroxide electrosynthesis, Electrochim. Acta. 54 (2008) 808–815. doi: 10.1016/j.electacta.2008.06.038.

[5] E. Brillas, J.C. Calpe, J. Casado, Mineralization of 2,4-D by advanced electrochemical oxidation processes, Water Res. 34 (2000) 2253–2262. doi: 10.1016/S0043-1354(99)00396-6.

[6] E. Guivarch, S. Trevin, C. Lahitte, M.A. Oturan, Degradation of azo dyes in water by Electro-Fenton process, Environ. Chem. Lett. 1 (2003) 38–44. doi: 10.1007/s10311-002-0017-0.

[7] V. Perazzolo, C. Durante, R. Pilot, A. Paduano, J. Zheng, G.A. Rizzi, A. Martucci, G. Granozzi, A. Gennaro, Nitrogen and sulfur doped mesoporous carbon as metal-free electrocatalysts for the in situ production of hydrogen peroxide, Carbon, 95 (2015) 949–963. doi: 10.1016/j.carbon.2015.09.002.

[8] V. Perazzolo, C. Durante, A. Gennaro, Nitrogen and sulfur doped mesoporous carbon cathodes for water treatment, J. Electroanal. Chem., 782 (2016) 264-269. doi: 10.1016/j.jelechem.2016.10.037

Future Perspectives

In this work nitrogen and sulphur doped and codoped mesoporous carbon were synthesized via a hard template approach and modified with Pt NPs in order to obtain catalysts for the oxygen reduction reaction.

During the first year of Ph.D. the comprehensive characterization of hard template technique was carried out. The aim was to evaluate the effect of different pyrolysis condition on the properties of the final porous carbon. In particular, the effect of silica template, pyrolysis temperature and carbon precursors was evaluated in properties such as morphology, porosity, surface area, chemical composition, thermal stability, electrical conductivity and activity toward oxygen reduction. A pyrolysis temperature of 750 °C allows to obtain a proper amount of dopant heteroatom in the carbon structure, together with good thermal stability and electrochemical activity. Silica P200 allows to have the highest surface area, good pore dimensions and electrical conductivity, so it was selected as representative template.

In the second year of Ph.D. the deposition of Pt NPs on the synthesized mesoporous carbon supports was investigated. Different deposition strategies and Pt precursor salts were tested, showing that the solid state deposition under N_2/H_2 at high temperature with Pt(II) salt allows to obtain the best distribution of Pt NPs on the whole surface of the mesoporous carbon. S doping is responsible for an improved electrochemical activity toward oxygen reduction compared to N doping, and both Pt modified N-MC and S-MC are more active than Pt on an undoped mesoporous carbon support. XPS proved an electronic effect consisting in a charge transfer from Pt to S-MC, which turns out to be favourable for oxygen reduction.

During the third and last year of Ph.D. the improvement of experimental protocol was carried out at Toyota Motor Europe, Zaventem, Belgium. The electrochemical characterization was repeated in controlled and proper experimental conditions, confirming a 20% increase of MA in the case of Pt@S-MC compared to commercial Pt-based catalyst (TKK). Stability tests were performed in order to evaluate the modification occurring at Pt and doped mesoporous carbons along with electrochemical stress. They proved that Pt is slightly more stable on N-MC, but the

homemade mesoporous carbon are less stable than commercial mesoporous carbon as a high potential is applied for a long time. Pt@N-MC and Pt@S-MC were incorporated in the cathodic site of a MEA, to test their properties toward oxygen reduction in a PEMFC. The fast corrosion of doped mesoporous carbons highlighted during the stability tests and the low performance generated in PEMFC are ascribed to two main issues:

i. Low graphitization degree, due to the low employed pyrolysis temperature (750°C) which allows a proper content of heteroatoms, but at the same time it prevents the fully formation of sp^2 carbon, responsible for electrical conductivity. This results also in the presence of oxygen containing groups, which decrease the electrochemical stability of the carbon supports.
ii. The low pore dimensions. N-MC and S-MC have mean pore diameter around 4 nm, good for gas diffusion, but not big enough to allow proper Nafion distribution inside the pore system. This prevent the exposure of inner Pt NPs to reactants, resulting in a lower amount of active Pt in PEMFC.

So, graphitization and pore size are the two main parameter to be modified in order to improve the realized doped carbon support. Higher graphitization degree can be obtained simply by higher pyrolysis temperature. It's more challenging to maintain high amount of heteroatoms in the carbon structure: in fact, with high pyrolysis temperature, heteroatoms are eliminated from the carbon structures. It's fundamental to find different ways of doping carbon materials. A suitable procedure could be post-treatment: in this case high graphitic carbon can be easily obtained via hard template process, and the heteroatoms can be introduced during a second step, i.e. by reaction with $NH_{3(g)}$ or H_2SO_4. Secondly, it's important to realize bigger pore size that allow a good nafion distribution also in the inner part of the pores. Pore dimension depends directly on the distance between adjacent pores, so silica which possess this morphology could be useful to realize mesoporous carbon with bigger pore size than that obtained with silica P200. Also alternatives routes may be taken in account, i.e. soft template.

Nowadays non platinum group (NPG) metals are becoming more and more important in the realization of ORR catalyst. As already stated in the introduction, Pt is expensive and rare, so it's fundamental to reduce its employment and to substitute it with cheap and common metals. However, the activity toward ORR of other metals than Pt is low, but it can be improved by realising strong metal-support interaction that modify the metal electronic structure with a positive effect on the catalytic activity. In this case doped mesoporous carbons might represent a suitable starting point, given that in this thesis is proved that they're responsible for a

modification of Pt activity toward ORR via a charge transfer process taking place between the metal and the support. A good example of NPG catalyst consists in the system Fe-phenanthroline on high surface area carbon, but its catalytic activity remains still low compared to that of Pt. A good compromise is represented by ‘hybrid’ catalysts, in which Pt is still present but its amount is drastically reduced, and it is combined with a co-catalyst.

Appendix A

Instruments and Chemicals

Instruments

All electrochemical measurements were conducted with Autolab 100N (Eco-Chimie, Utrecht, The Nederlands), Parc 273a (EG&G Princeton Applied Research) or Biologic SP-300 potentiostats, all connected to a computer running Nova, or respectively. The working electrode was a GC rotating disk electrode tip (Metrohm, 3 mm diameter) employed in both static and hydrodynamic conditions, according the experiment. The reference electrode was a sat. Calomel (SCE, $Hg|Hg_2Cl_2|KCl_{(sat.)}$) (Shott) or a homemade reversible hydrogen electrode (RHE), the counter electrode was a Pt wire for the ORR performance experiments or a graphite rod for the stability test. Scanning Electron Microscopy (SEM) images were obtained using a Zeiss Supra 35VP Gemini scanning electron microscope operating at 5 kV. Trasmission Electron Microscopy (TEM) images were obtained using a FEI Tecnai G2 transmission electron microscope operating at 100 Kv. The specific surface areas of the samples were calculated by a multipoint Brunauer Emmett Teller (BET) analysis of the nitrogen adsorption/desorption isotherms recorded at 77 K using a Quantachrome Nova 1200e Surface Area and Pore Analyzer, whereas the pore size distribution curves were derived using density functional theory (DFT), both on the adsorption and desorption branches. Thermogravimetric analysis (TGA) was carried using a Q5000IR TGA instrument (TA Waters). Elemental analyses were performed by Thermo Scientific Flash 2000 analyzer. X-ray photoemission spectroscopy (XPS) measurements were performed in an UHV chamber (base pressure < $5x10^{-9}$ mbar), equipped with a double anode X-ray source (Omicron DAR-400), a hemispherical electron analyser (Omicron EIS-125) at r.t., using non-monochromatized Mg-Kα radiation (hv = 1253.6 eV) and a pass energy of 50 eV and 20 eV for the survey and the single spectral windows, respectively. The calibration of the Binding Energy (BE) scale was carried out using Au 4f as reference (BE Au 4f = 84.0 eV). Mesoporous carbon syntheses were conducted on a Carbolite EHA, solid state deposition of Pt was conducted on a Carbolite MTF.

Catalyst precursors

Carbon precursors: Carbazole (>95%), 1,10 phenanthroline (>99.5%), phenothiazine (>98%), dibenzothiophene (>98%), indigo carmine (>98%), antracene (>98%) and sucrose (>99%) were all purchased from Sigma-Aldrich and used without further purification.

Silica templates: silica P200, SBA-15, MSU-H, MCM-41 and P20 are all purchased from Sigma-Aldrich and used without further treatment.

Platinum precursors: $Pt(acac)_2$ (97%), $PtCl_2$ (98%), H_2PtCl_6 xH_2O (99.9%), K_2PtCl_6 (98%) were all purchased by Sigma-Aldrich and used without further purifications.

Other chemicals

H_2O (Milli-Q or Ultrapure), Ethanol (Fluka HPLC, >99,8%), Nafion (Sigma Aldrich, 5 ww% in a mixture of lower aliphatic alcohols and water), Acetone (Sigma Aldrich, >99,5%), Isopropanol (Sigma Aldrich, >99.8%, puriss. p.a., ACS reagent), H_2SO_4 (Fluka, >95%, TraceSELECT®), NaOH (VWR, >99%), $NaBH_4$ (Sigma Aldrich, 98%), Nochromix® (Sigma Aldrich), commercial mesoporous carbon (C-MC, Sigma Aldrich, <500 nm particle size, 99.95%) were all used as received.

Appendix B

Papers and Conferences

Papers

Perazzolo, V.; Durante, C.; Gennaro, A., Nitrogen and Sulfur Doped Mesoporous Carbon Cathodes for Water Treatment, *J. Electroanal. Chem.*, **2016**, 782, 264-269.

Perazzolo, V.; Grądzka, E.; Durante, C.; Pilot, R.; Vicentini, N.; Rizzi, G.A.; Granozzi, G.; Gennaro, A., Chemical and Electrochemical Stability of Nitrogen and Sulphur Doped Mesoporous Carbons, *Electrochim. Acta,* **2016**, 197, 251-262.

Perazzolo, V.; Durante, C.; Pilot, R.; Paduano, A.; Zheng, J.; Rizzi, G.A.; Martucci, A.; Granozzi, G.; Gennaro, A., Nitrogen and sulfur doped mesoporous carbon as metal-free electrocatalysts for the *in situ* production of hydrogen peroxide, *Carbon*, **2015**, 95, 949-963.

Perini, L.; Durante, C.; Favaro, M.; **Perazzolo, V.**; Agnoli, S.; Schneider, O.; Granozzi, G.; Gennaro, A., Metal-support interaction in platinum and palladium nanoparticles loaded on nitrogen-doped mesoporous carbon for oxygen reduction reaction, *ACS Appl. Mater. Interfaces*, **2015**, 7 (2), 1170–1179.

Durante, C.; **Perazzolo, V.**; Isse, A.A.,; Favaro, M.; Granozzi, G.; Gennaro, A., Electrochemical Activation of Carbon-Halogen bonds: Electrocatalysis at Palladium/Copper Nanoparticles, *ChemElectroChem*, **2014**, 1, 1370-1381.

Durante, C.; **Perazzolo, V.**; Perini, L.; Favaro, M.; Granozzi, G.; Gennaro, A., Electrochemical Activation of Carbon-Halogen bonds: Electrocatalysis at Silver/Copper Nanoparticles, *Appl. Catal., B,* **2014**, 158-159, 286-295.

Conferences

Perazzolo, V.; Durante, C.; Rizzi, G.A.; Granozzi, G.; Gennaro, A., Nitrogen and Sulphur Doped Mesoporous Carbon as Support for Platinum Nanoparticles, 67th Annual Meeting of the International Society of Electrochemistry, 21-26 August 2016, The Hague, The Netherlands.

Perazzolo, V.; Astier-Perret, R.; Durante, C.; Cerri, I.; Gennaro, A., Controlled Size Pt-Nanoparticles on N- and S-Doped Mesoporous Carbon as Cathode Materials for PEMFCs, 67th Annual Meeting of the International Society of Electrochemistry, 21-26 August 2016, The Hague, The Netherlands.

Gennaro, A.; Picelli, L.; **Perazzolo, V.**; Pilot, R.; Martucci, M.; Causin, V.; Durante, C., Chemical and Electrochemical Properties of Mesoporous Carbon Nitride suitable for Oxygen Reduction Reaction, 67th Annual Meeting of the International Society of Electrochemistry, 21-26 August 2016, The Hague, The Netherlands.

Durante, C.; Gennaro, A.; Granozzi, G.; **Perazzolo, V.**; Picelli, L.; Rizzi, G.A., Synergistically Enhanced Performances of Pt Nanoparticles on Doped Mesoporous Carbon for Oxygen Reduction Reaction, 18th Topical Meeting of the International Society of Electrochemistry, 8 - 11 March 2016, Gwangju, South Korea.

Durante, C.; Gennaro, A.; Picelli, L.; Granozzi, G.; **Perazzolo, V.**; Rizzi, G.A., Synergistically Enhanced Performances of Pt Nanoparticles on Doped Mesoporous Carbon for Oxygen Reduction Reaction, Enerchem-1, 18-20 February 2016, Florence.

Durante, C.; **Perazzolo, V.**; Pilot, R.; Paduano, A.; Zheng, J.; Rizzi, G.A.; Martucci, A.; Granozzi, G.; Gennaro, A., Nitrogen and Sulphur Doped Mesoporous Carbon as Metal Free Electrocatalyst for the in Situ Production of Hydrogen Peroxide, Giornate dell'Elettrochimica Italiana (GEI), 20-24 Settembre 2015, Bertinoro.

Perazzolo, V.; Durante, C.; Rizzi, G.A.; Granozzi, G.; Gennaro, A., Platinum Nanoparticles on Nitrogen and Sulphur Doped Mesoporous Carbon for Oxygen Reduction Reaction, Giornate dell'Elettrochimica Italiana (GEI), 20-24 Settembre 2015, Bertinoro.

Durante, C.; **Perazzolo, V.**; Pilot, R.; Zheng, J.; Paduano, A.; Rizzato, V.; Rizzi, G.A.; Maddalena, A.; Bozio, R.; Granozzi, G.; Gennaro, A., Nitrogen and Sulphur Doped Mesoporous Carbon as Support for Pt Electrocatalyst in Oxygen Reduction Reaction, 13th International Fischer Symposium: a Meeting on Nanoscale Electrochemistry, June 7 - 11, 2015.

Durante, C.; **Perazzolo, V.**; Isse, A.A.; Favaro, M.; Granozzi, G.; Gennaro, A., Electrochemical Activation of Carbon-Halogen Bonds: Electrocatalysis at Palladium/Copper Nanoparticles, ISE 2014, 65th Annual Meeting, 31 August - 5 September 2014, Lausanne, Switzerland.